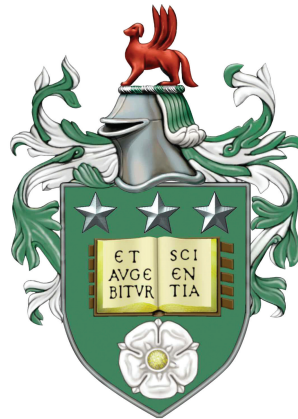


Wave Propagation In Staggered-Grid Finite-Difference Models With Boundaries

Muhamad Najib Bin Zakaria



Submitted in accordance with the requirements for
the degree of Doctor of Philosophy

The University of Leeds
School of Mathematics

June 2019

The candidate confirms that the work submitted is his own and that appropriate credit has been given where reference has been made to the work of others.

This copy has been supplied on the understanding that it is copyright material and that no quotation from the thesis may be published without proper acknowledgement.

Acknowledgements

I would like to express my deepest gratitude to my supervisor, Dr. Stephen Griffiths for his superb guidance and advice. I sincerely appreciate his patience, motivation and helps offered in doing my research. His enthusiasm for this work and all things scientific has been inspiring. Thanks also to my advisor, Prof Mark Kelmanson for his input, helpful discussions and support in this research. Besides, I sincerely have to thank all those who have supported and helped me in completing this thesis.

My special thanks to my lovely wonderful wife, Hazzirah Izzati Mat Hassim, for her unconditional love, understanding, sacrifice and endless moral support. I overwhelmingly owe a lot to my sweet and precious son, Muhammad Zharif Daniel. Staying apart during final year was the hardest thing but makes all of us stronger people.

Thanks also to my beloved parents, Zakaria Mohd Said and Sarah Ahmad, for being very supportive and understanding. Not to be forgotten, I wish to express my appreciation to all my siblings and friends for always being with me in undergo the hard times together.

Abstract

Finite-difference numerical models are widely used in acoustics, electrodynamics and fluid dynamics. In particular, the so-called C-grid (or Yee grid) is a popular staggered-grid formulation, with excellent conservation properties and a natural positioning of nodes. However, domain boundaries are typically treated as staircases, and these degrade the accuracy of the numerical solutions. Here that degradation is quantified for various linear wave propagation problems in idealised geometries.

Here, the discrete solution is studied for three important models: (i) wave propagation along a channel, (ii) wave reflection at a planar wall, (iii) the long-time dynamics of waves sloshing in two simple closed domains (square and circle). The first two problems are solved analytically, using asymptotics to examine the limit of small grid spacing h , with expressions for the wavespeed reduction (in (i)) and a phase error (in (ii)) being derived. The third problem is examined numerically, using a high-order time-stepping scheme so that the effects of the staircase boundaries can be isolated. We typically find first-order convergence in grid spacing h , although there are some variations, according to whether we consider convergence in velocities or pressure, and also whether we use L_2 or L_∞ -norm.

Some extensions to the propagation of internal waves in a density stratified medium are also considered, which is a less standard scenario, but which has considerable significance in geophysical fluid dynamics.

Contents

Acknowledgements	ii
Abstract	iii
Contents	iv
List of figures	ix
List of tables	xxviii
1 INTRODUCTION	1
1.1 Waves	1
1.2 Mathematical modelling of waves	3
1.3 Numerical solutions of wave equations	6
1.4 Staggered-grid finite difference methods in two spatial dimensions	8
1.5 Aims and outline of this thesis	11
2 MATHEMATICAL BACKGROUND: WAVES AND STAGGERED FINITE-DIFFERENCE SCHEMES IN UNBOUNDED DOMAINS	15
2.1 Introduction	15
2.2 Physical Systems	17
2.2.1 Acoustic waves	17
2.2.2 Electromagnetic waves	19
2.2.3 Shallow-water flows	22
2.3 Conservation Laws	25
2.3.1 Conservation of mass	26

2.3.2	Conservation of energy	27
2.4	Wave Propagation	28
2.5	Finite-Difference Approximations	30
2.5.1	A-grid	31
2.5.2	B-grid	32
2.5.3	C-grid	33
2.6	Discrete Conservation Laws	33
2.6.1	Discrete Conservation of Mass	34
2.6.2	Discrete Conservation of Energy	35
2.7	Discrete Waves	38
2.7.1	A-grid solutions	39
2.7.2	B-grid solutions	40
2.7.3	C-grid solutions	41
2.7.4	Comparison of discrete frequency on the A-, B-, and C-grid	42
2.8	Summary	45
3	WAVE PROPAGATION ALONG A CHANNEL	49
3.1	Introduction	49
3.1.1	Nondimensional equations	52
3.2	Continuum Solutions	52
3.3	Boundary Aligned with the Grid	55
3.3.1	Numerical solutions	57
3.3.2	Analytical solutions	61
3.3.3	Asymptotic analysis as $h \rightarrow 0$	63
3.4	Boundary aligned at 45° to the grid	64
3.4.1	Rotated coordinate system	65
3.4.2	Wavelike solutions	67
3.4.3	Numerical solutions	68

3.4.4	Analytical solution	71
3.4.5	Behaviour as $h \rightarrow 0$	75
3.4.6	Numerical verification	80
3.5	Summary	81
4	WAVE REFLECTION AT A PLANAR WALL	85
4.1	Introduction	85
4.2	Boundary Aligned with the Grids	88
4.2.1	Continuum solutions	88
4.2.2	Discrete solutions	91
4.2.3	Numerical visualisation	94
4.3	Tilted boundary: Continuum solution	96
4.4	Tilted boundary: Discrete solution	99
4.4.1	Alternative derivation of amplitude error	106
4.4.2	Spatial structure of discrete solution	108
4.5	Summary	112
5	NUMERICAL SOLUTIONS: THE EFFECT OF STAIRCASE BOUNDARY	121
5.1	Introduction	121
5.2	Numerical Methods	123
5.2.1	Spatial discretization	123
5.2.2	Temporal discretization	127
5.3	Waves in an aligned square	128
5.3.1	Continuum solutions	130
5.3.2	Numerical solutions	135
5.4	Waves in a square tilted at 45° : perfect staircases	147
5.5	Effects of tilt angle on simulated waves	155
5.5.1	Quantification of spatial convergence	159
5.5.2	Frequency reduction	161

5.6	Waves in a circular domain	172
5.6.1	Continuum solutions	172
5.6.2	Numerical solutions	175
5.6.3	Low resolution: $h = 0.1$	176
5.6.4	High resolution: $h = 0.01$	177
5.6.5	The effect of circular mode	178
5.6.6	The effect of cell selection	190
5.7	Summary	201
6	REFLECTION AND FOCUSSING OF INTERNAL GRAVITY WAVES	223
6.1	Introduction	223
6.2	Equations of Motion for Stratified Fluid	229
6.3	Internal gravity waves in an unbounded domain	233
6.3.1	Continuum internal waves	233
6.3.2	Discrete internal waves	235
6.4	Internal Gravity Waves at A Sloping Boundary	237
6.4.1	Continuum Solution	238
6.4.2	Discrete solution	243
6.5	Internal Waves Attractor	250
6.5.1	Numerical setting	251
6.5.2	Freely evolving flow	254
6.5.3	Parametric excitation	257
6.6	Summary	258
7	CONCLUSION	263
7.1	Summary	263
7.2	Overview	267
	Appendices	275

A Stability Testing 277

Bibliography **297**

List of Figures

1.4.1	Spatial distributions of the dependent variables on a square grid. (Taken from [6]).	9
2.2.1	Electromagnetic waves propagate in a channel.	21
2.2.2	Schematic showing a shallow water flow.	22
2.5.1	Distributions of the dependent variables on A-, B-, C-grids. (The figure is reillustrated from [6]).	31
2.6.1	The arrangement of variables on a C-grid.	34
2.7.1	(a) The frequency, (b) the wave speed, and (c) the group speed for the case $f = 0$	45
2.7.2	The dispersion relations for the continuum and finite-difference approximation based on the A, B, and C-grids without rotation effects, $f = 0$	46
2.7.3	The dispersion relations for the continuum and finite-difference approximation based on the A, B, and C-grids with the effects of rotation. The left column is for $L_D/h = 2$, and the right for $L_D/h = 0.1$	47
3.1.1	Wave propagation in a channel.	53
3.3.1	(a) The Arakawa C-grid and (b) the configuration of aligned boundaries for a channel.	55

3.3.2	The numerical solution \hat{v} for wave propagation along the aligned channel at different mode $j = 1, 2, 3$ with along channel wavenumber $k = 1$, and grid spacing $h = 1/20$	59
3.3.3	The convergence plot of ω_d for wave propagation along a channel with aligned boundaries for mode $j = 1, 2, 3$ and $k = 1$. The slope of the lines are 1.9992 (mode $j = 1$), 1.9971 (mode $j = 2$) and 1.9935 (mode $j = 3$), indicate second-order convergence.	59
3.3.4	The convergence plot of v for wave propagation along the channel with aligned boundaries for mode $j = 1, 2, 3$ with $k = 1$. The slope of the lines are 1.9907 (mode $j = 1$), 1.9659 (mode $j = 2$), and 1.9467 (mode $j = 3$), indicate second-order convergence.	60
3.3.5	The frequency ω for wave propagation along the channel with aligned boundaries with horizontal wavenumber $k = 1$ and modes $j = 1, 2, 3$ at various grid spacing h . Black represents ω for $j = 1$, blue for $j = 2$, and red for $j = 3$	60
3.4.1	(a) The new indices in the transformation coordinate axes, and (b) the computational domain of the tilted channel with staircase boundaries.	65
3.4.2	The continuum and numerical solutions for \hat{P} at four different cross-channel modes j for along-channel wavenumber $k = 1$ with grid boxes across channel $N^* = 100$, i.e., $h = \sqrt{2}/100$	69
3.4.3	The differences in \hat{P} for different cross-channel modes j for along-channel wavenumber $k = 1$ with grid boxes across channel $N^* = 100$, i.e., $h = \sqrt{2}/100$	70

3.4.4	(a) The solutions for along-channel flow u at $j = 2$ for along-channel wavenumber $k = 1$. (b) The differences between continuum and numerical solutions.	72
3.4.5	(a) The solutions for cross-channel flow v at $j = 2$ for along-channel wavenumber $k = 1$. (b) The differences between continuum and numerical solutions.	72
3.4.6	The dispersion relations for the channel aligned at 45° from the x -axis with staircase boundaries for cross-channel mode $j = 0, 1, 2, 3$ with along channel wavenumber $k = 1$	73
3.4.7	The graph of $\log_{10} h$ against $\log_{10} \omega_d - \omega_c $ for cross-channel mode $j = 0, 1, 2, 3$ with along channel wavenumber $k = 1$. The slope of the lines are 0.9942, 0.9961, 1.0061 and 1.0218, indicate first order of convergence.	74
3.4.8	The scaling factor $A(k)$ for across channel mode $j = 1, 2, 3$ at various grid spacing h	82
4.2.1	The wave reflection at a solid wall.	89
4.2.2	The wave reflects at boundary aligned with the grid.	91
4.2.3	The continuum solutions of p , u , and v for wave reflection at aligned boundary at $t = 0$, with horizontal wavenumber $k = 1$, vertical wavenumber $l = -2$. The left column is the incident wave component, centre column is the reflected component, and the right column is the total component (i.e., incident + reflected). The top row is the solution for pressure p , second row is velocity u , and third row is the velocity v	95
4.3.1	The wave reflects at a planar wall tilted 45° from x -axis.	96
4.4.1	The wave reflects at boundary unaligned with the grid.	100

-
- 4.4.2 Blue is φ determined directly from A_R/A_I (4.4.26), and is constrained via $-\pi < \varphi \leq \pi$; red is the linear approximation for φ (4.4.28) when $h \ll 1$ 109
- 4.4.3 The continuum solutions of wave reflection at a straight boundary $y = x$ with horizontal wavenumber $k_I = 1$ and vertical wavenumber $l_I = -2$. Shown are the solutions for p (first row), u (second row) and v (third row) at $t = 0$. The left column is the incident wavecomponent, the centre column is the reflected wave component, and the right column is the total (i.e., incident + reflected) component. 113
- 4.4.4 The total wave component of p for wave reflection at staircase boundaries with horizontal wavenumber $k = 1$, vertical wavenumber $l = -2$, grid spacing $h = 2\pi/50 \approx 0.1257$, at three different values t . The first column is the continuum solution, the second column is the discrete solution, and the third column is the error (i.e., continuum – discrete). First row is the solution at $t = 0$, second row at $t = \pi/2\omega$, and third row at $t = \pi/\omega$ 114
- 4.4.5 The total wave component of u for wave reflection at staircase boundaries with horizontal wavenumber $k = 1$, vertical wavenumber $l = -2$, grid spacing $h = 2\pi/50 \approx 0.1257$, at three different values t . The first column is the continuum solution, the second column is the discrete solution, and the third column is the error (i.e., continuum – discrete). First row is the solution at $t = 0$, second row at $t = \pi/2\omega$, and third row at $t = \pi/\omega$ 115

-
- 4.4.6 The total wave component of v for wave reflection at staircase boundaries with horizontal wavenumber $k = 1$, vertical wavenumber $l = -2$, grid spacing $h = 2\pi/50 \approx 0.1257$, at three different values t . The first column is the continuum solution, the second column is the discrete solution, and the third column is the error (i.e., continuum – discrete). First row is the solution at $t = 0$, second row at $t = \pi/2\omega$, and third row at $t = \pi/\omega$ 116
- 4.4.7 The solutions for u , v and p along with the error at $t = 0$ at high resolution ($h = \sqrt{2}/100 \approx 0.0628$). The first column is the continuum, the second column is the discrete, and the third column is the error (i.e., continuum – discrete). 117
- 5.2.1 Example of grid generation. The active grid cells on the left column are activated by cell-centre condition, while the right column by the four corner condition. Black circles represent u nodes, white circles represent v nodes, and black squares represent p nodes. 129
- 5.3.1 The numerical solutions of p for aligned square at $t = 9T, 9.25T, 9.5T, 9.75T, 10T$, with $h = 0.01$ and $dt = 0.005$. Left column: continuum solutions. Centre column: numerical solutions. Right column: error (i.e., continuum–numerical). 138
- 5.3.2 The numerical solutions of u at $t = 9T, 9.25T, 9.5T, 9.75T, 10T$, with $h = 0.01$ and $dt = 0.005$. Left column: continuum solutions. Centre column: numerical solutions. Right column: error (i.e., continuum-numerical). 139

5.3.3	The numerical solutions for v at $t = 9T, 9.25T, 9.5T, 9.75T, 10T$, with $h = 0.01$ and $dt = 0.005$. Left column: continuum solutions. Centre column: numerical solutions. Right column: error (i.e., continuum-numerical).	140
5.3.4	Mass difference and energy difference for aligned square domain, with $h = 0.01$ and $dt = 0.005$	141
5.3.5	Maximum error for aligned square domain over $0 < t < 10T$, with $h = 0.01$ and $dt = 0.005$	141
5.3.6	The maximum of $ p $ for aligned square domain over $0 < t < 10T$ for aligned square domain, with $h = 0.01$ and $dt = 0.005$	142
5.3.7	The numerical solutions of p for aligned square domain at $t = 0, T/4, T/2, 3T/4, T$, with $h = 0.1$ and $dt = 0.01$. Left column: continuum solutions. Centre column: numerical solutions. Right column: error (i.e., continuum-numerical).	143
5.3.8	The numerical solutions of p for aligned square domain at $t = 9T, 9.25T, 9.5T, 9.75T, 10T$, with $h = 0.1$ and $dt = 0.01$. Left column: continuum solutions. Centre column: numerical solutions. Right column: error (i.e., continuum-numerical).	144
5.3.9	The maximum of $ p $ for aligned square domain over $0 < t < 10T$ for aligned square domain, with $h = 0.1$ and $dt = 0.01$	145
5.3.10	Maximum error for aligned square domain over $0 < t < 10T$, with $h = 0.1$ and $dt = 0.01$	145
5.3.11	Mass difference and energy difference for aligned square domain, with $h = 0.1$ and $dt = 0.01$	146
5.3.12	Convergence plot for aligned square domain at various h in range $0.1 < h < 0.01$ at fixed $dt = 0.01$. The error in (a) is calculated in max norm, and (b) in L_2 norm over domain at various h . Slope of the lines indicate the rate of convergence.	146

5.3.13	Error for u, v and p in aligned square domain at $h = 0.01$ and $dt = 0.01$	147
5.4.1	The solutions of p for square domain tilted at 45° at $t = 0, T/4, T/2, 3T/4, T$, with $h = 0.1$ and $dt = 0.01$. Left column: continuum solutions. Centre column: numerical solutions. Right column: error (i.e., continuum-numerical).	149
5.4.2	The solutions of p for square domain tilted at 45° at $t = 9T, 9.25T, 9.5T, 9.75T, 10T$, with $h = 0.1$ and $dt = 0.01$. Left column: continuum solutions. Centre column: numerical solutions. Right column: error (i.e., continuum-numerical).	150
5.4.3	The solutions of u for square domain tilted at 45° at $t = 0, T/4, T/2, 3T/4, T$, with $h = 0.1$ and $dt = 0.01$. Left column: continuum solutions. Centre column: numerical solutions. Right column: error (i.e., continuum-numerical).	151
5.4.4	The solutions of v for square domain tilted at 45° at $t = 0, T/4, T/2, 3T/4, T$, with $h = 0.1$ and $dt = 0.01$. Left column: continuum solutions. Centre column: numerical solutions. Right column: error (i.e., continuum-numerical).	152
5.4.5	The maximum of $ p $ over square domain tilted at 45° at $h = 0.1, dt = 0.01$ over $0 < t < 10T$	153
5.4.6	Maximum error over square domain tilted at 45° , over $0 < t < 10T$ at $h = 0.1, dt = 0.01$	153
5.4.7	Mass and energy difference for square domain tilted at 45° , at $h = 0.1, dt = 0.01$	154
5.4.8	The solutions of p for square domain tilted at 45° at $t = 9T, 9.25T, 9.5T, 9.75T, 10T$, with $h = 0.01$ and $dt = 0.005$. Left column: continuum solutions. Centre column: numerical solutions. Right column: error (i.e., continuum-numerical).	156

5.4.9	The solutions of u for square domain tilted at 45° at $t = 9T, 9.25T, 9.5T, 9.75T, 10T$, with $h = 0.01$ and $dt = 0.005$. Left column: continuum solutions. Centre column: numerical solutions. Right column: error (i.e., continuum-numerical).	157
5.4.10	The solutions of v for square domain tilted at 45° at $t = 9T, 9.25T, 9.5T, 9.75T, 10T$, with $h = 0.01$ and $dt = 0.005$. Left column: continuum solutions. Centre column: numerical solutions. Right column: error (i.e., continuum-numerical).	158
5.4.11	The maximum $ p $ for square domain tilted at 45° with $h = 0.01$, $dt = 0.005$ over $0 < t < 10T$	159
5.4.12	Maximum error for square domain tilted at 45° , at $h = 0.01$ and $dt = 0.005$ over $0 < t < 10T$	159
5.4.13	Mass and energy difference for square domain tilted at 45° , with $h = 0.01$, $dt = 0.005$ over $0 < t < 10T$	160
5.4.14	Convergence plot for square domain tilted at 45° , at various h in range $0.003 < h < 0.03$ at fixed $dt = 0.003$. (a) is convergence in max norm, and (b) in L_2 norm over domain. Slope of the lines indicate the rate of convergence.	160
5.4.15	Maximum error for u, v and p in square domain tilted at 45° , at $h = 0.003$ and $dt = 0.003$	161
5.5.1	Maximum error for u, v and p in square domain tilted at 5° , at $h = 0.003$ and $dt = 0.003$	162
5.5.2	Maximum error for u, v and p in square domain tilted at 10° , at $h = 0.003$ and $dt = 0.003$	162
5.5.3	Maximum error for u, v and p in square domain tilted at 15° , at $h = 0.003$ and $dt = 0.003$	162
5.5.4	Maximum error for u, v and p in square domain tilted at 30° , at $h = 0.003$ and $dt = 0.003$	163

5.5.5	Maximum error of u , v and p for square domain tilted at various angle of rotation with grid spacing (a) $h = 0.1$, (b) $h = 0.01$. The maximum error is calculated over $0 < t < 10T \approx t = 9$	163
5.5.6	Convergence plot for square domain tilted at 5° , at various h in range $0.003 < h < 0.03$ at fixed $dt = 0.003$. (a) is convergence in max norm, and (b) in L_2 norm over domain. Slope of the lines indicate the rate of convergence.	165
5.5.7	Convergence plot for square domain tilted at 10° , at various h in range $0.003 < h < 0.03$ at fixed $dt = 0.003$. (a) is convergence in max norm, and (b) in L_2 norm over domain. Slope of the lines indicate the rate of convergence.	165
5.5.8	Convergence plot for square domain tilted at 15° , at various h in range $0.003 < h < 0.03$ at fixed $dt = 0.003$. (a) is convergence in max norm, and (b) in L_2 norm over domain. Slope of the lines indicate the rate of convergence.	166
5.5.9	Convergence plot for square domain tilted at 30° , at various h in range $0.003 < h < 0.03$ at fixed $dt = 0.003$. (a) is convergence in max norm, and (b) in L_2 norm over domain. Slope of the lines indicate the rate of convergence.	166
5.5.10	Time series of kinetic and potential energy for waves in a square domain over $0 < t < 1$	168
5.5.11	The frequency of wave in aligned square domain, and log-log plot error in frequency at various h . The slope of the line is 1.80398 with 95% confidence interval (1.045, 2.563).	169
5.5.12	The frequency of wave in square domain tilted at 5° , and log-log plot error in frequency at various h . The slope of the line is 1.2491.	169

5.5.13	The frequency of wave in square domain tilted at 10° , and log-log plot error in frequency at various h . The slope of the line is 1.0505.	170
5.5.14	The frequency of wave in square domain tilted at 15° , and log-log plot error in frequency at various h . The slope of the line is 1.064.	170
5.5.15	The frequency of wave in square domain tilted at 30° , and log-log plot error in frequency at various h . The slope of the line is 1.0417.	171
5.5.16	The frequency of wave in square domain tilted at 45° , and log-log plot error in frequency at various h . The slope of the line is 1.27522, with 95% confidence interval (0.9113, 1.639).	171
5.6.1	The solutions of p for circle domain at $t = 0, T/4, T/2, 3T/4, T$, with $h = 0.1$ and $dt = 0.01$ for mode $m = 1, n = 0$. Left column: continuum solutions. Centre column: numerical solutions. Right column: error (i.e., continuum-numerical).	179
5.6.2	The solutions of p for circle domain at $t = 9T, 9.25T, 9.5T, 9.75T, 10T$, with $h = 0.1$ and $dt = 0.01$ for mode $m = 1, n = 0$. Left column: continuum solutions. Centre column: numerical solutions. Right column: error (i.e., continuum-numerical).	180
5.6.3	The maximum $ p $ over circle domain at $h = 0.1, dt = 0.01$ for mode $m = 1, n = 0$	181

-
- 5.6.4 The solutions of u for circle domain at $t = 0, T/4, T/2, 3T/4, T$, with $h = 0.1$ and $dt = 0.01$ for mode $m = 1, n = 0$. Left column: continuum solutions. Centre column: numerical solutions. Right column: error (i.e., continuum-numerical). 182
- 5.6.5 The solutions of u for circle domain at $t = 9T, 9.25T, 9.5T, 9.75T, 10T$, with $h = 0.1$ and $dt = 0.01$ for mode $m = 1, n = 0$. Left column: continuum solutions. Centre column: numerical solutions. Right column: error (i.e., continuum-numerical). 183
- 5.6.6 The solutions of v for circle domain at $t = 0, T/4, T/2, 3T/4, T$, with $h = 0.1$ and $dt = 0.01$ for mode $m = 1, n = 0$. Left column: continuum solutions. Centre column: numerical solutions. Right column: error (i.e., continuum-numerical). 184
- 5.6.7 The solutions of v for circle domain at $t = 9T, 9.25T, 9.5T, 9.75T, 10T$, with $h = 0.1$ and $dt = 0.01$ for mode $m = 1, n = 0$. Left column: continuum solutions. Centre column: numerical solutions. Right column: error (i.e., continuum-numerical). 185
- 5.6.8 Maximum error over domain for $0 < t < 17 \approx 10T$, at $h = 0.1, dt = 0.01$, for mode $m = 1, n = 0$ 186
- 5.6.9 Mass and energy difference for circle domain, at $h = 0.1, dt = 0.01$ over $0 < t < 17 \approx 10T$, for mode $m = 1, n = 0$ 186

-
- 5.6.10 The solutions p for circle domain at $t = 9T, 9.25T, 9.5T, 9.75T, 10T$, with $h = 0.01$ and $dt = 0.005$ for mode $m = 1, n = 0$. Left column: continuum solutions. Centre column: numerical solutions. Right column: error (i.e., continuum-numerical). 187
- 5.6.11 The maximum of $|p|$ over $0 < t < 17 \approx 10T$ at $h = 0.01$ with $dt = 0.005$ for circle domain mode $m = 1, n = 0$ 188
- 5.6.12 Maximum error over domain at $0 < t < 17 \approx 10T, h = 0.01, dt = 0.005$ for mode $m = 1, n = 0$ 188
- 5.6.13 Mass and energy difference for circle domain, at $h = 0.01, dt = 0.005$ over $0 < t < 17 \approx 10T$, for mode $m = 1, n = 0$ 189
- 5.6.14 Convergence plot for circle domain with mode $m = 1, n = 0$ at various h in range $0.2 < h < 0.02$ at fixed $dt = 0.02$. The error in (a) is calculated in max norm, and (b) in L_2 norm over domain. Slope of the line is summarised in Table 5.9, indicate the rate of convergence. 189
- 5.6.15 The frequency of wave in circle domain with mode $m = 1, n = 0$, and log-log plot error in frequency at various h . The slope of the line is 1.66158, with 95% confidence interval (1.002, 2.321). The scaling factor is 1.00801. 190
- 5.6.16 The solutions for p at $t = 0, 0.25T, 0.5T, 0.75T, T$ with $h = 0.1, dt = 0.05$, for $m = 1, n = 1$. Left column: continuum solutions. Centre column: numerical solutions. Right column: error (i.e., continuum-numerical). 191
- 5.6.17 The solutions for p at $t = 9T, 9.25T, 9.5T, 9.75T, 10T$ with $h = 0.1, dt = 0.05$, for $m = 1, n = 1$. Left column: continuum solutions. Centre column: numerical solutions. Right column: error (i.e., continuum-numerical). 192

5.6.18	The solutions for u at $t = 0, 0.25T, 0.5T, 0.75T, T$ with $h = 0.1, dt = 0.05$, for $m = 1, n = 1$. Left column: continuum solutions. Centre column: numerical solutions. Right column: error (i.e., continuum-numerical).	193
5.6.19	The solutions for u at $t = 9T, 9.25T, 9.5T, 9.75T, 10T$ with $h = 0.1, dt = 0.05$, for $m = 1, n = 1$. Left column: continuum solutions. Centre column: numerical solutions. Right column: error (i.e., continuum-numerical).	194
5.6.20	The solutions for v at $t = 0, 0.25T, 0.5T, 0.75T, T$ with $h = 0.1, dt = 0.05$, for $m = 1, n = 1$. Left column: continuum solutions. Centre column: numerical solutions. Right column: error (i.e., continuum-numerical).	195
5.6.21	The solutions for v at $t = 9T, 9.25T, 9.5T, 9.75T, 10T$ with $h = 0.1, dt = 0.05$, for $m = 1, n = 1$. Left column: continuum solutions. Centre column: numerical solutions. Right column: error (i.e., continuum-numerical).	196
5.6.22	The maximum $ p $ for circle domain at $h = 0.1$ with $dt = 0.01$, over $0 < t < 10T$ with mode $m = 1, n = 1$	197
5.6.23	Maximum error over $0 < t < 10T$ for circle domain at $h = 0.1, dt = 0.01$ with mode $m = 1, n = 1$	197
5.6.24	Mass and energy difference for circle domain, at $h = 0.1, dt = 0.01$ over $0 < t < 10T \approx t = 35$, for mode $m = 1, n = 1$	198
5.6.25	The solutions for p at $t = 9T, 9.25T, 9.5T, 9.75T, 10T$ with $h = 0.01, dt = 0.005$, for $m = 1, n = 1$. Left column: continuum solutions. Centre column: numerical solutions. Right column: error (i.e., continuum-numerical).	199

5.6.26	The solutions for u at $t = 9T, 9.25T, 9.5T, 9.75T, 10T$ with $h = 0.01, dt = 0.005$, for $m = 1, n = 1$. Left column: continuum solutions. Centre column: numerical solutions. Right column: error (i.e., continuum-numerical).	204
5.6.27	The solutions for v at $t = 9T, 9.25T, 9.5T, 9.75T, 10T$ with $h = 0.01, dt = 0.005$, for $m = 1, n = 1$. Left column: continuum solutions. Centre column: numerical solutions. Right column: error (i.e., continuum-numerical).	205
5.6.28	The maximum $ p $ for circle domain at $h = 0.01$ with $dt = 0.005$, over $0 < t < 10T$ with mode $m = 1, n = 1$	206
5.6.29	Maximum error for u, v and p over $0 < t < 10T$, for circle domain, at $h = 0.01, dt = 0.005$ with mode $m = 1, n = 1$	206
5.6.30	Mass and energy difference for circle domain, at $h = 0.01, dt = 0.005$ over $0 < t < 10T \approx t = 35$, for mode $m = 1, n = 1$	207
5.6.31	Convergence plot for circle domain with mode $m = 1, n = 1$ at various h in range $0.2 < h < 0.02$ at fixed $dt = 0.02$. The error in (a) is calculated in max norm, and (b) in L_2 norm over domain. Slope of the lines is summarised in Table 5.10.	207
5.6.32	Maximum error in u, v and p for circle domain with mode $m = 1, n = 1$, at $h = 0.01$ and $dt = 0.01$	208
5.6.33	The frequency of wave in circle domain with mode $m = 1, n = 1$ at various h , and log-log plot error in frequency at various h . The slope of the line is 1.08843, with 95% confidence interval (0.7236, 1.453). The scaling factor is 0.305429.	208

-
- 5.6.34 The solutions of p for circle domain at $t = 0, 0.25T, 0.5T, 0.75T, T$, with $h = 0.1$ and $dt = 0.01$, with mode $m = 1, n = 0$ using 4 corners of cell activation. Left column: continuum solutions. Centre column: numerical solutions. Right column: error (i.e., continuum-numerical). 209
- 5.6.35 The solutions of p for circle domain at $t = 9T, 9.25T, 9.5T, 9.75T, 10T$, with $h = 0.1$ and $dt = 0.01$, with mode $m = 1, n = 0$ using 4 corners of cell activation. Left column: continuum solutions. Centre column: numerical solutions. Right column: error (i.e., continuum-numerical). 210
- 5.6.36 The maximum $|p|$ for circle domain at $h = 0.1$ with $dt = 0.01$, over $0 < t < 10T$ with mode $m = 1, n = 0$. The active grid is chosen according to 4 corners of each cells. 211
- 5.6.37 Maximum error for u, v and p over $0 < t < 10T \approx t = 17$, for circle domain, at $h = 0.1, dt = 0.01$ with mode $m = 1, n = 0$. The active grid is chosen according to 4 corners of each cells. . . . 211
- 5.6.38 The solutions of u for circle domain at $t = 0, 0.25T, 0.5T, 0.75T, T$, with $h = 0.1$ and $dt = 0.01$, with mode $m = 1, n = 0$ using 4 corners of cell activation. Left column: continuum solutions. Centre column: numerical solutions. Right column: error (i.e., continuum-numerical). 212
- 5.6.39 The solutions of v for circle domain at $t = 0, 0.25T, 0.5T, 0.75T, T$, with $h = 0.1$ and $dt = 0.01$, with mode $m = 1, n = 0$ using 4 corners of cell activation. Left column: continuum solutions. Centre column: numerical solutions. Right column: error (i.e., continuum-numerical). 213

5.6.40	The maximum $ u $ for circle domain at $h = 0.1$ with $dt = 0.01$, over $0 < t < 10T$ with mode $m = 1, n = 1$. The active grid is chosen according to 4 corners of each cells.	214
5.6.41	The maximum $ v $ for circle domain at $h = 0.1$ with $dt = 0.01$, over $0 < t < 10T$ with mode $m = 1, n = 1$. The active grid is chosen according to 4 corners of each cells.	214
5.6.42	Mass and energy difference for circle domain, at $h = 0.1$, $dt = 0.01$ over $0 < t < 10T \approx t = 17$, for mode $m = 1, n = 0$. The active grid is chosen according to 4 corners of each cells. . . .	215
5.6.43	The solutions of p for circle domain at $t = 0, 0.25T, 0.5T, 0.75T, T$, with $h = 0.01$ and $dt = 0.005$, with mode $m = 1, n = 0$ using 4 corners of cell activation. Left column: continuum solutions. Centre column: numerical solutions. Right column: error (i.e., continuum-numerical).	216
5.6.44	The solutions of p for circle domain at $t = 9T, 9.25T, 9.5T, 9.75T, 10T$, with $h = 0.01$ and $dt = 0.005$, with mode $m = 1, n = 0$ using 4 corners of cell activation. Left column: continuum solutions. Centre column: numerical solutions. Right column: error (i.e., continuum-numerical).	217
5.6.45	The maximum $ p $ for circle domain at $h = 0.01$ with $dt = 0.005$, over $0 < t < 10T$ with mode $m = 1, n = 1$. The active grid is chosen according to 4 corners of each cells.	218
5.6.46	Maximum error for u, v and p over $0 < t < 10T$, for circle domain, at $h = 0.01, dt = 0.005$ with mode $m = 1, n = 0$. The active grid is chosen according to 4 corners of each cells.	218

5.6.47	The solutions of u for circle domain at $t = 9T, 9.25T, 9.5T, 9.75T, 10T$, with $h = 0.01$ and $dt = 0.005$, with mode $m = 1, n = 0$ using 4 corners of cell activation. Left column: continuum solutions. Centre column: numerical solutions. Right column: error (i.e., continuum-numerical).	219
5.6.48	The solutions of v for circle domain at $t = 9T, 9.25T, 9.5T, 9.75T, 10T$, with $h = 0.01$ and $dt = 0.005$, with mode $m = 1, n = 0$ using 4 corners of cell activation. Left column: continuum solutions. Centre column: numerical solutions. Right column: error (i.e., continuum-numerical).	220
5.6.49	Mass and energy difference for circle domain, at $h = 0.01$, $dt = 0.005$ over $0 < t < 10T \approx t = 17$, for mode $m = 1, n = 0$. The active grid is chosen according to 4 corners of each cells. . . .	221
5.6.50	The log-log plot of maximum error over (a) $0 < t < 10T \approx t = 17$, and (b) $0 < t < t \approx 2 > T$, at various grid spacing h . The slope of the lines indicate the rate of convergence. The slope in (b) are: u and v are 0.905945, with 95% confidence interval (0.8362, 0.9757), p is 0.5498, with 95% confidence interval (0.5049, 0.5948). The active grid is chosen according to 4 corners of each cells.	221
6.3.1	Different choice of variables staggering on a C-grid.	236
6.4.1	The mechanism of internal wave reflection at a sloping boundary. (a) reflection at a shallow slope, (b) reflection at $\beta > \varphi$. This figure is re-illustrated from [53].	238
6.4.2	Internal wave reflection at staircase boundary on the C-grid.	243

6.5.1	Evolution of buoyancy, b at $t = 0, 100, 200, 300, 400, 500$ (i.e., $0 < t < 50T$) with mode $(l, n) = (1, 1)$ at $h = 0.002$, $dt = 0.05$. The period of wave is $T = 2\pi/\omega = 2\sqrt{2}\pi \approx 8.8858$	255
6.5.2	Evolution of buoyancy, b at $t = 1000, 1500, 2000, 2500, 3000, 3500$ (i.e., $100T < t < 350T$) with mode $(l, n) = (1, 1)$ at $h = 0.002$, $dt = 0.05$	255
6.5.3	Evolution of buoyancy, b at $t = 0, 100, 200, 300, 400, 500$ (i.e., $0 < t < 25T$) with mode $(l, n) = (1, 3)$ at $h = 0.002$, $dt = 0.05$. The period is $T = 2\pi/\omega = 2\sqrt{10}\pi \approx 19.8692$	256
6.5.4	Evolution of buoyancy, b at $t = 1000, 1500, 2000, 2500, 3000, 3500$ (i.e., $50T < t < 175T$) with mode $(l, n) = (1, 3)$ at $h = 0.002$, $dt = 0.05$	256
6.5.5	The evolution of buoyancy b at $t = 5, 50, 100, 150, 200$ for $(l, n) = (1, 1)$, $\bar{\omega}/N_f = 0.74$. Gravity tilted at angle $7\pi/72$. The left column is the results using [11] attractor initial condition. On the right column, the results with (6.5.5) normal mode initial condition with parametric excitation.	259
6.5.6	Energy analysis for the simulations on normal mode (right column Figure 6.5.5), $(l, n) = (1, 1)$, $\omega_c = 1.55786$, $\omega_d = 1.50097$, $ \omega_c - \omega_d = 0.056882$	260
6.5.7	The evolution of buoyancy b at $t = 5, 50, 100, 150, 200$ for $(l, n) = (1, 3)$, $\bar{\omega}/N_f = 0.34$. Gravity tilted at angle $\pi/18$. The left column is the results with [11] attractor initial condition. On the right column, the results with (6.5.5) normal mode initial condition with parametric excitation.	261

6.5.8	Energy analysis for the simulations on normal mode (right column Figure 6.5.7), $(l, n) = (1, 3)$, $\omega_c = 1.54485$, $\omega_d = 1.46097$, $ \omega_c - \omega_d = 0.0838847$	262
A.0.1	Modulus of amplification factor for the Euler's scheme as a function of Δt	280
A.0.2	Convergence plot for RK-2 method.	282
A.0.3	Modulus of amplification factor for the RK-4 scheme as a function of Δt	284
A.0.4	Convergence plot for RK-4 method.	285
A.0.5	Modulus of amplification factor for the AB-2 scheme as a function of Δt	287
A.0.6	Convergence plot for AB-2 method.	287
A.0.7	Convergence plot for Leapfrog method.	289
A.0.8	Modulus of amplification factor for the AB-3 scheme as a function of Δt	290
A.0.9	Convergence plot for AB-3 method.	291

List of Tables

5.1	The convergence rate of u , v and p in max norm and L_2 norm, for aligned square domain.	142
5.2	The confidence interval of u , v and p in max norm for aligned square domain.	142
5.3	The convergence rate of u , v and p in max norm and L_2 norm, for square domain tilted at 45°	155
5.4	The convergence rate of u , v and p in max norm and L_2 norm, for square domain tilted at 5°	163
5.5	The convergence rate of u , v and p in max norm and L_2 norm, for square domain tilted at 10°	164
5.6	The convergence rate of u , v and p in max norm and L_2 norm, for square domain tilted at 15°	164
5.7	The convergence rate of u , v and p in max norm and L_2 norm, for square domain tilted at 30°	164
5.8	The scaling factors C and scaling exponents n , along with 95% confidence interval for error in frequency, at various θ . The values are numerically determined at fixed $dt = 0.003$ and grid spacing $0.003 < h < 0.03$	168
5.9	The convergence rate of u , v and p in max norm and L_2 norm, for circle domain with mode $m = 1, n = 0$. The slope of the lines in Figure 5.6.14.	178

5.10	The convergence rate of u , v and p in max norm and L_2 norm, for circle domain with mode $m = 1, n = 1$. The slope is for the lines in Figure 5.6.31, indicate the rate of convergence.	188
5.11	The convergence rate for u , v and p in max norm and L_2 norm, at various h for the specific domain.	203
5.12	The convergence rate obtained by [67] for the case of wave reflection at specific domain in L_2 norm. The convergence rate is measured at three grid spacings.	203
7.1	The relative error Δ for wave propagation along a channel with aligned boundaries and unaligned boundaries for $j = 0, k = 1$	271
7.2	The relative error Δ for wave propagation along a channel with aligned boundaries and unaligned boundaries for $j = 0, k = 2$	271
7.3	The relative error Δ for wave propagation along a channel with aligned boundaries and unaligned boundaries for $j = 1, k = 1$	272
7.4	The relative error Δ for wave propagation along a channel with aligned boundaries and unaligned boundaries for $j = 5, k = 1$	272
7.5	The convergence rate for u , v and p in max norm and L_2 norm, at various h for the specific domain.	273

Chapter 1

INTRODUCTION

1.1 Waves

Wave phenomena are abundant in nature. They exist across a wide range of lengthscales and timescales, from short wavelength electromagnetic waves moving at the speed of light, to planetary-scale waves moving in the deep ocean at walking pace. Perhaps the most common waves are water waves (visible on the surface of the sea), sound waves (or acoustic waves) that we hear everyday, and light waves electromagnetic waves – all of them are around us. Such waves have long been a phenomenon of great scientific interest. But they are not only a curiosity for us, due to the fundamental role that they play in many systems, and the possibility of exploiting their abundance. For example, waves have enabled us to infer the structure of the Earth through seismology, and form the basis of modern communication.

Waves are generated by a disturbance of a material parcel around an equilibrium position. In doing so, a so-called ‘restoring force’ is often generated, which pulls back the parcel towards its original position. However, in the absence of friction or other damping, the parcel overshoots in the opposite direction. The restoring force continues to act, but now to reverse the direction of the original motion. This process continues, leading to an oscillatory

motion of the material parcel. This well-understood mechanism is fundamental to almost all waves, which can then be categorised by the different restoring forces that drive them.

In the case where the restoring force is induced by fluid pressure, the waves propagate as regions of compression and rarefaction. In an elastic solid, these are the P-waves of seismology; in a fluid, these are sound waves, first studied by [56]. These are examples of longitudinal waves, as particle movement is in the direction of wave travel (or the wavevector), with an initial disturbance creating an area of high pressure. Particles are then forced out of this region, only to 'bump' into more particles, creating another high pressure area further from the initial perturbation, and so on. They propagate through the Earth's atmosphere very quickly compared to other atmospheric effects such as the wind (at around 350 ms^{-1}) and through the ocean quicker still (around 1500 ms^{-1}), owing to the higher density of the water. They are also relatively small scale, compared with, say the familiar waves on a beach; the wavelength of the sound of a typical human voice is around 3cm.

The restoring force can also be gravity. A displaced fluid parcel is forced back towards equilibrium through gravitational buoyancy, leading to so-called gravity waves. These waves which sometimes categorised as surface gravity waves can be observed on the surface of the sea, where gravity playing a dominant role in the driving of the waves. In 1834, Scott Russell observed a solitary wave propagating down a canal, maintaining its shape for extended periods of time [59]. These waves propagate at much slower speeds than sound waves, typically at around $1\text{-}200 \text{ ms}^{-1}$ compared to the 1500 ms^{-1} sound speed in water. Another example of gravity waves is tsunami waves. These waves are a hundred kilometers long which will propagate faster in the deep ocean. Surface tension can also contribute to the restoring force of waves. The waves that travel by both the effects of surface tension and gravity are called gravity-capillary waves. These waves are common in nature, and are often referred to as ripples. Typically, the wavelength of these waves is less than the wavelength of the gravity waves.

The other category of gravity wave is internal gravity wave, which occur within a fluid. The

first internal waves were documented in 1792 by Benjamin Franklin, who conducted an experiment with oil on water. Later, in 1898, Bjerknes attempted to explain the ‘dead water’ phenomenon using internal waves, which were subsequently investigated experimentally by Ekman in 1904 [49]. These have also been observed in the ocean, with tracers or detectors suspended in the fluid, or by using satellites such as the Earth Resources Technology Satellite [5]. These waves arise in regions with changing bottom topography and tidal forcing [e.g., [55, 9]]. Internal waves can also be found in the atmosphere. For example, the so-called Morning Glory waves that are observed around 150m above the Australian coast, first documented in the Royal Australian air force in 1942, travel at around 10 ms^{-1} . As well as travelling slower than sound waves, internal gravity waves also occur on much larger spatial scales: a crest of a wave in the Morning Glory wavetrain will have a wavelength of approximately 10km, as documented by [18], compared to the 3cm wavelength of sound waves.

There are many other examples of forces that give rise to waves; inertial waves, for example, arise from the Coriolis force arising from the Earth’s rotation. Of course, when we say ‘the restoring force’, we really mean the *dominating* restoring force; in reality this is not the only force present on any system. For example, in the Earth’s oceans, typically both background rotation and gravity simultaneously act, so that we are often interested in inertia-gravity waves.

This thesis is concerned with waves in a quite general context, but we are mostly thinking of applications to waves in fluids. So we are generally use terminology relating to sound waves and gravity waves.

1.2 Mathematical modelling of waves

The mathematical modelling of waves date back to many scientists across many fields across the centuries. Among many others, Daniel Bernoulli, Jean le Rond d’Alembert,

Leonhard Euler, and Pierre-Simon Laplace realised that there was a similarity in the maths of how to describe waves through solids and fluids. Common scientific concepts of wave can connect seemingly disparate areas of science. In 1720s, Bernoulli, a Swiss mathematician, applied Isaac Newton's laws of motion to understand the propagation of waves in the surrounding air which is interpreted as sound. He was a pioneer of the mathematical theory of sound from vibrated violin string with fixed at each end.

For many systems, the waves are described by the *wave equation*

$$\eta_{tt} - c^2 \nabla^2 \eta = 0. \quad (1.2.1)$$

Here η is a scalar representing a disturbance quantity (such as fluid pressure), t is time, c is the (scalar) wave speed of the system, and ∇^2 is the Laplacian operator (perhaps in several spatial dimensions). In one spatial dimension x , (1.2.1) has the famous d'Alembert solutions

$$\eta = A(x \pm ct), \quad (1.2.2)$$

representing steady non-dispersive wave propagation in each direction. An underlying assumption in (1.2.1) is that the waves can be modelled linearly, meaning that nonlinear terms in the governing equations can be neglected. This is always the case for waves of sufficiently small amplitude, but the assumption of linearity is often useful even for larger amplitude waves, since it captures the restoring force that is fundamental to wave motion.

More generally, the waves will be governed by a system of partial differential equations (PDEs), which will be more complicated than (1.2.1). However, again under the assumption of linearity, these can often be reduced to an equation that is similar in form to (1.2.1). Such equations are commonly analysed by seeking solutions $\propto \Re(\hat{\eta} \exp(i(kx + ly - \omega t)))$, where ω is the frequency of the wave, and k and l are wavenumbers in the x and y directions – here we are assuming just two dimensions, for simplicity, as in much of this thesis. The governing PDE then only has non-trivial solutions, i.e., $\hat{\eta} \neq 0$, when a so-called dispersion

relation is satisfied:

$$\omega = \omega(k, l). \quad (1.2.3)$$

For example, for (1.2.1) in two dimensions we obtain the simple dispersion relation $\omega^2 = c^2(k^2 + l^2)$. However, dispersion relations can be somewhat more complex. For example, for internal gravity waves in 2D with x horizontal and y vertical, we obtain $\omega^2 = N^2 k^2 / (k^2 + l^2)$, where N is the buoyancy frequency of the fluid.

The above analysis ignores the presence of boundaries. Although these are usually irrelevant to the underlying restoring mechanism that drives the wave motion, their presence is often critical in determining the spatial structure and frequency of the response. For example, in a tubular music instrument, the boundaries lead to the possibility of musical tones of discrete frequencies. In contrast, in the ocean, the boundaries can sometimes lead to the existence of new classes of waves, such as the famous Kelvin wave that exists in coastal waters. In all such examples, the governing PDEs must be solved subject to an appropriate boundary condition. This means we must impose a correct boundary conditions at every point of our domain. For example, for a fluid medium and a solid boundary, there can be no flow through it and thus the normal component of the velocity must be set to be zero. This is commonly known as the no normal-flow boundary condition, and will be used throughout this study.

When such boundaries are present, the dispersion relation is typically modified, in the form

$$\omega = \omega(k_j, l_j; \mathbf{L}), \quad (1.2.4)$$

where \mathbf{L} encodes information about the shape and length of the domain, and the wavenumbers k_j and l_j now form a discrete set. For example, when solving (1.2.1) in a square domain $0 < x < L$ and $0 < y < L$, it is possible to show that there exist solutions

$\eta \propto \Re(\hat{\eta} \sin kx \sin ly \exp(-i\omega t))$ provided

$$\omega^2 = c^2(k_m^2 + l_n^2), \text{ where } k_m = \frac{m\pi}{L} \text{ and } l_n = \frac{n\pi}{L}. \quad (1.2.5)$$

1.3 Numerical solutions of wave equations

The solution of a wave equation is a main aim in any wave investigations. One can obtain the solution by solving the equation analytically with the satisfied boundary condition. However, the usefulness of these solutions is sometimes restricted to problems involving shapes for which the boundary conditions can be satisfied. If this is the case, approximation methods, whether analytical or numerical in character are the only means of solution, apart from the use of analogue devices.

The oldest and most popular method to solve wave equation numerically is called finite-difference method. It was first utilized by L. Euler in 1768 in one dimension, and was extended to two dimensions by C. Runge in 1908 [14, 15]. The advent of the method in real numerical calculations was documented by Lewis Fry Richardson in 1911 [57]. The development of the method was stimulated by the emergence of computers that offered a convenient framework for dealing with complex problems of science and technology. The main principle in this method is the approximation of derivatives in the system of PDEs by using the famous Taylor series expansion at the grid points. In this principle, the partial derivatives are replaced by algebraic difference equations that are based on Taylor series expansions. The set of continuum PDEs is totally converted into a large discrete system of algebraic equations. For example, in one spatial dimension x , the Laplacian operator in (1.2.4) is approximated at the grid point as

$$\frac{\partial^2 \eta}{\partial x^2} = \frac{\eta(x+h) - 2\eta + \eta(x-h)}{h^2} + O(h^2), \quad (1.3.1)$$

where h is the grid spacing. The accuracy of (1.3.1) is second order accuracy since the

leading order of error term is two.

Typically, the resulting of algebraic equations can be solved on a computer. For a certain case, like a simple domain, these algebraic equations can be solved analytically, which will give discrete solutions. Analogous to the continuum system, this algebraic system of equations must be solved with an appropriate boundary condition. In a wave context, the presence of boundaries will give discrete version of dispersion relations, which then will be analysed by comparing with the continuum version in terms of accuracy and the rate of convergence.

There are of course other existing numerical methods that can be used in approximating the wave equation. Among of them are finite-element methods, finite-volume methods and spectral methods. Finite-element methods have become popular in recent years especially when involving a complex domain. In all existing numerical methods, implementation of boundary conditions is very important. In the finite-difference method this can be fiddly, and perhaps it is easy for finite-element and finite-volume method. All these methods provide their own advantages and drawbacks in providing discrete solutions of any problems. However, in this thesis we only focus with the oldest and popular method which is the finite-difference method which is still widely used today in many applications due to its simplicity and robustness, and the ease in which it can handle things like spatially varying coefficients.

1.4 Staggered-grid finite difference methods in two spatial dimensions

We consider a two-dimensional system (x, y, t) , with horizontal flow (u, v) and a pressure variable p , govern by

$$\frac{\partial u}{\partial t} = -\frac{\partial p}{\partial x}, \quad \frac{\partial v}{\partial t} = -\frac{\partial p}{\partial y}, \quad \frac{\partial p}{\partial t} + c^2 \left(\frac{\partial u}{\partial x} + \frac{\partial v}{\partial y} \right) = 0. \quad (1.4.1)$$

As discussed in chapter 2, these equations govern wave phenomena in a range of physical systems.

To solve (1.4.1) using finite-differences, the arrangement of the grid points is a serious matter. There are five different grids that were introduced by [6] to calculate different variables in governing equations, namely A, B, C, D and E-grid. Of these grids, A is an unstaggered grid where the dependent variables (which are u , v and p) are defined at the same points. The B-grid through E are all staggered grids where the variables are defined at different points. All of these grids are shown in Figure 1.4.1.

In B-grid, the velocities variables (u and v) are defined either at the center of a grid or at the grid corner, while the pressure p is defined either at the corner or at the center of the grid. In the C-grid, u and v are defined at the mid-point between grid cells while p is calculated at the corner of a grid. In this research, we only focus on discretizing the governing equation on grid A, B and C since grid D is a slight variation of grid C with the u and v variables being oriented with a rotation of 90° while staggered grid E is rotated 45° relative to B-grid [20].

As mentioned earlier, the most common finite-difference representations of derivatives are based on Taylor series expansions. The equations are linked through Taylor expansions. For example, on the C-grid, the spatial derivative $u'(x) = \partial u / \partial x$ is approximated by the

1.4. STAGGERED-GRID FINITE DIFFERENCE METHODS IN TWO SPATIAL DIMENSIONS 9

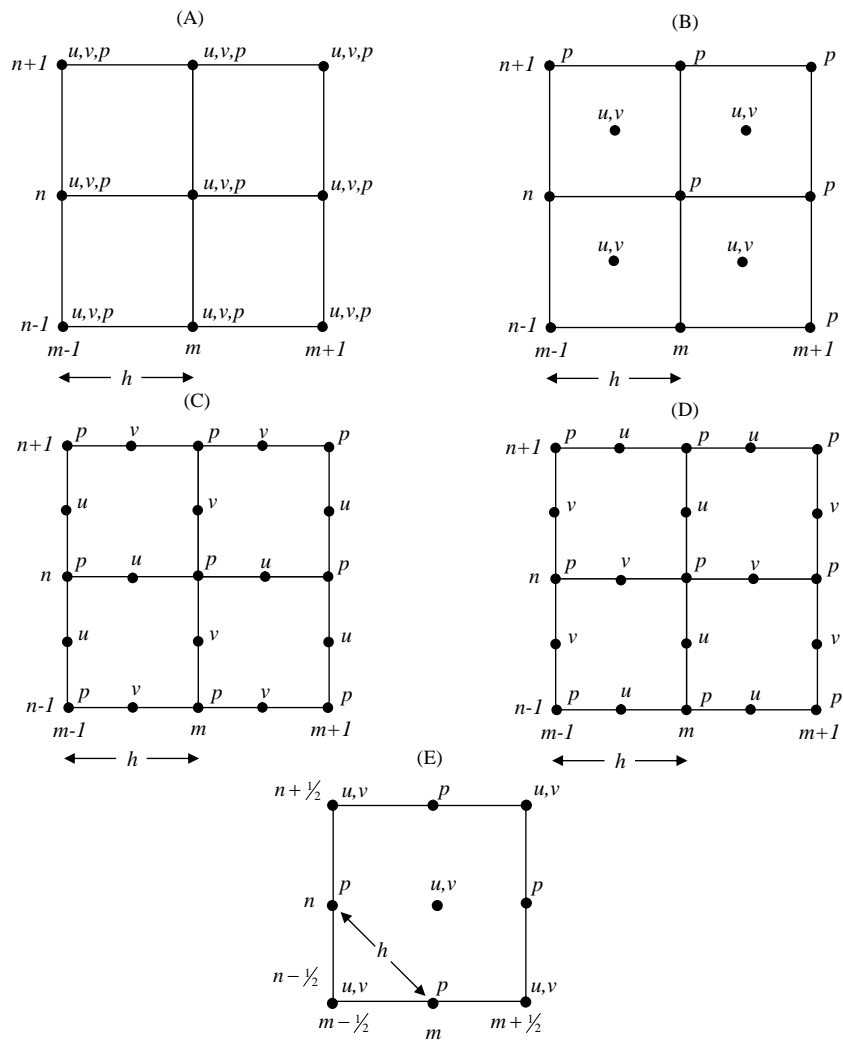


Figure 1.4.1: Spatial distributions of the dependent variables on a square grid. (Taken from [6]).

following second order central difference

$$\frac{\partial u}{\partial x} = \frac{u(x + h/2) - u(x - h/2)}{h} + O(h^2), \quad (1.4.2)$$

with interval h . The accuracy of the above expression is second order since it is the leading order error term in the Taylor series expansion.

Among these five finite-difference grids, the C-grid is widely used as the basis for horizontal discretisations. This grid is also known as Yee grid in electromagnetism [71] and the Arakawa C-grid in fluid dynamics [6]. The arrangement of the physical quantities on a regular Cartesian grid made it special and becomes more popular in finite-difference study [65, 4, 24]. The popularity of the C-grid in oceanography also increasing over the years [19, 12]. Generally, the C-grid is commonly used by ocean modellers in terms of resolution perspective either in the presence of boundaries or unbounded domains [30]. The arrangement of the pressure p nodes at the centre of the grid gives a naturality to evaluate derivatives using second-order centred differences. It is because ∇p is easily evaluated at u nodes, which is optimal for the discretised equations of motion. So that given (1.4.1), this means that we need to evaluate $\partial p/\partial x$ on u nodes, $\partial p/\partial y$ on v nodes, and both $\partial u/\partial x$ and $\partial v/\partial y$ on p nodes, with all four operations are trivially achieved with second-order centred differences using C-grid. Moreover, it is also easy to ensure that the resulting schemes conserve mass, and it is possible to conserve additional quantities such as energy and enstrophy [7].

One aspect that always been discussed in finite-difference method is the implementation of the boundaries when the domain is not smooth or unaligned with the grid [68, 67]. In the presence of such irregular domain, the Cartesian structure of many finite-difference grids lead to a so called staircase boundaries. It is the famous treatment to overcome the problem of boundary implementation in the presence of irregular boundary where the basis of this treatment is to introduce a numerical boundary that differs with the continuum boundary. The nature of the C-grid means that nodes of the normal velocity may be chosen to lie on

the numerical boundary, which make the zero flux boundary condition easy to implement. However, it is not clear how the resulting numerical solution will converge to the continuum solution as the grid size $h \rightarrow 0$. On the numerical boundary, the normal vector is nowhere approaches the continuum boundary as $h \rightarrow 0$, so it is not obvious how the no flux boundary condition may be applied correctly. One expects that such staircase boundaries can degrade the accuracy of the numerical solutions [67]. However, it is not obvious how large the degradation can be occurred.

The numerical errors induced by staircase boundaries on the C-grid have been investigated in various specific configurations. However in some of these studies there is no quantification of the rate of convergence towards continuum solution, and in others the quantification is insufficient to accurately determine the rate of convergence. For example, for electromagnetism reflection study with Maxwell's equation, there is no quantification is reported in [17]. For acoustic wave reflection problems, [67] estimate convergence rates between 0.5 and 1 for the pressure in L_2 norm. And for the related problem of acoustic wave reflection in three dimensions, [33] report errors of $O(\sqrt{h})$ for pressure and velocity in the L_2 norm. For a non-rotating shallow-water flow, [51] showed analytically that a gravity waves reflected from a staircase boundary aligned at 45° to the grid inherits a phase-shift of $O(h)$. For the inviscid shallow-water model, it is shown in [32] that staircase boundary reduces the approximation of the Kelvin wave speed down to the first order in h and degrades the accuracy of numerical simulation of physical phenomena.

1.5 Aims and outline of this thesis

The aim of this thesis is to quantify the degradation caused by staircase boundaries on C-grid finite-difference solutions of standard wave equations. We study a sequence of linear problems in idealised geometries, so that the degradation can be studied thoroughly. For most of the thesis we will focus on the standard set of acoustic wave equations (1.4.1),

in part because they have wide application outside of acoustics – for example, they are also equivalent to the non-rotating shallow-water equations, which describe the evolution of long waves in a shallow fluid layer. However, in the final chapter, we do additionally consider an internal gravity wave system, with different governing equations.

Wherever possible, we consider harmonic waves in time, so that the effects of time-differencing are neglected, and we can thus exclusively focus on the effects spatial differencing and staircase boundaries. In many cases, this enables to first find an exact analytical solution for the continuum problem of interest – whether it be a dispersion relation for a wave propagating along a channel, or a reflection coefficient – and then to solve an analogous discrete problem on the C-grid. We then compare the discrete prediction (for wave frequency or a reflection coefficient) with the continuum result, by performing asymptotics in the limit of small grid spacing h . We can then assess whether the implied error is second-order in h , or if there is degradation of order of convergence due to the staircasing.

We start, in Chapter 2, by reviewing well-known and standard (but essential) background on wave equations, and their solution using staggered finite-difference schemes. Several distinct physical systems that describe waves are discussed (acoustics, electromagnetics, shallow-water), together with their governing equations, which are shown to be essentially equivalent to (1.4.1). Various conservation laws (mass and energy) are discussed of these continuum equations. We then examine the discrete version of both the governing equations and conservations laws on staggered grids, focussing on the Arakawa C-grid. Finally, we discuss the representation of periodic travelling wave solutions in unbounded domains, where there are no effects of staircase boundaries.

In Chapter 3, wave propagation along a channel is examined. We first derive the continuum analytical solution, and the discrete solution in the case where the grid and boundary are aligned. We then turn to the main question of interest, which is how the discrete solutions are degraded when wave propagate along a channel with a staircase boundary, obtained by tilting the boundaries of the channel by 45° relative to the grid. The staircase boundaries

are said to have a perfect staircase. The discrete solutions in this configuration are obtained analytically and a discussion of the results is presented in terms of degradation of the rate of convergence. Our focus is on the frequency of the waves for specified along-channel and cross-channel wavenumbers.

In Chapter 4, wave reflection at a hard boundary is examined. Again, we first derive the continuum analytical solution, and the discrete solution in the case where the grid and boundary are aligned. We then calculate the discrete solution for waves reflecting from a perfect staircase boundary, and quantify the degradation relative to the continuum solution. Here of focus is on the (complex) reflection coefficient, and whether there are errors in amplitude and/or phase of the reflected waves.

Chapter 5 brings together the results of Chapter 3 and 4, by finding solutions in various bounded domains (squares, tilted squared, circles). Here, it is not possible to find the discrete solutions analytically, so we resort to numerical simulations, using a high-order time-stepping scheme, so that time-differencing errors remain much smaller than spatial-differencing errors. However, continuum analytical solutions are available in these cases, so that we can still quantify the errors of the discrete solutions for suitably chosen initial conditions. Here we are interested in what happens after multiple wave reflections. For example, does the discrete solution become incoherent? Or does it remain coherent but perhaps evolve at a different frequency to the continuum solution?

In Chapter 6, we move onto the distinct problem of internal gravity waves, which are governed by a different set of equations. Our focus is on reflection of internal gravity waves, and we are again able (as in chapter 4) to solve a wave reflection problem for a perfect staircase boundary. Finally, we briefly discuss the possible effects of staircase boundaries on internal gravity wave attractors, which are a special dynamical feature of internal gravity waves in a closed domain.

We conclude in Chapter 7.

Chapter 2

MATHEMATICAL BACKGROUND: WAVES AND STAGGERED FINITE-DIFFERENCE SCHEMES IN UNBOUNDED DOMAINS

2.1 Introduction

In this chapter, we review standard background material relating to the issue of wave propagating on staggered finite-difference schemes, in the absence of boundaries. These ideas are fundamental to the remaining chapters, which contain new research on waves in the presence of boundaries. We focus on waves in two space dimensions, and time.

We start, in section 2.2, by showing how several very different physical systems are governed by the same linear partial differential equations (PDEs):

$$\frac{\partial u}{\partial t} = -\frac{\partial p}{\partial x}, \quad \frac{\partial v}{\partial t} = -\frac{\partial p}{\partial y}, \quad \frac{\partial p}{\partial t} + c^2 \left(\frac{\partial u}{\partial x} + \frac{\partial v}{\partial y} \right) = 0, \quad (2.1.1)$$

involving u and v representing velocity, p the accompanying pressure, c is a constant wavespeed of the system. By eliminating u and v , we can obtain a single equation for p :

$$\frac{\partial^2 p}{\partial t^2} = c^2 \left(\frac{\partial^2 p}{\partial x^2} + \frac{\partial^2 p}{\partial y^2} \right). \quad (2.1.2)$$

This is the famous wave equation, which is hyperbolic. The meaning of u , v , and p varies according the physical system, and we show how each of acoustic waves, electromagnetic waves, and shallow-water waves fit in this framework.

The formulation of a problem requires a complete specification of the geometry with an appropriate boundary conditions. In this section, we also will look at a standard ‘no normal flow’ condition for fluid systems. For a closed domain D with no normal flow through it, the boundary condition is mathematically written as

$$\mathbf{u} \cdot \mathbf{n} = 0 \quad \text{on} \quad \partial D, \quad (2.1.3)$$

where $\mathbf{u} = (u, v)$ and \mathbf{n} is the unit vector perpendicular to the boundary.

In sections 2.3 and 2.4, we establish some key properties of the PDEs system (2.1.1). In section 2.3, we establish some local conservation laws and global conserved properties, subject to (2.1.3): conservation of mass (which means slightly different things in each physical system), and conservation of energy. In a possible situation, these conservation laws should be respected by the discretized equations of motion. In section 2.4, we establish the fundamental wave dynamics of (2.1.1) in unbounded domains, and discuss the corresponding phase and group velocities.

In section 2.5, we turn to finite-difference grids. We present three common spatial discretisations of (2.1.1), corresponding to the A, B and C grids of fluid dynamics. The A grid is non-staggered, whilst the B and C grid, which is distinguished grid or staggered grid. As discussed in previous chapter, the C-grid is the main subject of the remainder of this thesis.

In section 2.6, we present discrete conservation laws which analogous to the continuum conservation laws (section 2.3). In section 2.7, we derive the discrete dispersion relationships for waves (in unbounded domains) on each of the A, B and C grids, and consider the implied errors in the frequency and group velocities.

2.2 Physical Systems

In this section, we discuss system of equations that we use to analyse certain physical systems. We will then show that each system of equations is governed by (2.1.1). We establish this here because these equations will be heavily studied in later chapters.

2.2.1 Acoustic waves

The equations of acoustics may be used to describe the propagation of sound waves through a compressible medium, such as air, a process which is important in various physical phenomenon. For an inviscid fluid in (x, y, t) the equations of motion are

$$\frac{\partial u}{\partial t} + u \frac{\partial u}{\partial x} + v \frac{\partial u}{\partial y} = -\frac{1}{\rho} \frac{\partial p}{\partial x}, \quad (2.2.1a)$$

$$\frac{\partial v}{\partial t} + v \frac{\partial v}{\partial y} + u \frac{\partial v}{\partial x} = -\frac{1}{\rho} \frac{\partial p}{\partial y}, \quad (2.2.1b)$$

$$\frac{\partial \rho}{\partial t} + \frac{\partial}{\partial x}(\rho u) + \frac{\partial}{\partial y}(\rho v) = 0, \quad (2.2.1c)$$

$$p = p(\rho, T), \quad (2.2.1d)$$

where u and v are the velocity in the x and y directions, respectively, ρ is the density, p is the pressure, T is the temperature. (2.2.1d) is an equation of state; for example, if we are dealing with a perfect gas, then (2.2.1d) would be $p = \rho RT$ where R is a perfect gas constant. In (2.2.1a) - (2.2.1d), the temperature must be prescribed, otherwise we have five

unknown functions u, v, p, ρ and T with four equations which is overdetermined. However, we will take T to be constant here.

We now take a basic state of rest $u = v = 0$, with constant density ρ_0 , constant temperature T , and constant pressure $p_0 = p(\rho_0, T)$. We then consider small disturbances to this basic state by writing $u = 0 + u', v = 0 + v', \rho = \rho_0 + \rho', p = p_0 + p'$ with prescribed constant T . Equations (2.2.1a)-(2.2.1d) then become

$$(\rho_0 + \rho') \left(\frac{\partial u'}{\partial t} + u' \frac{\partial u'}{\partial x} + v' \frac{\partial u'}{\partial y} \right) = -\frac{\partial}{\partial x} (p_0 + p'), \quad (2.2.2a)$$

$$(\rho_0 + \rho') \left(\frac{\partial v'}{\partial t} + v' \frac{\partial v'}{\partial y} + u' \frac{\partial v'}{\partial x} \right) = -\frac{\partial}{\partial y} (p_0 + p'), \quad (2.2.2b)$$

$$\frac{\partial}{\partial t} (\rho_0 + \rho') + \frac{\partial}{\partial x} ((\rho_0 + \rho') u') + \frac{\partial}{\partial y} ((\rho_0 + \rho') v') = 0, \quad (2.2.2c)$$

$$(p_0 + p') = p(\rho_0 + \rho', T). \quad (2.2.2d)$$

Waves can be identified by seeking small-amplitude disturbances u', v', ρ' and p' . For sufficiently small disturbances, the nonlinear terms that are products of disturbance quantities can be neglected. To make this clear, we rewrite (2.2.2a)-(2.2.2d) as

$$\begin{aligned} \rho_0 \frac{\partial u'}{\partial t} + \left[\rho' \frac{\partial u'}{\partial t} + (\rho_0 + \rho') \left(u' \frac{\partial u'}{\partial x} + v' \frac{\partial u'}{\partial y} \right) \right] &= -\frac{\partial p'}{\partial x}, \\ \rho_0 \frac{\partial v'}{\partial t} + \left[\rho' \frac{\partial v'}{\partial t} + (\rho_0 + \rho') \left(v' \frac{\partial v'}{\partial y} + u' \frac{\partial v'}{\partial x} \right) \right] &= -\frac{\partial p'}{\partial y}, \\ \frac{\partial \rho'}{\partial t} + \rho_0 \left(\frac{\partial u'}{\partial x} + \frac{\partial v'}{\partial y} \right) + \left[\frac{\partial}{\partial x} (\rho' u') + \frac{\partial}{\partial y} (\rho' v') \right] &= 0, \\ p_0 + p' = p(\rho_0, T) + \rho' \frac{\partial p}{\partial \rho}(\rho_0, T) + [O(\rho'^2)]. \end{aligned}$$

These equations are linearised by neglecting the nonlinear terms in square brackets, yielding

$$\frac{\partial u'}{\partial t} = -\frac{1}{\rho_0} \frac{\partial p'}{\partial x}, \quad (2.2.3a)$$

$$\frac{\partial v'}{\partial t} = -\frac{1}{\rho_0} \frac{\partial p'}{\partial y}, \quad (2.2.3b)$$

$$\frac{\partial \rho'}{\partial t} + \rho_0 \left(\frac{\partial u'}{\partial x} + \frac{\partial v'}{\partial y} \right) = 0, \quad (2.2.3c)$$

$$p' = c^2 \rho', \quad (2.2.3d)$$

where $c^2 = \partial p(\rho_0, T) / \partial \rho$. For example, for air $c \approx 285 \text{m s}^{-1}$, and water, $c \approx 1500 \text{m s}^{-1}$.

By writing $P = p' / \rho_0$, we thus obtain

$$\frac{\partial u'}{\partial t} = -\frac{\partial P'}{\partial x}, \quad \frac{\partial v'}{\partial t} = -\frac{\partial P'}{\partial y}, \quad \frac{\partial P'}{\partial t} + c^2 \left(\frac{\partial u'}{\partial x} + \frac{\partial v'}{\partial y} \right) = 0. \quad (2.2.4)$$

Equation (2.2.4) is a simply equations (2.1.1). These equations must be solved subject to any initial conditions, plus the spatial boundary conditions that the normal component of the flow must match that of the boundary. For a stationary boundary which we consider here, we then have

$$\mathbf{u} \cdot \mathbf{n} = 0 \quad \text{on } \partial D, \quad (2.2.5)$$

where \mathbf{n} is the outward normal vector to the boundary. Note that, this boundary condition is equivalent to (2.1.3).

2.2.2 Electromagnetic waves

The waves that can propagate in the vacuum are known as electromagnetic waves. The waves consist of two waves propagating perpendicular; one of the wave is an oscillating magnetic field and the other one is an oscillating electric field. Since both waves propagate perpendicular with each other, they also are called transverse waves. The example of

electromagnetic waves include the radio waves that is generated with low frequency.

The electromagnetic waves can be studied by using the Maxwell's equations, a system of equations that was formulated around 1870 by Scottish scientist James Clerk Maxwell. These equations provide a complete description of electromagnetic phenomena [31, 39, 65].

For a region of space that has no magnetic charges and magnetic current sources, and in a vacuum with no electric charges or currents, Maxwell's equations are

$$\nabla \cdot \mathbf{E} = 0, \quad (2.2.6a)$$

$$\nabla \times \mathbf{E} = -\mu \frac{\partial \mathbf{H}}{\partial t}, \quad (2.2.6b)$$

$$\nabla \cdot \mathbf{H} = 0. \quad (2.2.6c)$$

$$\nabla \times \mathbf{H} = \epsilon \frac{\partial \mathbf{E}}{\partial t}, \quad (2.2.6d)$$

where \mathbf{H} is the magnetic field, \mathbf{E} is the electric field, ϵ is the electric permittivity and μ is the magnetic permeability. In this region, ϵ and μ are constant at value $8.8541878 \times 10^{-12} \text{ C}^2\text{s}^2/\text{kg m}^3$ and $4\pi \times 10^{-7} \text{ m kg /C}^2$. Equations (2.2.6a) and (2.2.6c) are scalar equations and theoretically a direct consequence of the curl equations (i.e., a vector field can be satisfied almost completely if its divergence and curl are given everywhere in space).

The real power of these equations is realised by combining them together to produce the wave equation which is equivalent to (2.1.1) under certain circumstances. To do this, we consider a domain with boundaries in (x, y) plane. Ideally, we consider a channel with waves propagating along the channel as depicted in Figure 2.2.1. Note that this domain can be extended in the z direction to $\pm\infty$, however there are no z variation is considered here. So that the channel is really the gap between two plates with doubly unbounded in z . The boundary plates are considered to be perfectly conducting. If the boundary has a unit normal \mathbf{n} directed outwards the plates, the relevant boundary conditions are then

$$\mathbf{H} \cdot \mathbf{n} = 0 \quad \text{and} \quad \mathbf{E} \times \mathbf{n} = 0. \quad (2.2.7)$$

Since (2.2.6a,b,c,d) are vectors equations and there are no variations in z , then we admit solutions with $H = (0, 0, H_z)$ and $E = (E_x, E_y, 0)$. By taking the curl of both sides (2.2.6b) and inserting in (2.2.6d) we have

$$\epsilon \frac{\partial E_x}{\partial t} = \frac{\partial H_z}{\partial y}, \quad (2.2.8a)$$

$$\epsilon \frac{\partial E_y}{\partial t} = -\frac{\partial H_z}{\partial x}, \quad (2.2.8b)$$

$$\mu \frac{\partial H_z}{\partial t} = \frac{\partial E_x}{\partial y} - \frac{\partial E_y}{\partial x}. \quad (2.2.8c)$$

Equations (2.2.8) are equivalent to (2.1.1) with the mapping of $(u, v) = (E_y, -E_x)$, $p = H_z/\mu$, and $c^2 = 1/\epsilon\mu$. We note that c is the relationship between ϵ and μ where its value is approximately 3×10^8 m/s. As we know, this is the speed of light. It is agreed that light is an example of electromagnetic wave which travel in the vacuum and obeys all the electromagnetic laws. To be more accurate, the constant c in the electromagnetic wave study is called the speed of an electromagnetic wave.

Note that $\mathbf{H} \cdot \mathbf{n} = 0$, whilst $\mathbf{E} \times \mathbf{n} = 0$ implies $E_y n_x - E_x n_y = 0$. With the mapping $u = E_y$ and $v = -E_x$, this becomes $u n_x + v n_y = 0$, which is also $\mathbf{u} \cdot \mathbf{n} = 0$. By doing this, (2.2.6c) is automatically satisfied, whilst (2.2.6a) implies $\partial u/\partial y - \partial v/\partial x$. Since it has a relationship with ρ (charge density), we either need a charge density ($\partial u/\partial y - \partial v/\partial x \neq 0$) or not ($\partial u/\partial y - \partial v/\partial x = 0$). The latter case would apply for a vacuum (or other insulator). Note that $d/dt(\nabla \cdot \mathbf{E}) = 0$ is guaranteed, so $du/dy - dv/dx$ retains its initial value.

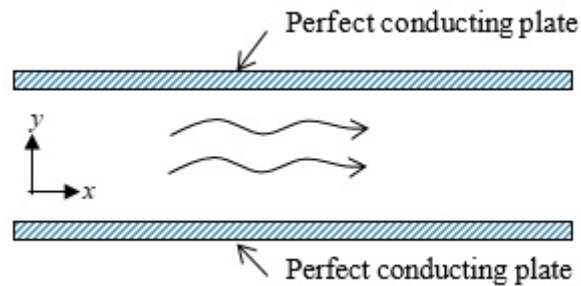


Figure 2.2.1: Electromagnetic waves propagate in a channel.

2.2.3 Shallow-water flows

The simplest way to describe the propagation of water waves is by using the shallow-water equations. They were first derived by Laplace in 1775 to study ocean tides [70, 42]. Then Laplace's equation were derived for flow on a rotating sphere, but we instead consider flow in a planar geometry (x, y, t) . However, given the clear applications in the ocean and atmosphere, we retain the effects of background rotation by including a Coriolis force in the equations, which enter using the Coriolis parameter f , which we take to be constant. A centrifugal force is also necessary in principle when working in a rotating frame, but it is so small (on Earth) that it can be neglected [66].

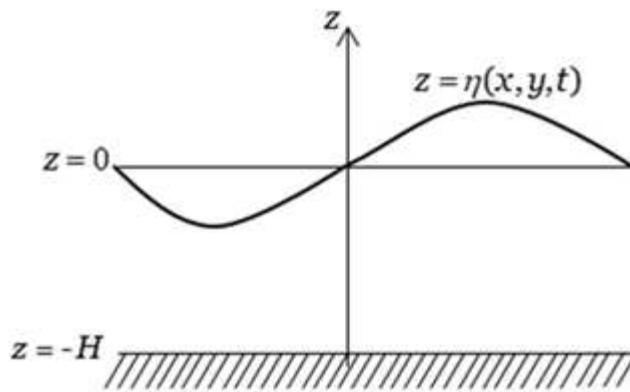


Figure 2.2.2: Schematic showing a shallow water flow.

Since the shallow-water equations are so central to this study, here we present a brief derivation. We consider an inviscid fluid, which, at rest, has uniform depth H . The coordinate z is measured upward from the undisturbed free surface, thus the sea-floor is at $z = -H$, and the upper free surface is at $z = \eta(x, y, t)$, as shown in Figure 2.2.2. The equation of

motions are

$$\frac{Du}{Dt} - fv = -\frac{1}{\rho} \frac{\partial p}{\partial x}, \quad (2.2.9a)$$

$$\frac{Dv}{Dt} + fu = -\frac{1}{\rho} \frac{\partial p}{\partial y}, \quad (2.2.9b)$$

$$\frac{\partial p}{\partial z} = -\rho g, \quad (2.2.9c)$$

$$0 = \frac{\partial u}{\partial x} + \frac{\partial v}{\partial y} + \frac{\partial w}{\partial z}. \quad (2.2.9d)$$

where g is the gravitational acceleration and the operator D/Dt is the material derivative defined by

$$\frac{D}{Dt} = \frac{\partial}{\partial t} + \left(u \frac{\partial}{\partial x} + v \frac{\partial}{\partial y} + w \frac{\partial}{\partial z} \right).$$

Here we have taken hydrostatic balance in the vertical since the uniform depth is small compared to the wavelength of the disturbance. Therefore, hydrostatic balance is consistent with the shallowness of the water (p.80, [70]). Then, the pressure at the free surface is equal to atmospheric pressure p_{atm} , (2.2.9c) implies

$$p(x, y, z, t) = p_{atm} + \rho g \eta(x, y, t) - \rho g z.$$

Thus,

$$-\frac{1}{\rho} \frac{\partial p}{\partial x} = -g \frac{\partial \eta}{\partial x}, \quad -\frac{1}{\rho} \frac{\partial p}{\partial y} = -g \frac{\partial \eta}{\partial y},$$

are independent of z ; it follows from (2.2.9a) and (2.2.9b) that if u and v are independent of z at some instant, they will remain independent of z for all time. We thus seek solutions $u = u(x, y, t)$ and $v = v(x, y, t)$ with

$$\frac{\partial u}{\partial t} + u \frac{\partial u}{\partial x} + v \frac{\partial u}{\partial y} - fv = -g \frac{\partial \eta}{\partial x}, \quad (2.2.10a)$$

$$\frac{\partial v}{\partial t} + u \frac{\partial v}{\partial x} + v \frac{\partial v}{\partial y} + fu = -g \frac{\partial \eta}{\partial y}. \quad (2.2.10b)$$

These are two equations, involving three unknowns u , v and η .

We now have to find an equation for η to close the system. We do this by integrating equation (2.2.9d) over the layer we have

$$w(z = \eta) = - \left(\frac{\partial u}{\partial x} + \frac{\partial v}{\partial y} \right) (\eta + H), \quad (2.2.11)$$

since u and v are independent of z , and $w = 0$ at $z = -H$. The moving boundary condition at the upper surface $z = \eta(x, y, t)$, is given as

$$\mathbf{u} \cdot \mathbf{n} = \mathbf{u}_b \cdot \mathbf{n}, \quad (2.2.12)$$

where \mathbf{n} is the normal vector to $z = \eta(x, y, t)$. At the upper surface

$$\mathbf{u}_b = \left(0, 0, \frac{\partial \eta}{\partial t} \right), \quad (2.2.13)$$

and the surface $z - \eta(x, y, t) = 0$ has

$$\mathbf{n} = \nabla(z - \eta(x, y, t)) = \left(-\frac{\partial \eta}{\partial x}, -\frac{\partial \eta}{\partial y}, 1 \right). \quad (2.2.14)$$

Then, by using (2.2.13) and (2.2.14), (2.2.12) gives

$$(u, v, w) \cdot \left(-\frac{\partial \eta}{\partial x}, -\frac{\partial \eta}{\partial y}, 1 \right) = \left(0, 0, \frac{\partial \eta}{\partial t} \right) \cdot \left(-\frac{\partial \eta}{\partial x}, -\frac{\partial \eta}{\partial y}, 1 \right) \quad \text{at } z = \eta,$$

or

$$w = \frac{\partial \eta}{\partial t} + u \frac{\partial \eta}{\partial x} + v \frac{\partial \eta}{\partial y} \quad \text{at } z = \eta. \quad (2.2.15)$$

Substituting into equation (2.2.11) gives

$$\frac{\partial \eta}{\partial t} + \frac{\partial}{\partial x}((\eta + H)u) + \frac{\partial}{\partial y}((\eta + H)v) = 0. \quad (2.2.16)$$

Equations (2.2.10a), (2.2.10b) and (2.2.16) are known as the shallow water equations.

We now assume that amplitudes of the disturbances are small. Thus, this allows the problem to be linearised. To analyse this, a basic state of rest is taken where $\mathbf{u} = 0$ with constant depth H . So, we write $u = 0 + u'$, $v = 0 + v'$, $\eta = 0 + \eta'$, then equations (2.2.10a), (2.2.10b) and (2.2.16) are linearised by neglecting the nonlinear terms that are products of disturbance quantities, i.e., the second and third left-hand terms of the momentum equation (2.2.10a), (2.2.10b). Then, the equations become

$$\frac{\partial u'}{\partial t} - f v' = -g \frac{\partial \eta'}{\partial x}, \quad (2.2.17a)$$

$$\frac{\partial v'}{\partial t} + f u' = -g \frac{\partial \eta'}{\partial y}, \quad (2.2.17b)$$

$$\frac{\partial \eta'}{\partial t} + H \left(\frac{\partial u'}{\partial x} + \frac{\partial v'}{\partial y} \right) = 0. \quad (2.2.17c)$$

Equations (2.2.17a,b,c) are called linear shallow water equations. These are exactly (2.1.1), but with the effects of earth's rotation f in the momentum equations (2.2.17a,b), $c^2 = gH$, and $p = g\eta$. This system must be solved with boundary conditions where there can be no flow across the boundary and thus the normal component of the velocity is always zero:

$$\mathbf{u} \cdot \mathbf{n} = 0, \quad \text{on } \partial D, \quad (2.2.18)$$

where ∂D is the boundary of the domain D .

2.3 Conservation Laws

This section is devoted to discuss the conservation laws. These laws are important property of mechanical systems. Typically, they express something fundamental about a property of physical interest such as mass and energy. In fluid dynamics, a conservation laws takes the

form

$$\frac{\partial A}{\partial t} + \nabla \cdot \mathbf{J} = 0. \quad (2.3.1)$$

Over an arbitrary volume V we will see that \mathbf{J} is the flux of quantity A across a surface. While over the entire domain D , the quantity A is integrated and will give a conserved quantity $\int_D A \, dV$, if $\mathbf{J} \cdot \mathbf{n} = 0$ on the boundary. We will work with quantities like A which can be defined at points and are thus functions of \mathbf{x} and t .

2.3.1 Conservation of mass

We now derive a conservation law for the mass. We can see that the third equation in (2.1.1) is already in the form

$$\frac{\partial A}{\partial t} + \nabla \cdot \mathbf{J} = 0, \quad (2.3.2)$$

with $A = p$ and $\mathbf{J} = c^2 \mathbf{u}$. Since $\mathbf{J} \cdot \mathbf{n}$ is proportional to $\mathbf{u} \cdot \mathbf{n} = 0$ on ∂D , we then will have a conserved quantity

$$\int_D p \, dV. \quad (2.3.3)$$

We call this the mass. In the acoustics, the mass is indeed proportional to the mass perturbation which is the integral of perturbation density with units of kg s^{-1} for a flow through a surface. In the shallow-water flow, the mass is the mass perturbation, since it is proportional to surface displacement. While in electromagnetism the mass is proportional to an integral of the z - component of the magnetic field, and is thus some sort of magnetic flux.

2.3.2 Conservation of energy

We now proceed with the conservation law of energy for equations (2.1.1). Analogous to the continuum case the energy equation can be obtained by taking the dot product of the momentum equation in (2.1.1) with velocity as

$$u \frac{\partial u}{\partial t} = -u \frac{\partial p}{\partial x}, \quad v \frac{\partial v}{\partial t} = -v \frac{\partial p}{\partial y}. \quad (2.3.4)$$

Adding both equations in (2.3.4) yield

$$\frac{\partial}{\partial t} \left(\frac{1}{2}(u^2 + v^2) \right) = -u \frac{\partial p}{\partial x} - v \frac{\partial p}{\partial y} = -\mathbf{u} \cdot \nabla p. \quad (2.3.5)$$

By writing the right-hand side (2.3.5) as a divergence and using the third equation in (2.1.1) yield

$$-\mathbf{u} \cdot \nabla p = -\nabla \cdot (p\mathbf{u}) - p\nabla \cdot \mathbf{u} = -\nabla \cdot (p\mathbf{u}) - \frac{\partial}{\partial t} \left(\frac{p^2}{2c^2} \right). \quad (2.3.6)$$

Substituting (2.3.6) into (2.3.5) we then have

$$\frac{\partial E}{\partial t} + \nabla \cdot \mathbf{J} = 0, \quad \text{where } E = \frac{p^2}{2c^2} + \frac{1}{2}(u^2 + v^2), \quad \text{and } \mathbf{J} = p\mathbf{u}. \quad (2.3.7)$$

This is the standard energy equation for (2.1.1). Over a fixed volume V , E is the conserved quantity, and we call it energy. The wave energy E has two components which are kinetic energy per unit volume ($\mathbf{u}^2/2$), and some kind internal energy per unit volume ($p^2/2c^2$). The wave energy flux \mathbf{J} tells us in what direction and at what rate wave energy is transferred around the fluid by waves. For example, in the acoustic mode the energy is the summation of velocity and the perturbation density. For shallow-water flow, the energy is the relationship between gravity and surface displacement, since wave energy generated from fluctuation below the surface.

2.4 Wave Propagation

We now examine wave propagation in our two-dimensional system of wave equations

$$\frac{\partial u}{\partial t} - fv = -\frac{\partial p}{\partial x}, \quad (2.4.1a)$$

$$\frac{\partial v}{\partial t} + fu = -\frac{\partial p}{\partial y}, \quad (2.4.1b)$$

$$\frac{\partial p}{\partial t} + c^2 \left(\frac{\partial u}{\partial x} + \frac{\partial v}{\partial y} \right) = 0. \quad (2.4.1c)$$

Here, we are retaining Coriolis terms for greater generality and comparison with the great literature from atmosphere-ocean dynamics, although for most of this thesis these terms will be dropped.

For these rotationally-modified two-dimensional wave equations there is no d'Alembert wave solution (like (1.2.2)). Instead, we seek solutions of the form

$$u = \text{Re} \left(\hat{u} e^{i(kx+ly-\omega_c t)} \right), \quad v = \text{Re} \left(\hat{v} e^{i(kx+ly-\omega_c t)} \right), \quad p = \text{Re} \left(\hat{p} e^{i(kx+ly-\omega_c t)} \right), \quad (2.4.2)$$

where \hat{u} , \hat{v} , and \hat{p} are complex wave amplitudes, k is the wave number in the x -direction, l is the wave number in y -direction, and ω_c is the frequency (with the subscript c denoting the *continuum* frequency, rather than the *discrete* frequency as obtained in a numerical approximation). Then, by substituting (2.4.2) into (2.4.1a,b,c) we have

$$-i\omega_c \hat{u} - fv = -ik\hat{p}, \quad (2.4.3a)$$

$$-i\omega_c \hat{v} + fu = -il\hat{p}, \quad (2.4.3b)$$

$$-i\omega_c \hat{p} + c^2 (ik\hat{u} + il\hat{v}) = 0. \quad (2.4.3c)$$

We wish to find solutions for which $(\hat{u}, \hat{v}, \hat{p})^T$ is not identically zero, and here we introduce the matrix method which performs process of elimination. System (2.4.3a,b,c) can be

written as

$$\begin{pmatrix} -i\omega_c & -f & ik \\ f & -i\omega_c & il \\ c^2ik & c^2il & -i\omega_c \end{pmatrix} \begin{pmatrix} \hat{u} \\ \hat{v} \\ \hat{p} \end{pmatrix} = \begin{pmatrix} 0 \\ 0 \\ 0 \end{pmatrix}. \quad (2.4.4)$$

For non-trivial solutions, the determinant of the matrix must be zero which gives

$$\omega_c (\omega_c^2 - f^2 - c^2(k^2 + l^2)) = 0.$$

The possible solutions are $\omega_c = 0$ which is non wave-like solution, or

$$\omega_c^2 = f^2 + c^2(k^2 + l^2). \quad (2.4.5)$$

Equation (2.4.5) is called dispersion relation and the wave-like solutions can only occur if there is a particular relationship between the frequency, ω_c , and wavenumbers, k, l . In the special case where $l = 0$, the wave crests and troughs propagate at the phase speed, c_p , which from (2.4.5) is

$$c_p = \frac{\omega_c}{k} = \pm c \left(1 + \frac{f^2}{c^2k^2} \right)^{1/2}. \quad (2.4.6)$$

So the phase speed is a function of wavenumber, and waves of different wavenumbers move at different speeds. However, in the absence of rotation effects (i.e., $f = 0$), one can have dispersion relation for the acoustic and electromagnetic case. In that particular case, the phase speed (2.4.6) now is

$$c_p = \frac{\omega_c}{k} = \pm c. \quad (2.4.7)$$

This shows that the wave move at speed c , independent of the wavenumber, k .

Another interesting property that can be derived from dispersion relation is called group velocity. It is the speed of a compact group of waves. It is sometimes written as c_g and is

defined as

$$\mathbf{c}_g(k) = \left(\frac{\partial \omega_c}{\partial k}, \frac{\partial \omega_c}{\partial l} \right). \quad (2.4.8)$$

So, from (2.4.5) we have

$$\mathbf{c}_g = \left(\frac{\partial \omega_c}{\partial k}, \frac{\partial \omega_c}{\partial l} \right) = \pm \frac{c^2}{[f^2 + (k^2 + l^2)]^{1/2}} (k, l). \quad (2.4.9)$$

In the absence of rotation effects, the group velocity is

$$\mathbf{c}_g = \pm \frac{c}{(k^2 + l^2)^{1/2}} (k, l). \quad (2.4.10)$$

We can see that the group velocity is in the same direction as the wavevector $\mathbf{k} = (k, l)$.

2.5 Finite-Difference Approximations

The development of accurate numerical approximation scheme is an essential tool for extracting quantitative information for the deep understanding of the basic physical system. Besides, we can accurately test a proposed numerical scheme by running it on a known solution. Numerical methods also can provide us a better understanding of a given governing equations in their simplest form. So that, we will discuss the numerical approximation by finite-difference method for the system of wave equations (2.4.1). As in section 2.4, we retain the Coriolis terms to make a link to the important work on atmosphere-ocean fluid dynamics, where many of these discretizations were first proposed.

A key issue is whether or not the three variables u, v, p are staggered. In Figure 1.4.1, five possible arrangements were noted. Here, we will examine in detail the discretizations of the so-called A-grid, B-grid and C-grid, as illustrated in Figure 2.5.1, using the terminology of AL77 [6]. It remains to introduce discretizations in both space and time. The former are

introduced according to second-order finite-difference approximations, as discussed in the following sections, each of which follow the classical work of AL77. The latter are avoided completely, by seeking time-harmonic solutions proportional to $\exp(-i\omega_d t)$, where ω_d is the discrete wave frequency. We thus only focus on the effects of the spatial discretization.

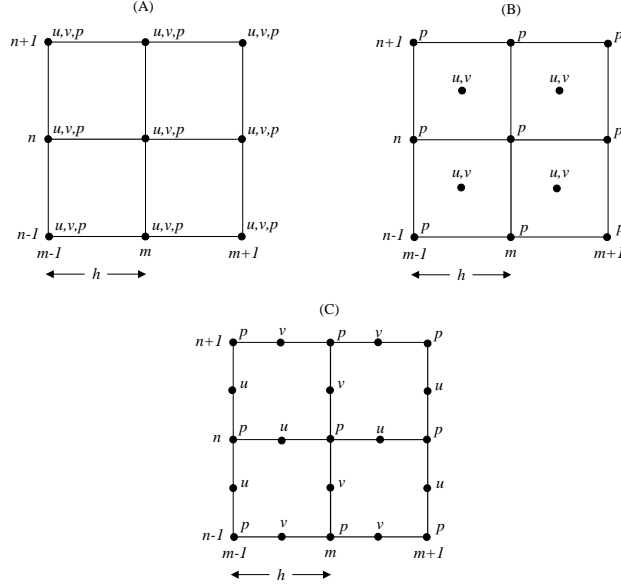


Figure 2.5.1: Distributions of the dependent variables on A-, B-, C-grids. (The figure is reillustrated from [6]).

2.5.1 A-grid

On the A-grid where all variables are located at the same node, (2.4.1a,b,c) are discretised by using second-order centered finite-differences formulation as

$$-i\omega_d u_{m,n} - f v_{m,n} = -\frac{p_{m+1,n} - p_{m-1,n}}{2h}, \quad (2.5.1a)$$

$$-i\omega_d v_{m,n} + f u_{m,n} = -\frac{p_{m,n+1} - p_{m,n-1}}{2h}, \quad (2.5.1b)$$

$$-i\omega_d p_{m,n} + \frac{c^2}{2h} \left(u_{m+1,n} - u_{m-1,n} + v_{m,n+1} - v_{m,n-1} \right) = 0, \quad (2.5.1c)$$

with subscript $m, n \in \mathbb{Z}$ and h is the grid spacing.

These set of discrete equations are need to be solved together with the boundary condition $\mathbf{u} \cdot \mathbf{n} = 0$. Note that, all nodes for u, v and p are co-located. This means that it is easy to set the appropriate combination to be zero, but then need to evolve $\mathbf{u} \cdot \mathbf{t}$, where \mathbf{t} is the tangent vector. However, there is no pressure nodes outside the domain to calculate the necessary $\partial p/\partial x$ and $\partial p/\partial y$. So that it is not obvious how to do this.

2.5.2 B-grid

On the B-grid, the velocity variables u, v are located at the corner of the cell while the pressure p is located at the centre of the cell. Then, by using the second-order centred finite-difference formulation (2.4.1a,b,c) are discretized as

$$-i\omega_d u_{m+\frac{1}{2},n+\frac{1}{2}} - f v_{m+\frac{1}{2},n+\frac{1}{2}} = -\frac{p_{m+1,n+1} + p_{m+1,n} - p_{m,n+1} + p_{m,n}}{2h}, \quad (2.5.2a)$$

$$-i\omega_d v_{m+\frac{1}{2},n+\frac{1}{2}} + f u_{m+\frac{1}{2},n+\frac{1}{2}} = -\frac{p_{m+1,n+1} + p_{m,n+1} - p_{m+1,n} + p_{m,n}}{2h}, \quad (2.5.2b)$$

$$-i\omega_d p_{m,n} + \frac{c^2}{2h} \left(u_{m+\frac{1}{2},n+\frac{1}{2}} + u_{m+\frac{1}{2},n-\frac{1}{2}} - u_{m-\frac{1}{2},n+\frac{1}{2}} - u_{m-\frac{1}{2},n-\frac{1}{2}} \right. \\ \left. + v_{m+\frac{1}{2},n+\frac{1}{2}} + v_{m-\frac{1}{2},n+\frac{1}{2}} - v_{m+\frac{1}{2},n-\frac{1}{2}} - v_{m-\frac{1}{2},n-\frac{1}{2}} \right) = 0, \quad (2.5.2c)$$

where $m, n \in \mathbb{Z}$. We can see here that, the approximation of the derivative is using only a step of grid spacing h , and the derivative are calculated at the mid-way between other variables. Note that the derivative expressions look unwieldy because of the way the nodes are located.

Again, discrete equations (2.5.2a,b,c) need to be solved subject to boundary condition $\mathbf{u} \cdot \mathbf{n} = 0$. However, same issue as the A-grid arises since the pressure nodes are located at the centre of the cell, not outside the cell.

2.5.3 C-grid

Next, on the the C-grid. The big difference here is that u and v are not defined at same nodes, so the Coriolis term f must be approximated thoroughly using the neighbour points. In this case, there are various way to approximate the Coriolis term in the momentum equations [20, 23]. Here, we use the simplest and standard formulation, by taking the average over four neighboring points which can be found in [6]. Then on C-grid, (2.4.1a,b,c) are discretised as

$$-i\omega_d u_{m,n+\frac{1}{2}} - f \frac{v_{m+\frac{1}{2},n+1} + v_{m+\frac{1}{2},n} + v_{m-\frac{1}{2},n} + v_{m-\frac{1}{2},n+1}}{4} = -\frac{p_{m+\frac{1}{2},n} - p_{m-\frac{1}{2},n+\frac{1}{2}}}{h}, \quad (2.5.3a)$$

$$-i\omega_d v_{m+\frac{1}{2},n} + f \frac{u_{m+1,n+\frac{1}{2}} + u_{m+1,n-\frac{1}{2}} + u_{m,n-\frac{1}{2}} + u_{m,n+\frac{1}{2}}}{4} = -\frac{p_{m+\frac{1}{2},n+\frac{1}{2}} - p_{m+\frac{1}{2},n-\frac{1}{2}}}{h}, \quad (2.5.3b)$$

$$-i\omega_d p_{m+\frac{1}{2},n+\frac{1}{2}} + \frac{c^2}{h} \left(u_{m+1,n+\frac{1}{2}} - u_{m,n+\frac{1}{2}} + v_{m+\frac{1}{2},n+1} - v_{m+\frac{1}{2},n} \right) = 0. \quad (2.5.3c)$$

First we note that all the spatial derivatives are easy (and natural) to calculate. As previous grids, these discrete equations must be solved with the no normal flow boundary conditions. Here, this is easy to implement by setting $v = 0$ on the boundary. In the special case (i.e., staircase boundary), one can set either $u = 0$ or $v = 0$ on the boundary. This is naturally satisfied since the u and v nodes are lie on the cell edge centers. Further, no extra (ghost) nodes are required outside of the domain, as can be seen in Figure 2.5.1.

2.6 Discrete Conservation Laws

We now consider the analogue of the conservation laws established in section 2.3 for the discrete equations of motion. We only do this for the C grid, which is the focus of the remainder of this thesis. In particular, we consider a grid cell of the C-grid at $[x_{m-\frac{1}{2}}, x_{m+\frac{1}{2}}]$

and $[y_{n-\frac{1}{2}}, y_{n+\frac{1}{2}}]$, as illustrated in Figure 2.6.1. Further, we perform our analysis for a system where rotation is neglected. This is, of course, natural for acoustics or electromagnetic waves. For shallow-water waves on a rotating planet, it can be justified when the Rossby number of the flow is large. More precisely, for a representative lengthscale of motion L and speed of flow U , the inertial terms are of size $\text{Ro} = (U^2/L)/(fU) = U/fL$ relative to the Coriolis terms, and we demand $\text{Ro} \gg 1$.

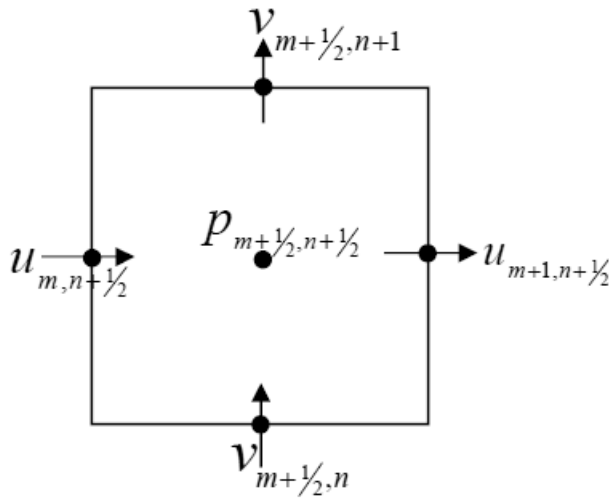


Figure 2.6.1: The arrangement of variables on a C-grid.

2.6.1 Discrete Conservation of Mass

In this section, we will derive a discrete version of conservation of mass. We now recall equation (2.5.3c) to begin the derivation. On the C-grid this equation is discretized as

$$\frac{\partial}{\partial t} p_{m+\frac{1}{2}, n+\frac{1}{2}} + \frac{c^2}{h} \left(u_{m+1, n+\frac{1}{2}} - u_{m, n+\frac{1}{2}} + v_{m+\frac{1}{2}, n+1} - v_{m+\frac{1}{2}, n} \right) = 0. \quad (2.6.1)$$

If we integrate this equation over a grid square, we then obtain

$$\begin{aligned} \frac{d}{dt} h^2 \left(p_{m+\frac{1}{2}, n+\frac{1}{2}} \right) dx dy \\ + c^2 h \left(u_{m+1, n+\frac{1}{2}} - u_{m, n+\frac{1}{2}} + v_{m+\frac{1}{2}, n+1} - v_{m+\frac{1}{2}, n} \right) dx dy = 0. \end{aligned} \quad (2.6.2)$$

Note that all the four terms in the bracket are fluxes which are in and out at each cell edge. Then, for all grid cells we then will have a summation of all fluxes at each grid edges and pressure at the centre of the grid. Since the flux is going inside and outside at every cells, all the interior fluxes are cancel. So that we only left with boundary fluxes. However, with staircase boundaries, all boundary fluxes are zero. Therefore we have

$$\frac{d}{dt} h^2 \sum_{m,n} p_{m+\frac{1}{2}, n+\frac{1}{2}} = 0, \quad (2.6.3)$$

where this sum is taken over all grid cells.

2.6.2 Discrete Conservation of Energy

We now proceed with the derivation of discrete conservation law of energy on the C-grid. We begin by writing momentum equation and also continuity equation (2.1.1) on the C-grid as

$$\frac{\partial}{\partial t} u_{m, n+\frac{1}{2}} = -\frac{1}{h} \left(p_{m+\frac{1}{2}, n+\frac{1}{2}} - p_{m-\frac{1}{2}, n+\frac{1}{2}} \right), \quad (2.6.4a)$$

$$\frac{\partial}{\partial t} v_{m+\frac{1}{2}, n} = -\frac{1}{h} \left(p_{m+\frac{1}{2}, n+\frac{1}{2}} - p_{m+\frac{1}{2}, n-\frac{1}{2}} \right), \quad (2.6.4b)$$

$$\frac{\partial}{\partial t} p_{m+\frac{1}{2}, n+\frac{1}{2}} + \frac{c^2}{h} \left(u_{m+1, n+\frac{1}{2}} - u_{m, n+\frac{1}{2}} + v_{m+\frac{1}{2}, n+1} - v_{m+\frac{1}{2}, n} \right) = 0, \quad (2.6.4c)$$

where we are neglecting the Coriolis terms which are also absent for most of this thesis, since they complicate the discussion.

Analogous to the continuum case, the energy equation can be obtained by multiplying momentum equation with velocity. So, by multiplying (2.6.4a) and (2.6.4b) with $u_{m,n+\frac{1}{2}}$ and $v_{m+\frac{1}{2},n}$, we have

$$\frac{\partial}{\partial t} \left(\frac{u_{m,n+\frac{1}{2}}^2}{2} \right) = -\frac{1}{h} u_{m,n+\frac{1}{2}} \left(p_{m+\frac{1}{2},n+\frac{1}{2}} - p_{m-\frac{1}{2},n+\frac{1}{2}} \right), \quad (2.6.5a)$$

$$\frac{\partial}{\partial t} \left(\frac{v_{m+\frac{1}{2},n}^2}{2} \right) = -\frac{1}{h} v_{m+\frac{1}{2},n} \left(p_{m+\frac{1}{2},n+\frac{1}{2}} - p_{m+\frac{1}{2},n-\frac{1}{2}} \right). \quad (2.6.5b)$$

We can form corresponding expressions for the right-hand edge and top edge of the cell:

$$\frac{\partial}{\partial t} \left(\frac{u_{m+1,n+\frac{1}{2}}^2}{2} \right) = -\frac{1}{h} u_{m+1,n+\frac{1}{2}} \left(p_{m+\frac{3}{2},n+\frac{1}{2}} - p_{m+\frac{1}{2},n+\frac{1}{2}} \right), \quad (2.6.6a)$$

$$\frac{\partial}{\partial t} \left(\frac{v_{m+\frac{1}{2},n+1}^2}{2} \right) = -\frac{1}{h} v_{m+\frac{1}{2},n+1} \left(p_{m+\frac{1}{2},n+\frac{3}{2}} - p_{m+\frac{1}{2},n+\frac{1}{2}} \right). \quad (2.6.6b)$$

All four expressions are relevant for the energy equation, since motivated by the trapezoidal rule we have

$$\iint u^2 \, dx \, dy \approx h^2 \frac{u_{m,n+\frac{1}{2}}^2 + u_{m+1,n+\frac{1}{2}}^2}{2}. \quad (2.6.7)$$

Thus adding (2.6.5) and (2.6.6), we have

$$\begin{aligned} \frac{\partial}{\partial t} \left(\frac{u_{m,n+\frac{1}{2}}^2 + u_{m+1,n+\frac{1}{2}}^2}{4} \right) &= -\frac{1}{2h} u_{m,n+\frac{1}{2}} \left(p_{m+\frac{1}{2},n+\frac{1}{2}} - p_{m-\frac{1}{2},n+\frac{1}{2}} \right) \\ &\quad - \frac{1}{2h} u_{m+1,n+\frac{1}{2}} \left(p_{m+\frac{3}{2},n+\frac{1}{2}} - p_{m+\frac{1}{2},n+\frac{1}{2}} \right). \end{aligned} \quad (2.6.8)$$

Similarly, considering v , we find

$$\begin{aligned} \frac{\partial}{\partial t} \left(\frac{v_{m+\frac{1}{2},n}^2 + v_{m+\frac{1}{2},n+1}^2}{4} \right) = & -\frac{1}{2h} v_{m+\frac{1}{2},n} \left(p_{m+\frac{1}{2},n+\frac{1}{2}} - p_{m+\frac{1}{2},n-\frac{1}{2}} \right) \\ & - \frac{1}{2h} v_{m+\frac{1}{2},n+1} \left(p_{m+\frac{1}{2},n+\frac{3}{2}} - p_{m+\frac{1}{2},n+\frac{1}{2}} \right). \end{aligned} \quad (2.6.9)$$

So we have an expression for the time evolution of the kinetic energy in each cell, with energy fluxes at the cell edges. This must be complemented by a potential energy equation, which is found by multiplication of (2.6.4c) by $p_{m+\frac{1}{2},n+\frac{1}{2}}$:

$$\frac{\partial}{\partial t} \left(\frac{p_{m+\frac{1}{2},n+\frac{1}{2}}^2}{2c^2} \right) = -\frac{1}{h} \left(u_{m+1,n+\frac{1}{2}} - u_{m,n+\frac{1}{2}} + v_{m+\frac{1}{2},n+1} - v_{m+\frac{1}{2},n} \right), \quad (2.6.10)$$

which can be simplified by adding all (2.6.8), (2.6.9) and (2.6.10) and give

$$\begin{aligned} \frac{\partial}{\partial t} \left(\frac{u_{m,n+\frac{1}{2}}^2 + u_{m+1,n+\frac{1}{2}}^2}{4} + \frac{v_{m+\frac{1}{2},n}^2 + v_{m+\frac{1}{2},n+1}^2}{4} + \frac{p_{m+\frac{1}{2},n+\frac{1}{2}}^2}{2c^2} \right) = \\ \frac{1}{h} u_{m,n+\frac{1}{2}} \left[\frac{p_{m+\frac{1}{2},n+\frac{1}{2}} + p_{m+\frac{1}{2},n+\frac{3}{2}}}{2} \right] - \frac{1}{h} u_{m+1,n+\frac{1}{2}} \left[\frac{p_{m+\frac{1}{2},n+\frac{1}{2}} + p_{m+\frac{3}{2},n+\frac{1}{2}}}{2} \right] \\ + \frac{1}{h} v_{m+\frac{1}{2},n} \left[\frac{p_{m+\frac{1}{2},n+\frac{1}{2}} + p_{m+\frac{1}{2},n-\frac{1}{2}}}{2} \right] - \frac{1}{h} v_{m+\frac{1}{2},n+1} \left[\frac{p_{m+\frac{1}{2},n+\frac{1}{2}} + p_{m+\frac{1}{2},n+\frac{3}{2}}}{2} \right]. \end{aligned} \quad (2.6.11)$$

The square brackets each contain a speed \times pressure term, which is an energy flux. In particular, these terms correspond to a speed combined with a pressure formed by averaging the two adjacent pressure nodes. Thus, the energy flux on the right of cell m, n is equal and opposite to the energy flux on left of cell $m+1, n$, and that at the top of cell m, n is equal and opposite to the energy flux at the bottom of cell $m, n+1$, due to the pressure averaging. Thus, when summed over all grid cells, all interior energy fluxes cancel, and we are simply left with the energy fluxes at the boundary nodes. However, for a staircase boundary, where the corresponding velocity component is zero, there are no energy fluxes. Thus, there is a

discrete energy conservation law:

$$\frac{d}{dt} \sum_{m,n} \left(\frac{p_{m+\frac{1}{2},n+\frac{1}{2}}^2}{2c^2} + \frac{u_{m,n+\frac{1}{2}}^2 + u_{m+1,n+\frac{1}{2}}^2 + v_{m+\frac{1}{2},n}^2 + v_{m+\frac{1}{2},n+1}^2}{4} \right) = 0. \quad (2.6.12)$$

2.7 Discrete Waves

To get an idea of the different performances of the grids, we consider waves propagating in a doubly periodic domain (i.e., with no boundaries) and the analysis were done for equations (2.4.3) on A-, B- and C-grid. Note that all calculations in this section also can be found in [6]. On every grid, we used notation as in Figure 2.5.1 with

$$x_m = mh, \quad y_n = nh.$$

The wave propagation on finite-difference grid can be seen by seeking discrete wavelike solution of the form

$$u_{m,n} = \text{Re} \left(\hat{u} e^{i(kx_m + ly_n)} \right), \quad v_{m,n} = \text{Re} \left(\hat{v} e^{i(kx_m + ly_n)} \right), \quad p_{m,n} = \text{Re} \left(\hat{p} e^{i(kx_m + ly_n)} \right), \quad (2.7.1)$$

with time-periodicity assumed to be proportional to $\exp(-i\omega_d t)$, where ω_d is the discrete wave frequency. Note that, in this section we again retain the Coriolis terms, to make a connection to well-known results in atmosphere-ocean dynamics. Also note that we will apply Euler's formula $\exp(ikx_m) = \cos(kx_m) + i \sin(kx_m)$ for the simplification of the resulting discrete equations for each grids.

2.7.1 A-grid solutions

By substituting (2.7.1) into (2.5.1a), (2.5.1b), (2.5.1c) and applying the Euler's formula we now have

$$-i\omega_d \hat{u} - f \hat{v} + i \frac{\sin kh}{h} \hat{p} = 0, \quad (2.7.2)$$

$$-i\omega_d \hat{v} + f \hat{u} + i \frac{\sin lh}{h} \hat{p} = 0, \quad (2.7.3)$$

$$-i\omega_d \hat{p} + i \frac{c^2}{h} (\sin kh \hat{u} + \sin lh \hat{v}) = 0, \quad (2.7.4)$$

and written in matrix form we have

$$\begin{pmatrix} -i\omega_d & -f & i \frac{\sin kh}{h} \\ f & -i\omega_d & i \frac{\sin lh}{h} \\ i \frac{c^2}{h} \sin kh & i \frac{c^2}{h} \sin lh & -i\omega_d \end{pmatrix} \begin{pmatrix} \hat{u} \\ \hat{v} \\ \hat{p} \end{pmatrix} = \begin{pmatrix} 0 \\ 0 \\ 0 \end{pmatrix}. \quad (2.7.5)$$

For non-trivial solutions, the determinant of the matrix must be zero. There is one root $\omega_d = 0$ (which corresponding to $\omega_c = 0$); the other two roots are from

$$\omega_d^2 = f^2 + \frac{c^2}{h^2} (\sin^2 kh + \sin^2 lh). \quad (2.7.6)$$

This is the discrete analogue of (2.4.5), which is called discrete dispersion relation.

We now examine the accuracy of (2.7.6). By using Taylor series expansion, (2.7.6) has the form

$$\begin{aligned} \omega_d^2 &= f^2 + \frac{c^2}{h^2} \left[\left((kh)^2 - \frac{1}{3}(kh)^4 + \frac{1}{60}(kh)^6 + \dots \right) + \left((lh)^2 - \frac{1}{3}(lh)^4 + \frac{1}{60}(lh)^6 + \dots \right) \right], \\ &= \omega_c^2 - \frac{h^2 c^2}{3} (k^4 + l^4) - \frac{c^2 h^4}{60} (k^6 + l^6) + O(h^6). \end{aligned}$$

So to leading-order in h , we have

$$\omega_d^2 = f^2 + \frac{c^2}{h^2} (\sin^2(kh) + \sin^2(lh)) = \omega_c^2 - \frac{h^2 c^2}{3} (k^4 + l^4) + O(h^4). \quad (2.7.7)$$

The discrete frequency for A-grid is second-order accurate as expected since we have use the second-order centred finite-difference formulation to discretise the equations. We can see for the A-grid, $\omega_d^2 < \omega_c^2$: the discrete frequency ω_d underestimates the continuum frequency ω_c . We will further make a comparison and analysis of this result in section 2.7.4.

2.7.2 B-grid solutions

On the B-grid, by substituting (2.7.1) into (2.5.2a), (2.5.2b), (2.5.2c) yield

$$-i\omega_d \hat{u} - f\hat{v} + i\frac{1}{h} \left[\sin\left(\frac{kh}{2} + \frac{lh}{2}\right) + \sin\left(\frac{kh}{2} - \frac{lh}{2}\right) \right] \hat{p} = 0, \quad (2.7.8a)$$

$$-i\omega_d \hat{v} + f\hat{u} + i\frac{1}{h} \left[\sin\left(\frac{kh}{2} + \frac{lh}{2}\right) - \sin\left(\frac{kh}{2} - \frac{lh}{2}\right) \right] \hat{p} = 0, \quad (2.7.8b)$$

$$\begin{aligned} -i\omega_d \hat{p} + i\frac{c^2}{h} \left[\sin\left(\frac{kh}{2} + \frac{lh}{2}\right) + \sin\left(\frac{kh}{2} - \frac{lh}{2}\right) \right] \hat{u} \\ + i\frac{c^2}{h} \left[\sin\left(\frac{kh}{2} + \frac{lh}{2}\right) - \sin\left(\frac{kh}{2} - \frac{lh}{2}\right) \right] \hat{v} = 0. \end{aligned} \quad (2.7.8c)$$

For non-trivial solutions, we recovered one root which is $\omega_d = 0$, and the other two roots are

$$\omega_d^2 = f^2 + 4\frac{c^2}{h^2} \left[\sin^2\left(\frac{kh}{2}\right) \cos^2\left(\frac{lh}{2}\right) + \cos^2\left(\frac{kh}{2}\right) \sin^2\left(\frac{lh}{2}\right) \right]. \quad (2.7.9)$$

In order to examine the numerical error of (2.7.9), we applied the Taylor series expansion. In the limit of small kh and lh ($kh \ll 1$, $lh \ll 1$), (2.7.9) has the form

$$\begin{aligned}\omega_d^2 &= f^2 + 4\frac{c^2}{h^2} \left[\left(\left(\frac{kh}{2} \right)^2 - \frac{1}{3} \left(\frac{kh}{2} \right)^4 + \dots \right) \left(1 - \left(\frac{lh}{2} \right)^2 + \frac{1}{3} \left(\frac{lh}{2} \right)^4 + \dots \right) \right] \\ &\quad \left[+ \left(1 - \left(\frac{kh}{2} \right)^2 + \frac{1}{3} \left(\frac{kh}{2} \right)^4 + \dots \right) \left(\left(\frac{lh}{2} \right)^2 - \frac{1}{3} \left(\frac{lh}{2} \right)^4 + \dots \right) \right], \\ &= \omega_c^2 - \frac{c^2 h^2}{12} (k^4 + l^4 + 6k^2 l^2) + O(h^4).\end{aligned}$$

Therefore, discrete frequency for B-grid can be written as

$$\begin{aligned}\omega_d^2 &= f^2 + 4\frac{c^2}{h^2} \left[\sin^2 \left(\frac{kh}{2} \right) \cos^2 \left(\frac{lh}{2} \right) + \cos^2 \left(\frac{kh}{2} \right) \sin^2 \left(\frac{lh}{2} \right) \right] \\ &= \omega_c^2 - \frac{c^2 h^2}{12} (k^4 + l^4 + 6k^2 l^2) + O(h^4).\end{aligned}\tag{2.7.10}$$

Again, on the B-grid $\omega_d^2 < \omega_c^2$: the discrete frequency underestimates the continuum frequency.

2.7.3 C-grid solutions

On the C-grid, by substituting (2.7.1) into (2.5.3a), (2.5.3b), (2.5.3c) yields

$$-i\omega_d \hat{u} - \frac{f}{2} \left[\cos \left(\frac{kh}{2} + \frac{lh}{2} \right) + \sin \left(\frac{kh}{2} - \frac{lh}{2} \right) \right] \hat{v} + i\frac{2}{h} \sin \left(\frac{kh}{2} \right) \hat{p} = 0, \tag{2.7.11a}$$

$$-i\omega_d \hat{v} + \frac{f}{2} \left[\cos \left(\frac{kh}{2} + \frac{lh}{2} \right) + \cos \left(\frac{kh}{2} - \frac{lh}{2} \right) \right] \hat{u} + i\frac{2}{h} \sin \left(\frac{lh}{2} \right) \hat{p} = 0, \tag{2.7.11b}$$

$$-i\omega_d \hat{p} + 2i\frac{c^2}{h} \left[\sin \left(\frac{kh}{2} \right) \hat{u} + \sin \left(\frac{lh}{2} \right) \hat{v} \right] = 0. \tag{2.7.11c}$$

For non trivial solutions, we recovered one roots which is $\omega_d = 0$ and the other two roots are from

$$\omega_d^2 = f^2 \cos^2 \left(\frac{kh}{2} \right) \cos^2 \left(\frac{lh}{2} \right) + 4 \frac{c^2}{h^2} \left[\sin^2 \left(\frac{kh}{2} \right) + \sin^2 \left(\frac{lh}{2} \right) \right]. \quad (2.7.12)$$

In the limit of small kh and lh , (i.e., $kh \ll 1, lh \ll 1$), the discrete dispersion relation has the form

$$\begin{aligned} \omega_d^2 &= f^2 \left(1 - \left(\frac{kh}{2} \right)^2 + \frac{1}{3} \left(\frac{kh}{2} \right)^4 + \dots \right) \left(1 - \left(\frac{lh}{2} \right)^2 + \frac{1}{3} \left(\frac{lh}{2} \right)^4 + \dots \right) \\ &\quad + 4 \frac{c^2}{h^2} \left[\left(\left(\frac{kh}{2} \right)^2 - \frac{1}{3} \left(\frac{kh}{2} \right)^4 + \dots \right) + \left(\left(\frac{lh}{2} \right)^2 - \frac{1}{3} \left(\frac{lh}{2} \right)^4 + \dots \right) \right], \\ &= f^2 \left(1 - \frac{h^2}{4} (k^2 + l^2) \right) + c^2 \left(k^2 + l^2 - \frac{1}{12} h^2 (k^4 + l^4) \right) + O(h^4). \end{aligned}$$

Discrete frequency for C-grid can be written as

$$\begin{aligned} \omega_d^2 &= f^2 \cos^2 \left(\frac{kh}{2} \right) \cos^2 \left(\frac{lh}{2} \right) + 4 \frac{c^2}{h^2} \left[\sin^2 \left(\frac{kh}{2} \right) + \sin^2 \left(\frac{lh}{2} \right) \right], \\ &= \omega_c^2 - \frac{c^2 h^2}{12} \left(\frac{3f^2}{c^2} (k^2 + l^2) + k^4 + l^4 \right) + O(h^4). \end{aligned} \quad (2.7.13)$$

So we found that on the C-grid, $\omega_d^2 < \omega_c^2$: the discrete frequency underestimates the continuum frequency ω_c .

2.7.4 Comparison of discrete frequency on the A-, B-, and C-grid

All discrete frequencies for A-, B- and C-grid are rewritten as the following:

A-grid:

$$\begin{aligned}\omega_d^2 &= f^2 + \frac{c^2}{h^2} [\sin^2(kh) + \sin^2(lh)] \\ &= \omega_c^2 - \frac{c^2 h^2}{3} (k^4 + l^4) + O(h^4).\end{aligned}$$

B-grid:

$$\begin{aligned}\omega_d^2 &= f^2 + 4\frac{c^2}{h^2} \left[\sin^2\left(\frac{kh}{2}\right) \cos^2\left(\frac{lh}{2}\right) + \cos^2\left(\frac{kh}{2}\right) \sin^2\left(\frac{lh}{2}\right) \right] \\ &= \omega_c^2 - \frac{c^2 h^2}{12} (k^4 + l^4 + 6k^2 l^2) + O(h^4).\end{aligned}$$

C-grid:

$$\begin{aligned}\omega_d^2 &= f^2 \cos^2\left(\frac{kh}{2}\right) \cos^2\left(\frac{lh}{2}\right) + 4\frac{c^2}{h^2} \left[\sin^2\left(\frac{kh}{2}\right) + \sin^2\left(\frac{lh}{2}\right) \right], \\ &= \omega_c^2 - \frac{c^2 h^2}{12} \left(\frac{3f^2}{c^2} (k^2 + l^2) + k^4 + l^4 \right) + O(h^4).\end{aligned}$$

From all three discrete frequency equations, we can see that all are second-order accurate in h when $h \ll 1$, so they are equally accurate in that sense. However, there are important differences for larger h , which we now analyse.

We first consider the simplest case, which is in one-dimension (i.e., $l = 0$) and with no rotation ($f = 0$). In Figure 2.7.1, we show the non-dimensional phase speed $(\omega/k)/c = \omega/(ck)$ and nondimensional group speed $(1/c)\partial\omega/\partial k$ as a function of kh . We consider values of kh in $(0, \pi)$: when $kh = \pi$, the wave is minimally resolved, with $u_{n+1}/u_n = \exp(ikh) = \exp(i\pi) = -1$, i.e., a grid-scale wave. We can see that the performance of the B and C grids are identical. Wave speed takes the correct sign (even if underestimated), and group speed is also the correct sign, although it is zero for marginally resolved waves. Note that a group speed of zero is not good, because it implies that energy will not propagate away, so that the grid-scale waves is stationary. On the A grid, it can be seen that the phase

speed takes the correct sign, but group speed can take the wrong sign which is physically very undesirable.

We next consider two-dimensional frequency without rotation. Figure 2.7.2 shows the comparison of the continuum and discrete A, B and C-grid frequencies. The top left panel shows the continuum frequency and it can be seen that the frequency increases monotonically with wavenumbers in the x and y directions. For the A-grid (top left panel), the discrete frequency has a false extrema at $k = \pi/2h$ which means that the group velocity at $kh = \pi/2$ is zero. Note that, A-grid has group velocity error for modes higher than $k = l = \pi/2h$ and a consequent lack of energy propagation for this wavenumber. In the discrete frequency for B-grid (bottom left panel), we can see that the frequency is underestimated for short two-dimensional waves. From the figure, it can be seen that at high resolution the only grid that produces a monotonically increasing frequency is the C-grid (bottom right panel). As we know finite difference can serve a good approximate solution in the case of small size of grid spacing. So in this case, C-grid is the most satisfactory choice of grid in producing a better solution.

We now consider two-dimensional frequency with rotation. In this case, there is a special characteristic in the frequency, which is the Rossby radius of deformation that defined by $L_D = c/f = \sqrt{gH}/f$, which is the scale distance over which the gravitational tendency to render the free surface flat is balanced by the tendency of Coriolis acceleration to deform the surface [52]. In order to obtain the satisfactory result, great care must be taken on the value of L_D . As investigated and discussed in [6] and [54], C-grid will produce a better result when $L_D > 1/2$. Shown in Figure 2.7.3 are comparison of the frequencies by using two values of L_D . The left column shows the frequency with $L_D = 2$ while the right column shows the frequency with $L_D = 0.1$. Note that this figure also same as Figure 2 in [54]. As can be seen from the frequency plots for $L_D = 2$, the continuum frequency increases monotonically with wavenumber. The frequencies for both A and B grid agree with the continuum frequency only in the third quadrant. Outside third quadrant, the frequency for

A and B grid decreases as the wavenumber increasing which contradict with the continuum frequency. Unlike the other frequencies, the frequency for C grid shows the same monotonic increase of frequency as the continuum frequency. For $L_D = 0.1$, both frequencies for A and B grid show the same distortion as $L_D = 2$. However, the C-grid frequency now shows a monotonic decrease with increasing wavenumber. Hence all discrete frequencies contrary to the continuum frequency. Thus, for the two dimensional case with rotation C-grid is the most satisfactory choice of grid in producing a better solution with an appropriate value of L_D .

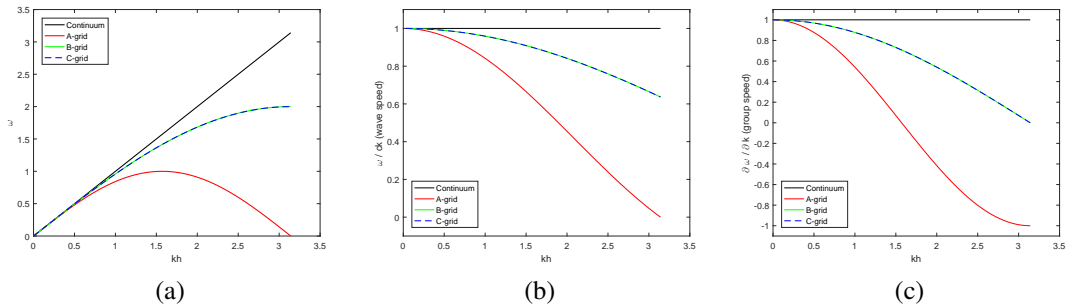


Figure 2.7.1: (a) The frequency, (b) the wave speed, and (c) the group speed for the case $f = 0$.

2.8 Summary

The chapter began with a review of a standard set of two-dimensional wave equations and showed that three different physical systems (i.e., acoustic, electromagnetism, shallow-water flow) has equivalent equations. We also reviewed some important conservation laws for this equations. We next examined wave propagation using the standard set of wave equations by looking at the frequency and property related to it: phase speed and group velocity.

Then, we have reviewed a numerical scheme by finite-difference methods on three different finite-difference grids, namely A, B, and C-grid. We also have reviewed some discrete

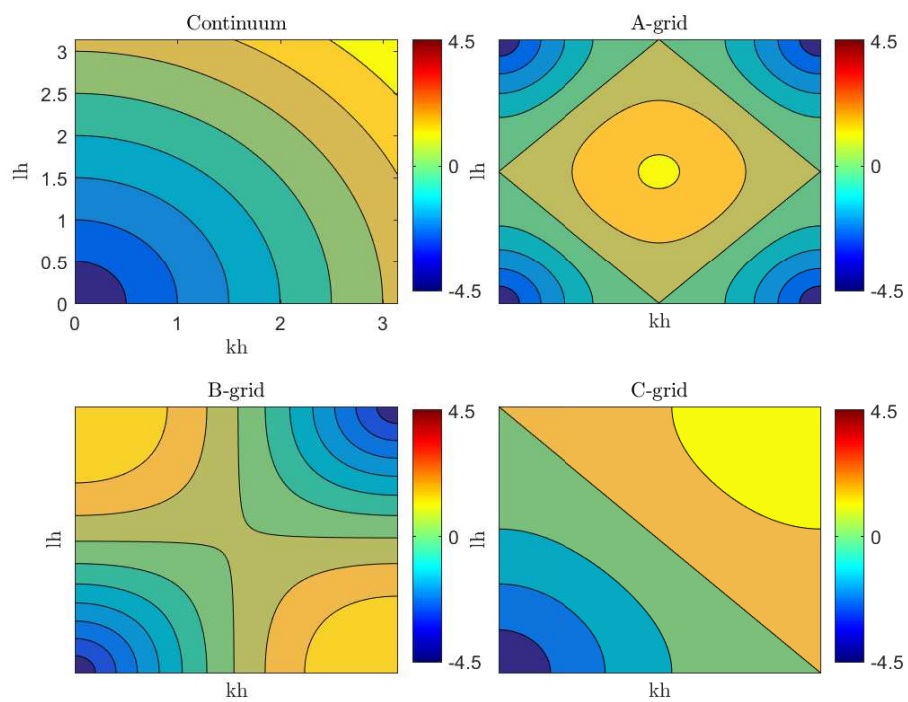


Figure 2.7.2: The dispersion relations for the continuum and finite-difference approximation based on the A, B, and C-grids without rotation effects, $f = 0$.

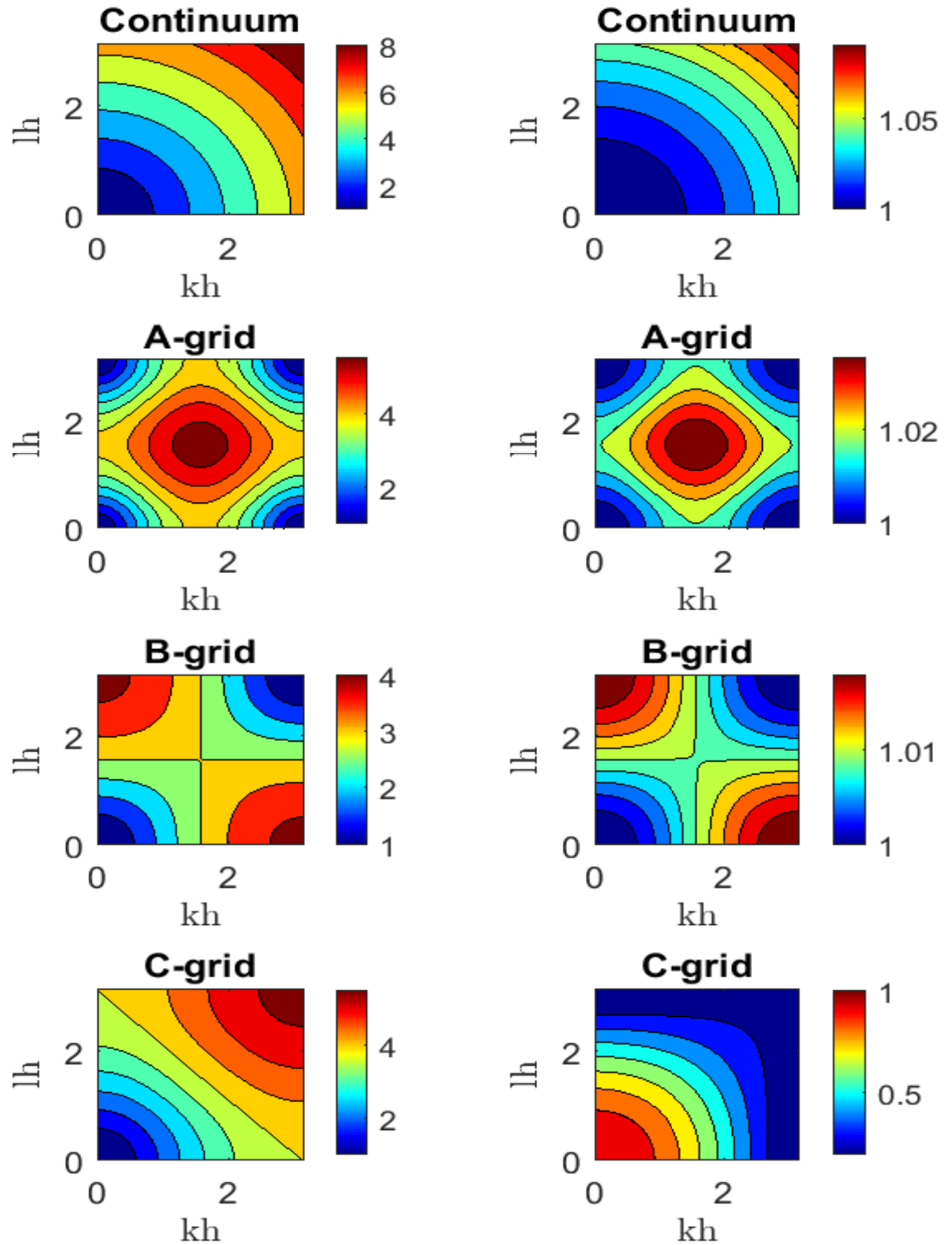


Figure 2.7.3: The dispersion relations for the continuum and finite-difference approximation based on the A, B, and C-grids with the effects of rotation. The left column is for $L_D/h = 2$, and the right for $L_D/h = 0.1$.

conservation laws that are discrete mass and energy conservation laws on the C-grid. By using second-order centred finite-difference formulation, the equations are discretized and we showed that there are three different sets of discrete equations, correspond for each grid. Analogous to the continuum domain, we reviewed some works done in [6]; wave propagation in a doubly periodic domain. We analysed the performance of each grid in terms of discrete frequency. For all grids, we recovered second-order discrete frequency, and the discrete frequency underestimated by continuum frequency. So they are equally accurate as grid spacing $h \rightarrow 0$. However, there is important differences for larger h .

We then reviewed some works done in [54] on performance of discrete frequency on the finite-difference grids. We showed that by retaining the Earth's rotation effects in the wave equations, Rossby radius of deformation takes account in the discrete frequency, and great care must be taken in producing discrete solution. We have compared all discrete frequencies with the continuum frequency. We showed that discrete frequency on the C-grid is the most satisfactory grid to represent the discrete frequency. For the rest of this thesis, we only consider discrete solution on the C-grid. As the variables on this grid are staggered, the spatial derivatives are evaluating naturally on this grid, which is optimal for the discretized of equations of motion. It is also easy to ensure that the mass and energy quantities are conserved.

Chapter 3

WAVE PROPAGATION ALONG A CHANNEL

3.1 Introduction

In this chapter we consider the two-dimensional linearised wave equations

$$\frac{\partial \tilde{u}}{\partial \tilde{t}} = -\frac{\partial \tilde{p}}{\partial \tilde{x}}, \quad \frac{\partial \tilde{v}}{\partial \tilde{t}} = -\frac{\partial \tilde{p}}{\partial \tilde{y}}, \quad \frac{\partial \tilde{p}}{\partial \tilde{t}} = -\tilde{c}^2 \left(\frac{\partial \tilde{u}}{\partial \tilde{x}} + \frac{\partial \tilde{v}}{\partial \tilde{y}} \right), \quad (3.1.1)$$

where \tilde{c} is the wavespeed. As we discussed in chapter 2, these equations can correspond to the equations of acoustics, electromagnetics, or shallow-water flow. Here, we use the language of acoustics and shallow-water, (\tilde{u}, \tilde{v}) as the velocity, and \tilde{p} as the pressure. In the context of shallow-water flow, we consider non-rotating dynamics.

In chapter 2, we discussed the properties of waves in (3.1.1) on various finite-difference grids, in doubly-infinite domains. However, in almost all cases, the flow has a boundary that constrains the flow and directs the waves. For acoustics, this could be hard walls surrounding the compressible medium, such as in a musical instrument or inside the ear. For TM mode in electromagnetics, this could be perfect conductor surrounding the insulating

di-electric in the plate geometry illustrated in Figure 2.2.1. For shallow-water flow, this could be the banks of a river, or the coastline of an ocean. In this chapter, we consider the effects of such boundaries upon the discrete wave propagation, albeit it in the simplest possible case of wave propagation along an infinitely long channel with parallel and straight side walls.

As in the rest of this thesis, we now focus on the C grid that was introduced in chapter 2. The standard treatment in this method to approximate the complex boundaries is to introduce a numerical boundary that differs from the real boundary which typically contains staircases. Such staircase boundaries might be expected to reduce the accuracy of the resulting numerical solution, because the numerical boundary deviates from the continuum boundary by a distance of $O(h)$. However, it is not clear how the resulting numerical solution will converge to the continuum solution as the grid size $h \rightarrow 0$. Further, if the solution does converge, then at what rate does this happen? This chapter is devoted to quantifying the convergence rate – analytically in the limit $h \rightarrow 0$ – for wave propagation along staircase boundaries.

There are a handful of studies on the effects of staircase boundaries on wave propagation. The most relevant example is [51], who studied system (3.1.1) on the C-grid for a channel with a perfect staircase boundaries (i.e., boundaries aligned at 45° to grid). By using the standard centred second order finite-difference formulation in space, he derived the discrete dispersion relation for waves propagation along the channel and he showed that the non-dimensional phase speed, i.e., $(1 + 1/m)^{-1/2}$ – Eq. (34) in [51], is reduced to first-order accuracy in grid spacing. He also concluded that the waves in the channel propagate with the criss-cross form which then give delay with a first-order accuracy in the phase-shift. This first-order phase shift error is confirmed in the wave reflection analysis which will be discussed in the next chapter. However, this result does not apparently apply to the main problem of interest, which is what happens when $h \rightarrow 0$ but with $m \rightarrow \infty$, so that the width of the channel remains finite. Further, it does not apparently distinguish between

waves with different cross-channel wavenumbers.

In a more specific application, the propagation of Kelvin wave along straight boundaries in C-grid finite-difference models has been studied by [32]. By considering the two-dimensional shallow-water equations with the effects of Earth's rotation, he showed analytically that the frequency and horizontal structure of the discrete Kelvin wave on the C-grid with staircase boundary converge at first order in h . The results also are verified numerically at other angle θ between the coastline and the grid, and the solution remain at first order accurate. In the limit of $h \rightarrow 0$, he showed that the discrete solutions of frequency and horizontal velocity converge towards the continuum solutions along the straight and staircase boundary. He concluded that the discrete solutions induced by the staircase boundaries degrade the accuracy of the discrete solutions. However, Kelvin wave existence relies upon a coastline and the derived solutions may not be appropriate for the bounded problem, i.e. channel. The effects of rotation may be one of the factor of degradation of the accuracy.

In this chapter we adopt many of the methods introducing in [32] to the non-rotating channel problem, as partially studied by [51]. We start, in Section 3.1.1, by introducing a non-dimensional set of governing equations, involving a non-dimensional frequency ω , which is the main quantity of interest. In Section 3.2, we derive the continuum solution, which provides the benchmark for the discrete calculations to follow. The first of those, in Section 3.3, is for the case with boundary-aligned grids, where we confirm that second-order accuracy can be achieved. The second of those calculations, in Section 3.4, is for the case of a perfect staircase (i.e., with boundary aligned at 45° to the grid). In both cases we use both numerical and asymptotic methods.

3.1.1 Nondimensional equations

Suppose that the channel has width \tilde{L} , which we use as our lengthscale, in which case the corresponding timescale is \tilde{L}/\tilde{c} . We thus introduce nondimensional coordinates

$$x = \frac{\tilde{x}}{\tilde{L}}, \quad y = \frac{\tilde{y}}{\tilde{L}}, \quad t = \frac{\tilde{t}\tilde{c}}{\tilde{L}}, \quad (u, v) = \frac{(\tilde{u}, \tilde{v})}{\tilde{U}}, \quad p = \frac{\tilde{p}}{\tilde{U}\tilde{c}}. \quad (3.1.2)$$

We then seek solutions of the form

$$\begin{aligned} \tilde{u} &= \tilde{U} \operatorname{Re}(u(x, y) \exp(-i\omega t)), \\ \tilde{v} &= \tilde{U} \operatorname{Re}(v(x, y) \exp(-i\omega t)), \\ \tilde{p} &= \tilde{U}\tilde{c} \operatorname{Re}(p(x, y) \exp(-i\omega t)), \end{aligned} \quad (3.1.3)$$

where \tilde{U} is an arbitrary dimensional amplitude of motion. Then (3.1.1) become

$$-i\omega u = -\frac{\partial p}{\partial x}, \quad (3.1.4a)$$

$$-i\omega v = -\frac{\partial p}{\partial y}, \quad (3.1.4b)$$

$$-i\omega p + \frac{\partial u}{\partial x} + \frac{\partial v}{\partial y} = 0. \quad (3.1.4c)$$

The boundary conditions of no normal flow at the upper and lower channel are

$$v(x, 0) = 0, \quad \text{and} \quad v(x, 1) = 0. \quad (3.1.5)$$

3.2 Continuum Solutions

Here, we derive the continuum solutions of our problem which will be used to assess our discrete solutions in further discussions. Let us consider the periodic unbounded channel

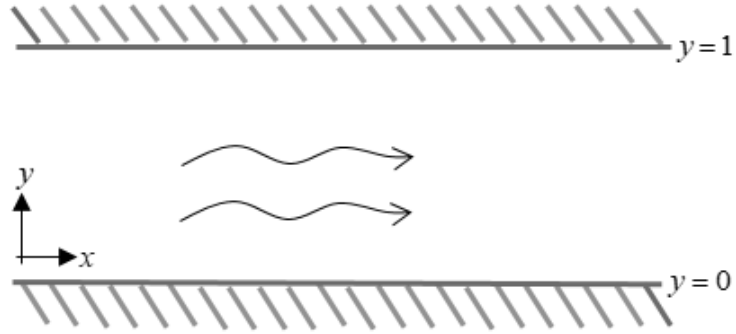


Figure 3.1.1: Wave propagation in a channel.

in the x direction, bounded in the y direction as shown in Figure 3.1.1. The domain is $-\infty < x < \infty$ in the x direction and $0 < y < 1$ in the y direction. The simplest way to see a wavelike solution is by seeking a solution of the form

$$u = \operatorname{Re}(\hat{u}e^{ikx}), \quad v = \operatorname{Re}(\hat{v}e^{ikx}), \quad p = \operatorname{Re}(\hat{p}e^{ikx}), \quad (3.2.1)$$

where k is the horizontal wave number and \hat{u} , \hat{v} and \hat{p} are complex wave amplitudes. Substituting into (3.1.4) gives

$$-i\omega_c \hat{u}(y) = -ik\hat{p}(y), \quad (3.2.2a)$$

$$-i\omega_c \hat{v}(y) = -\frac{d\hat{p}}{dy}, \quad (3.2.2b)$$

$$-i\omega_c \hat{p}(y) + ik\hat{u} + \frac{d\hat{v}}{dy} = 0, \quad (3.2.2c)$$

where we replace ω by ω_c to denote the continuum frequency. Then, by eliminating \hat{u} in (3.2.2c) and substituting (3.2.2b) into (3.2.2c), we obtain a second-order homogeneous ordinary differential equation

$$\frac{d^2\hat{v}}{dy^2} + \kappa^2\hat{v} = 0, \quad \hat{v}(0) = 0, \quad \hat{v}(1) = 0, \quad \text{where } \kappa^2 = \omega_c^2 - k^2, \quad (3.2.3)$$

where we have added the boundary condition (3.1.5) in that equation. We notice that this is an eigenvalue problem for ω_c and $\hat{v}(y)$. We need to find the special values of ω_c for which non-zero solutions exist for $\hat{v}(y)$. There are three cases to be considered.

1. $\kappa = 0$. Then $\hat{v} = Ay + B$, for some constant A and B . Then, $\hat{v}(0) = 0$ implies $B = 0$; and $\hat{v}(1) = 0$ implies $A = 0$. So $\hat{v}(y) = 0$, which is not a solution of interest.
2. $\kappa < 0$. Then $\hat{v} = A \exp(\kappa y) + B \exp(-\kappa y)$, for some constant A and B . Then, $\hat{v}(0) = 0$, implies $B = -A$, so that $\hat{v} = A(\exp(\kappa)y - \exp(-\kappa)y)$. Then, $\hat{v}(1) = 0$ implies $A = 0$. So $\hat{v}(y) = 0$, which is not a solution of interest.
3. $\kappa > 0$. Then, $\hat{v} = A \cos \kappa y + B \sin \kappa y$, for some constant A and B . Then $\hat{v}(0) = 0$ implies $A = 0$, so that $\hat{v} = B \sin \kappa y$. Then $\hat{v}(1) = 0$ implies $B \sin \kappa = 0$, so either $B = 0$ but then gives $\hat{v}(y) = 0$, which is not a solution of interest, or $\sin \kappa = 0$, which implies $\kappa = j\pi$, for some positive integer j .

Thus, we only obtained non-trivial solutions when $\kappa = j\pi$, so that

$$\kappa^2 = j^2\pi^2 \quad \Rightarrow \quad \omega_c^2 - k^2 = j^2\pi^2 \quad \Rightarrow \quad \omega_c^2 = k^2 + j^2\pi^2, \quad (3.2.4)$$

where $j \in \mathbb{N}$. Since $\sin \kappa y = \sin j\pi y$, the corresponding solution for \hat{v} is

$$\hat{v}(y) = B \sin(j\pi y) \quad \Rightarrow \quad v(x, y) = \text{Re} \left(B \sin(j\pi y) e^{(ikx)} \right). \quad (3.2.5)$$

This is the standard well-known solution for channel waves with modenummer j . To complete all the solutions, we also calculate \hat{p} and \hat{u} from (3.2.2a), (3.2.2c), which then simply give the full solutions of wave in the channel (3.2.1). They are written as

$$\hat{u}(y) = \frac{Bk\omega}{j\pi} \cos(j\pi y) \quad \Rightarrow \quad u(x, y) = \text{Re} \left(\frac{Bk\omega}{j\pi} \cos(j\pi y) e^{(ikx)} \right) = \frac{Bk\omega}{j\pi} \cos(j\pi y) \cos(kx), \quad (3.2.6)$$

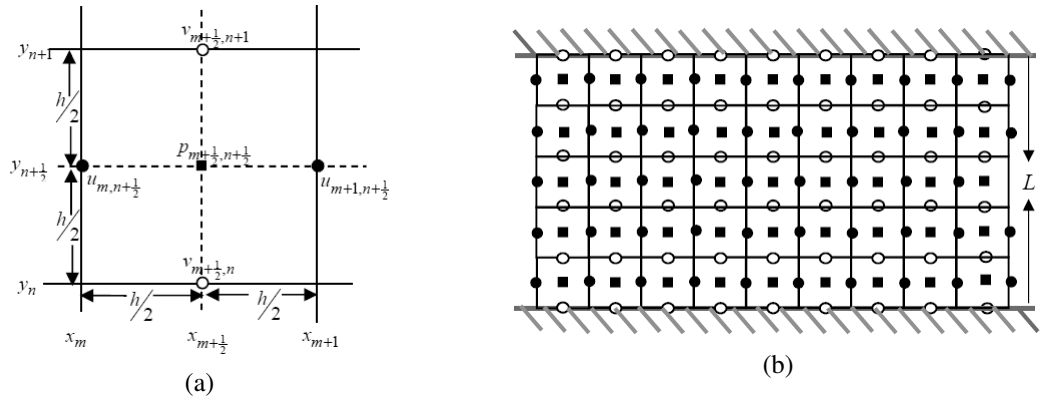


Figure 3.3.1: (a) The Arakawa C-grid and (b) the configuration of aligned boundaries for a channel.

and

$$\hat{p}(y) = \frac{iB\omega}{j\pi} \cos(j\pi y) \Rightarrow p(x, y) = \operatorname{Re} \left(\frac{iB\omega}{j\pi} \cos(j\pi y) e^{(ikx)} \right) = -\frac{B\omega}{j\pi} \cos(j\pi y) \sin(kx). \quad (3.2.7)$$

We have found that solutions of the form (3.2.1) are possible if there is a particular relationship – a dispersion relation – between the frequency ω_c and the horizontal wavenumber k . In the finite difference solution, the discrete frequency ω_d must converge towards ω_c as $h \rightarrow 0$.

3.3 Boundary Aligned with the Grid

We now examine the discrete solutions of the channel when the boundaries are aligned with the C-grid as shown in Figure 3.3.1b. We thus require

$$1 = Nh. \quad (3.3.1)$$

As discussed in previous chapter, we use the popular staggered C-grid where all variables in our system of equations are distributed in every cells as demonstrated in Figure 3.3.1a. Then, for every discrete points in computational domain we have index m for the x variable and index n for the y variable. So that we have point x_m which represents the m th grid point in space and y_n represents n th grid point in space and discrete coordinates at any point m and n are $x_m = mh$ and $y_n = nh$, where $m, n \in \mathbb{Z}$. By using second-order centred finite-difference formulation, our system of equations which are (3.1.4a,b,c) are discretised as

$$-i\omega_d u_{m,n+\frac{1}{2}} = -\frac{p_{m+\frac{1}{2},n+\frac{1}{2}} - p_{m-\frac{1}{2},n+\frac{1}{2}}}{h}, \quad (3.3.2a)$$

$$-i\omega_d v_{m+\frac{1}{2},n} = -\frac{p_{m+\frac{1}{2},n+\frac{1}{2}} - p_{m+\frac{1}{2},n-\frac{1}{2}}}{h}, \quad (3.3.2b)$$

$$-i\omega_d p_{m+\frac{1}{2},n+\frac{1}{2}} + \frac{1}{h} \left(u_{m+1,n+\frac{1}{2}} - u_{m,n+\frac{1}{2}} + v_{m+\frac{1}{2},n+1} - v_{m+\frac{1}{2},n} \right) = 0, \quad (3.3.2c)$$

where ω_d now is the discrete frequency and we will assess the rate of convergence of this unknown. The discrete boundary conditions of no normal flow at the upper and lower channel are

$$v_{m+\frac{1}{2},0} = v_{m+\frac{1}{2},N} = 0. \quad (3.3.3)$$

The easiest way to derive the discrete solution for this problem is by seeking wavelike solutions of the form

$$\begin{aligned} u_{m,n+\frac{1}{2}} &= \text{Re} \left(\hat{u}_{n+\frac{1}{2}} e^{ikx_m} \right), \\ v_{m+\frac{1}{2},n} &= \text{Re} \left(\hat{v}_n e^{ikx_{m+\frac{1}{2}}} \right), \\ p_{m+\frac{1}{2},n+\frac{1}{2}} &= \text{Re} \left(\hat{p}_{n+\frac{1}{2}} e^{ikx_{m+\frac{1}{2}}} \right). \end{aligned}$$

By substituting these ansatz into (3.3.2a,b,c) we have

$$-i\omega_d \hat{u}_{n+\frac{1}{2}} = -\frac{2i}{h} \sin\left(\frac{kh}{2}\right) \hat{p}_{n+\frac{1}{2}}, \quad (3.3.4a)$$

$$-i\omega_d \hat{v}_n = -\frac{1}{h} \left(\hat{p}_{n+\frac{1}{2}} - \hat{p}_{n-\frac{1}{2}} \right), \quad (3.3.4b)$$

$$-i\omega_d \hat{p}_{n+\frac{1}{2}} + \frac{1}{h} \left(2i \sin\left(\frac{kh}{2}\right) \hat{u}_{n+\frac{1}{2}} + \hat{v}_{n+1} - \hat{v}_n \right) = 0. \quad (3.3.4c)$$

With a straightforward elimination of $\hat{u}_{n+\frac{1}{2}}$ in (3.3.4c) using (3.3.4a), and eliminating $\hat{p}_{n+\frac{1}{2}}$ and $\hat{p}_{n-\frac{1}{2}}$ in (3.3.4b) using (3.3.4c), we then obtain a linear second-order difference equation for \hat{v} written as

$$\hat{v}_{n+1} - 2(1 - \mu)\hat{v}_n + \hat{v}_{n-1} = 0, \quad \text{where} \quad \mu = \frac{h^2}{2} \left(\omega_d^2 - \frac{4 \sin^2 \frac{kh}{2}}{h^2} \right), \quad (3.3.5)$$

together with the boundary conditions

$$\hat{v}_0 = \hat{v}_N = 0. \quad (3.3.6)$$

Again, this is an eigenvalue problem for ω_d and \hat{v}_n and we need to find the special values of ω_d for which non-zero solutions exist for \hat{v}_n .

We notice that the non-zero solution of \hat{v}_n can be found by solving (3.3.5) either analytically or numerically. Therefore, we will discuss both solutions followed by the asymptotic solutions as $h \rightarrow 0$ for the analytical case.

3.3.1 Numerical solutions

There are many existing numerical methods for solving second order linear boundary value problem and the common method is shooting method. Shooting method works by reducing the boundary value problem to an iterative sequence of initial value problems. The shooting method is initialised with an initial guess ω_1 for ω_d , and then stepping (3.3.5) across the

domain from $n = 0$ to $n = N$ subject to $\hat{v}_0 = 0$ and $\hat{v}_1 = 1$ (the latter being an arbitrary choice for this homogeneous and linear problem). This leads to some value \hat{v}_N , which is required to be zero for the actual eigenvalue, but which is generally non-zero for any guess; we thus call this a residual, R_1 . Next, the initial guess ω_1 is changed by a small amount to give ω_2 , and the shooting process is repeated, leading to another residual R_2 . In order to obtain a residual of 0, the guess for ω must be sensibly updated. This can be done by implementing Newton-Raphson iterations method using

$$\omega_{\text{new}} = \omega_1 - \frac{R_1}{R'_1}, \text{ where } R'_1 = \frac{(R_2 - R_1)}{(\omega_2 - \omega_1)}. \quad (3.3.7)$$

With this new value of ω_{new} , the process is repeated until a chosen stopping convergence is satisfied. Here we choose $(\omega_2 - \omega_1) \ll 10^{-8}$ and $|R_1| \ll 10^{-8}$ as our stopping criteria.

When the convergence is satisfied, we now have the value of ω_d in (3.3.5), and the numerical solutions of (3.3.5) can be obtained. Note that we can solve for different cross-channel modes by choosing our initial guess ω_1 to be close to the known-continuum value, with a chosen value of j . In Figure 3.3.2, we are showing solutions of \hat{v}_n for the case of grid spacing $h = 0.05$ (i.e., $N = 20$) for corresponding wavenumber along the channel $k = 1$ to values $j = 1, 2, 3$, where the solutions have been normalised to $\max |v| = 1$.

We can check the rate of convergence of this plot by plotting the log-log plot of the differences between continuum frequency ω_c and numerical frequency ω_d versus grid spacing h as can be seen in Figure 3.3.3. In this figure, we are showing slope of convergence for mode $j = 2$. We note that, the plot has a straight line with slope two which means the rate of convergence of our numerical frequency is second-order as expected, since we have used second order finite-difference formulation to discretise equations of motion.

One can also measure the convergence in \hat{v}_n . This is shown in Figure 3.3.4, where we measure the slope of log-log plot of the error in \hat{v} at various grid spacing for mode $j = 2$. It can be seen that the slope of the line is two which indicates second-order convergence as

expected. Note that slope of approximately two also can be achieved for other mode j .

We next repeat the shooting procedure with different values of h , and we plot value of ω_d as a function of h with a cross plot as shown in Figure 3.3.5. We are showing solutions for $j = 1, 2, 3$ with horizontal wavenumber $k = 1$. We can see that for all grid spacing the numerical solutions approaching to continuum solution as $h \rightarrow 0$.

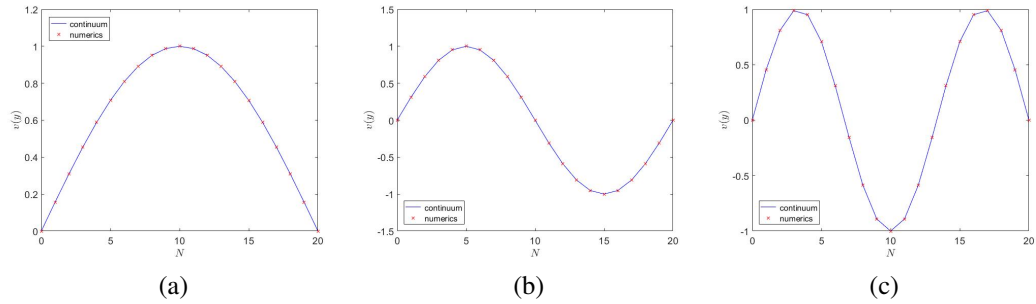


Figure 3.3.2: The numerical solution \hat{v} for wave propagation along the aligned channel at different mode $j = 1, 2, 3$ with along channel wavenumber $k = 1$, and grid spacing $h = 1/20$.

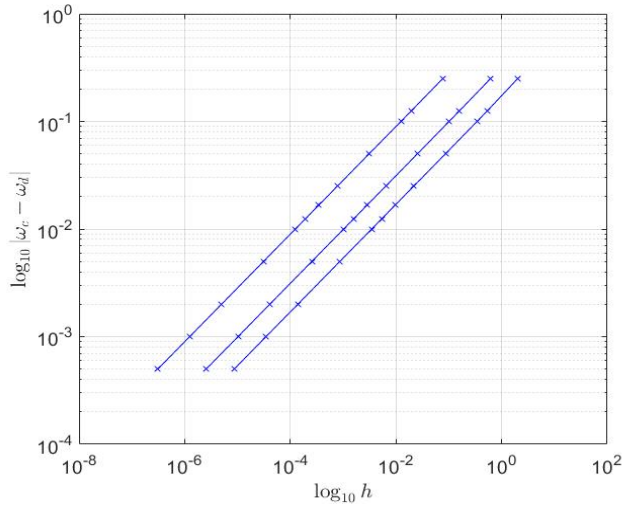


Figure 3.3.3: The convergence plot of ω_d for wave propagation along a channel with aligned boundaries for mode $j = 1, 2, 3$ and $k = 1$. The slope of the lines are 1.9992 (mode $j = 1$), 1.9971 (mode $j = 2$) and 1.9935 (mode $j = 3$), indicate second-order convergence.

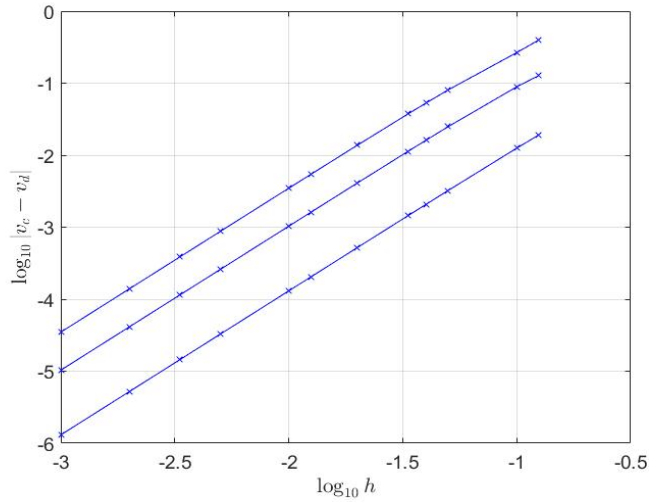


Figure 3.3.4: The convergence plot of v for wave propagation along the channel with aligned boundaries for mode $j = 1, 2, 3$ with $k = 1$. The slope of the lines are 1.9907 (mode $j = 1$), 1.9659 (mode $j = 2$), and 1.9467 (mode $j = 3$), indicate second-order convergence.

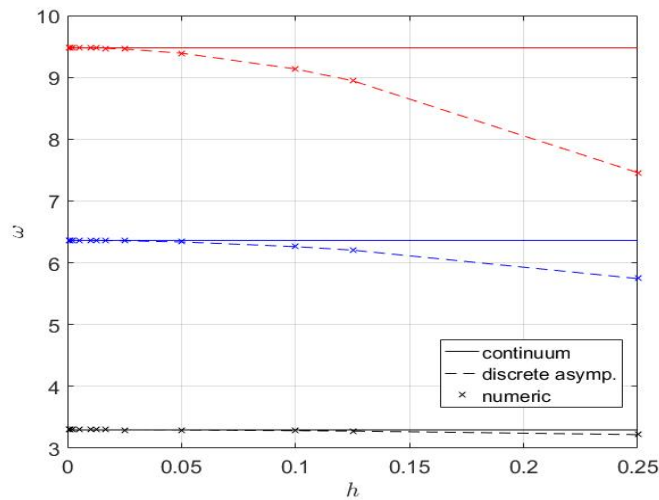


Figure 3.3.5: The frequency ω for wave propagation along the channel with aligned boundaries with horizontal wavenumber $k = 1$ and modes $j = 1, 2, 3$ at various grid spacing h . Black represents ω for $j = 1$, blue for $j = 2$, and red for $j = 3$.

3.3.2 Analytical solutions

Analytical solution of the second-order difference equation (3.3.5) can be obtained in the usual way. As we are trying to get the solution of \hat{v}_n , we now let the solution to be $\hat{v}_n = A\lambda^n$, for some constants A and λ . Then, by substituting into (3.3.5), we have

$$A\lambda^n(\lambda^2 - 2(1 - \mu)\lambda + 1) = 0. \quad (3.3.8)$$

We need solutions with both $A \neq 0$ and $\lambda \neq 0$. There are thus non-zero solutions for λ , with

$$\lambda_{1,2} = (1 - \mu) \pm i\sqrt{1 - (1 - \mu)^2}, \quad \text{where } \mu = \frac{h^2}{2} \left(\omega_d^2 - \frac{4 \sin^2 \frac{kh}{2}}{h^2} \right). \quad (3.3.9)$$

The roots are coincident when either (i) $\mu = 0$, in which case $\lambda = 1$ (twice), implying a general solution $\hat{v}_n = A + Bn$, (ii) $\mu = 2$, in which case $\lambda = -1$ (twice), implying a general solution $\hat{v}_n = (-1)^n(A + Bn)$. In both of these cases, the boundary conditions $v_0 = v_N$ imply $A = B = 0$ and thus trivial solutions. So for non-trivial solutions there are two distinct roots, and $\mu \neq 0, 2$.

If $0 < \mu < 2$, these roots occur as a complex conjugate pair, which will be discussed below. Otherwise, both roots are real and of the same sign, since $\lambda_1\lambda_2 = 1$ from (3.3.8). Then the general solution takes the form $\hat{v}_n = A\lambda_1^n + B\lambda_2^n$, and the boundary conditions imply

$$A + B = 0 \quad \text{and} \quad A\lambda_1^N + B\lambda_2^N = 0, \quad (3.3.10)$$

which only have non-trivial solution for A and B when $\lambda_2^N - \lambda_1^N = 0$. However, this is not possible when λ_1 and λ_2 are real and distinct, and of the same sign. So there are no non-trivial solutions with $\mu < 0$ or $\mu > 2$.

We thus only need analyse the case with $0 < \mu < 2$. Then $|\lambda_{1,2}|^2 = (1 - \mu)^2 + (1 - (1 - \mu)^2) = 1$, so that the complex conjugate pair has complex amplitude unity. We can thus

write

$$\lambda_{1,2} = \cos \theta \pm i \sin \theta = \exp(\pm i\theta), \quad (3.3.11)$$

where $\cos \theta = 1 - \mu$ and $\sin \theta = \sqrt{(1 - (1 - \mu)^2)} = \sqrt{(2\mu - \mu^2)}$, enabling θ to be uniquely determined from μ , and vice-versa. Then

$$\hat{v}_n = A \exp(in\theta) + B \exp(-in\theta) = C \cos n\theta + D \sin n\theta. \quad (3.3.12)$$

But $v_0 = 0$ implies $C = 0$, and then $v_N = 0$ implies $\sin N\theta = 0$ (since $D \neq 0$), i.e., $N\theta = j\pi$ for some positive integer j . Thus

$$\mu = 1 - \cos \theta = 1 - \cos \left(\frac{j\pi}{N} \right) = 2 \sin^2 \left(\frac{j\pi}{2N} \right) = 2 \sin^2 \left(\frac{j\pi h}{2} \right), \quad (3.3.13)$$

since $h = 1/N$, from (3.3.1).

With a straightforward algebraic manipulation, we obtained a discrete dispersion relation, ω_d , as

$$\omega_d^2 = \frac{4}{h^2} \left(\sin^2 \frac{kh}{2} + \sin^2 \frac{j\pi h}{2} \right), \quad \text{where } j \in \mathbb{N}. \quad (3.3.14)$$

The solutions for \hat{p} and \hat{u} also can be calculated. From (3.3.4c), we obtain the discrete solutions for pressure as

$$\hat{p}_{n+\frac{1}{2}} = \frac{i\omega_d D}{h \left(\omega_d^2 - \frac{4}{h^2} \sin^2 \frac{kh}{2} \right)} \left[2 \sin j\pi n h \sin^2 \frac{j\pi h}{2} - \sin j\pi h \cos j\pi n h \right], \quad (3.3.15)$$

where the expressions in the square bracket are obtain from the discrete solution of \hat{v} . And from (3.3.4a) the solution of the horizontal velocity \hat{u} is obtain as

$$\hat{u}_{n+\frac{1}{2}} = \frac{2}{\omega h} \sin \frac{kh}{2} \hat{p}_{n+\frac{1}{2}}, \quad (3.3.16)$$

where $\hat{p}_{n+\frac{1}{2}}$ is given in (3.3.15).

3.3.3 Asymptotic analysis as $h \rightarrow 0$

The accuracy of ω_d is then assessed by comparing the discrete solution with the continuum solution (3.2.4). By using Taylor series expansion, (3.3.14) now is written as

$$\begin{aligned}\omega_d^2 &= \frac{4}{h^2} \left(\left(\frac{kh}{2} \right)^2 + \left(\frac{j\pi h}{2} \right)^2 - \frac{1}{3} \left(\left(\frac{kh}{2} \right)^4 + \left(\frac{j\pi h}{2} \right)^4 \right) \right) + \dots \\ &= k^2 + j^2\pi^2 - \frac{1}{12}h^2 (k^4 + j^4\pi^4) + \dots \\ &= \omega_c^2 - \frac{1}{12}h^2 (k^4 + j^4\pi^4) + \dots \quad (3.3.17)\end{aligned}$$

It is found that in the limit of $h \rightarrow 0$, the discrete frequency ω_d is second order accurate in h and ω_d^2 is always underestimates ω_c^2 . This behaviour is show in Figure 3.3.5 where we plot both continuum and discrete frequency for three different modes j against various values of grid spacing h . It can be seen that, for every mode j , the discrete frequency ω_d is always underestimates the continuum frequency ω_c and as the grid size decreases (i.e., $h \rightarrow 0$), the discrete solutions are approaching continuum solutions as expected from (3.3.17).

The analytical discrete solution that has been derived in this section has been shown to agree with the numerical solutions and both solutions are approaching to the continuum solutions as the grid spacing $h \rightarrow 0$. The rate of convergence for numerical and analytical discrete solutions also agree with each other with both being second-order accurate in h . This is desired results in the case of the channel boundaries and grid are aligned. However, we cannot easily assume that same accuracy can be recovered when the channel's boundaries are not aligned with the grids. Therefore, in the next section, we will discuss its effect where we considered the same channel rotated 45° from the axis.

3.4 Boundary aligned at 45° to the grid

We now turn to a somewhat more realistic setting where the boundary is not aligned with the grid, although we take the simplest such idealisation of this, with the channel tilted at 45° to the x axis, so that the channel walls appear as a perfect staircase on the C grid. In this section, we will discuss the discrete solution only since the continuum solutions in the previous section are valid and can be used to assess the discrete solutions. As we have tilted our original coordinate, we are now in a new coordinate axes and the representation of the boundaries are said to be in a perfect staircase condition as can be seen in Figure 3.4.1b. Since the width of the channel is 1, so that the distance across the channel in the x direction is $\sqrt{2}$. As we are now looking at the staircasing errors only, this distance must be retained. So that the number of grid points across the channel N^* has to be carefully chosen in combination with h . Upon tilted at 45° the lower channel's boundary now is lying between $y = x$ and $y = x - h$, while the boundary at the upper channel is now between $y = x + \sqrt{2}$ and $y = (x + \sqrt{2}) + h$, as illustrated in Figure 3.4.1b. Here we need to choose grid boxes so that the boundaries perfectly split boundary cells along the diagonals. Suppose that there are $N^* + 1$ split cells, then $N^*h = \sqrt{2}$. There are two obvious ways to retain the distance of the channel in x :

- a) split cells retained – the computational boundary are raise at the upper cells and lower for the lower cells,
- b) cell centre retention – the computational boundary are lower for both upper and lower boundaries.

Thus, the boundary conditions for the channel now are

$$u_{j,j-\frac{1}{2}} = 0, \quad v_{j+\frac{1}{2},j} = 0, \quad u_{N+\frac{1}{2}-j,j} = 0, \quad v_{j,N-\frac{1}{2}+j} = 0, \quad j \in \mathbb{Z}. \quad (3.4.1)$$

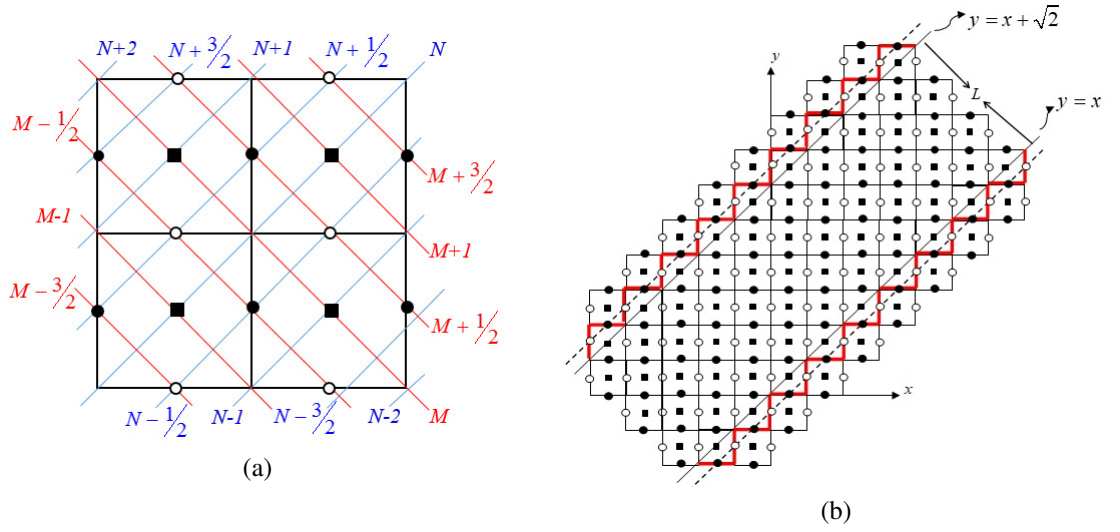


Figure 3.4.1: (a) The new indices in the transformation coordinate axes, and (b) the computational domain of the tilted channel with staircase boundaries.

3.4.1 Rotated coordinate system

As we have tilted the channel, it is convenient to introduce a rotated coordinate system (X, Y) with $X = (x + y)/\sqrt{2}$, $Y = (y - x)/\sqrt{2}$. This result can be seen by consider a point in the (x, y) system. The angle of this point from the x axis is φ which is measured anticlockwise from the x axis. The point is defined as $(x, y) = (r \cos \varphi, r \sin \varphi)$ where r is the distance from the origin. We supposed that the rotated coordinate system has angle θ from the x axis. Then, the point now is define as

$$(X, Y) = (r \cos(\varphi - \theta), r \sin(\varphi - \theta)) = (x \cos \theta + y \sin \theta, y \cos \theta - x \sin \theta),$$

$$\begin{pmatrix} X \\ Y \end{pmatrix} = \begin{pmatrix} \cos \theta & \sin \theta \\ -\sin \theta & \cos \theta \end{pmatrix} \begin{pmatrix} x \\ y \end{pmatrix}.$$

However, the indices of the staggered finite-difference grid refer to the original (x, y) coordinate system. We find it convenient to also introduce rotated indices, via $M = m + n$ which measuring distance along the channel, like X , and $N = n - m$ which measuring

distance across the channel, like Y . By using these new indices, any variable in the system now written as

$$u_{m,n} = U_{M,N}, \quad v_{m,n} = V_{M,N}, \quad p_{m,n} = P_{M,N},$$

where (M, N) in terms of (m, n) . Then, equations (3.1.4a,b,c) are discretized by using second-order centred finite difference as

$$-i\omega U_{M-\frac{1}{2}, N-\frac{1}{2}} = -\frac{1}{h} (P_{M, N-1} - P_{M-1, N}), \quad (3.4.2a)$$

$$-i\omega V_{M-\frac{3}{2}, N-\frac{1}{2}} = -\frac{1}{h} (P_{M-1, N} - P_{M-2, N-1}), \quad (3.4.2b)$$

$$-i\omega P_{M-1, N} + \frac{1}{h} \left(U_{M-\frac{1}{2}, N-\frac{1}{2}} - U_{M-\frac{3}{2}, N+\frac{1}{2}} + V_{M-\frac{1}{2}, N+\frac{1}{2}} - V_{M-\frac{3}{2}, N-\frac{1}{2}} \right) = 0, \quad (3.4.2c)$$

which is equivalent to

$$-i\omega U_{M, N} = -\frac{1}{h} \left(P_{M+\frac{1}{2}, N-\frac{1}{2}} - P_{M-\frac{1}{2}, N+\frac{1}{2}} \right), \quad (3.4.3a)$$

$$-i\omega V_{M, N} = -\frac{1}{h} \left(P_{M+\frac{1}{2}, N+\frac{1}{2}} - P_{M-\frac{1}{2}, N-\frac{1}{2}} \right), \quad (3.4.3b)$$

$$-i\omega P_{M, N} + \frac{1}{h} \left(U_{M+\frac{1}{2}, N-\frac{1}{2}} - U_{M-\frac{1}{2}, N+\frac{1}{2}} + V_{M+\frac{1}{2}, N+\frac{1}{2}} - V_{M-\frac{1}{2}, N-\frac{1}{2}} \right) = 0. \quad (3.4.3c)$$

Note that, this is the same system used in [32] but with the Coriolis terms omitted. This system needs to be solved together with the boundary conditions. At the lower channel, for both ways of cell retain (a) and (b) we obtain $N = -1/2$ as the boundary nodes from (3.4.1). So that boundary conditions at the lower channel for both cases in the rotated system are

$$U_{M, -1/2} = V_{M, -1/2} = 0, \quad \text{for all } M. \quad (3.4.4)$$

At the upper channel, the boundary conditions are

$$U_{M, N^* \pm \frac{1}{2}} = 0, \quad \text{and} \quad V_{M, N^* \pm \frac{1}{2}} = 0, \quad (3.4.5)$$

where N^* being the total number of grid across the channel defined by

$$N^* = \frac{\sqrt{2}}{h}. \quad (3.4.6)$$

3.4.2 Wavelike solutions

We seek solutions that are periodic in the along-channel direction X . We thus seek solutions of the form

$$U_{M,N} = \hat{U}_N e^{iM\theta}, \quad V_{M,N} = \hat{V}_N e^{iM\theta}, \quad P_{M,N} = \hat{P}_N e^{iM\theta}. \quad (3.4.7)$$

If we suppose that there is a spatial wavenumber k in the along channel, then increasing M by unity at fixed N increases the phase by $kh/\sqrt{2}$, where the moving distance of this phase is $h/\sqrt{2}$. So that we set

$$\theta = \frac{kh}{\sqrt{2}}. \quad (3.4.8)$$

By substituting (3.4.7) into equations (3.4.3a,b,c) with some algebraic manipulation we then have

$$-i\omega\hat{U}_N = -\frac{1}{h} \left(\hat{P}_{N-\frac{1}{2}} e^{i\frac{\theta}{2}} + \hat{P}_{N+\frac{1}{2}} e^{-i\frac{\theta}{2}} \right), \quad (3.4.9a)$$

$$-i\omega\hat{V}_N = -\frac{1}{h} \left(\hat{P}_{N+\frac{1}{2}} e^{i\frac{\theta}{2}} - \hat{P}_{N-\frac{1}{2}} e^{-i\frac{\theta}{2}} \right), \quad (3.4.9b)$$

$$-i\omega\hat{P}_N + \frac{1}{h} \left(\hat{U}_{N-\frac{1}{2}} e^{i\frac{\theta}{2}} - \hat{U}_{N+\frac{1}{2}} e^{-i\frac{\theta}{2}} + \hat{V}_{N+\frac{1}{2}} e^{i\frac{\theta}{2}} - \hat{V}_{N-\frac{1}{2}} e^{-i\frac{\theta}{2}} \right) = 0. \quad (3.4.9c)$$

By eliminating $\hat{U}_{N-1/2}$, $\hat{U}_{N+1/2}$, $\hat{V}_{N-1/2}$, $\hat{V}_{N+1/2}$ in (3.4.9c), we then obtain a single second-order difference equation for \hat{P} as

$$\hat{P}_{N+2} + \mu\hat{P}_{N+1} + \hat{P}_N = 0, \quad \text{where} \quad \mu = \frac{\omega_d^2 h^2 - 4}{2 \cos \theta}, \quad \text{and} \quad \theta = \frac{kh}{\sqrt{2}}. \quad (3.4.10)$$

As before, this is an eigenvalue problem for ω_d and \hat{P}_N . So that we need to find the special values of ω_d for which non-zero solutions for \hat{P}_N exist. We are now in peculiar situation since our boundary conditions (3.4.4) are in terms of \hat{U} and \hat{V} . However, we can derive a relevant boundary conditions in terms of P nodes near the boundary. We do this by first setting $N = 0$ in (3.4.9c) giving

$$-i\omega\hat{P}_0 + \frac{1}{h} \left(\hat{V}_{\frac{1}{2}} e^{i\frac{\theta}{2}} - \hat{U}_{\frac{1}{2}} e^{-i\frac{\theta}{2}} \right) = 0. \quad (3.4.11)$$

We then set $N = 1/2$ into (3.4.9a,b) yielding

$$\hat{U}_{\frac{1}{2}} = -\frac{i}{\omega h} \left(e^{i\frac{\theta}{2}} - \hat{P}_1 e^{-i\frac{\theta}{2}} \right), \quad (3.4.12)$$

$$\hat{V}_{\frac{1}{2}} = -\frac{i}{\omega h} \left(\hat{P}_1 e^{i\frac{\theta}{2}} - e^{-i\frac{\theta}{2}} \right). \quad (3.4.13)$$

Eliminating $\hat{U}_{\frac{1}{2}}$ and $\hat{V}_{\frac{1}{2}}$ in (3.4.11) by using (3.4.12), (3.4.13) and $\hat{P}_0 = 1$ (linearity) to set some boundary values to 0, we obtained

$$\hat{P}_1 = \alpha \hat{P}_0 \quad \text{where} \quad \alpha = \frac{2 - \omega_d^2 h^2}{2 \cos \theta} = -\mu - \frac{1}{\cos \theta}. \quad (3.4.14)$$

Performing a corresponding manipulation near the other boundary we obtain

$$\hat{P}_{M-1} = \alpha \hat{P}_M. \quad (3.4.15)$$

With N^* cells across the channel, so that we might take $M = N^*$ (split cells retained) or $M = N^* - 1$ (cell centre retention), where N^* is defined by (3.4.6).

3.4.3 Numerical solutions

In this section, we are going to solve (3.4.10) subject to (3.4.14) and (3.4.15) using the shooting method. Note that we could do either case a) or b), however we just give numerical

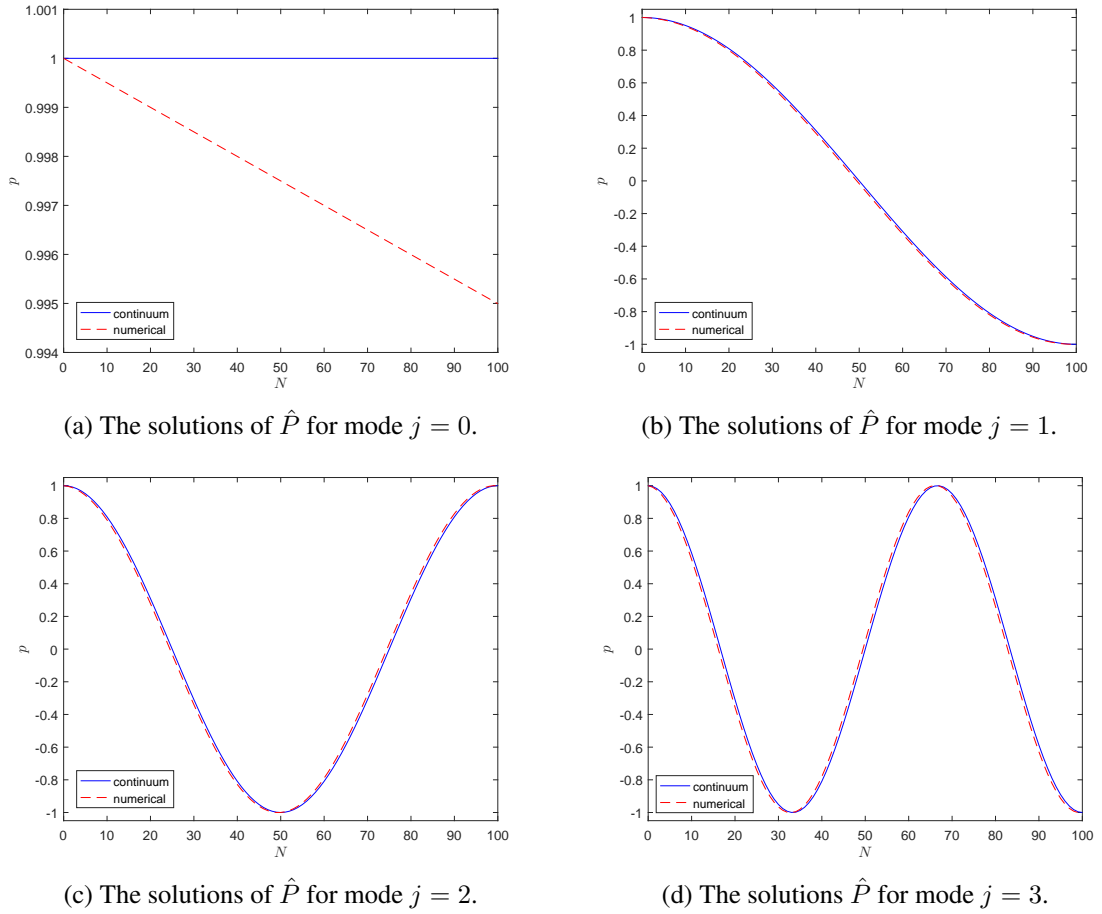


Figure 3.4.2: The continuum and numerical solutions for \hat{P} at four different cross-channel modes j for along-channel wavenumber $k = 1$ with grid boxes across channel $N^* = 100$, i.e., $h = \sqrt{2}/100$.

solutions for boundary conditions a) (i.e., split cells retained). By making appropriate initial guesses for ω , we obtain solutions for \hat{P}_n for cross-channel modes $j = 0, 1, 2, 3$ for along-channel wavenumber $k = 1$, as shown in Figure 3.4.2. These solutions were calculated with $h = \sqrt{2}/20$, i.e., $N^* = 100$. We also show the corresponding continuum solutions. The differences between both solutions also are plotted as in Figure 3.4.3. As we can see from the figure, we have normalised our solution so that $\max \hat{P} = 1$.

Having numerical solution for \hat{P} , we now can find the solution for \hat{U} and \hat{V} in (3.4.9a) and (3.4.9b), respectively. Figures 3.4.4 and 3.4.5 show the solution for along-channel flow U

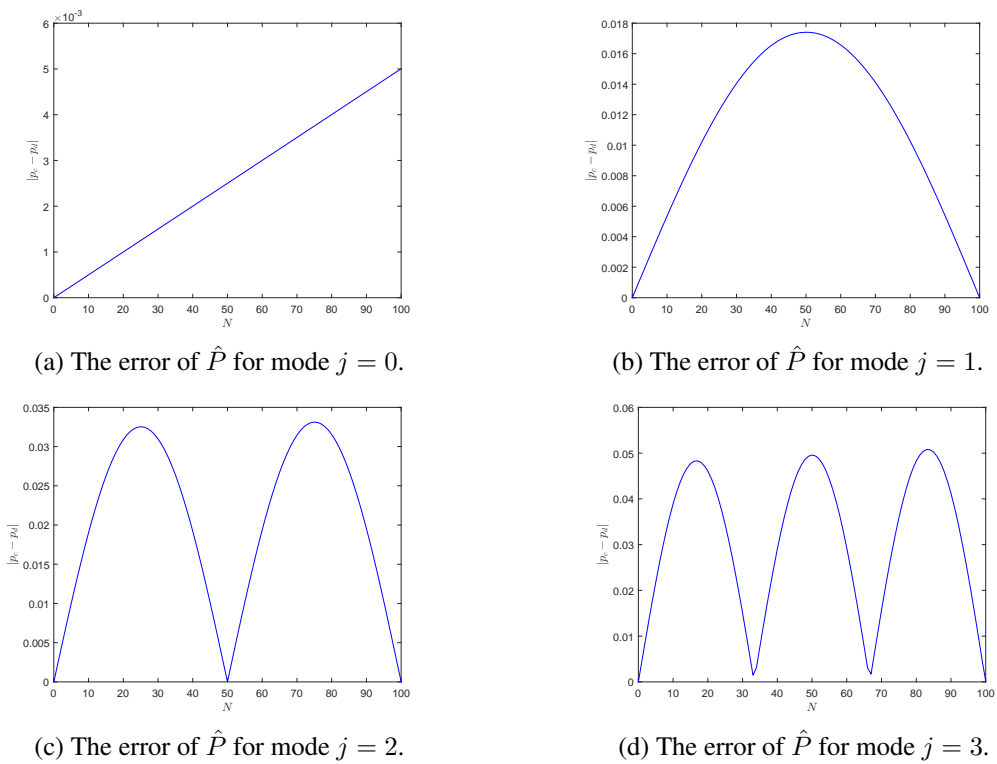


Figure 3.4.3: The differences in \hat{P} for different cross-channel modes j for along-channel wavenumber $k = 1$ with grid boxes across channel $N^* = 100$, i.e., $h = \sqrt{2}/100$.

and cross-channel flow V for the cross-channel mode $j = 2$ for along-channel wavenumber $k = 1$, with $N^* = 20$. We also calculated the error between continuum and numerical solutions. From the figures we can clearly see that there is large disagreement for the solutions at the boundary as illustrated in Figures 3.4.4b and 3.4.5b. This large error arise because the velocity at the boundary in numerical calculations is set to be zero since they are on the staircase. We have put the no normal flow boundary condition at staircase in the numerical computation while the continuum boundary is not exactly zero.

We now vary h from 0.1171 to 0.0001, and track the corresponding changes in eigenvalue or discrete frequency ω_d , for along-channel wavenumber $k = 1$. The results are shown in Figure 3.4.6, for cross-channel modes $j = 0, 1, 2, 3$, which thus have continuum frequencies $\omega_c = \sqrt{1^2 + j^2\pi^2}$, i.e., $\omega_c \approx 1, 3.2969, 6.3623, \text{ and } 9.4777$. These continuum frequencies – which are independent of h – are shown as solid lines. The numerical results, shown as crosses, show that $\omega_d < \omega_c$, but that $\omega_d \rightarrow \omega_c$ as $h \rightarrow 0$. The rate of convergence is quantified via log-log plot of the error $|\omega_d - \omega_c|$ against h , as can be seen in Figure 3.4.7 for cross-channel mode $j = 0, 1, 2, 3$. The slope is 0.9942, 0.9961, 1.0061 and 1.0218 for each j , respectively, indicating first-order convergence in h . This means that there is reduction of order in the numerical solutions since we have used the second-order finite-difference formulation to discretise the equations. This also means that the staircase boundaries has degraded the order of numerical solution from second-order to first-order accurate in h .

3.4.4 Analytical solution

We now derive the analytical solution for the problem with staircase boundaries by solving the linear second-order difference equation (3.4.10) with boundary conditions (3.4.14) and (3.4.15). The analytical solution for the problem is derived analagous to the problem in the section 3.3.2. In this section we provide both boundary conditions cases a) and b). We first let $\hat{P}_n = \lambda^n$ to be a solution, for some constant λ . Following the same procedure in the

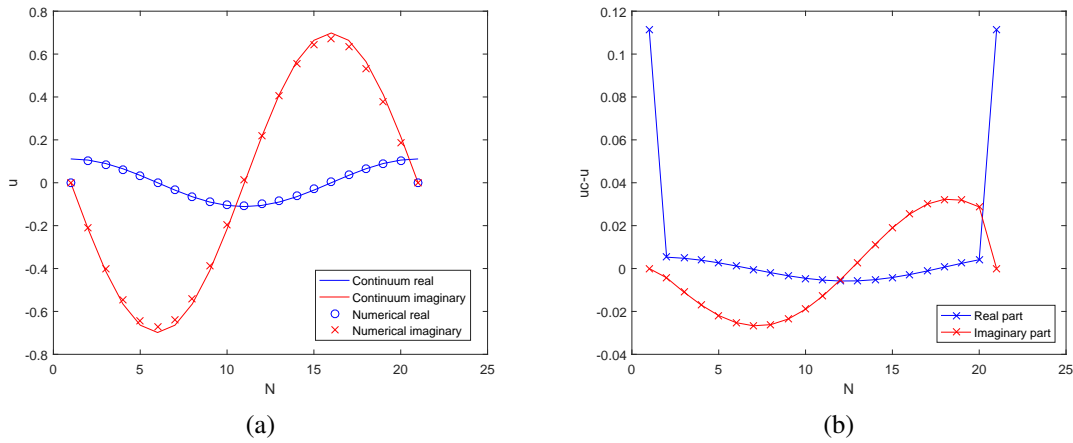


Figure 3.4.4: (a) The solutions for along-channel flow u at $j = 2$ for along-channel wavenumber $k = 1$. (b) The differences between continuum and numerical solutions.

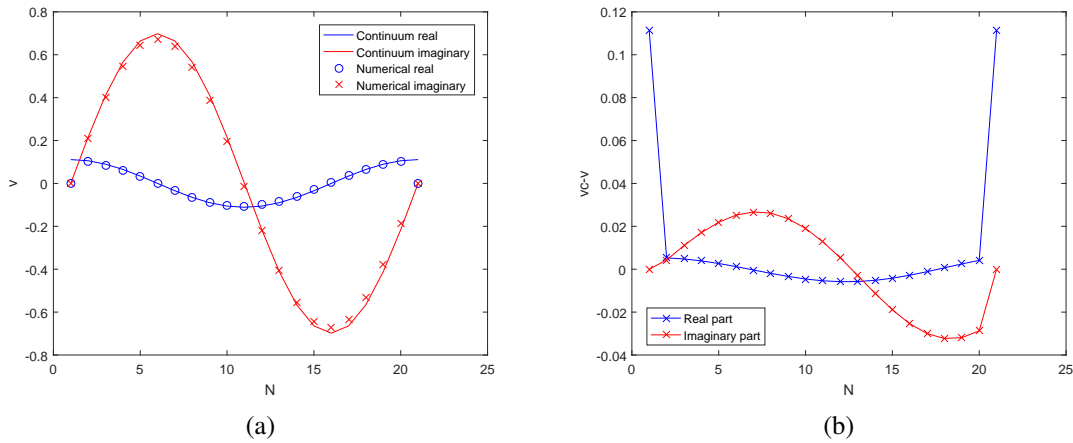


Figure 3.4.5: (a) The solutions for cross-channel flow v at $j = 2$ for along-channel wavenumber $k = 1$. (b) The differences between continuum and numerical solutions.

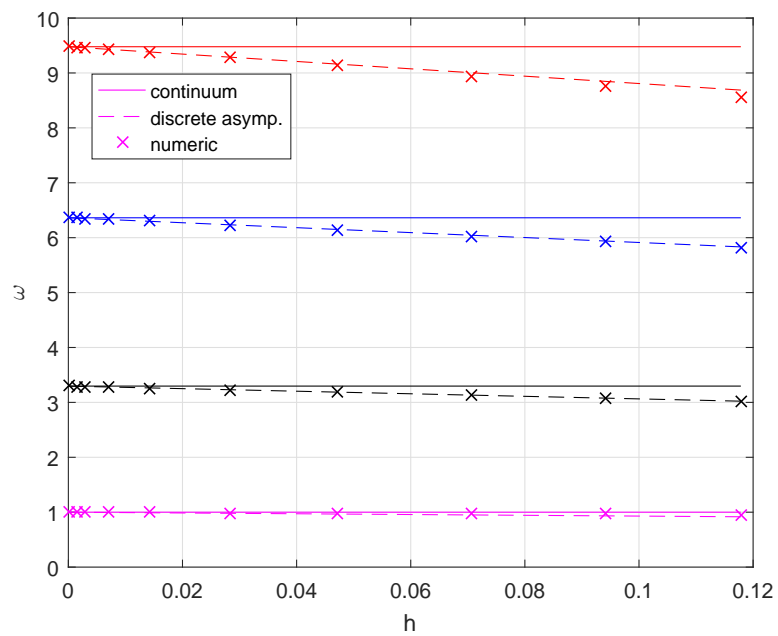


Figure 3.4.6: The dispersion relations for the channel aligned at 45° from the x -axis with staircase boundaries for cross-channel mode $j = 0, 1, 2, 3$ with along channel wavenumber $k = 1$.

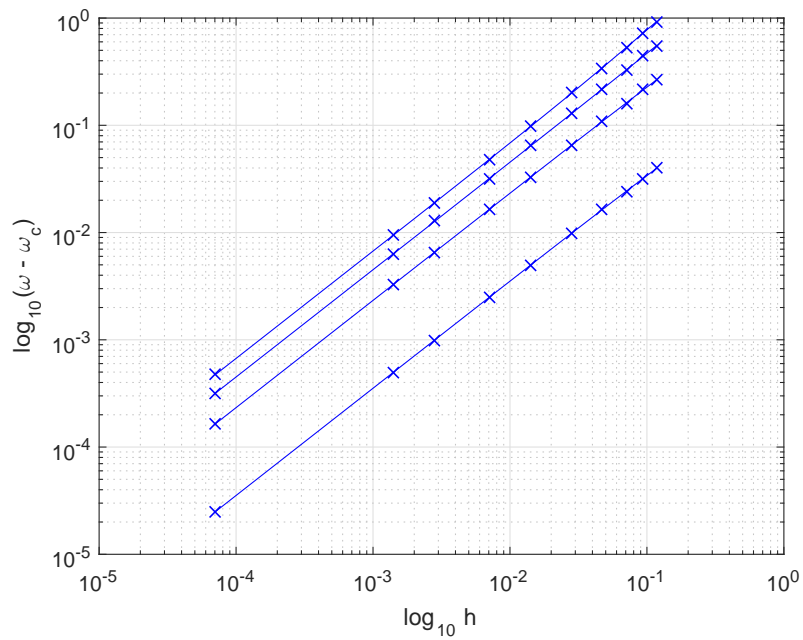


Figure 3.4.7: The graph of $\log_{10} h$ against $\log_{10} |\omega_d - \omega_c|$ for cross-channel mode $j = 0, 1, 2, 3$ with along channel wavenumber $k = 1$. The slope of the lines are 0.9942, 0.9961, 1.0061 and 1.0218, indicate first order of convergence.

early section 3.3.2, the general solution (3.4.10) is

$$\hat{P}_n = A_1 \lambda_1^n + A_2 \lambda_2^n, \quad \text{where } \lambda^2 + \mu\lambda + 1 = 0 \Rightarrow \lambda = \frac{-\mu \pm \sqrt{\mu^2 - 4}}{2}, \quad (3.4.16)$$

$$\mu = \frac{\omega_d^2 h^2 - 4}{2 \cos \theta}, \quad (3.4.17)$$

$$\text{and } \theta = \frac{kh}{\sqrt{2}}. \quad (3.4.18)$$

The boundary conditions (3.4.14) and (3.4.15) then imply

$$\begin{aligned} A_1 \lambda_1 + A_2 \lambda_2 &= \alpha A_1 + \alpha A_2, & A_1 \lambda_1^{M-1} + A_2 \lambda_2^{M-1} &= \alpha A_1 \lambda_1^M + \alpha A_2 \lambda_2^M, \\ \Rightarrow \begin{pmatrix} \lambda_1 - \alpha & \lambda_2 - \alpha \\ \alpha \lambda_1^M - \lambda_1^{M-1} & \alpha \lambda_2^M - \lambda_2^{M-1} \end{pmatrix} \begin{pmatrix} A_1 \\ A_2 \end{pmatrix} &= 0. \end{aligned}$$

For nontrivial solutions we require

$$(\lambda_1^M - \lambda_2^M) \alpha^2 - 2(\lambda_1^{M-1} - \lambda_2^{M-1}) \alpha + (\lambda_1^{M-2} - \lambda_2^{M-2}) = 0, \quad (3.4.19)$$

where we have used $\lambda_1 \lambda_2 = 1$, which follows from (3.4.16). Equation (3.4.19) is an implicit relation for ω_d , which appears directly via α , and indirectly via $\lambda_{1,2}$, which depend upon μ , which in turn depends on ω_d via (3.4.17).

3.4.5 Behaviour as $h \rightarrow 0$

We anticipate that the waves are retarded from the continuum frequency ω_c as $h \rightarrow 0$, where $\omega_c^2 = k^2 + j^2 \pi^2$, with j an integer. We thus write

$$\omega_d^2 = \omega_c^2 - a_1 h - a_2 h^2 + \dots = k^2 + j^2 \pi^2 - a_1 h - a_2 h^2 + \dots. \quad (3.4.20)$$

We wish to find a_1 (and perhaps a_2).

As $h \rightarrow 0$, (3.4.17) and (3.4.18) imply

$$\mu = \left(-2 + \frac{\omega_d^2 h^2}{2} \right) \left(1 + \frac{k^2 h^2}{4} + O(h^4) \right) = -2 + \frac{h^2(\omega_d^2 - k^2)}{2} + O(h^4) \quad (3.4.21)$$

$$\Rightarrow \mu^2 - 4 = -2h^2(\omega_d^2 - k^2) + O(h^4) = -2h^2 j^2 \pi^2 + 2a_1 h^3 + O(h^4). \quad (3.4.22)$$

So the discriminant $\mu^2 - 4$ in (3.4.16) is thus negative (at least when $j > 0$), implying complex roots for λ :

$$\lambda_1 = \exp(+i\varphi), \quad \lambda_2 = \exp(-i\varphi), \quad \text{where} \quad \exp(i\varphi) = \frac{-\mu + i\sqrt{4 - \mu^2}}{2}, \quad (3.4.23)$$

$$\Rightarrow \cos \varphi = -\frac{\mu}{2} = 1 - \frac{h^2(\omega_d^2 - k^2)}{4} + O(h^4) = 1 - \frac{h^2 j^2 \pi^2}{4} + \frac{a_1 h^3}{4} + O(h^4), \quad (3.4.24)$$

$$\sin \varphi = \sqrt{1 - \frac{\mu^2}{4}} = \sqrt{\frac{h^2 j^2 \pi^2}{2} - \frac{a_1 h^3}{2} + O(h^4)} = \frac{j\pi h}{\sqrt{2}} - \frac{a_1 h^2}{2\sqrt{2}j\pi} + O(h^3). \quad (3.4.25)$$

With this assumption of complex conjugate roots for $\lambda_{1,2}$, the eigenvalue condition (3.4.19) becomes

$$(\sin M\varphi)\alpha^2 - 2(\sin(M-1)\varphi)\alpha + \sin(M-2)\varphi = 0 \quad (3.4.26)$$

$$\Rightarrow \alpha = \frac{\sin(M-1)\varphi \pm \sqrt{\sin^2(M-1)\varphi - (\sin M\varphi)(\sin(M-2)\varphi)}}{\sin M\varphi}. \quad (3.4.27)$$

But

$$\begin{aligned} 2 \sin M\varphi \sin(M-2)\varphi &= \cos 2\varphi - \cos 2(M-1)\varphi = 1 - 2 \sin^2 \varphi - 1 + 2 \sin^2(M-1)\varphi \\ &\Rightarrow \sin^2(M-1)\varphi - \sin M\varphi \sin(M-2)\varphi = \sin^2 \varphi, \end{aligned}$$

so that the square root in (3.4.27) simplifies, and we have

$$\alpha = \frac{\sin(M-1)\varphi \pm \sin \varphi}{\sin M\varphi}. \quad (3.4.28)$$

This is our modified eigencondition, which is valid whenever $\lambda_{1,2}$ are complex (e.g., as

$h \rightarrow 0$ with $j > 0$).

It is possible to simply expand all terms in (3.4.28) to find the frequency reduction coefficient a_1 . However, further trigonometrical expansions reduce the burden. Using boundary conditions (3.4.14) and (3.4.15), and (3.4.24) to write $\alpha = 2 \cos \varphi - 1/\cos \theta$, (3.4.28) becomes

$$\frac{1}{\cos \theta} = \frac{2 \cos \varphi \sin M\varphi - \sin(M-1)\varphi \pm \sin \varphi}{\sin M\varphi}.$$

But $2 \cos \varphi \sin M\varphi = \sin(M+1)\varphi + \sin(M-1)\varphi$, so there is a further reduction:

$$\frac{1}{\cos \theta} = \frac{\sin(M+1)\varphi \pm \sin \varphi}{\sin M\varphi}. \quad (3.4.29)$$

We now split into two cases, using $\sin A + \sin B = 2 \sin \frac{A+B}{2} \cos \frac{A-B}{2}$:

- taking the positive root in (3.4.29) gives

$$\begin{aligned} \frac{1}{\cos \theta} &= \frac{2 \sin((M+2)\varphi/2) \cos(M\varphi/2)}{2 \sin(M\varphi/2) \cos(M\varphi/2)} = \frac{\sin((M+2)\varphi/2)}{\sin(M\varphi/2)} \\ &= \cos \varphi + \frac{\cos(M\varphi/2) \sin \varphi}{\sin(M\varphi/2)}. \end{aligned}$$

As $h \rightarrow 0$, we can write $1/\cos \theta = 1 + k^2 h^2/4 + \dots$, and use the expansions in (3.4.24) and (3.4.25) for $\cos \varphi$ and $\sin \varphi$ to obtain

$$\begin{aligned} 1 + \frac{k^2 h^2}{4} + \dots - \left(1 - \frac{h^2 j^2 \pi^2}{4} + \dots \right) &= \frac{j\pi h/\sqrt{2} + \dots}{\tan(M\varphi/2)} \\ \Rightarrow \tan \frac{M\varphi}{2} &= \frac{2\sqrt{2}j\pi}{h(k^2 + j^2\pi^2)} + \dots. \quad (3.4.30) \end{aligned}$$

We will be choosing $M = N^* = \sqrt{2}/h$, or $M = N^* - 1$. Also using (3.4.25), we

thus write

$$\begin{aligned}
M\varphi &= (N^* + (M - N^*))\varphi = \left(\frac{\sqrt{2}}{h} + (M - N^*) \right) \left(\frac{j\pi h}{\sqrt{2}} - \frac{a_1 h^2}{2\sqrt{2}j\pi} + \dots \right) \\
&= \left(1 + \frac{h(M - N^*)}{\sqrt{2}} \right) \left(j\pi - \frac{a_1 h}{2j\pi} + \dots \right) = j\pi + h \left(\frac{(M - N^*)j\pi}{\sqrt{2}} - \frac{a_1}{2j\pi} \right) + \dots .
\end{aligned} \tag{3.4.31}$$

A balance in (3.4.30) is thus possible if j is odd, since then $\tan(M\varphi/2)$ approaches $\tan(j\pi/2)$. More precisely,

$$\tan \frac{M\varphi}{2} = \frac{\sin(j\pi/2)(1 + \dots)}{-\sin(j\pi/2) \sin \left(\frac{h}{2} \left[\frac{(M - N^*)j\pi}{\sqrt{2}} - \frac{a_1}{2j\pi} \right] + \dots \right)} = -\frac{2}{h \left[\frac{(M - N^*)j\pi}{\sqrt{2}} - \frac{a_1}{2j\pi} \right]} + \dots$$

So (3.4.30) becomes

$$\begin{aligned}
-\frac{2}{h \left[\frac{(M - N^*)j\pi}{\sqrt{2}} - \frac{a_1}{2j\pi} \right]} + \dots &= \frac{2\sqrt{2}j\pi}{h(k^2 + j^2\pi^2)} + \dots \\
\Rightarrow \frac{(M - N^*)j\pi}{\sqrt{2}} - \frac{a_1}{2j\pi} &= -\frac{k^2 + j^2\pi^2}{\sqrt{2}j\pi} \\
\Rightarrow a_1 &= \sqrt{2} (k^2 + (M - N^* + 1)j^2\pi^2) .
\end{aligned}$$

We can now analyse our two cases of interest:

- a) when $M = N^*$ (i.e., split cell retention), we have $a_1 = \sqrt{2}(k^2 + j^2\pi^2) = \sqrt{2}\omega_c^2$,
so that

$$\begin{aligned}
\omega_d^2 &= \omega_c^2 - \sqrt{2}h\omega_c^2 + \dots = \left(1 - \sqrt{2}h + \dots \right) \omega_c^2 \\
\Rightarrow \omega_d &= \left(1 - \frac{h}{\sqrt{2}} + \dots \right) \omega_c . \tag{3.4.32}
\end{aligned}$$

Thus, the frequency is reduced by a factor of $\sqrt{2}h$: this, of course, is a first-order error in h .

b) When $M = N^* - 1$ (i.e., cell-centre retention), we have $a_1 = \sqrt{2}k^2$, so that

$$\begin{aligned}\omega_d^2 &= \omega_c^2 - \sqrt{2}k^2h + \dots = \omega_c^2 \left(1 - \sqrt{2} \left(\frac{k^2}{k^2 + j^2\pi^2} \right) h + \dots \right) \\ \Rightarrow \omega_d &= \omega_c \left(1 - \left(\frac{k^2}{k^2 + j^2\pi^2} \right) \frac{h}{\sqrt{2}} + \dots \right).\end{aligned}\quad (3.4.33)$$

The relative error now is always less than $h/\sqrt{2}$. Further, the relative error becomes much smaller than $h/\sqrt{2}$ when $j \gg k/\pi$, i.e., for modes with large cross-channel wavenumber j .

- Alternatively, taking the negative root in (3.4.29) gives

$$\begin{aligned}\frac{1}{\cos \theta} &= \frac{2 \sin(M\varphi/2) \cos((M+2)\varphi/2)}{2 \sin(M\varphi/2) \cos(M\varphi/2)} = \frac{\cos((M+2)\varphi/2)}{\cos(M\varphi/2)} \\ &= \cos \varphi - \frac{\sin(M\varphi/2) \sin \varphi}{\cos(M\varphi/2)}.\end{aligned}$$

In the same way that we found (3.4.30), we now find

$$\begin{aligned}1 + \frac{k^2h^2}{4} + \dots - \left(1 - \frac{h^2j^2\pi^2}{4} + \dots \right) &= -\frac{j\pi h}{\sqrt{2}} \tan \frac{M\varphi}{2} + \dots \\ \Rightarrow \tan \frac{M\varphi}{2} &= -\frac{h(k^2 + j^2\pi^2)}{2\sqrt{2}j\pi} + \dots.\end{aligned}\quad (3.4.34)$$

We again have (3.4.31) for $M\varphi$. A balance in (3.4.34) is thus possible if j is even, since then $\tan(M\varphi/2)$ approaches $\tan(j\pi/2) = 0$. More precisely,

$$\begin{aligned}\tan \frac{M\varphi}{2} &= \frac{\cos(j\pi/2) \sin\left(\frac{h}{2} \left[\frac{(M-N^*)j\pi}{\sqrt{2}} - \frac{a_1}{2j\pi} \right] + \dots\right)}{\cos(j\pi/2) (1 + \dots)} \\ &= \frac{h}{2} \left[\frac{(M-N^*)j\pi}{\sqrt{2}} - \frac{a_1}{2j\pi} \right] + \dots.\end{aligned}$$

So (3.4.34) becomes

$$\begin{aligned} \frac{h}{2} \left[\frac{(M - N^*)j\pi}{\sqrt{2}} - \frac{a_1}{2j\pi} \right] + \dots &= -\frac{h(k^2 + j^2\pi^2)}{2\sqrt{2}j\pi} + \dots \\ \Rightarrow \frac{(M - N^*)j\pi}{\sqrt{2}} - \frac{a_1}{2j\pi} &= -\frac{k^2 + j^2\pi^2}{\sqrt{2}j\pi} \Rightarrow a_1 = \sqrt{2} (k^2 + (M - N^* + 1)j^2\pi^2), \end{aligned}$$

which is exactly the result that we derived before, when j was odd. So our approximate discrete dispersion relations (3.4.32) and (3.4.33) for all modes with $j \neq 0$.

3.4.6 Numerical verification

We now confirm the analysis of the relative error numerically. Note that we only verified the relative error for boundary conditions a) (i.e., split cell retention). As discussed in section 3.4.3, we have obtained the eigenvalue ω_d using a shooting method. Further, from both the existing numerics and our asymptotics, we have shown that $|\omega_c - \omega_d| = A(k)h$ for some $A(k)$ as $h \rightarrow 0$. Our asymptotics imply that $\omega_d = \omega_c(1 - h/\sqrt{2}\dots)$ (via (3.4.32)) as $h \rightarrow 0$, and so that

$$A(k) = \frac{\omega_c}{\sqrt{2}} = \sqrt{\frac{k^2 + j^2\pi^2}{2}}. \quad (3.4.35)$$

We now verify that this is consistent with the numerical results of section 3.4.3.

Numerically, the scaling factor is determined by calculating ω_d and ω_c at various values of h (bearing in mind that we need $h = \sqrt{2}/N^*$, via (3.4.6)), and then fitting a straight line to $\log_{10} |\omega_c - \omega_d|$ versus $\log_{10} h$. The intercept is then A . By repeating for different values of k , we can numerically construct $A(k)$, for a given cross-channel mode j .

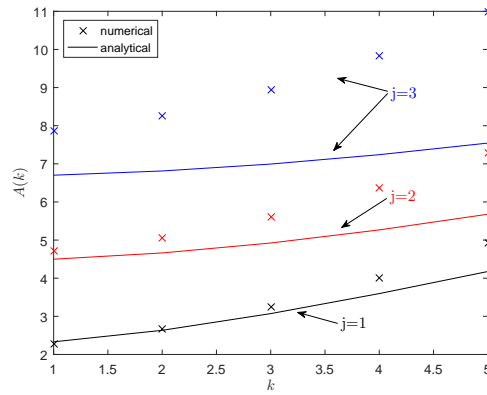
Figure 3.4.8a shows the scaling factor $A(k)$ determined both numerically and analytically, for $j = 1, 2, 3$. The numerical results have been determined taking 6 values of h with $\sqrt{2}/1000 \leq h \leq \sqrt{2}/20$ (i.e., each cross in the figure requires 6 separate shooting calculations, followed by a straight line fit). The agreement between the asymptotics and the numerical results is good for $j = 1$ and small k , but worsens as j and k both increase.

However, better agreement can be found by considering yet smaller values of h , where the numerical results should be increasingly in line with the asymptotic predictions. Shown in Figure 3.4.8b and 3.4.8c are results calculated with 6 values of h over each of $\sqrt{2}/10000 < h < \sqrt{2}/500$ and $\sqrt{2}/29000 < h < \sqrt{2}/5000$. One can see that the agreement between the asymptotics and the numerics improves in each case, and we can be confident (from Figure 3.4.8c) that the asymptotics is indeed correct. So, in Figure 3.4.8a, the number of grid points was insufficient to resolve the wave structure, especially at $j = 3$.

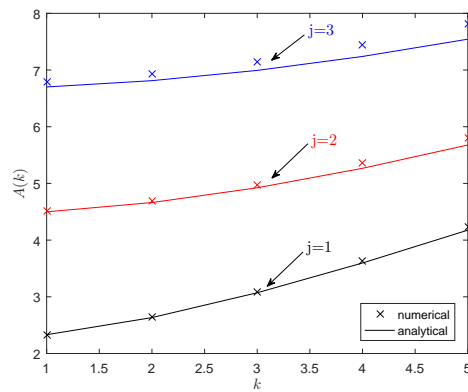
3.5 Summary

Building upon previous studies in [51, 32], we have examined the accuracy of discrete wave solutions in a straight channel with perfect staircase walls. Here we have considered standard non-rotating shallow-water waves (or acoustic waves), and the staggered C-grid. We have shown that the staircase boundaries mean that the discrete wave frequency is only determined at first order in grid spacing h , despite the second-order finite difference formulations used in the interior of the domain. This convergence is to be contrasted with solutions for which the channel's boundaries and grid are aligned, where we proved that the frequency is obtained at second-order in h .

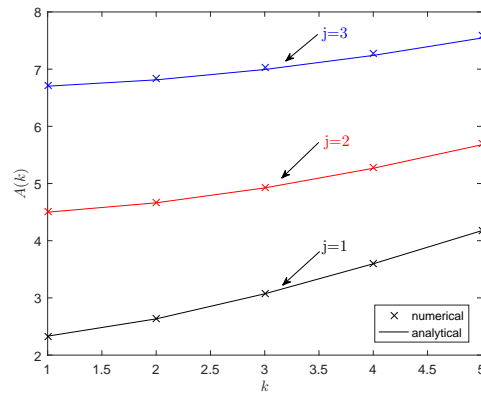
Our main calculations were asymptotics for the two cases of an aligned channel and a perfect staircase channel. In the former case, the relative error $\Delta = \frac{|\omega_d - \omega_c|}{|\omega_c|} = h^2/12(k^4 + j^4\pi^4)/(k^2 + j^2\pi^2)$, from (3.3.17), which is second-order accurate in h . In the latter case, the relative error is $\Delta = h/\sqrt{2}$, (via (3.4.32)), for the boundary condition choice a) (i.e., split cell retention), and $\Delta = (k^2/k^2 + j^2\pi^2) h/\sqrt{2}$, (via (3.4.32)) for the boundary condition choice b) (i.e., cell-centre retention), as $h \rightarrow 0$. We note that the relative error for aligned boundaries is dependent of k . While the relative error for the unaligned boundaries is independent of k for the split cell retention boundary condition choice and dependent of k for the cell-centre retention staircase boundary conditions. For the unaligned



(a) The scaling factor for mode $j = 1, 2, 3$ at various k with $N^* = 20, 50, 100, 200, 500, 1000$ across the channel.



(b) The scaling factor for mode $j = 1, 2, 3$ at various k with $N^* = 500, 1000, 2000, 5000, 8000, 10000$ across the channel.



(c) The scaling factor for mode $j = 1, 2, 3$ at various k with $N^* = 5000, 10000, 15000, 20000, 25000, 29000$ across the channel.

Figure 3.4.8: The scaling factor $A(k)$ for across channel mode $j = 1, 2, 3$ at various grid spacing h .

case both relative errors have a staircasing error. For the split cell retention choice, there is geometrical error generated – as the channel is widened by $O(h)$.

So for the case of mode $j = 0$, to obtain the frequency accurate to within 1% (i.e., $\Delta < 0.01$), we need $kh = \sqrt{0.12}$ or 18 grid points per along-channel wavelength for the case of aligned boundaries. On the other hand, for the case of unaligned boundaries we need $h = \sqrt{2}$, or 71 grid boxes across the channel, for both boundary condition (a) and (b). To obtain the frequency accurate to within 10% (i.e., $\Delta < 0.1$), we need 6 grid points per along-channel for the aligned boundaries, and 7 grid boxes across the channel for the unaligned case.

For the case of mode $j = 1$, in order to obtain the frequency accurate to within 1%, we need 9 grid boxes across the channel for the aligned boundary. For the case of unaligned boundary, again we need 71 grid boxes across the channel for split cell retention boundary condition. However, for cell-centre retention boundary condition we need only 7 grid boxes across the channel.

Thus, we have been able to make a clear conclusion about the influence of staircase boundaries on wave propagation along a channel. In particular, the formula for the relative error

$$\Delta = \frac{h}{\sqrt{2}} \quad \text{and} \quad \Delta = \left(\frac{k^2}{k^2 + j^2\pi^2} \right) \frac{h}{\sqrt{2}},$$

allows a quick estimation of the degradation due to staircase error, in this ‘worst-case’ scenario where the channel and grid are aligned at 45° . From the results of [32] for Kelvin waves, we can anticipate that the error would be reduced as the angle between walls and grid is reduced, whilst remaining first order.

Most of these results are new. Presumably the grid-aligned analysis leading to (3.3.17) exists somewhere in the vast research literature covering acoustics, electromagnetic waves and shallow-water waves, but we have not found it. However, the perfectly-aligned staircase analysis is completely original, as far as we can tell. The closest study is that of [51], but

he used rather different methods and gave no results for $h \rightarrow 0$ at fixed channel width, and thus gave nothing analogous to our main results (3.4.32) and (3.4.33). The study of [32] used similar methods to here, but was completely focussed on the case of Kelvin waves for an unbounded channel and shallow-water dynamics. Those results rely upon rotation, and cannot be converted to our results here for non-rotating dynamics.

However, what we have not done is examine the spatial structure of the solution. In particular, we know that the continuum solution has along channel flow even at the walls (i.e., tangential flow), even though the normal flow vanishes. Of course, both components of the flow of the discrete solution are forced to vanish at the staircase wall via (3.4.5), and it would be interesting to calculate how these flow change from zero to something close to the continuum values as we move away from the wall. In [32], it was shown that there was a thin computational boundary layer of width h^2 (see Eq. (31) of [32]).

Chapter 4

WAVE REFLECTION AT A PLANAR WALL

4.1 Introduction

In this chapter, we consider the linearised wave equations

$$\frac{\partial u}{\partial t} = -\frac{\partial p}{\partial x}, \quad \frac{\partial v}{\partial t} = -\frac{\partial p}{\partial y}, \quad \frac{\partial p}{\partial t} + \frac{\partial u}{\partial x} + \frac{\partial v}{\partial y} = 0, \quad (4.1.1)$$

where (u, v) is the velocity vector, p is the pressure, following the same notation of acoustic and shallow-water flow.

In chapter 3, we discussed the propagation of waves on the C grid along a channel with two boundaries. However, when waves propagate through a medium, they also can reflect at a boundary. In many cases, waves propagate carrying information from the source and are reflected back to the source region. The information from the reflected component can then be analysed. For example, acoustic wave reflection is used to explore oil and gas reservoirs under the sea. The human hearing mechanism also uses a similar process that often relies upon sound wave reflection. In classical electrodynamics, electromagnetic

waves also propagate and reflect at surfaces. For shallow-water flow, ocean waves can propagate to the coast and be completely or partially reflected at boundaries such as cliffs or seawalls. These wave reflections can be important for the behaviour of coastal waves.

The nature of the wave reflection depends upon the structure of the boundary, and any numerical solutions will be sensitive to how this boundary is represented. Study of reflection at a straight wall is possible even in a finite-difference model, because the straight boundary can be aligned with the finite-difference grid. However, on a non-planar boundary the accuracy of the resulting numerical solutions is not clear. As mentioned in chapter 3, the classic technique in finite-difference methods based on the staggered C-grid to represent the non-smooth boundary is to introduce a numerical boundary that contain staircases. Typically, these staircases introduce an error and may reduce the accuracy of the numerical solution. The aim of this chapter is to study this numerical error for wave reflection at a planar boundary.

Analysis of the error induced by staircase boundaries on wave reflection is not a new subject. For example, [17] studied the error of electromagnetic wave reflection on a hard wall with staircase boundary. The error analysis was performed using the two-dimensional Maxwell's equations. There are two different waves that propagate in electromagnetism: one corresponds to electric field, and the other one corresponds to magnetic field. These waves propagate perpendicular to each other, and are thus a type of transverse wave. The error analysis of [17] was performed for both transverse electric (TE_z) and magnetic (TM_z) modes subject to a perfect conductor boundary condition. By assuming a total solution of incoming and reflected wave at the boundary, the reflection coefficient was derived for both modes. From the analysis of the reflection coefficient for TM_z mode, they showed graphically that there is phase error generated upon reflection at the staircase boundary, depending on the angle of incident wave with respect to the normal. They also showed graphically that the phase error increased as the angle of incident wave increased. However, there is no obvious phase error from the analysis of the reflection coefficient in TE_z mode. In the study,

they also analysed the discrete dispersion relation for waves propagating along the boundary $x = y$. From the analysis, they concluded that the presence of the staircase boundary decreased the phase velocity and one can expect to see a delay in a travelling pulse. The analysis was verified by using two time-dependent numerical experiments and they showed that there was a delay for a wave pulse traveling with the rotated boundary for the TM_z mode, but there was no delay in the TE_z mode, as expected from their analyses. Furthermore, they concluded that the phase errors in the TE_z mode are significantly greater than those in the TM_z mode, which supported their analysis.

The above study implies that the staircase approximation could generate a significant error. However, these errors are not quantified via a rate of convergence. In this chapter, we study wave reflection at a staircase boundary for (4.1.1), which is equivalent to the equations in [17]. The study will provide more detail about the wave reflection at staircase boundary.

In other studies, analysis of wave reflection at a boundary for one-dimensional equations by using staggered grid finite-difference method was discussed in [68]. The acoustic wave formulations involving pressure p and velocity u and v , has been used in the study instead of the Maxwell's electromagnetism formulation. Note that, the equations are also equivalent to the non-rotating shallow water dynamics used for water wave applications. In the study, the hard boundary condition which is equivalent to no normal flow boundary conditions in fluid dynamics was used to investigate the effects of the reflection. From the analysis, they showed that both velocity and pressure has first-order of accuracy in the size of grid spacing. The analysis was verified numerically with a test wave function propagating against a boundary. In the experiment, they quantified the error numerically by measuring the maximum error at three different grid spacings. They showed that the accuracy of numerical solutions for pressure and velocity degraded from second-order to first-order when the wave reflects at the boundary.

In a subsequent study, numerical investigations of two-dimensional wave reflection against an inclined boundary and a solid circle were given in [67]. The study was the continuation

of [68], using the same equations and boundary conditions as in [68]. The study focus on the effects of wave reflection with staircase boundaries based on three numerical experiments. For all numerical experiments, the relative error of u , v and p is investigated in terms of the accuracy of numerical solutions. By using only three different grid sizes, they estimated the rate of convergence for the pressure p to be between 0.3 and 1 in the L_∞ norm. However, convergence rates for the velocity were found to be $\mathcal{O}(1)$. Meanwhile, in the L^2 norm they estimate convergence rates for all variables between 0.6 and 1. The same convergence rates were found numerically for wave reflection against a solid circle.

In this chapter, we begin in section 4.2 by looking for the continuum solutions for wave reflection at a planar wall. We also derive the discrete solutions for the same problem when the grid and wall are aligned. In sections 4.3 and 4.4, we study the wave reflection at an inclined boundary (45° to the C-grid) for both continuum and discrete models. For the discrete case, the boundary now has perfect staircases, where the effects of these staircases can be investigated in terms of the amplitude of the reflected wave, the angle of the reflected wave, and the phase error of the reflected wave.

4.2 Boundary Aligned with the Grids

We first consider the aligned boundary case, where a wave propagates inwards from large y to a planar wall at $y = 0$, and then reflects back outwards to large y , as depicted in Figure 4.2.1.

4.2.1 Continuum solutions

We first derive the continuum solution. We consider a solution of the form

$$v = \operatorname{Re}[A_I \exp\{i(k_I x + l_I y - \omega_I t)\}] + \operatorname{Re}[A_R \exp\{i(k_R x + l_R y - \omega_R t)\}], \quad (4.2.1)$$

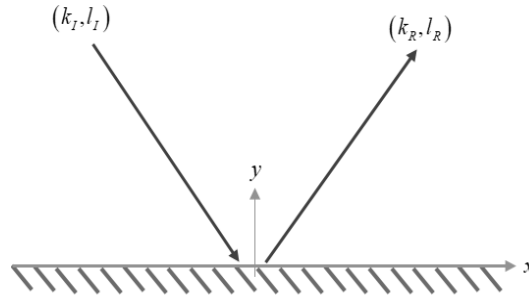


Figure 4.2.1: The wave reflection at a solid wall.

where A_I is the wave amplitude for the incident wave, k_I and l_I are the incident wavenumbers in the x and y directions, respectively, ω_I is the frequency of the incident wave, A_R is the wave amplitude for the reflected wave, k_R and l_R are the reflected wavenumber in the x and y directions respectively, and ω_R is the frequency of the reflected wave.

We can take $\omega_I > 0$ without loss of generality. Then we need to ensure the incident wave is indeed propagating towards the wall, i.e., that the y -component of the group velocity is negative. However, substituting (4.2.1) into (4.1.1a,b,c) we know that $\omega_I^2 = k_I^2 + l_I^2$, so that

$$\mathbf{c}_g = (\omega_k, \omega_l) = \left(\frac{k_I}{\omega_I}, \frac{l_I}{\omega_I} \right). \quad (4.2.2)$$

Since we have taken $\omega_I > 0$, we thus need to take $l_I < 0$ for an *incoming* wave. In the same way, to ensure that the reflected wave is outgoing, we need to take

$$\frac{l_R}{\omega_R} > 0, \quad (4.2.3)$$

where $\omega_R^2 = k_R^2 + l_R^2$.

The no normal flow condition require that velocity normal to the wall vanishes, which is

$$v = 0 \quad \text{at} \quad y = 0, \quad (4.2.4)$$

and gives

$$\begin{aligned} \operatorname{Re}[A_I \exp\{i(k_I x - \omega_I t)\} + A_R \exp\{i(k_R x - \omega_R t)\}] &= 0 \\ \Rightarrow A_R \exp\{i(k_I - k_R)x\} &= -A_I \exp\{i(\omega_I - \omega_R)t\}. \end{aligned} \quad (4.2.5)$$

This can only be true if the function of x on the left-hand side and the function of t on the right hand side are both constants, which requires

$$k_I = k_R \quad \text{and} \quad \omega_I = \omega_R. \quad (4.2.6)$$

Then we also require

$$A_R = -A_I. \quad (4.2.7)$$

It remains to find l_R . But, $l_R^2 = \omega_R^2 - k_R^2 = \omega_I^2 - k_I^2 = l_I^2$, so $l_R = \pm l_I$. Since $l_I < 0$, and we require l_R to take the same sign as $\omega_R = \omega_I$ (which is positive), we thus need $l_R = -l_I$. Hence the full solution for v is

$$\begin{aligned} v(x, y, t) &= \operatorname{Re}[A_I \exp\{i(k_I x + l_I y - \omega_I t)\}] - \operatorname{Re}[A_I \exp\{i(k_I x - l_I y - \omega_I t)\}] \\ &= \operatorname{Re}[A_I \exp\{i(k_I x - \omega_I t)\}] (\exp\{il_I y\} - \exp\{-il_I y\}) \\ &= 2 \sin(l_I y) \operatorname{Re}[i A_I \exp\{i(k_I x - \omega_I t)\}]. \end{aligned} \quad (4.2.8)$$

To complete the solution, we also calculate p and u . By looking at (4.1.1b), differentiating (4.2.8) with respect to t we have

$$\frac{\partial v}{\partial t} = \operatorname{Re}(-i\omega_I A_I \exp(i(k_I x + l_I y - \omega_I t)) + i\omega_I A_I \exp(i(k_I x - l_I y - \omega_I t))) = -\frac{\partial p}{\partial y},$$

and by integrating with respect to y , we have the solution for p as

$$\begin{aligned} p(x, y, t) &= \frac{\omega_I}{l_I} \operatorname{Re} [A_I (\exp\{i(k_I x + l_I y - \omega_I t)\}) + \exp\{i(k_I x - l_I y - \omega_I t)\}] \\ &= \frac{2\omega_I}{l_I} \cos(l_I y) \operatorname{Re} [A_I \exp\{i(k_I x - \omega_I t)\}]. \end{aligned} \quad (4.2.9)$$

The solution for horizontal velocity u also is obtain in the same approach as p , which is by differentiating (4.2.9) with respect to x , and by integrating with respect to t as

$$\begin{aligned} u(x, y, t) &= \frac{k_I}{l_I} \operatorname{Re} [A_I (\exp\{i(k_I x + l_I y - \omega_I t)\}) + \exp\{i(k_I x - l_I y - \omega_I t)\}] \\ &= \frac{2k_I}{l_I} \cos(l_I y) \operatorname{Re} [A_I \exp\{i(k_I x - \omega_I t)\}]. \end{aligned} \quad (4.2.10)$$

Thus, the full solutions of the two-dimensional wave reflection at a boundary are (4.2.8), (4.2.9) and (4.2.10).

4.2.2 Discrete solutions

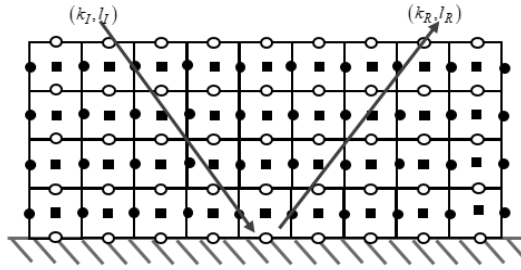


Figure 4.2.2: The wave reflects at boundary aligned with the grid.

We now examine discrete solutions of the two-dimensional wave reflection at a boundary. In discrete coordinates, we have $x_m = mh$ and $y_n = nh$, where h is the grid spacing of a cell, (m, n) are the indices in the x, y directions. Analogous to the previous setting, we consider the boundary at $y = 0$. Then, by using the C-grid the v nodes can be chosen at the boundary, as can be seen in Figure 4.2.2. We can see that the boundary is perfectly aligned

with the grid (the optimal choice), so that our boundary condition is

$$v_{m,0} = 0 \text{ for all } m. \quad (4.2.11)$$

Analogous to the derivation of the continuum solutions, we consider a discrete free wave solution of the form

$$v_{m,n} = \text{Re}[A_I \exp\{i(k_I x_m + l_I y_n - \omega_I t)\}] + \text{Re}[A_R \exp\{i(k_R x_m + l_R y_n - \omega_R t)\}]. \quad (4.2.12)$$

Then by using the boundary condition (4.2.11), we obtain

$$\begin{aligned} A_I \exp\{i(k_I m h - \omega_I t)\} + A_R \exp\{i(k_R m h - \omega_R t)\} &= 0 \\ \Rightarrow A_I \exp\{i(k_I - k_R)m h\} + A_R \exp\{i(\omega_I - \omega_R)t\} &= 0. \end{aligned} \quad (4.2.13)$$

If this is to be true for all m and t , then the exponential terms must be equal to zero, i.e.,

$$(k_I - k_R)m h = 0, \quad \forall h \Rightarrow k_I = k_R, \text{ and} \quad (4.2.14)$$

$$(\omega_I - \omega_R)t = 0, \quad \forall t \Rightarrow \omega_I = \omega_R. \quad (4.2.15)$$

Then, (4.2.13) will give

$$A_R = -A_I. \quad (4.2.16)$$

This means that the amplitude of the reflected wave is perfectly reproduced, and is unaffected by the finite-difference approximation. The solution now is

$$v = \text{Re}[A_I \exp\{i(k_I x_m + l_I y_n - \omega_I t)\}] - \text{Re}[A_I \exp\{i(k_R x_m + l_R y_n - \omega_R t)\}]. \quad (4.2.17)$$

It remains to find l_R . There are two considerations here. First, we need to ensure that the incident wave is indeed incident, and the outgoing wave is indeed outgoing. To do this, we consider the discrete dispersion relation, i.e., equation (2.7.12) with $f = 0$ and $c = 1$

$$\omega^2 = \frac{4}{h^2} \left(\sin^2 \frac{kh}{2} + \sin^2 \frac{lh}{2} \right). \quad (4.2.18)$$

Thus,

$$\begin{aligned} 2\omega\omega_l &= \left(\frac{4}{h^2} \right) 2 \left(\frac{h}{2} \right) \cos \left(\frac{lh}{2} \right) \sin \left(\frac{lh}{2} \right) = \left(\frac{2}{h} \right) \sin(lh) \\ &\Rightarrow \omega_l = \frac{\sin(lh)}{h\omega} \approx \frac{l}{\omega} \text{ when } lh \ll 1. \end{aligned} \quad (4.2.19)$$

We take $\omega_I > 0$, without loss of generality. Thus, for the incoming wave we need $l_I/\omega_I < 0$, so that $l_I < 0$ (at least when $h \ll 1$). For the reflected wave, we need $0 < l_R/\omega_R = l_R/\omega_I$, so that $l_R > 0$.

The second consideration is that both incident and reflected waves satisfy the discrete dispersion relation. So

$$\begin{aligned} \frac{4}{h^2} \left(\sin^2 \frac{k_I h}{2} + \sin^2 \frac{l_I h}{2} \right) &= \frac{4}{h^2} \left(\sin^2 \frac{k_R h}{2} + \sin^2 \frac{l_R h}{2} \right), \\ \Rightarrow \sin^2(l_I h) - \sin^2(l_R h) &= 0, \text{ since } k_I = k_R \text{ by 4.2.14} \\ \Rightarrow \cos(l_I h) - \cos(l_R h) &= 0, \\ \Rightarrow \sin \left(\frac{(l_I + l_R)h}{2} \right) \sin \left(\frac{(l_I - l_R)h}{2} \right) &= 0. \end{aligned}$$

Thus $(l_I + l_R)h/2 = n\pi$ or $(l_I - l_R)h/2 = n\pi$. At least as $h \rightarrow 0$, the only possibilities are $l_I + l_R = 0$ or $l_I - l_R = 0$. But, since we know that l_I and l_R take opposite signs, we must have

$$l_R = -l_I. \quad (4.2.20)$$

Thus, the full discrete solution for wave reflection at a boundary is

$$\begin{aligned} v_{m,n} &= \operatorname{Re}[A_I \exp\{i(k_I x_m + l_I y_n - \omega_I t)\}] - \operatorname{Re}[A_I \exp\{i(k_I x_m - l_I y_n - \omega_I t)\}] \\ &= 2 \sin(l_I y_n) \operatorname{Re}[i A_I \exp\{i(k_I x_m - \omega_I t)\}]. \end{aligned} \quad (4.2.21)$$

We can see that discrete solution (4.2.21) is exactly same as continuum solution (4.2.8) without any error terms. Therefore, the discrete solution is as good a solution as the continuum solution, which shows perfect reflection at the boundary. However, note that the discrete solution is not perfect, simply because there is a small error in the discrete frequency, via (4.2.18).

4.2.3 Numerical visualisation

In this section, we visualised the solution of wave reflection at a planar wall. We consider incident wave traveling towards a planar wall with incident wavenumber $k_I = 1$ and $l_I = -2$ in the x and y direction, respectively. There is no normal flow at the wall, so that when hitting the wall the wave reflects and traveling away from the wall. Figure 4.2.3 shows the solutions for pressure p along the first row, and velocity (u, v) along the second and third row, for wave reflection at the planar wall. The wall and grid are aligned at $y = 0$. The wave incident component is given in column one, the reflected wave component in second column, and the total solution (incident + reflected) in third column. From all the figures, we can see that the wave is traveling towards the boundary and then reflected back propagates away from the boundary. In the total solutions, there is a complete wave with wavelength 2π in x direction which represents wavenumber $k_I = 1$, and two complete wave in y direction which illustrated $l_I = -2$. Note that, the negative value in l_I represents the direction of wave propagation.

In the above discussion, we have focused on the solution where planar boundary at $y = 0$, which implies that boundary is aligned with the grid in discrete solution. In further

discussion, the effect of unaligned boundary with the grid will be discussed.

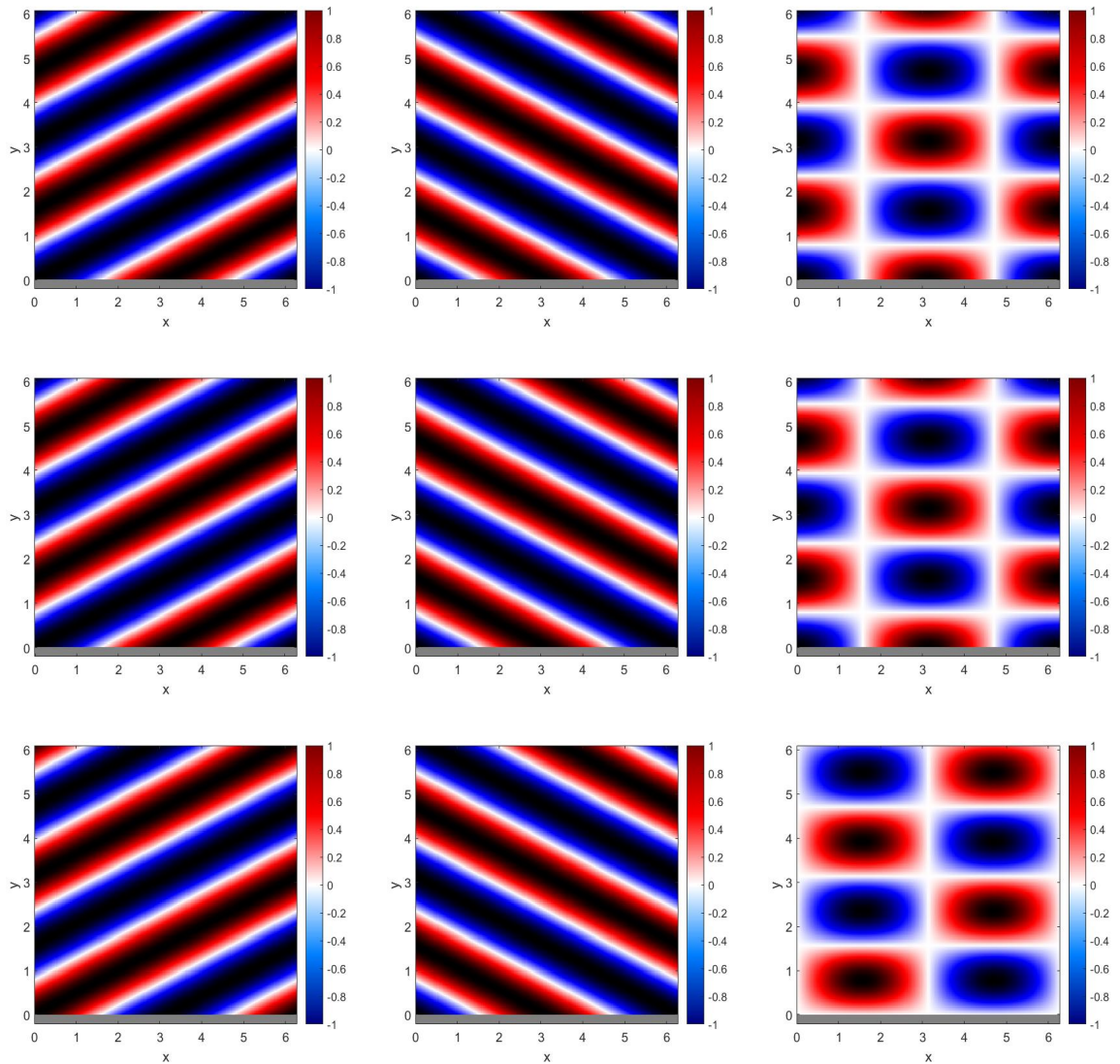


Figure 4.2.3: The continuum solutions of p , u , and v for wave reflection at aligned boundary at $t = 0$, with horizontal wavenumber $k = 1$, vertical wavenumber $l = -2$. The left column is the incident wave component, centre column is the reflected component, and the right column is the total component (i.e., incident + reflected). The top row is the solution for pressure p , second row is velocity u , and third row is the velocity v .

4.3 Tilted boundary: Continuum solution

We now turn to the next setting which is boundary tilted at 45° from the x axis as depicted in Figure 4.3.1. The straight boundary lies along the line $y = x$, at which there is no normal flow $\mathbf{u} \cdot \mathbf{n} = 0$. So there is perfect reflection when a wave with wavenumber (k_I, l_I) propagates towards the wall. Our task is to find the reflected wave, with wavenumber (k_R, l_R) , both in the continuum solution and the discrete solution. Note that we rederive the continuum solution in this particular geometry, now using the free wave solution for p , instead of v as in the previous section. This is because the discrete solution to be presented in section 4.4, will use a corresponding solution method.

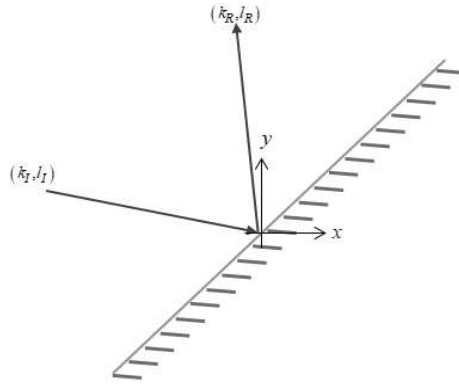


Figure 4.3.1: The wave reflects at a planar wall tilted 45° from x -axis.

The continuum solution is derived by considering a free wave solution of the form

$$p(x, y, t) = \text{Re} \left[A_I \exp\{i(k_I x + l_I y - \omega_I t)\} + A_R \exp\{i(k_R x + l_R y - \omega_R t)\} \right], \quad (4.3.1)$$

where k_I is the incident wavenumber in the x direction, l_I is the incident wavenumber in the y direction, to be determined. Again we suppose that $\omega_I > 0$. Then $\mathbf{c}_g = \left(\frac{k_I}{\omega_I}, \frac{l_I}{\omega_I} \right)$, so for incident wave propagation towards the wall with outwards pointing normal $(-1, 1)$

we need

$$\mathbf{c}_g \cdot (-1, 1) < 0 \Rightarrow \frac{(l_I - k_I)}{\omega_I} < 0 \Rightarrow l_I - k_I < 0. \quad (4.3.2)$$

Conversely, for the reflected wave to be propagating away from the wall we need

$$\frac{(l_R - k_R)}{\omega_R} < 0. \quad (4.3.3)$$

To proceed, we also calculate the corresponding expressions for u and v . Substituting (4.3.1) into (4.1.1) we have

$$-i\omega u = -ikp \Rightarrow u = \frac{k}{\omega}p, \quad (4.3.4)$$

$$-i\omega v = -ilp \Rightarrow v = \frac{l}{\omega}p, \quad (4.3.5)$$

$$-i\omega p + ik u + il v = 0. \quad (4.3.6)$$

At the boundary $y = x$, the no normal flow boundary condition $\mathbf{u} \cdot \mathbf{n} = 0$ will give $u = v$.

With this condition, (4.3.4) and (4.3.5) are equal and we have

$$\begin{aligned} & \frac{k_I}{\omega_I} A_I \exp(i(k_I x + l_I x - \omega_I t)) + \frac{k_R}{\omega_R} A_R \exp(i(k_R x + l_R x - \omega_R t)) \\ &= \frac{l_I}{\omega_I} A_I \exp(i(k_I x + l_I x - \omega_I t)) + \frac{l_R}{\omega_R} A_R \exp(i(k_R x + l_R x - \omega_R t)), \\ &\Rightarrow \exp(i(k_I x + l_I x - \omega_I t)) \frac{A_I}{\omega_I} (k_I - l_I) = \exp(i(k_R x + l_R x - \omega_R t)) \frac{A_R}{\omega_R} (l_R - k_R), \\ &\Rightarrow \exp(i(k_I - k_R + l_I - l_R)x) \frac{A_I}{\omega_I} (k_I - l_I) = \exp(-i(\omega_R - \omega_I)t) \frac{A_R}{\omega_R} (l_R - k_R). \end{aligned} \quad (4.3.7)$$

Thus, (4.3.7) is only true for all x and all t if

$$k_I - k_R + l_I - l_R = 0, \quad (4.3.8a)$$

$$\omega_R - \omega_I = 0, \quad (4.3.8b)$$

$$\text{and } \frac{A_I}{\omega_I} (k_I - l_I) = \frac{A_R}{\omega_R} (l_R - k_R). \quad (4.3.8c)$$

Finally, the dispersion relation must be satisfied for both incident and reflected waves. Thus

$$\omega_I^2 = (k_I^2 + l_I^2), \quad \text{and} \quad \omega_R^2 = (k_R^2 + l_R^2).$$

Since $\omega_R = \omega_I$ by (4.3.8b), it follows that

$$k_I^2 + l_I^2 = k_R^2 + l_R^2 \Rightarrow k_I^2 - k_R^2 = l_R^2 - l_I^2. \quad (4.3.9)$$

Substituting (4.3.8a) into (4.3.9) we have

$$(k_I + k_R)(l_R - l_I) = (l_R + l_I)(l_R - l_I) \Rightarrow (l_R - l_I)(k_I + k_R - l_R - l_I) = 0. \quad (4.3.10)$$

There are two possibilities. First, $l_R = l_I$, which then implies $k_I = k_R$ by (4.3.8a), and then $A_I = -A_R$ by (4.3.8c), (since $k_I \neq l_I$ by (4.3.2)). However, this is a trivial solution ($p = 0$). So we must have the other possibility, i.e.,

$$k_I + k_R - l_R - l_I = 0 \Rightarrow k_I - l_I = l_R - k_R, \quad (4.3.11)$$

in which case (4.3.8c) gives

$$A_R = A_I. \quad (4.3.12)$$

It remains to find k_R and l_R . From (4.3.8a), we have $k_R = l_R + l_I - k_I$, and substituting

into (4.3.11) yields

$$k_I - l_R - l_I + k_I + l_I - l_R = 0 \Rightarrow 2k_I = 2l_R \Rightarrow l_R = k_I, \text{ and } k_R = l_I. \quad (4.3.13)$$

Note that this reflected wave is indeed ‘reflected’, since

$$\mathbf{c}_g \cdot (-1, 1) = \left(\frac{k_R}{\omega_R}, \frac{l_R}{\omega_R} \right) \cdot (-1, 1) = \left(\frac{l_I}{\omega_I}, \frac{k_I}{\omega_I} \right) \cdot (-1, 1) = \frac{k_I - l_I}{\omega_I} > 0, \quad (4.3.14)$$

by (4.3.2).

Therefore, the full solution of wave reflection at the boundary $y = x$ is

$$p(x, y, t) = \text{Re} \left[A_I \exp\{i(k_I x + l_I y - \omega_I t)\} + A_I \exp\{i(l_I x + k_I y - \omega_I t)\} \right]. \quad (4.3.15)$$

We can calculate the solutions for u and v . By substituting (4.3.15) into (4.3.4), we obtain the solution for u as

$$u(x, y, t) = \text{Re} \left[\frac{k_I}{\omega_I} A_I \exp\{i(k_I x + l_I y - \omega_I t)\} + \frac{l_I}{\omega_I} A_I \exp\{i(l_I x + k_I y - \omega_I t)\} \right]. \quad (4.3.16)$$

While the solution for v is obtain by substituting (4.3.15) into (4.3.5) which is written as

$$v(x, y, t) = \text{Re} \left[\frac{l_I}{\omega_I} A_I \exp\{i(k_I x + l_I y - \omega_I t)\} + \frac{k_I}{\omega_I} A_I \exp\{i(l_I x + k_I y - \omega_I t)\} \right]. \quad (4.3.17)$$

4.4 Tilted boundary: Discrete solution

We now examine the discrete solutions for wave reflected at a boundary tilted at 45° , where we have chosen to align the grid so that the continuum boundary $y = x$ passes through p nodes, as shown in Figure 4.4.1. These cut cells are retained in the computational domain,

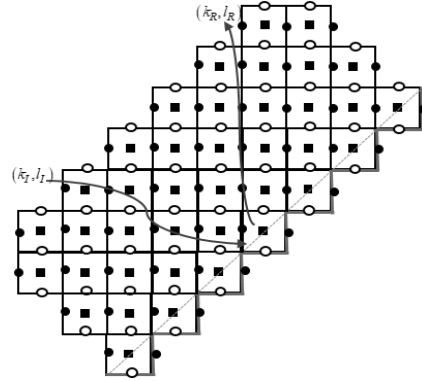


Figure 4.4.1: The wave reflects at boundary unaligned with the grid.

so the no normal flow boundary condition is $u = 0$ and $v = 0$ at the right and bottom of these cells. Then by connecting all the zero velocity nodes, we obtain the so called staircase boundary.

Using the standard second order C-grid formulation, the discrete solution is governed by

$$-i\omega u_{m,n+\frac{1}{2}} = -\frac{1}{h} \left(p_{m+\frac{1}{2},n+\frac{1}{2}} - p_{m-\frac{1}{2},n+\frac{1}{2}} \right), \quad (4.4.1a)$$

$$-i\omega v_{m+\frac{1}{2},n} = -\frac{1}{h} \left(p_{m+\frac{1}{2},n+\frac{1}{2}} - p_{m+\frac{1}{2},n-\frac{1}{2}} \right), \quad (4.4.1b)$$

$$-i\omega p_{m+\frac{1}{2},n+\frac{1}{2}} + \frac{1}{h} \left(u_{m+1,n+\frac{1}{2}} - u_{m,n+\frac{1}{2}} + v_{m+\frac{1}{2},n+1} - v_{m+\frac{1}{2},n} \right) = 0. \quad (4.4.1c)$$

At the staircases, the no normal flow boundary condition gives

$$u_{j+1,j+\frac{1}{2}} = 0, \quad v_{j+\frac{1}{2},j} = 0, \quad \text{for all } j \in \mathbb{Z}. \quad (4.4.2)$$

By setting $m = n = j$ in (4.4.1c), we obtain

$$-i\omega p_{j+\frac{1}{2},j+\frac{1}{2}} + \frac{1}{h} (-u_{j,j+\frac{1}{2}} + v_{j+\frac{1}{2},j+1}) = 0, \quad (4.4.3)$$

with two terms vanishing via (4.4.2). We then set $m = n = j$ in (4.4.1a) and $m = j$ and

$n = j + 1$ in (4.4.1b) to eliminate u and v , to obtain

$$p_{j+\frac{1}{2},j+\frac{3}{2}} + (\omega^2 h^2 - 2)p_{j+\frac{1}{2},j+\frac{1}{2}} + p_{j-\frac{1}{2},j+\frac{1}{2}} = 0. \quad (4.4.4)$$

This equation links the pressure node $p_{j+1/2,j+1/2}$ at the centre of a boundary cell, to pressure nodes at the centre of two cells away from the boundary $p_{j-1/2,j+1/2}$ and $p_{j+1/2,j+3/2}$ (i.e., to the left and above the boundary cell). In (4.4.4), j is taken to be an integer, but we can rewrite it as

$$p_{j,j+1} + (\omega^2 h^2 - 2)p_{j,j} + p_{j-1,j} = 0, \quad (4.4.5)$$

where j will now be an integer plus half.

We now assume a discrete solution of the form

$$p_{m,n} = \text{Re}[A_I \exp\{i(k_I x_m + l_I y_n - \omega_I t)\}] + \text{Re}[A_R \exp\{i(k_R x_m + l_R y_n - \omega_R t)\}]. \quad (4.4.6)$$

As before, we can take $\omega_R > 0$ without loss of generality, and there is a condition on (k_R, l_R) to ensure propagation towards the wall. Substituting (4.4.6) in (4.4.5) then gives

$$\begin{aligned} & A_I \exp(i(k_I j h + l_I (j+1) h - \omega_I t)) + A_R \exp(i(k_R j h + l_R (j+1) h - \omega_R t)) \\ & + (\omega^2 h^2 - 2) (A_I \exp(i(k_I j h + l_I j h - \omega_I t)) + A_R \exp(i(k_R j h + l_R j h - \omega_R t))) \\ & + A_I \exp\{i(k_I (j-1) h + l_I j h - \omega_I t)\} + A_R \exp\{i(k_R (j-1) h + l_R j h - \omega_R t)\} = 0. \end{aligned} \quad (4.4.7)$$

With a straightforward factorising the common terms we have

$$\begin{aligned} & A_I \exp\{i((k_I + l_I) j h - \omega_I t)\} (\exp\{-ik_I h\} + \omega^2 h^2 - 2 + \exp\{il_I h\}) \\ & = -A_R \exp\{i((k_R + l_R) j h - \omega_R t)\} (\exp\{-ik_R h\} + \omega^2 h^2 - 2 + \exp\{il_R h\}), \end{aligned} \quad (4.4.8)$$

or we can simply write as

$$A_R = -A_I \exp\{i(k_I + l_I - k_R - l_R)jh - (\omega_I - \omega_R)t\} \frac{(e^{-ik_I h} + \omega^2 h^2 - 2 + e^{il_I h})}{(e^{-ik_R h} + \omega^2 h^2 - 2 + e^{il_R h})}. \quad (4.4.9)$$

This equation, (4.4.9), has some similarities to equation (7) of [17]. The first main difference arises because they analysed the problem in a specific time-stepping framework, so that their expression also involved a time step δ . Here we simply assume time-periodic waves, the frequency of which will be consistent with the discrete dispersion relation. The second main difference arises because they made an assumption about the values of k_R and l_R , without deriving them from k_I and l_I . Here we make no such assumption, and rather determine k_R and l_R from k_I and l_I , leading to (4.4.15).

If (4.4.9) is to be true for all j and t , then

$$k_I + l_I - k_R - l_R = 0, \quad (4.4.10)$$

$$\omega_I - \omega_R = 0, \quad (4.4.11)$$

$$A_I (e^{-ik_I h} + \omega_I^2 h^2 - 2 + e^{il_I h}) = -A_R (e^{-ik_R h} + \omega_R^2 h^2 - 2 + e^{il_R h}). \quad (4.4.12)$$

Since we know all the components for the incident wave, (i.e., k_I , l_I , A_I , and ω_I), the remaining task is to find all the reflected wave components, (i.e., k_R , l_R , A_R , and ω_R).

Of course, we also know that the discrete dispersion relation (4.2.18) must be satisfied by

the incident and reflected waves, that is

$$\begin{aligned}\omega_I^2 &= \frac{4}{h^2} \left(\sin^2 \left(\frac{k_I h}{2} \right) + \sin^2 \left(\frac{l_I h}{2} \right) \right) = \frac{4}{h^2} \left(\sin^2 \left(\frac{k_R h}{2} \right) + \sin^2 \left(\frac{l_R h}{2} \right) \right) = \omega_R^2, \\ &\Rightarrow \frac{1 - \cos(k_I h)}{2} + \frac{1 - \cos(l_I h)}{2} = \frac{1 - \cos k_R h}{2} + \frac{1 - \cos l_R h}{2} \\ &\qquad \cos(k_I h) + \cos(l_I h) = \cos(k_R h) + \cos(l_R h), \\ 2 \cos \left(\frac{(k_I + l_I)h}{2} \right) \cos \left(\frac{(k_I - l_I)h}{2} \right) &= 2 \cos \left(\frac{(k_R + l_R)h}{2} \right) \cos \left(\frac{(k_R - l_R)h}{2} \right).\end{aligned}$$

However, using (4.4.10) we have

$$\begin{aligned}\cos \left(\frac{(k_R + l_R)h}{2} \right) \cos \left(\frac{(k_I - l_I)h}{2} \right) &= \cos \left(\frac{(k_R + l_R)h}{2} \right) \cos \left(\frac{(k_R - l_R)h}{2} \right). \\ \Rightarrow \cos \left(\frac{(k_R + l_R)h}{2} \right) \left[\cos \left(\frac{(k_I - l_I)h}{2} \right) - \cos \left(\frac{(k_R - l_R)h}{2} \right) \right] &= 0, \\ \Rightarrow \cos \left(\frac{(k_R + l_R)h}{2} \right) \sin \left(\frac{\frac{(k_I - l_I)h}{2} + \frac{(k_R - l_R)h}{2}}{2} \right) \sin \left(\frac{\frac{(k_I - l_I)h}{2} - \frac{(k_R - l_R)h}{2}}{2} \right) &= 0.\end{aligned}$$

At least as $h \rightarrow 0$, the first term cannot vanish, so we either need $\frac{(k_I - l_I)h}{2} + \frac{(k_R - l_R)h}{2} = 0$ or $\frac{(k_I - l_I)h}{2} - \frac{(k_R - l_R)h}{2} = 0$ (again as $h \rightarrow 0$). In terms of the wavenumbers, these options are

$$k_I - l_I + k_R - l_R = 0 \text{ or } k_I - l_I - k_R + l_R = 0. \quad (4.4.13)$$

Using (4.4.10), the second of these gives $l_R = l_I$ and then $k_R = k_I$, and then $A_I = -A_R$ from (4.4.12); this corresponds to a trivial solution with $p = 0$. So we are left (which would also fail to satisfy the group velocity condition) with

$$k_I - l_I + k_R - l_R = 0. \quad (4.4.14)$$

Combining with (4.4.10) then gives

$$k_R = l_I, \quad l_R = k_I. \quad (4.4.15)$$

So we have found the discrete reflected wavenumbers in term of the incident wavenumbers. It shows the surprising result that there is no error in the reflected wavenumber, i.e., we exactly recover the continuum reflection relationship (4.3.13). This appears to arise by some special chance, perhaps because of the simple form of the discrete dispersion relation, or because of its symmetry between k and l , i.e., $\omega^2 = (4/h^2)(\sin^2(kh/2) + \sin^2(lh/2))$. Indeed, as shown in section 6.4.2 for a case with internal waves, there is no necessity for a continuum (reflection) result to be recovered exactly in a discrete approximation. The result (4.4.15) was simply assumed in [17], which is one of the key differences between their study and this one. We should also note that if we were to generalise the problem and consider reflection at a non-perfect staircase (i.e., one not-aligned at 45 degrees to the grid), then this perfect reflection property may be lost.

It remains to find A_R . Expanding (4.4.12) with Taylor Series, we find

$$\begin{aligned} A_I & \left[\left\{ 1 + il_I h - \frac{1}{2}(l_I h)^2 - \frac{i}{6}(l_I h)^3 + O(h^4) \right\} + \omega_I^2 h^2 - 2 \right. \\ & \quad \left. + \left\{ 1 - ik_I h - \frac{1}{2}(k_I h)^2 + \frac{i}{6}(k_I h)^3 + O(h^4) \right\} \right] \\ & = -A_R \left[\left\{ 1 + il_R h - \frac{1}{2}(l_R h)^2 - \frac{i}{6}(l_R h)^3 + O(h^4) \right\} + \omega_R^2 h^2 - 2 \right. \\ & \quad \left. + \left\{ 1 - ik_{IR} h - \frac{1}{2}(k_R h)^2 + \frac{i}{6}(k_R h)^3 + O(h^4) \right\} \right], \quad (4.4.16) \end{aligned}$$

By rearranging the common terms we have

$$\begin{aligned} A_I & \left[i(l_I - k_I) + h \left(\omega_I^2 - \frac{k_I^2}{2} - \frac{l_I^2}{2} \right) + \frac{ih^2}{6} (k_I^3 - l_I^3) + O(h^3) \right] \\ & = -A_R \left[i(l_R - k_R) + h \left(\omega_R^2 - \frac{l_R^2}{2} - \frac{k_R^2}{2} \right) + \frac{ih^2}{6} (k_R^3 - l_R^3) + O(h^3) \right], \end{aligned} \quad (4.4.17)$$

and substituting (4.4.11) and (4.4.15) into (4.4.17) and multiplying by (-1) both side gives

$$\begin{aligned} A_I & \left[i(k_I - l_I) - h \left(\omega_I^2 - \frac{k_I^2}{2} - \frac{l_I^2}{2} \right) - \frac{ih^2}{6} (k_I^3 - l_I^3) + O(h^3) \right] \\ & = A_R \left[i(k_I - l_I) + h \left(\omega_R^2 - \frac{k_I^2}{2} - \frac{l_I^2}{2} \right) + \frac{ih^2}{6} (l_I^3 - k_I^3) + O(h^3) \right]. \end{aligned} \quad (4.4.18)$$

By making A_R as a subject we have

$$\begin{aligned} A_R & = A_I \frac{\left[i(k_I - l_I) - \frac{h}{2} (k_I^2 + l_I^2) - \frac{ih^2}{6} (k_I^3 - l_I^3) + O(h^3) \right]}{\left[i(k_I - l_I) + \frac{h}{2} (k_I^2 + l_I^2) + \frac{ih^2}{6} (l_I^3 - k_I^3) + O(h^3) \right]} \quad (4.4.19) \\ & = A_I \frac{i(k_I - l_I) \left[1 - \frac{h(k_I^2 + l_I^2)}{2i(k_I - l_I)} - \frac{ih^2(k_I - l_I)}{6i(k_I - l_I)} (k_I^2 + k_I l_I + l_I^2) + O(h^3) \right]}{i(k_I - l_I) \left[1 + \frac{h(k_I^2 + l_I^2)}{2i(k_I - l_I)} - \frac{ih^2(k_I - l_I)}{6i(k_I - l_I)} (k_I^2 + k_I l_I + l_I^2) + O(h^3) \right]}. \end{aligned} \quad (4.4.20)$$

Note that the case $k_I = l_I$ is excluded, since this corresponds to wave propagation along the wall. So we may cancel that factor, and obtain

$$A_R = A_I \frac{\left[1 + \frac{ih(k_I^2 + l_I^2)}{2(k_I - l_I)} - \frac{h^2(k_I^2 + k_I l_I + l_I^2)}{6} + O(h^3) \right]}{\left[1 - \frac{ih(k_I^2 + l_I^2)}{2(k_I - l_I)} - \frac{h^2(k_I^2 + k_I l_I + l_I^2)}{6} + O(h^3) \right]}. \quad (4.4.21)$$

Finally, using the binomial series on the denominator gives

$$A_R = A_I \left(1 + \frac{ih(k_I^2 + l_I^2)}{(k_I - l_I)} - \frac{h^2(k_I^2 + l_I^2)^2}{2(k_I - l_I)^2} \right) + O(h^3). \quad (4.4.22)$$

This is a key result. The corresponding continuum result was (4.3.12) $A_R = A_I$. However, we have not recovered that. Instead, we find a first-order in h phase error in the complex amplitude: this is solely due to the staircase boundary.

It is then of interest to ask if there is solely a phase error, or whether there is also an amplification (or suppression) upon reflection. To do this, we calculate

$$|A_R|^2 = |A_I|^2 \left(1 + \frac{ih(k_I^2 + l_I^2)}{(k_I - l_I)} - \frac{h^2(k_I^2 + l_I^2)^2}{2(k_I - l_I)^2} + O(h^3) \right) \left(1 - \frac{ih(k_I^2 + l_I^2)}{(k_I - l_I)} - \frac{h^2(k_I^2 + l_I^2)^2}{2(k_I - l_I)^2} + O(h^3) \right), \quad (4.4.23)$$

which gives

$$|A_R|^2 = |A_I|^2 (1 + O(h^3)). \quad (4.4.24)$$

So we cannot detect any change in the magnitude of the reflected wave from the incident wave. This analysis does not prove that $|A_R| = |A_I|$, other than up to $O(h^2)$.

4.4.1 Alternative derivation of amplitude error

We can improve upon (4.4.22) and (4.4.23) by returning to (4.4.12). Using (4.4.15) to substitute $k_R = l_I$ and $l_R = k_I$ gives

$$\frac{A_R}{A_I} = -\frac{\exp(-ikh) + \exp(+ilh) - 2 + \omega^2 h^2}{\exp(+ikh) + \exp(-ilh) - 2 + \omega^2 h^2}, \quad \text{where } \omega^2 = \frac{4}{h^2} \left(\sin^2 \frac{kh}{2} + \sin^2 \frac{lh}{2} \right). \quad (4.4.25)$$

This expression takes the form

$$\frac{A_R}{A_I} = -\frac{a}{a^*}, \text{ where } a = \exp(-ikh) + \exp(+ilh) - 2 + 4 \left(\sin^2 \frac{kh}{2} + \sin^2 \frac{lh}{2} \right). \quad (4.4.26)$$

Since $|a/a^*| = 1$, it follows that $|A_R/A_I| = 1$. So everything is contained in the (complex) phase function φ , i.e., $A_R/A_I = \exp(i\varphi)$. If we write $a = r \exp(i(\pi/2 + \theta))$, then

$$\exp(i\varphi) = \frac{A_R}{A_I} = -\frac{r \exp(i(\pi/2 + \theta))}{r \exp(-i(\pi/2 + \theta))} = -\exp(i(\pi + 2\theta)) = \exp(2i\theta) \Rightarrow \varphi = 2\theta.$$

It remains to determine θ , which we find by rewriting a as

$$a = r \exp(i(\pi/2 + \theta)) = r (\cos(\pi/2 + \theta) + i \sin(\pi/2 + \theta)) = r(-\sin \theta + i \cos \theta).$$

But from (4.4.26), we can rewrite a as

$$\begin{aligned} a &= \cos kh + \cos lh - 2 + 4 \left(\sin^2 \frac{kh}{2} + \sin^2 \frac{lh}{2} \right) + i(\sin lh - \sin kh) \\ &= 2 \left(\sin^2 \frac{kh}{2} + \sin^2 \frac{lh}{2} \right) + i(\sin lh - \sin kh) \\ &\Rightarrow r \cos \theta = \sin lh - \sin kh \text{ and } r \sin \theta = -2 \left(\sin^2 \frac{kh}{2} + \sin^2 \frac{lh}{2} \right) \\ &\Rightarrow \tan \theta = 2 \left(\frac{\sin^2 \frac{kh}{2} + \sin^2 \frac{lh}{2}}{\sin kh - \sin lh} \right). \end{aligned} \quad (4.4.27)$$

For example,

- if $h \ll 1$, then

$$\begin{aligned} \tan \theta &\approx 2 \left(\frac{k^2 h^2/4 + l^2 h^2/4}{kh - lh} \right) = \left(\frac{k^2 + l^2}{2(k-l)} \right) h \\ &\Rightarrow \theta \approx \left(\frac{k^2 + l^2}{2(k-l)} \right) h \Rightarrow \varphi = 2\theta \approx \left(\frac{k^2 + l^2}{k-l} \right) h, \end{aligned} \quad (4.4.28)$$

in agreement with the existing result (4.4.22) for small h .

- For an incident wave normal to the wall (i.e., $l = -k$), we have

$$\tan \theta = \frac{4 \sin^2(kh/2)}{2 \sin kh} = \frac{4 \sin^2(kh/2)}{4 \sin(kh/2) \cos(kh/2)} = \tan(kh/2) \Rightarrow \theta = \frac{kh}{2}$$

$$\Rightarrow \varphi = 2\theta = kh.$$

This expression is exact for all h (not just small h).

The behaviour for other values of k and l (or larger h) is best found by simply plotting φ versus h – see Figure 4.4.2. Note that for a wide range of incident angles (e.g., (a,b,c)), the small h approximation is excellent (especially for the values of $h \leq 1$) that would be used in most numerics. However, it is not so good when the wave approaches the wall at a small angle, as in panel (d). Then there can be large phase errors even for small values of h . Note that the behavior for other values of k and l can be deduced from these plots. For example, if we change the sign of k and l together, then φ changes sign.

4.4.2 Spatial structure of discrete solution

Having determined the amplitude error, we now find the discrete solutions for u and v , thus completing the spatial structure. From (4.4.1a), the discrete solution for u at node (x_m, y_n) is

$$u_{m,n} = \text{Re} \left(\frac{1}{i\omega h} \left(p_{m+\frac{1}{2},n} - p_{m-\frac{1}{2},n} \right) \right)$$

$$= \text{Re} \left(\frac{1}{i\omega h} A_I e^{i(k_I(m+\frac{1}{2})h+l_I n h - \omega t)} + A_R e^{i(k_R(m+\frac{1}{2})h+l_R n h - \omega t)} \right.$$

$$\left. - A_I e^{i(k_I(m-\frac{1}{2})h+l_I n h - \omega t)} - A_R e^{i(k_R(m-\frac{1}{2})h+l_R n h - \omega t)} \right), \quad (4.4.29)$$

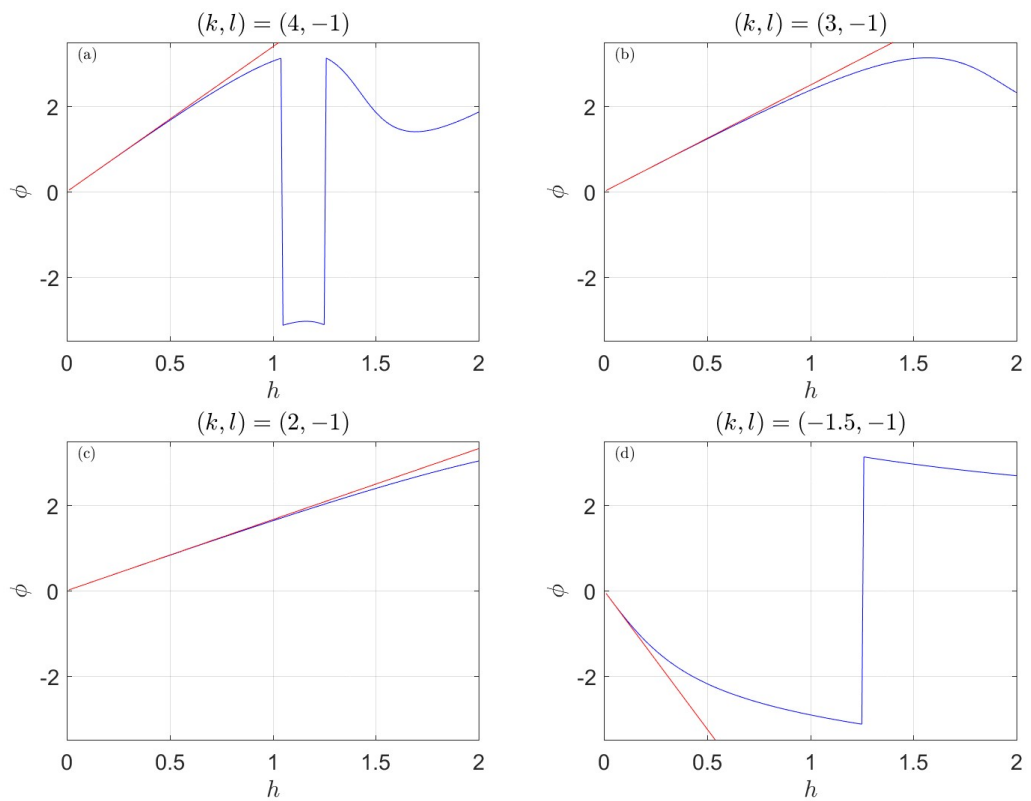


Figure 4.4.2: Blue is φ determined directly from A_R/A_I (4.4.26), and is constrained via $-\pi < \varphi \leq \pi$; red is the linear approximation for φ (4.4.28) when $h \ll 1$.

which is simplified as

$$u_{m,n} = \operatorname{Re} \left(\frac{2}{\omega h} \left(A_I e^{i(k_I m h + l_I n h - \omega t)} \sin \frac{k_I h}{2} + A_R e^{i(k_R m h + l_R n h - \omega t)} \sin \frac{k_R h}{2} \right) \right). \quad (4.4.30)$$

Then, in the limit of $h \rightarrow 0$, and by substituting A_R and k_R, l_R using (4.4.24) and (4.4.15), respectively, we obtain

$$u_{m,n} = \operatorname{Re} \left(\frac{A_I}{\omega} \left[k_I \exp(i(k_I m h + l_I n h - \omega t)) + l_I \exp(i(l_I m h + k_I n h - \omega t)) \left(1 + \frac{i h (k_I^2 + l_I^2)}{(k_I - l_I)} \right) \right] \right) + O(h^3). \quad (4.4.31)$$

Similarly, the structure of discrete solution for v also can be calculated. From (4.4.1b), the discrete solution for v at (x_m, y_n) is

$$\begin{aligned} v_{m,n} &= \operatorname{Re} \left(\frac{1}{i\omega h} \left(p_{m,n+\frac{1}{2}} - p_{m,n-\frac{1}{2}} \right) \right) \\ &= \operatorname{Re} \left(\frac{1}{i\omega h} A_I e^{i(k_I m h + l_I (n+\frac{1}{2})h - \omega t)} + A_R e^{i(k_R m h + l_R (n+\frac{1}{2})h - \omega t)} \right. \\ &\quad \left. - A_I e^{i(k_I m h + l_I (n-\frac{1}{2})h - \omega t)} - A_R e^{i(k_R m h + l_R (n-\frac{1}{2})h - \omega t)} \right), \quad (4.4.32) \end{aligned}$$

which is simplified as

$$v_{m,n} = \operatorname{Re} \left(\frac{2}{\omega h} \left(A_I e^{i(k_I m h + l_I n h - \omega t)} \sin \frac{l_I h}{2} + A_R e^{i(k_R m h + l_R n h - \omega t)} \sin \frac{l_R h}{2} \right) \right). \quad (4.4.33)$$

Again, as $h \rightarrow 0$ we obtain

$$v_{m,n} = \operatorname{Re} \left(\frac{A_I}{\omega} \left[l_I \exp(i(k_I m h + l_I n h - \omega t)) + k_I \exp(i(l_I m h + k_I n h - \omega t)) \left(1 + \frac{i h (k_I^2 + l_I^2)}{(k_I - l_I)} \right) \right] \right) + O(h^3). \quad (4.4.34)$$

Therefore, from both (4.4.31) and (4.4.34), and their analysis as $h \rightarrow 0$, (4.3.16) and (4.3.17), respectively, we can see that there is a first-order phase error in h in the discrete solution.

We have shown that the discrete analytical solutions of wave reflection inherit first-order phase error in h when the grid and boundary are aligned at 45° . We now visualise the results. The numerical visualisation is performed by considering same incident wavenumber as in the case of the grid and boundary are aligned, (i.e., $k_I = 1$, $l_I = -2$). Thus, the frequency of the incident wave is $\sqrt{5}$. Figure 4.4.3 shows the continuum solutions at $t = 0$ for the pressure p in the top row, and velocity (u, v) in the second and third row. The total contribution of the continuum solutions are also presented in the figure. We can see that the maximum value in both incident and reflected component is 1, since we set the amplitude to be 1. So that the maximum value in total wave component (i.e., incident + reflected) is 2.

We next visualise the results of the total wave component for continuum and discrete solution along with the error at different time. Figure 4.4.4 illustrates the total solutions of p for wave reflection at staircase boundaries along with the error using $h = \sqrt{2}/50 \approx 0.1257$, at $t = 0, \pi/2\omega$ and π/ω . Note that, the dotted line in the figure represents the staircase boundary which is chosen to be lower than the continuum boundary. In the third column, we can see that the maximum error at each t is approximately 10% (i.e., 0.2090 for $t = 0$, 0.2158 for $t = \pi/2\omega$ and 0.2229 for $t = \pi/\omega$). We also observed that the error pattern is similar to the reflected wave component in Figure 4.4.3. This means that the errors are generated from the reflected wave component, as proven in the analysis.

We also visualise the continuum and discrete solution for velocity u and v at three different t as shown in Figure 4.4.5 and 4.4.6, respectively. From the figures, we can see that the error is large at the staircase boundary. However, in the outside staircase region there is no such large error as at the staircase. The error at the staircase arise as a result from the no normal flow boundary conditions at the staircase, where the velocity is zero at the

staircase boundary. Meanwhile, in the continuum solutions they are not exactly zero. As in p , the error in velocity are also arise from the reflected components. Undoubtedly, the error in the solutions are minimised when we reduced the size of grid spacing h to be $\sqrt{2}/100 \approx 0.0141$, as illustrated in Figure 4.4.7. It can be seen that the error is improved by 5% error, since the maximum error is approximately 0.1046 .

4.5 Summary

In this chapter, we have studied reflection of waves (meaning acoustic waves or non-rotating shallow-water waves) at a straight boundary. In the underlying continuum problem, the (complex) wave amplitude of the reflected wave is the same as that of the incoming wave, the along-boundary wavenumber remains unchanged, and the across-boundary wavenumber changes sign.

We studied two versions of the discrete problem. In the first of these, the grid and boundary were aligned, at $y = 0$. We showed that the reflected amplitude was recovered exactly, as were the two components of the reflected wavenumber. The solution is ‘exact’ in this sense. However, we should remember that there is a second-order error in the wave frequency of both incident and reflected waves, as occurs for any wave problem on the C-grid, with or without boundaries.

In the second discrete problem, the boundary (at $y = x$) was aligned at 45° to the grid, thus forming a perfect staircase boundary. Here we showed that the wavenumbers of the reflected wave were recovered exactly, which is perhaps surprising. However, the (complex) amplitude A_R of the reflected wave was not recovered exactly. Even though its magnitude was recovered correctly, i.e., $|A_R| = |A_I|$, there was a phase error, i.e., A_R/A_I had non-zero imaginary part. We derived an expression for A_R/A_I (which was previously given by [17]), and analysed it in some detail. In particular, we showed that there is first-order error

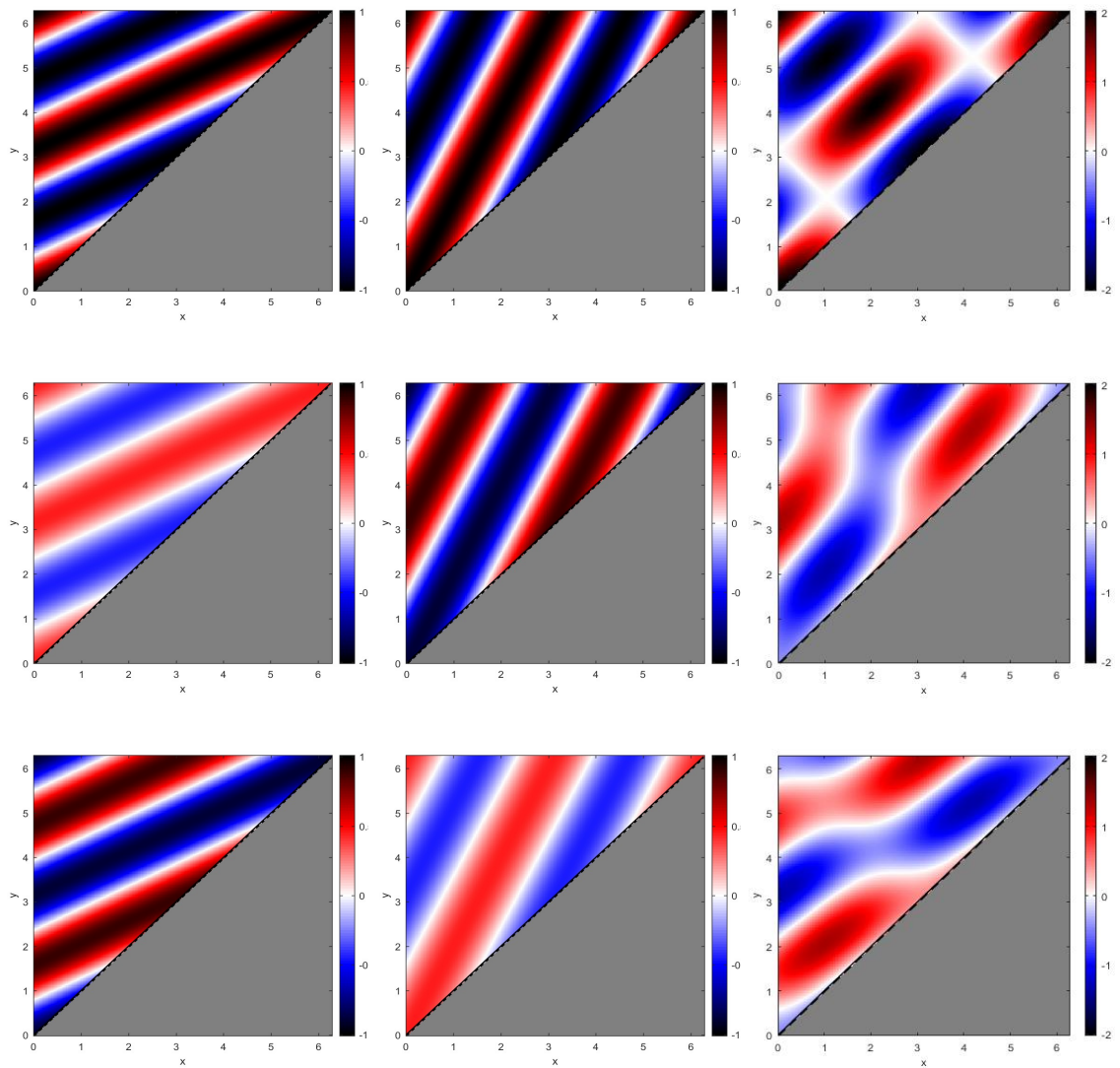


Figure 4.4.3: The continuum solutions of wave reflection at a straight boundary $y = x$ with horizontal wavenumber $k_I = 1$ and vertical wavenumber $l_I = -2$. Shown are the solutions for p (first row), u (second row) and v (third row) at $t = 0$. The left column is the incident wave component, the centre column is the reflected wave component, and the right column is the total (i.e., incident + reflected) component.

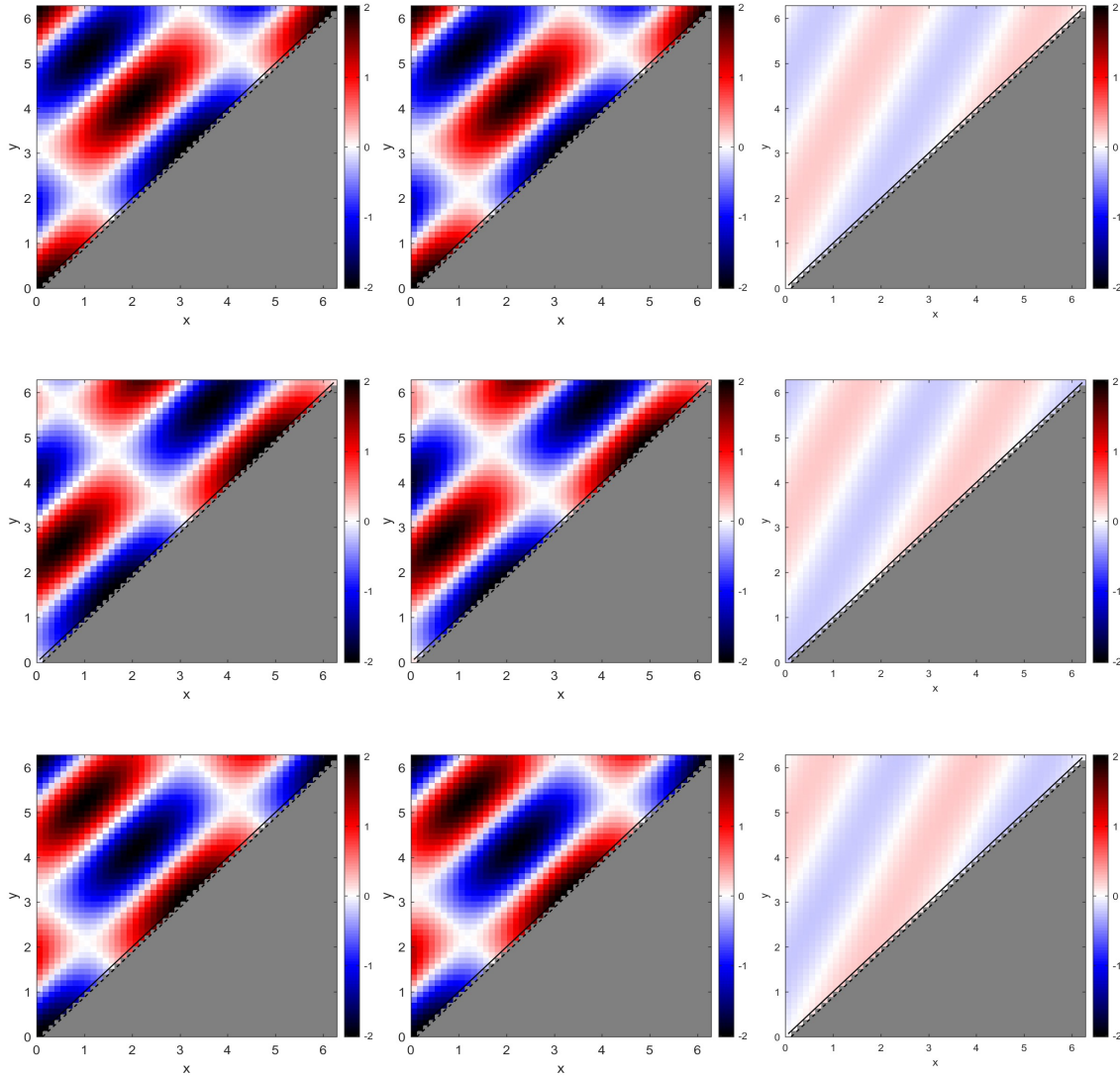


Figure 4.4.4: The total wave component of p for wave reflection at staircase boundaries with horizontal wavenumber $k = 1$, vertical wavenumber $l = -2$, grid spacing $h = 2\pi/50 \approx 0.1257$, at three different values t . The first column is the continuum solution, the second column is the discrete solution, and the third column is the error (i.e., continuum – discrete). First row is the solution at $t = 0$, second row at $t = \pi/2\omega$, and third row at $t = \pi/\omega$.

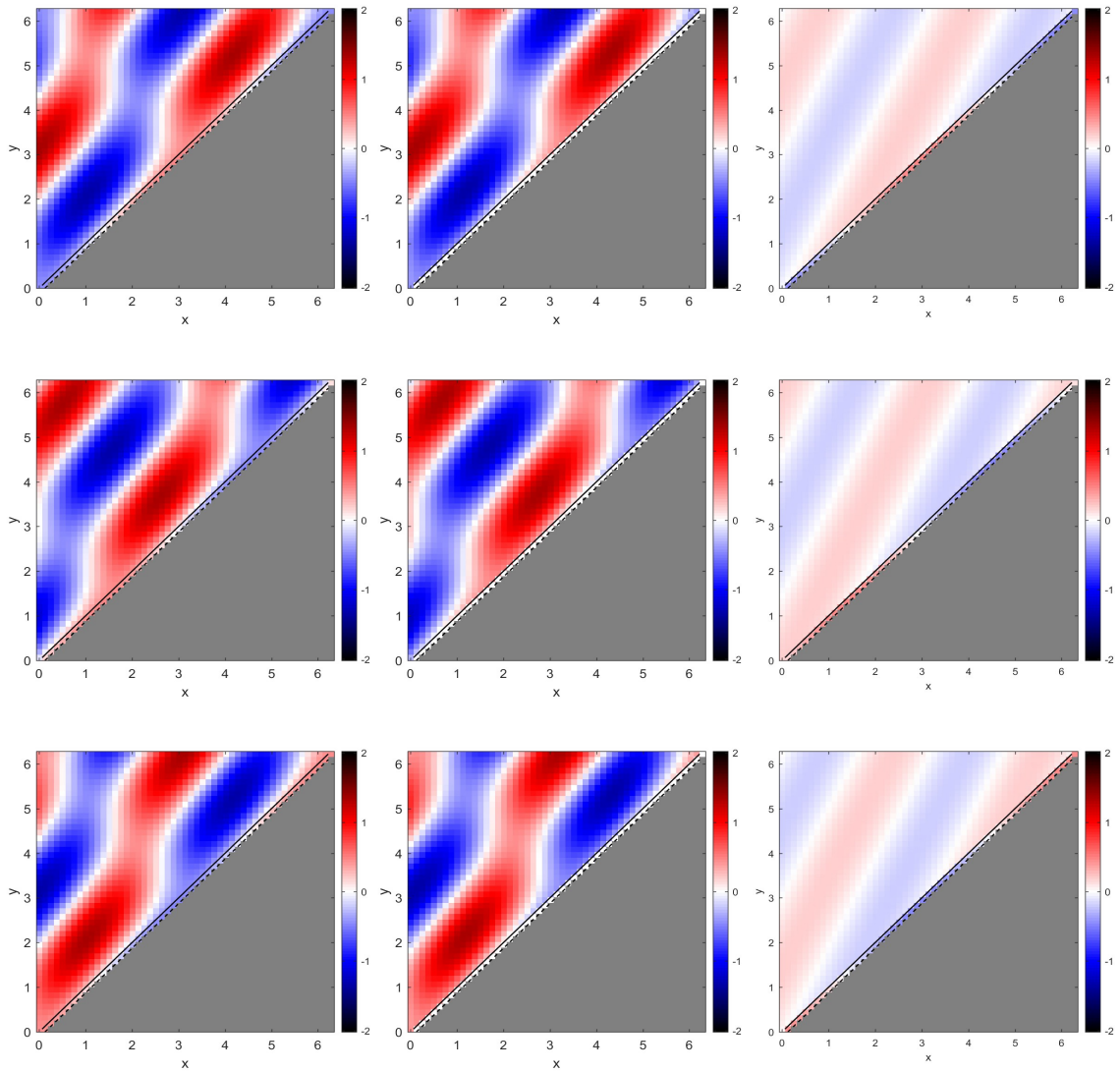


Figure 4.4.5: The total wave component of u for wave reflection at staircase boundaries with horizontal wavenumber $k = 1$, vertical wavenumber $l = -2$, grid spacing $h = 2\pi/50 \approx 0.1257$, at three different values t . The first column is the continuum solution, the second column is the discrete solution, and the third column is the error (i.e., continuum – discrete). First row is the solution at $t = 0$, second row at $t = \pi/2\omega$, and third row at $t = \pi/\omega$.

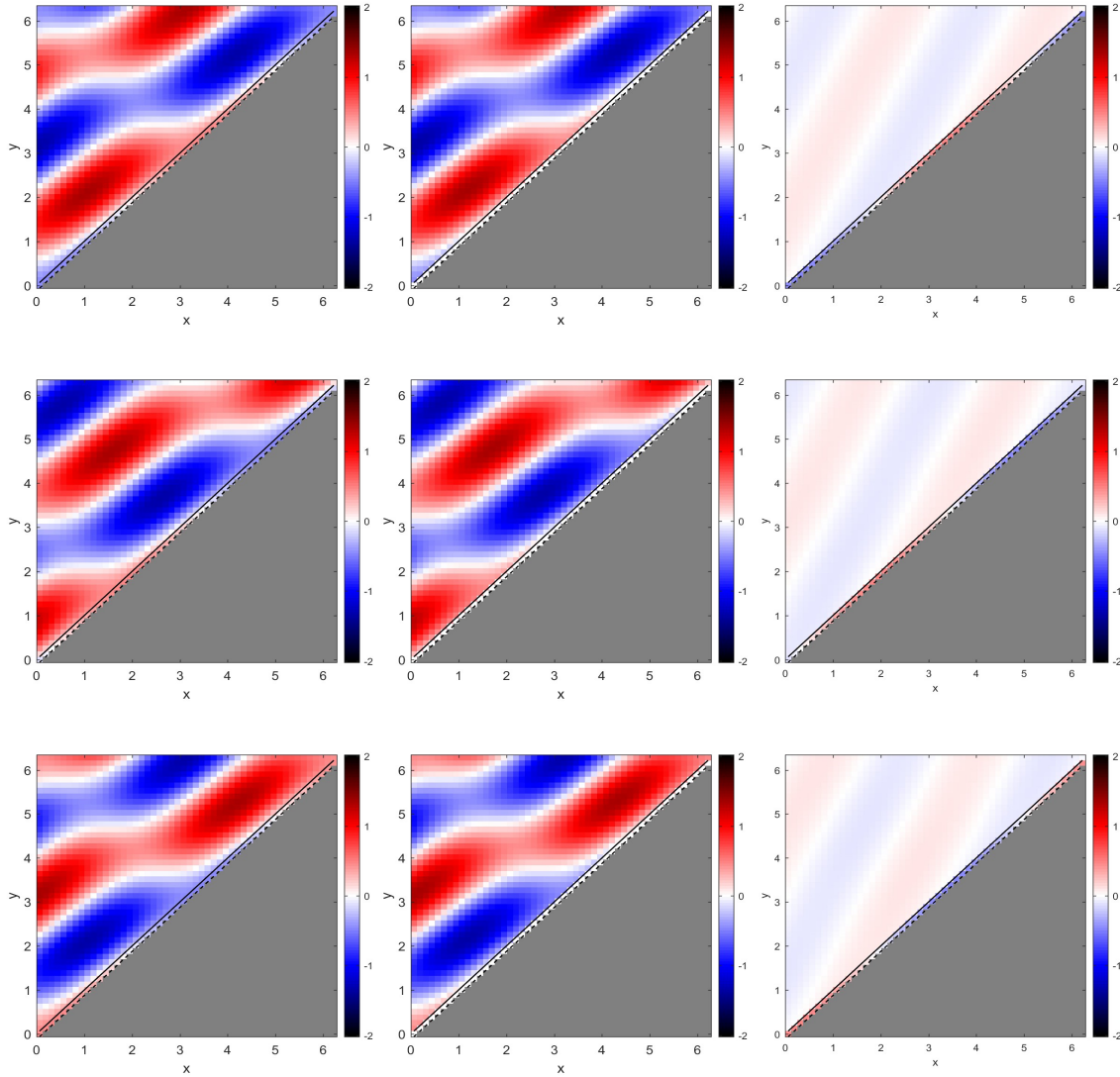


Figure 4.4.6: The total wave component of v for wave reflection at staircase boundaries with horizontal wavenumber $k = 1$, vertical wavenumber $l = -2$, grid spacing $h = 2\pi/50 \approx 0.1257$, at three different values t . The first column is the continuum solution, the second column is the discrete solution, and the third column is the error (i.e., continuum – discrete). First row is the solution at $t = 0$, second row at $t = \pi/2\omega$, and third row at $t = \pi/\omega$.

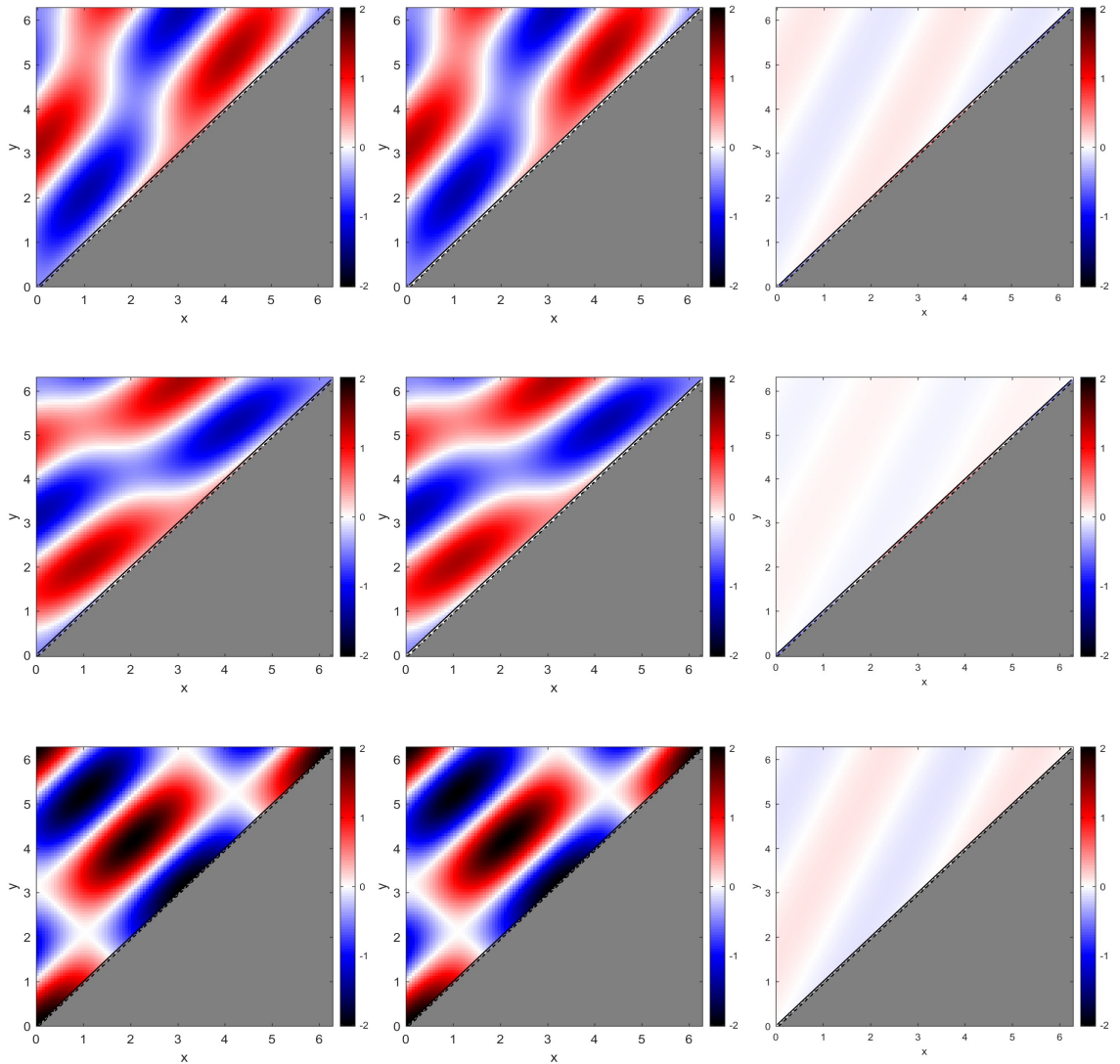


Figure 4.4.7: The solutions for u , v and p along with the error at $t = 0$ at high resolution ($h = \sqrt{2}/100 \approx 0.0628$). The first column is the continuum, the second column is the discrete, and the third column is the error (i.e., continuum – discrete).

φ in the phase, in terms of the grid spacing h , with

$$\varphi = (k^2 + l^2)h/(k - l),$$

where (k, l) is the wavevector of the incident wave. By comparison with evaluations of the exact phase error at finite h , we showed that our first-order asymptotic scaling for the phase error is remarkably accurate when $h \lesssim 0.5$, provided that the incident wave direction is not close to being parallel with the boundary. In that case, the phase errors are much larger (see Figure 4.4.2).

Consider, for example, the case when the incident wave is normal to the boundary, i.e., $l = -k$. Then the phase error $\varphi = kh$ (a result which we showed to be exact, even at finite h). For a minimally resolved wave with 4 grid points per wavelength (i.e., $4h = 2\pi/k \Rightarrow kh = \pi/2$), the phase error upon reflection is then $\pi/2$. So if the wave were to reflect off two such boundaries, then the phase error would be π (assuming that the phase errors were additive), and the wave would become completely out of phase with its continuum counterpart. However, note that the error in the wave frequency here would only be 19% (i.e., this might be considered to be an adequately resolved wave on the C-grid), since the continuum frequency $\omega_c^2 = 2k^2$ and discrete frequency

$$\begin{aligned} \omega_d^2 &= (8/h^2) \sin^2(kh/2) = (8k^2/(kh^2)) \sin^2(kh/2) \\ &= (8k^2)/(\pi/2)^2 \sin^2(\pi/4) = 2k^2(8/\pi^2) = (8/\pi^2)\omega_c^2. \end{aligned}$$

For what might be considered as a well-resolved wave with 16 grid points per wavelength (i.e., $16h = 2\pi/k \Rightarrow kh = \pi/8$), the phase error upon reflection is then $\pi/8$. This is clearly better, but only 8 reflections would be required for the wave to become completely out of phase with its continuum counterpart. The error in the wave frequency here would only be 1.3% (i.e., this might be considered to be a well resolved wave on the C-grid), since the

discrete frequency would be

$$\begin{aligned}\omega_d^2 &= (8/h^2) \sin^2(kh/2) = (8k^2/(kh^2)) \sin^2(kh/2) \\ &= (8k^2)/(\pi/8)^2 \sin^2(\pi/16) = 2k^2(256/\pi^2) \sin^2(\pi/16) = (8/\pi^2)\omega_c^2.\end{aligned}$$

The extension to better resolved waves is obvious. So, the effects of staircasing are clear, and how they could lead to serious errors in the phase of the wave after 1 (or, more likely, multiple) reflections.

Chapter 5

NUMERICAL SOLUTIONS: THE EFFECT OF STAIRCASE BOUNDARY

5.1 Introduction

This chapter is devoted to understanding possible implications of the previous mathematical analysis of the linearised wave equations

$$\frac{\partial u}{\partial t} = -\frac{\partial p}{\partial x}, \quad \frac{\partial v}{\partial t} = -\frac{\partial p}{\partial y}, \quad \frac{\partial p}{\partial t} + \frac{\partial u}{\partial x} + \frac{\partial v}{\partial y} = 0. \quad (5.1.1)$$

Here, we choose the same notation as in the chapters 3 and 4, where (u, v) denoted velocity of the flow while p the pressure.

In chapter 3, we discussed the wave propagation along a channel bounded by two parallel walls in the y direction. While in chapter 4, we discussed the waves reflection at a boundary. As we know, there are different kinds of error can be arise from the presented discrete solutions. As discussed chapter 3, we know that if wave goes along the boundary, it will slow down. And from chapter 4, we know that there could be a phase error from the reflection of wave at a boundary. But, the solution remains 'good', and just experiences

some effect of displacement. In this chapter, we investigate what will happen when both of these possible errors are combined together, from two numerical experiments on the C grid.

In the chapter 3 and 4, as grid spacing $h \rightarrow 0$, the discrete solutions were assessed with the continuum solutions in terms of the convergence. Here, the numerical experiments will be conducted and the error measurement is calculated from the continuum solution. For this reason, our numerical experiments are focused on the square and circular domain, since the continuum solution for these domains can be derived. Of course, numerical simulations can also be conducted for arbitrary domains, but this will not be discussed in this thesis.

The equations are discretised using the finite-difference method. It is arguably the simplest, easiest and efficient method to implement on the regular-spaced grid. However, this advantage offset by the curved boundaries and complex geometries where the finite-difference grid does not coincide with the boundary, i.e., staircases. As shown in previous two chapters, staircase boundaries introduce errors that affect the numerical solutions. However, those calculations were performed for time-harmonic oscillations. Thus, the emphasis of this chapter is to examine how does the error generated from the staircase boundaries influence the long-time dynamics of a wave sloshing in a closed domain.

Numerical simulations with staircase boundaries have been performed in various complex geometries. However, in such studies there is little or no quantification of the rate of convergence towards the continuum solution. For example, [13] has presented numerical simulations of room acoustic modelling over various complex geometries. By comparing finite-difference with staircase boundary and finite-volume method with fitted boundary, it was found that finite-volume method gave results much better than finite-difference method. However, at only one fixed resolution it is impossible to reach a conclusion on the rate of convergence of every method that has been performed. For electromagnetic waves, [67] studied two-dimensional wave reflection at a straight boundary tilted at some angle relative to x axis and a cylinder domain. Based on experiments at three different resolutions, convergence rates between 0.5 and 1 for the pressure in the L^2 norm is obtained. In the same

setting, [27, 33] reported errors of $O(h^{1/2})$ for pressure and velocity in the L^2 norm. In a different application, [29] estimate the rate of convergence for pressure in a linear wind-driven ocean circulation is between 1 and 2 in L^2 norm. By revisiting these problems we hope that we can understand how the model resolution effects on the staircase boundary, and reveal the convergence rate of finite-difference method as grid spacing $h \rightarrow 0$.

In setting up numerical solutions of two-dimensional acoustic wave equations, the equations are discretised such that finite-differencing is applicable to the Arakawa C-grid [6]. The analogous grid which is known as Yee-grid [71] is widely used in the modelling of acoustic and electromagnetic waves [34, 17]. The simplest application of this grid is to acoustic wave equations where velocity vector $\mathbf{u} = (u, v)$ is located at the boundary of a finite-difference cell and pressure p is located at the centre of cell. With this grid, it is easy to ensure that the resulting schemes conserve the fluid dynamics properties such as mass and energy, as discussed in Chapter 2.

5.2 Numerical Methods

We consider the same equations of motion (5.1.1) as considered in chapters previous two chapters and we solve these subject to $\mathbf{u} \cdot \mathbf{n} = 0$ and a specified initial condition, using a numerical method that works for an arbitrary closed domain.

5.2.1 Spatial discretization

As in previous chapters, we use the Arakawa C-grid, with nodes (u, v, p) staggered as shown in Figure 2.5.1. We choose the grid spacings $dx = dy = h$ for all experiments. We consider an arbitrary domain placed on top of this grid, and we then construct a grid on a quadrilateral of extend $2l_x \times 2l_y$ that just extends beyond the specified domain, where $2l_x = n_x h$ and $2l_y = n_y h$ for some integers n_x and n_y .

Of course, some of these cells will be retained in the numerical domain, and others will not. There are several ways to decide which cells are retained:

1. demand that the centre of the cell lies within the (continuum) domain,
2. demand that all four corners of the cell lie within the (continuum) domain,
3. demand that at least one corner of the cell lies within the (continuum) domain,
4. demand that some fractional area (e.g., 50%) of the cell lies within the (continuum) domain.

Figure 5.2.1 shows two different grid generations according to rules (i) and (ii), for aligned squares (a and b), unaligned squares (c and d), and a circle (e and f). Of course, there is no difference between (i) and (ii) for the aligned squares (a) and (b). For the others, it seems that (i) offers a better fit. So we will use (i) in this chapter, except for some circular domain experiments, to be discussed later.

All variables are stored as matrices. The matrix for u is $(n_x + 1) \times n_y$, that for v is $n_x \times (n_y + 1)$, and that for the pressure p is $n_x \times n_y$. In our experiments, we are using the same second-order centred differences as first discussed in Chapter 2, to evaluate the derivative in our model. For example, the staggered C-grid finite-difference formula for the derivative approximation

$$\frac{\partial p_{m,n}}{\partial x} = \frac{p(x_{m+1/2,n}) - p(x_{m-1/2,n})}{h} + O(h^2) \quad (5.2.1)$$

This approximation is naturally evaluated at u nodes.

As the variables are staggered, (5.1.1) are written in matrix form:

$$\frac{\partial U}{\partial t} = -D_{pu}P, \quad \frac{\partial V}{\partial t} = -PD_{pv}, \quad \frac{\partial P}{\partial t} + D_{up}U + VD_{vp} = 0, \quad (5.2.2)$$

where U, V, P are the matrices of the variables. Thus, we have four different differentiation matrices for the derivatives in our model. Mathematically, differentiation matrix D_{pu} is written as

$$\frac{\partial p}{\partial x} = \frac{1}{h} \begin{bmatrix} -1 & 1 & 0 & 0 & 0 \\ -1 & 1 & 0 & 0 & 0 \\ 0 & -1 & 1 & 0 & 0 \\ \vdots & \dots & \ddots & \ddots & \\ 0 & \dots & 0 & -1 & 1 \end{bmatrix}_{(n_x+1) \times n_x} \begin{bmatrix} p_{11} & p_{12} & \dots & p_{1n_y} \\ p_{21} & p_{22} & \dots & \vdots \\ p_{31} & p_{32} & \dots & \vdots \\ \vdots & \dots & \dots & \\ p_{n_x 1} & p_{n_x 2} & \dots & p_{n_x n_y} \end{bmatrix}. \quad (5.2.3)$$

So that, the output of this differentiation matrix is $(n_x + 1) \times n_y$. This will give the results on the u nodes. We note that, the top and bottom line are not needed, since u at x_1 and x_{n_x+1} located outside of our domain.

The second differentiation matrix is the differentiation matrix of velocity u on the p -grid which is written as

$$\frac{\partial u}{\partial x} = \frac{1}{h} \begin{bmatrix} -1 & 1 & 0 & 0 & 0 \\ 0 & -1 & 1 & 0 & 0 \\ 0 & 0 & -1 & 1 & 0 \\ \vdots & \dots & \ddots & \ddots & \\ 0 & \dots & 0 & -1 & 1 \end{bmatrix}_{n_x \times (n_x+1)} \begin{bmatrix} u_{11} & u_{12} & \dots & u_{1n_y} \\ u_{21} & u_{22} & \dots & \vdots \\ u_{31} & u_{32} & \dots & \vdots \\ \vdots & \dots & \dots & u_{n_x n_y} \\ u_{(n_x+1)1} & u_{(n_x+1)2} & \dots & u_{(n_x+1)n_y} \end{bmatrix}, \quad (5.2.4)$$

where, as for (5.2.3), again the differentiation matrix with respect to x is operated at the front.

Note that, we also will have differentiation matrices operating at the back when evaluating y -derivatives of variables. For example to evaluate $\partial v / \partial y$, it can be calculated on the p -grid

using the matrix form

$$\frac{\partial v}{\partial y} = \begin{bmatrix} v_{11} & v_{12} & \dots & v_{1(n_y+1)} \\ v_{21} & v_{22} & \dots & \vdots \\ v_{31} & v_{32} & \dots & \vdots \\ \vdots & \dots & \dots & v_{(n_x-1)(n_y+1)} \\ v_{n_x1} & v_{n_x2} & \dots & v_{n_x(n_y+1)} \end{bmatrix} \frac{1}{h} \begin{bmatrix} -1 & 0 & 0 & 0 & 0 \\ 1 & -1 & 0 & 0 & 0 \\ 0 & 1 & -1 & 1 & 0 \\ \vdots & \dots & & \ddots & \ddots \\ 0 & \dots & 0 & 0 & 1 \end{bmatrix}_{(n_y+1) \times n_y} \quad (5.2.5)$$

The last differentiation matrix is

$$\frac{\partial p}{\partial y} = \begin{bmatrix} p_{11} & p_{12} & \dots & p_{1n_y} \\ p_{21} & p_{22} & \dots & \vdots \\ p_{31} & p_{32} & \dots & \vdots \\ \vdots & \dots & \dots & \vdots \\ p_{n_x1} & p_{n_x2} & \dots & p_{n_xn_y} \end{bmatrix} \frac{1}{h} \begin{bmatrix} -1 & 0 & 0 & 0 & 0 \\ 1 & -1 & 0 & 0 & 0 \\ 0 & 1 & -1 & 1 & 0 \\ \vdots & \dots & & \ddots & \ddots \\ 0 & \dots & 0 & 0 & 1 \end{bmatrix}_{n_y \times (n_y+1)} \quad (5.2.6)$$

With these four differentiation matrices, we only apply $\partial U/\partial t$, $\partial V/\partial t$ for nodes that are inside the domain only. This calculation can be done via a pointwise element multiplication in MATLAB (i.e., `.*`), rather than a matrix multiplication. So

$$\partial U/\partial t \Rightarrow M_u .* \partial U/\partial t, \quad \partial V/\partial t \Rightarrow M_v .* \partial V/\partial t, \quad (5.2.7)$$

with $\partial U/\partial t$ and $\partial V/\partial t$ as calculated above. Here M_u and M_v are matrices of the same size as U and V , with entries of either 0 or 1. A 0 entry means a boundary nodes and thus no flow at that grid point, while a 1 means an active node within the domain.

5.2.2 Temporal discretization

In our experiment, the main objective is to measure the effects of spatial differencing on wave dynamics in our numerical model. So, we want time differencing errors to be small in comparison. Therefore, we time step via a method that offers high accuracy in time. There are a variety of possible choices, as discussed for example by [25]. We choose the fourth-order Runge-Kutta (RK) scheme. We choose the fourth-order Runge-Kutta (RK) scheme with $\Delta t < 0.01$ [or whatever], implying errors of $O(\Delta t^4) \leq 10^{-8}$; then the temporal differencing errors should be negligible compared with spatial differencing errors, and we can exclusively focus on the latter.

Throughout our experiments, in which the grid spacing h will be changed to examine spatial convergence, we need to choose the time-step Δt to ensure that our scheme remains stable. The concept of stability is discussed for several standard time-stepping schemes in Appendix A. For 4th-order RK, the stability condition can be expressed as

$$\lambda \Delta t \leq 2\sqrt{2}, \quad (5.2.8)$$

where λ is the the modulus of the largest (imaginary) eigenvalue of the governing set of equations. This can be calculated by using a simple von Neumann stability analysis. To do this, we seek solutions $u_{mn} = \text{Re}(\hat{u}(t) \exp(ikx_m + ily_n))$, $v_{mn} = \text{Re}(\hat{v}(t) \exp(ikx_m + ily_n))$, $p_{mn} = \text{Re}(\hat{p}(t) \exp(ikx_m + ily_n))$, so that the governing equations become

$$\frac{d\hat{u}}{dt} = -iK\hat{p}, \quad \frac{d\hat{v}}{dt} = -iL\hat{p}, \quad \frac{d\hat{p}}{dt} + iK\hat{u} + iL\hat{v} = 0, \quad (5.2.9)$$

where, on the C-grid,

$$iK = \frac{\exp(ikh/2) - \exp(-ikh/2)}{h} = \frac{2i \sin(kh/2)}{h} \Rightarrow K = \frac{2 \sin(kh/2)}{h}; \quad (5.2.10)$$

likewise $L = \frac{2}{h} \sin(lh/2)$.

So the equations may be written as

$$\frac{d}{dt} \begin{pmatrix} \hat{u} \\ \hat{v} \\ \hat{p} \end{pmatrix} = \begin{pmatrix} 0 & 0 & -iK \\ 0 & 0 & -iL \\ -iK & -iL & 0 \end{pmatrix} \begin{pmatrix} \hat{u} \\ \hat{v} \\ \hat{p} \end{pmatrix}, \quad (5.2.11)$$

and the relevant eigenvalues are then

$$\begin{vmatrix} -i\lambda & 0 & -iK \\ 0 & -i\lambda & -iL \\ -iK & -iL & -i\lambda \end{vmatrix} = 0 \Rightarrow \lambda = 0, \lambda^2 = \frac{4}{h^2} (\sin^2(kh/2) + \sin^2(lh/2)). \quad (5.2.12)$$

The largest value of λ comes for a grid scale wave with $2\pi/k = 2h$ which implies $kh = \pi$, and likewise $lh = \pi$. So

$$\lambda_{max}^2 = \frac{4}{h^2}(1 + 1) = \frac{8}{h^2} \Rightarrow \lambda_{max} = \frac{2\sqrt{2}}{h}. \quad (5.2.13)$$

Thus the RK4 stability condition becomes

$$\frac{2\sqrt{2}\Delta t}{h} \leq 2\sqrt{2} \Rightarrow \Delta t \leq h. \quad (5.2.14)$$

We respect this stability condition for all of our simulations.

5.3 Waves in an aligned square

In this section we analyse numerical simulations of a sloshing mode in a square domain, with the domain boundaries aligned with the C-grid. Our numerical method thus become second-order in space. Having established the relevant continuum solution in section 5.3.1, we measure (in section 5.3.2) the deviation of the numerical solution from the continuum solution, and show that this error is indeed second-order in space, for each of u , v and

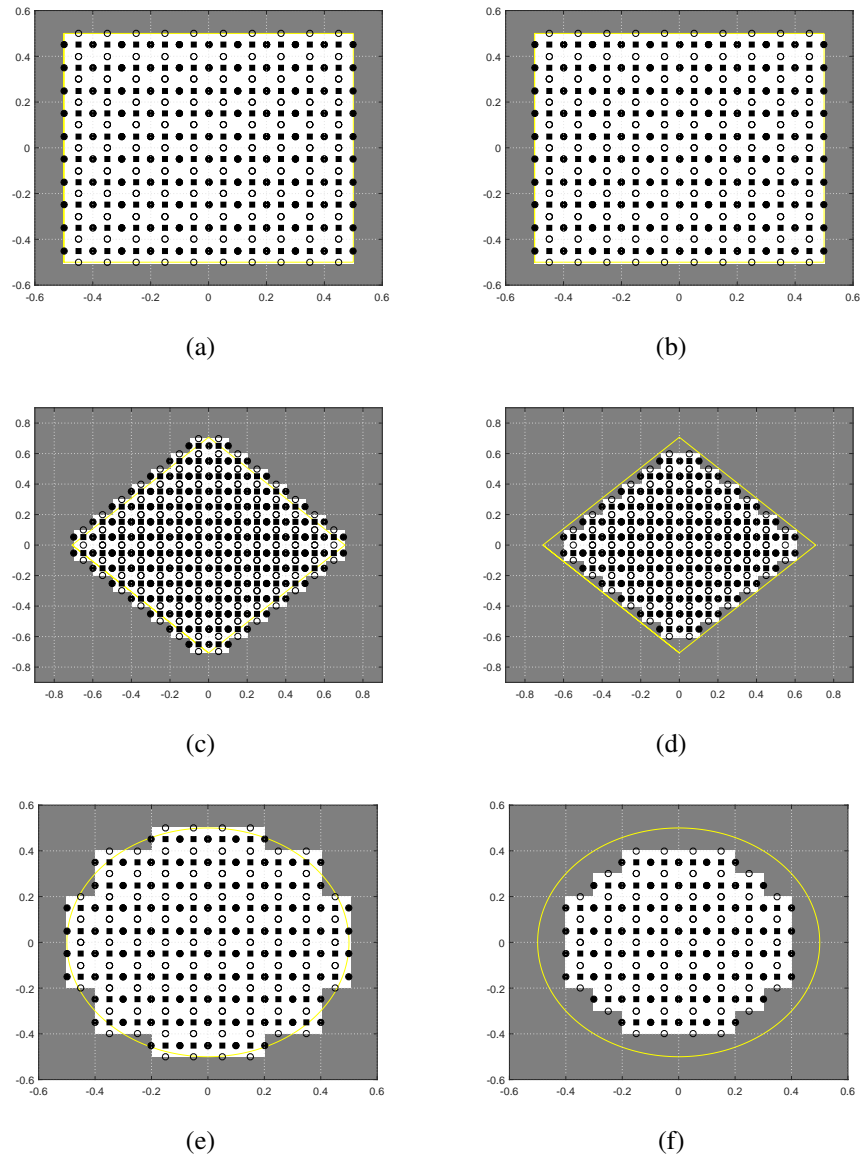


Figure 5.2.1: Example of grid generation. The active grid cells on the left column are activated by cell-centre condition, while the right column by the four corner condition. Black circles represent u nodes, white circles represent v nodes, and black squares represent p nodes.

p . These results, although not unexpected, set the context for the numerical simulations of section 5.4 (tilted square) and section 5.6 (circle) where the boundary and grid are not aligned.

5.3.1 Continuum solutions

We consider the acoustic wave equations (5.1.1) (or non-rotating shallow water equations).

We consider time-harmonic solutions of the form

$$(u, v, p) = \text{Re}((\hat{u}, \hat{v}, \hat{p})\exp(-i\omega t)), \quad (5.3.1)$$

for which we obtain

$$-i\omega\hat{u} = -\frac{\partial\hat{p}}{\partial x}, \quad -i\omega\hat{v} = -\frac{\partial\hat{p}}{\partial y}, \quad -i\omega\hat{p} + \frac{\partial\hat{u}}{\partial x} + \frac{\partial\hat{v}}{\partial y} = 0. \quad (5.3.2)$$

We solve these in a square domain $-l_x < x < l_x$, $-l_y < y < l_y$, subject to $\hat{u} = 0$ at $-l_x, l_x$ and $\hat{v} = 0$ at $-l_y, l_y$.

Eliminating \hat{u} and \hat{v} , we obtain

$$\hat{p} + \frac{1}{\omega^2} \left(\frac{\partial^2\hat{p}}{\partial x^2} + \frac{\partial^2\hat{p}}{\partial y^2} \right) = 0. \quad (5.3.3)$$

To solve this equation, we will apply a famous and useful method which is separation of variables. We first write the solution of (5.3.3) in the form

$$\hat{p}(x, y) = X(x)Y(y), \quad (5.3.4)$$

where X is a function of only x , and Y is a function of only y . By substituting (5.3.4) into

(5.3.3), we have

$$X(x)Y(y) + \frac{1}{\omega^2} (X''Y(y) + X(x)Y'') = 0, \quad (5.3.5)$$

and dividing by XY yield

$$\omega^2 + \frac{X''}{X} + \frac{Y''}{Y} = 0. \quad (5.3.6)$$

The next step is the key in the process of separation of variables. We are going to say that each of the terms in (5.3.6) is a constant because the second term is a function of only x and the third term is a function of only y . The basis of the process in separation of variables is the equation $f(x) = g(y)$, with x and y independent variables, is an identity if both functions are the same constant. Thus, we must have

$$\frac{X''}{X} = -k^2 \quad \Rightarrow \quad \frac{Y''}{Y} = k^2 - \omega^2 = -l^2. \quad (5.3.7)$$

The constant k^2 is called a separation constant. Now, we need to solve the ordinary differential equation (ODEs) (5.3.7) separately. We solve the ODE for x first. The general solution of (5.3.7) for X is

$$X(x) = A \cos(k(x + l_x)) + B \sin(k(x + l_x)). \quad (5.3.8)$$

The boundary conditions are $u = 0$ at $x = -l_x$ and $x = l_x$. Imposing the condition at $x = -l_x$ gives

$$u = 0 \Rightarrow \hat{u} = 0 \Rightarrow \frac{\partial \hat{p}}{\partial x} = 0 \Rightarrow X'Y = 0 \Rightarrow X'(-l_x) = 0. \quad (5.3.9)$$

From (5.3.8) we also have

$$X'(x) = -Ak \sin(k(x + l_x)) + Bk \cos(k(x + l_x)), \quad (5.3.10)$$

and with $x = -l_x$ we get $B = 0$. So, the general solution now is

$$X(x) = A \cos(k(x + l_x)). \quad (5.3.11)$$

Imposing $u = 0$ at $x = l_x$, imply

$$u = 0 \Rightarrow \hat{u} = 0 \Rightarrow \frac{\partial \hat{p}}{\partial x} = 0 \Rightarrow X'Y = 0 \Rightarrow X'(l_x) = 0, \quad (5.3.12)$$

and from (5.3.11) we have

$$X'(x) = -Ak \sin(k(x + l_x)), \quad (5.3.13)$$

and to satisfies the boundary condition $X'(l_x) = 0$ we now have eigenvalue condition, i.e.,

$$X'(l_x) = 0 \Rightarrow -Ak \sin(2kl_x) = 0 \Rightarrow \sin(2kl_x) = m\pi \Rightarrow k = \frac{m\pi}{2l_x}, \quad (5.3.14)$$

where m is an integer. Thus, the final solution of (5.3.7) for $X(x)$ is

$$X_m(x) = A_m \cos(k(x + l_x)), \text{ where } k = \frac{m\pi}{2l_x}, \quad (5.3.15)$$

Now, lets solve (5.3.7) for y variable. The ODE now is rewritten as

$$Y'' + l^2 Y = 0, \quad \text{where } l^2 = \frac{\omega^2}{c^2} - k^2. \quad (5.3.16)$$

The general solution of this ODE is

$$Y(y) = C \cos(l(y + l_y)) + D \sin(l(y + l_y)). \quad (5.3.17)$$

The no normal flow boundary condition at the upper and lower wall imply that $v = 0$ at

$y = -l_y$ and l_y . Then, imposing the lower wall boundary condition we have

$$v = 0 \Rightarrow \hat{v} = 0 \Rightarrow \frac{\partial \hat{p}}{\partial y} = 0 \Rightarrow XY' = 0 \Rightarrow Y'(-l_y) = 0, \quad (5.3.18)$$

which give

$$Y'(-l_y) = -Cl \sin(l(-l_y + l_y)) + Dl \cos(l(-l_y + l_y)) = 0 \Rightarrow D = 0. \quad (5.3.19)$$

Then, the solution now becomes

$$Y(y) = C \cos(l(y + l_y)). \quad (5.3.20)$$

Next, imposing the upper wall boundary condition, i.e., $v = 0$ at $y = l_y$, we have $Y'(l_y) = 0$, implies

$$Y'(l_y) = -Cl \sin(l(2l_y)) = 0 \Rightarrow \sin(l(2l_y)) = \sin(n\pi) \Rightarrow l = \frac{n\pi}{2l_y}, \quad (5.3.21)$$

where n is an integer. Thus, the solution for (5.3.7) for $Y(y)$ is

$$Y_n(y) = C \cos\left(\frac{n\pi}{2l_y}(y + l_y)\right), \quad (5.3.22)$$

Combining (5.3.15) and (5.3.22) into (5.3.6) yield

$$\begin{aligned} \hat{p} = XY &= A \cos\left(\frac{m\pi}{2l_x}(x + l_x)\right) \cdot C \cos\left(\frac{n\pi}{2l_y}(y + l_y)\right) \\ &= F \cos(k(x + l_x)) \cdot \cos(l(y + l_y)), \end{aligned} \quad (5.3.23)$$

where $F = AC$ is an arbitrary constant. By differentiating (5.3.23) with respect to x and y ,

we have

$$\frac{\partial \hat{p}}{\partial x} = -Fk \sin(k(x + l_x)) \cos(l(y + l_y)), \quad \text{and} \quad (5.3.24)$$

$$\frac{\partial \hat{p}}{\partial y} = -Fl \cos(k(x + l_x)) \sin(l(y + l_y)). \quad (5.3.25)$$

By using (5.3.1), we can derive the solution for \hat{u} and \hat{v} . The solution of \hat{u} is

$$\begin{aligned} -i\omega \hat{u} &= -\frac{\partial \hat{p}}{\partial x} = Fk \sin(k(x + l_x)) \cos(l(y + l_y)), \\ \Rightarrow \hat{u} &= \frac{iFk}{\omega} \sin(k(x + l_x)) \cos(l(y + l_y)), \end{aligned} \quad (5.3.26)$$

while solution of \hat{v} is

$$\begin{aligned} -i\omega \hat{v} &= -\frac{\partial \hat{p}}{\partial y} = Fl \cos(k(x + l_x)) \sin(l(y + l_y)), \\ \Rightarrow \hat{v} &= \frac{iFl}{\omega} \cos(k(x + l_x)) \sin(l(y + l_y)). \end{aligned} \quad (5.3.27)$$

Thus, the full solution for a time harmonic standing wave in a rectangle is

$$u(x, y, t) = \text{Re} \left(\frac{iFk}{\omega} \sin(k(x + l_x)) \cos(l(y + l_y)) \exp(-i\omega t) \right), \quad (5.3.28a)$$

$$v(x, y, t) = \text{Re} \left(\frac{iFl}{\omega} \cos(k(x + l_x)) \sin(l(y + l_y)) \exp(-i\omega t) \right), \quad (5.3.28b)$$

$$p(x, y, t) = \text{Re} \left(F \cos(k(x + l_x)) \cos(l(y + l_y)) \exp(-i\omega t) \right), \quad (5.3.28c)$$

with ω satisfies the dispersion relation between k and l , which is written as

$$\omega^2 = k^2 + l^2, \quad \text{where } k = \frac{m\pi}{2l_x}, \quad \text{and } l = \frac{n\pi}{2l_y}. \quad (5.3.29)$$

5.3.2 Numerical solutions

We now present and analyse numerical solutions of (5.1.1). We initialise, at $t = 0$, with the solution (5.3.28) with $u = v = 0$ but $p \neq 0$. This leads to a freely oscillating mode, bouncing back and forth between the domain boundaries. We also

- choose a domain with $l_x = l_y = 1/2$ (i.e., $-1/2 < x < 1/2$, $-1/2 < y < 1/2$);
- choose mode $m = 2$ in x , so that $k = 2\pi$, and mode $n = 1$ in y , so that $l = \pi$, (although we also checked the behaviour for other values of m and n);
- the frequency $\omega = \sqrt{5}\pi$;
- set the arbitrary constant $F = 1$;
- note that the amplitude of the oscillation in u is $Fk/\omega = 2\pi/\sqrt{5}\pi = 2/\sqrt{5} \approx 0.8944$ and that in v is $Fl/\omega = \pi/\sqrt{5}\pi = 1/\sqrt{5} \approx 0.4472$.

Since $\omega = \sqrt{5}\pi$, the period of the wave is $T = 2/\sqrt{5} \approx 0.8944$. The simulations are performed up to $t = 10T$, and with grid spacings $h = 0.1, 0.05, 0.02, 0.01$ and 0.005 , which correspond to 10, 20, 50, 100 and 200 grid cells in the x - and y -direction. The time-step is adjusted to satisfy (5.2.14).

Some typical solutions – at $h = 0.01$ and $dt = 0.005$ – are shown in Figures 5.3.1 (for p), 5.3.2 (for u), and 5.3.3 (for v). We are showing the last oscillation period, i.e., $9T < t < 10T$. It is clear that the numerical solutions remain in excellent agreement with the continuum solutions, at least out to $t = 10T$. It is also the case, as shown in Figure 5.3.4, that the code is also conserving energy and mass to a very high degree, as expected.

We can measure the error in each of (u, v, p) by calculating

$$E(t) = \max |\mu - \mu_{\text{num}}|, \quad (5.3.30)$$

where \max denotes the maximum value taken over the entire domain, excluding boundary nodes. Over the period $9T < t < 10T$ shown in Figure 5.3.5, the errors are small – less than 0.01. The full time evolution of the errors over $0 < t < 10$ is shown in Figure 5.3.5. Note that the size of the errors scales with the amplitude of modes: $p_{\max} = 1$, $u_{\max} = 0.8944$, $v_{\max} = 0.4472$. However, the reason for the growth of the errors is not clear from this graph alone: is it due to an amplitude error or a phase error? We can try to answer this by plotting a time series of $\max|p|$ versus time, as shown in Figure 5.3.6. However, there is no obvious phase or amplitude error in this Figure.

The reason for this slow increase in the error becomes clear by considering simulations at lower spatial resolution. We demonstrate this by showing results at $h = 0.1$. Shown in Figure 5.3.7 is the evolution of p over $0 < t < T$, and in Figure 5.3.8 the evolution of p over $9T < t < 10T$. The evolutions of u and v (not shown) are similar in nature. Even at $t = 3T/4$ it is possible to see a small error in p : when it should be zero everywhere, it is not suggesting a phase error. By $9T < t < 10T$, the errors are of order unity, with the shape of p being fine (i.e., no loss of coherence), but the phase being completely wrong.

This phase error is shown more clearly in Figure 5.3.9. This shows how $\max|p|$ evolves, with the numerically determined maxima in this lagging those of the continuum solution, i.e., the wave frequency is too small in the numerical solutions. There are similar pictures for $|u|$ and $|v|$ (not shown). This leads to the error plot shown in Figure 5.3.10, showing that errors of order unity are inevitable at moderately large times. For yet larger times, we would expect the errors to eventually decrease, as the numerical and continuum solutions slowly drift back into phase. Despite these errors, note that the C-grid code is still doing an excellent job conserving energy and mass, as shown in Figure 5.3.11.

We also carried out some experiments with various values of resolutions by changing the grid spacing h ranging from $0.01 < h < 0.1$, with the time-step dt fixed at $dt = 0.01$, so that the time-differencing error is same in all cases. For each grid spacing we also recorded the maximum error over $0 < t < T$ for each variable as can be seen in Figure 5.3.12.

In the usual way, the error is calculated from (5.3.30). In the figure, we take \log_{10} for each maximum error and plot them as function of $\log_{10} h$. By fitting the line $\log_{10} E = \log_{10} Ah^n$, we can calculate A and n numerically. Here, n is the slope of the straight line which represents the rate of convergence. In all of the convergence analyses, we fixed dt to be constant. This will not effects our analyses because we only used the higher order RK4, so that the time differencing error is the same in all cases, and negligible compared with the spatial differencing error. We used maximum norm, (i.e., maximum error over whole run), and L_2 norm (i.e., the spatially integrated norm) to fit the line. As can be seen in the figure, it is clear that both maximum errors decrease as the grid spacing h decreases. The slope of each line in the figure is summarised in Table 5.1. Here we obtained slope 1.89 for p , where we interpret this as slope 2, a second-order convergence in h .

In order to confirm the slope of convergence is consistent with second-order convergence, we also calculated several sets of confidence interval of the slope. This interval is an excellent way to specify our convergence analysis is precise. Table 5.2 shows the 95%, 90%, 75% and 50% confidence intervals for the slope of convergence. As can be seen, as we decrease the range, the interval is narrowed down to the slope of convergence. The wider the interval, the more confident we can be that it contains the slope of convergence. From the table, all the intervals are certainly include 2.0, which shows that the fitted slope 1.89 consistent with the second order convergence. This is the expected result since we have used a second-order centred finite-difference formulation. However, in all analyses, we only include the 95% confidence interval, that is we can say that the slope of convergence is 95% precise.

We also showing the maximum error for u , v and p with $h = 0.01$ at $dt = 0.01$ in Figure 5.3.13. It is clear that the maximum error is tiny (i.e., 0.0006), as illustrated in Figure 5.3.12(b). The analysis in this section is important because it can be used as a comparison to the next setting. In the next section, we will show the results where the square is tilted 45° from the grid. The question is, can we recover the same result for that setting?

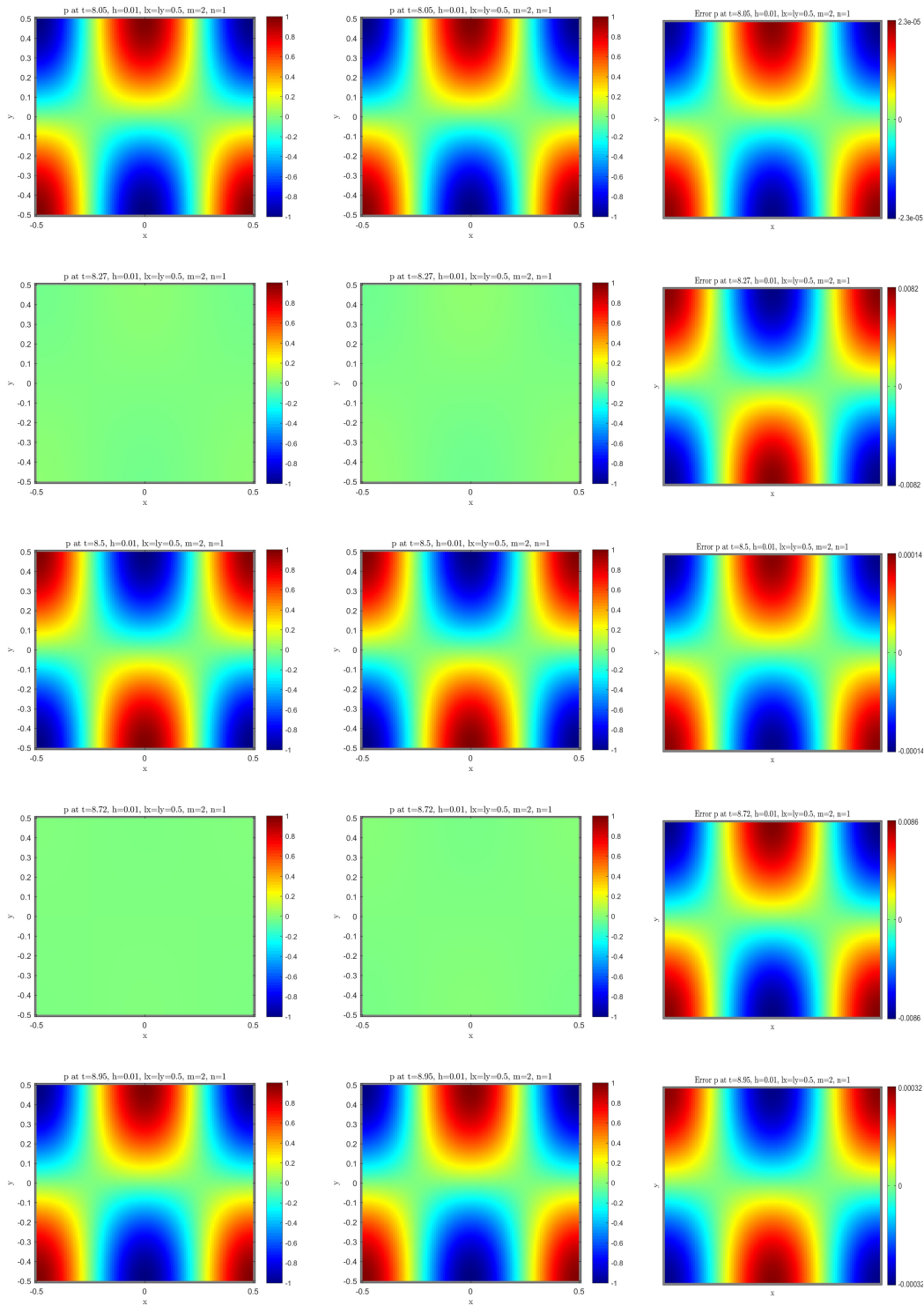


Figure 5.3.1: The numerical solutions of p for aligned square at $t = 9T, 9.25T, 9.5T, 9.75T, 10T$, with $h = 0.01$ and $dt = 0.005$. Left column: continuum solutions. Centre column: numerical solutions. Right column: error (i.e., continuum–numerical).

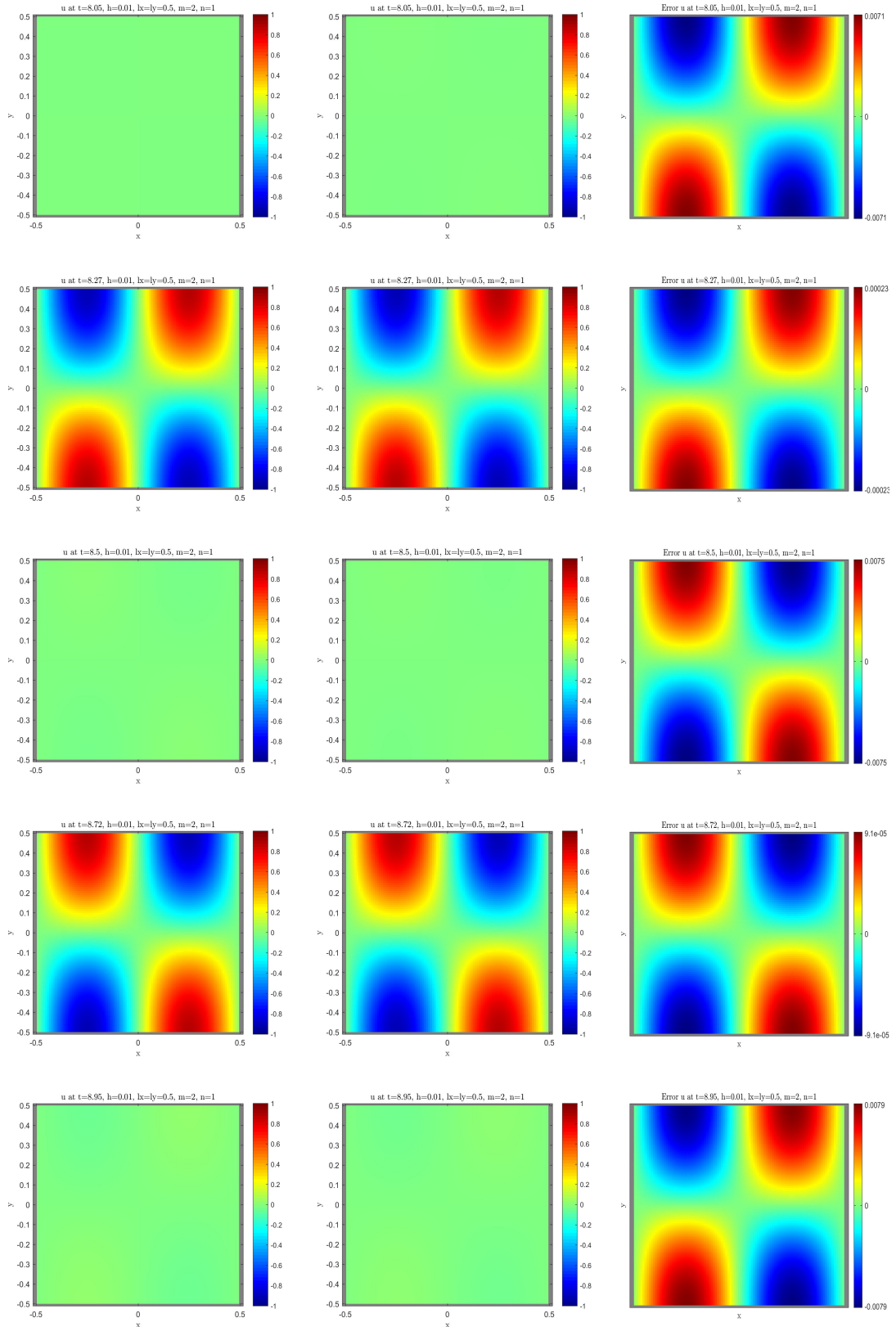


Figure 5.3.2: The numerical solutions of u at $t = 9T, 9.25T, 9.5T, 9.75T, 10T$, with $h = 0.01$ and $dt = 0.005$. Left column: continuum solutions. Centre column: numerical solutions. Right column: error (i.e., continuum-numerical).

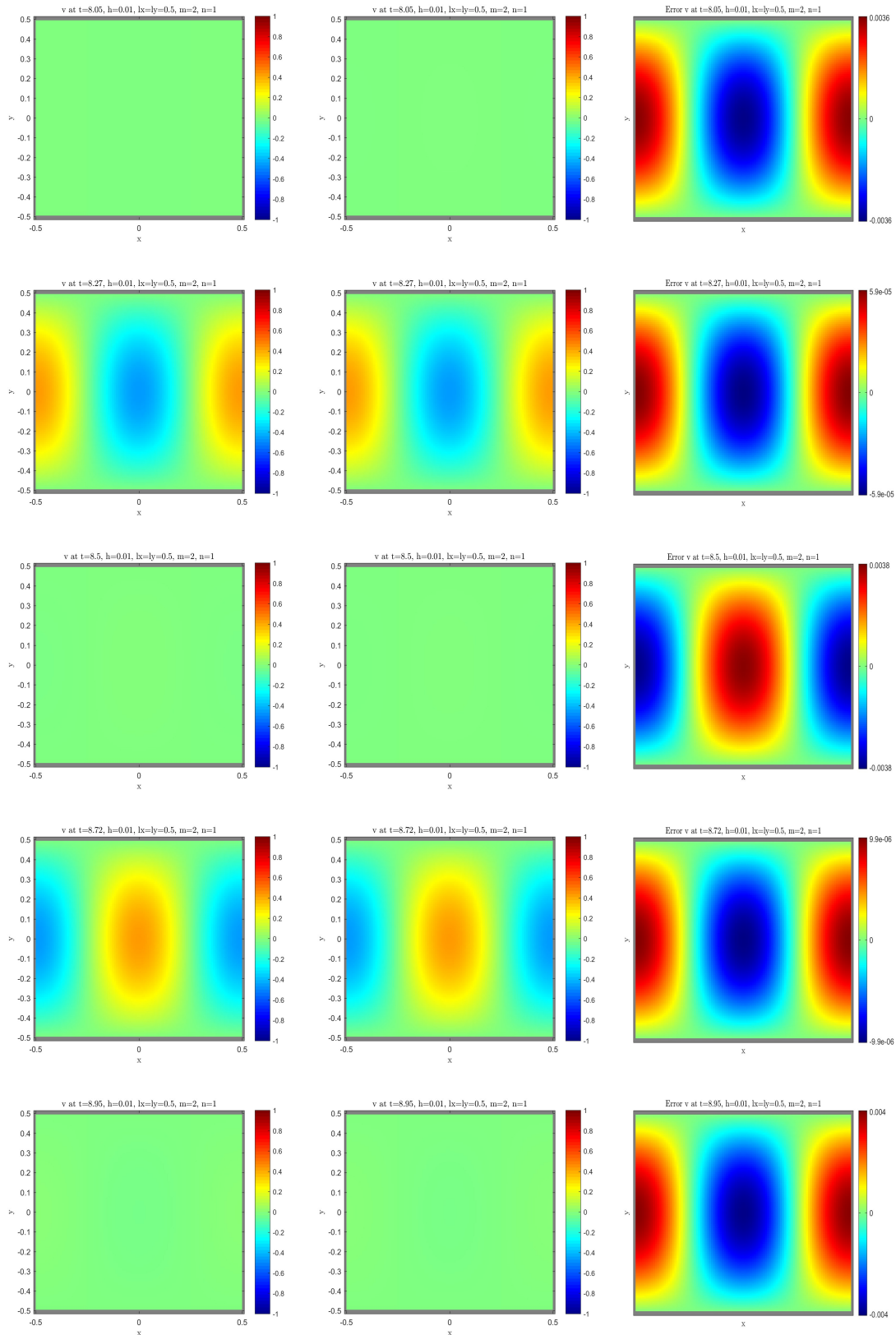


Figure 5.3.3: The numerical solutions for v at $t = 9T, 9.25T, 9.5T, 9.75T, 10T$, with $h = 0.01$ and $dt = 0.005$. Left column: continuum solutions. Centre column: numerical solutions. Right column: error (i.e., continuum-numerical).

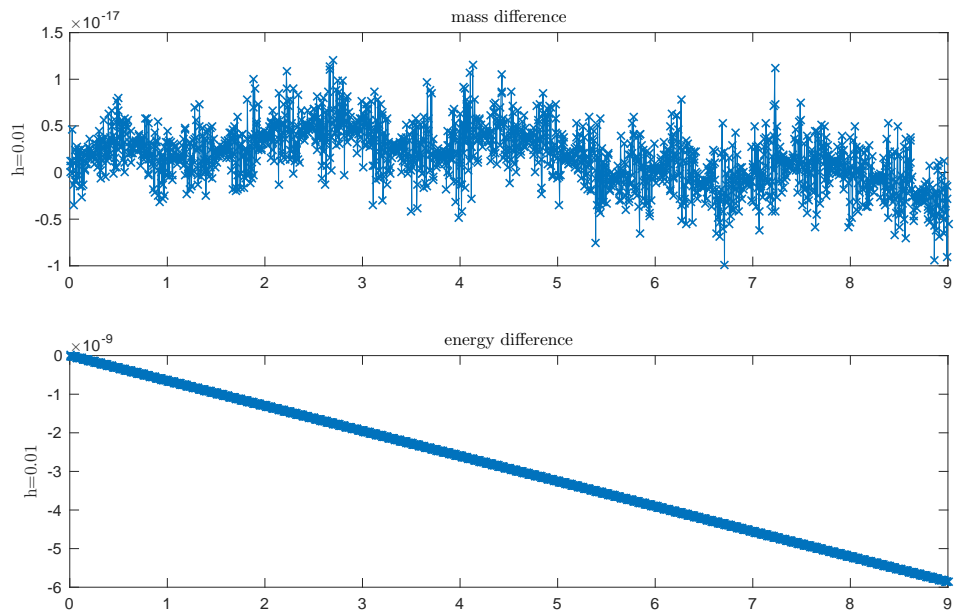


Figure 5.3.4: Mass difference and energy difference for aligned square domain, with $h = 0.01$ and $dt = 0.005$.

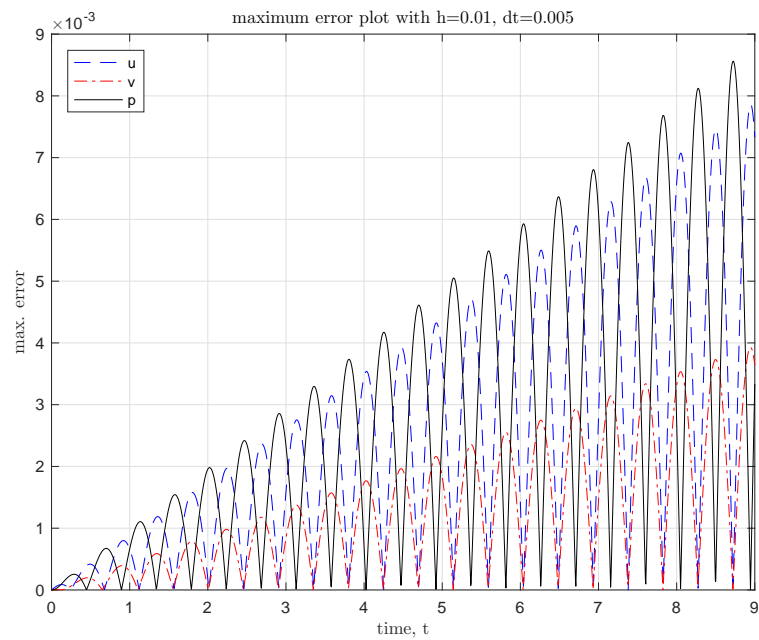


Figure 5.3.5: Maximum error for aligned square domain over $0 < t < 10T$, with $h = 0.01$ and $dt = 0.005$.

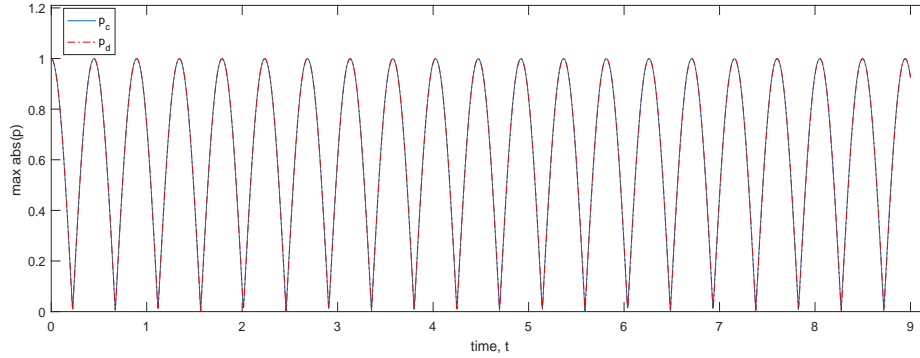


Figure 5.3.6: The maximum of $|p|$ for aligned square domain over $0 < t < 10T$ for aligned square domain, with $h = 0.01$ and $dt = 0.005$.

Table 5.1: The convergence rate of u , v and p in max norm and L_2 norm, for aligned square domain.

	max norm		L_2 norm	
	slope	scaling factor	slope	scaling factor
u	1.81706	18.7455	1.83682	9.87735
v	1.88788	13.465	1.85756	5.39464
p	1.88655	25.27	1.89323	11.2428

Table 5.2: The confidence interval of u , v and p in max norm for aligned square domain.

	max norm	confidence interval			
	slope	95%	90%	75%	50%
u	1.81706	(1.037, 2.597)	(1.1720, 2.4621)	(1.3736, 2.2605)	(1.5598, 2.0743)
v	1.88788	(1.073, 2.703)	(1.2136, 2.5622)	(1.4243, 2.3515)	(1.6189, 2.1568)
p	1.88655	(1.046, 2.727)	(1.1913, 2.5818)	(1.4085, 2.3646)	(1.6092, 2.1639)

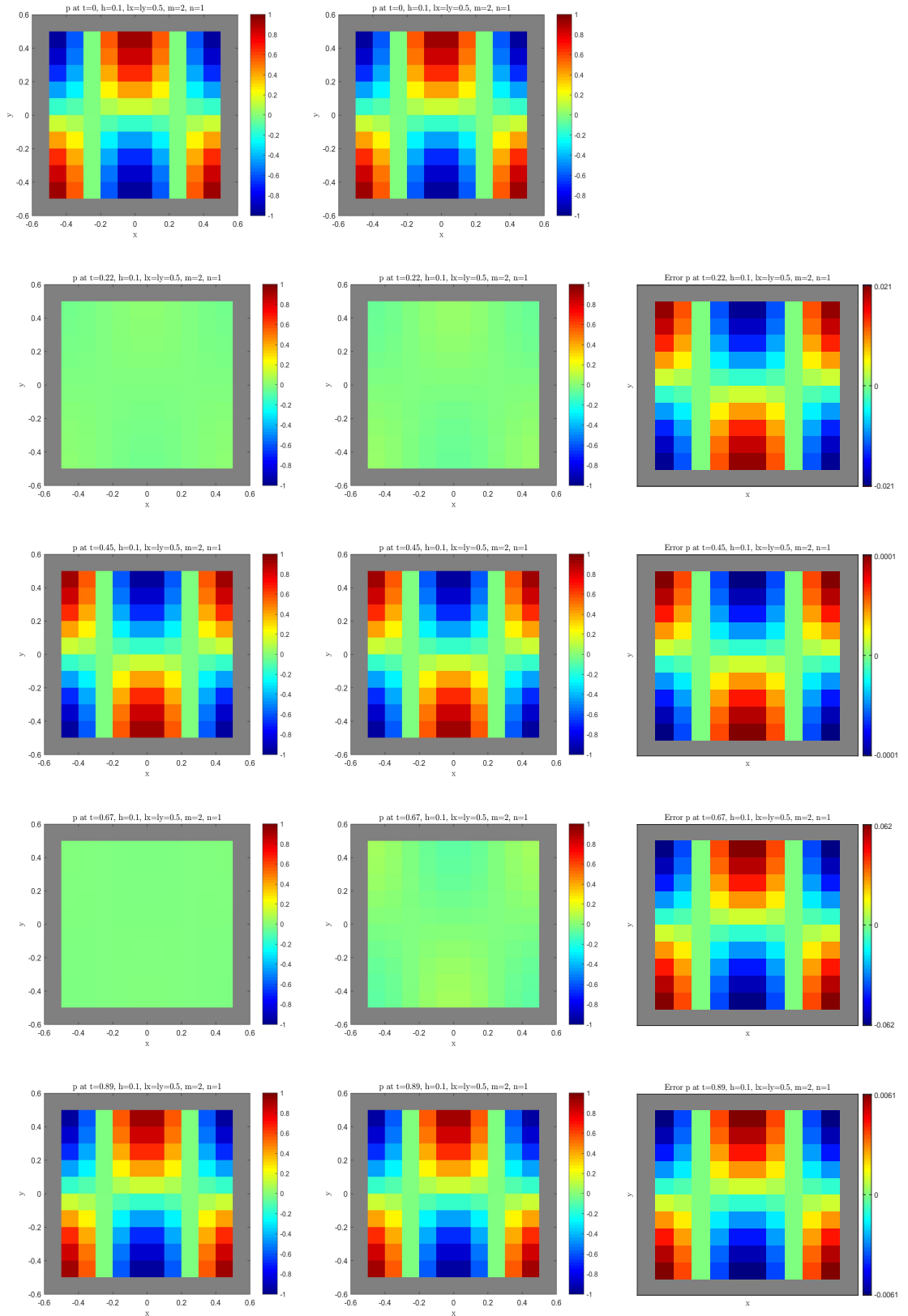


Figure 5.3.7: The numerical solutions of p for aligned square domain at $t = 0, T/4, T/2, 3T/4, T$, with $h = 0.1$ and $dt = 0.01$. Left column: continuum solutions. Centre column: numerical solutions. Right column: error (i.e., continuum-numerical).

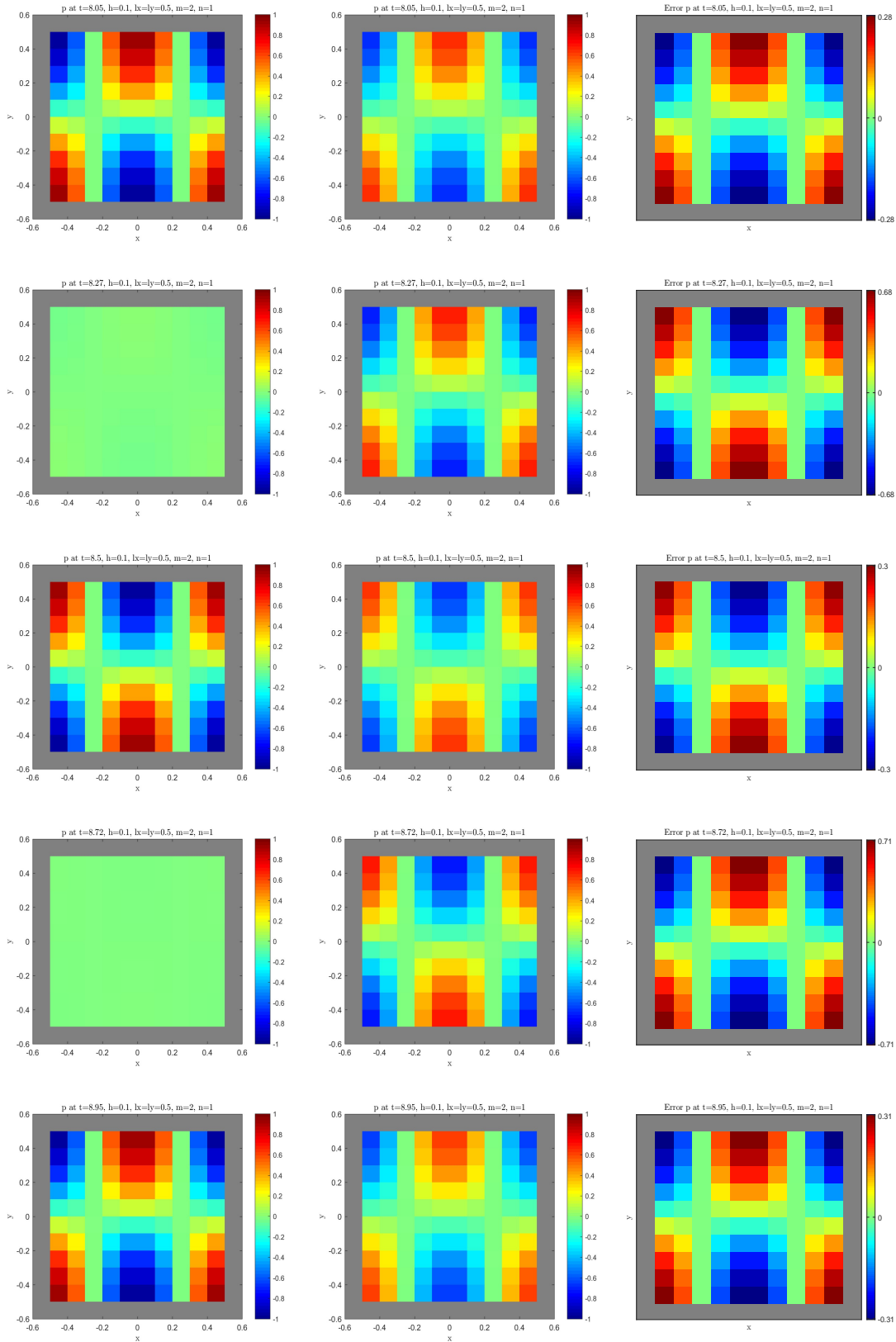


Figure 5.3.8: The numerical solutions of p for aligned square domain at $t = 9T, 9.25T, 9.5T, 9.75T, 10T$, with $h = 0.1$ and $dt = 0.01$. Left column: continuum solutions. Centre column: numerical solutions. Right column: error (i.e., continuum-numerical).

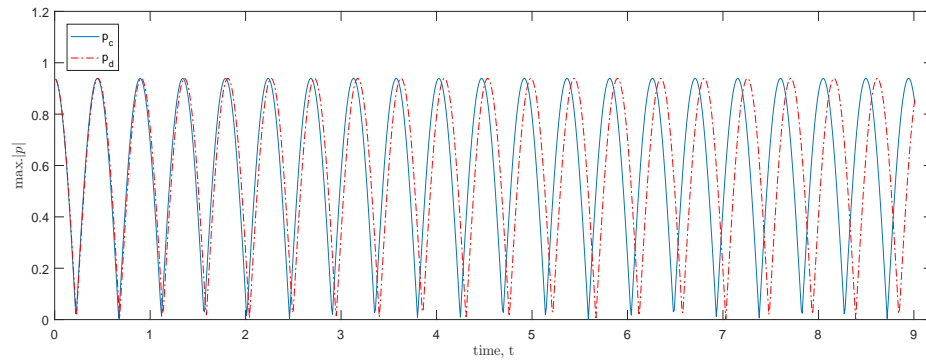


Figure 5.3.9: The maximum of $|p|$ for aligned square domain over $0 < t < 10T$ for aligned square domain, with $h = 0.1$ and $dt = 0.01$.

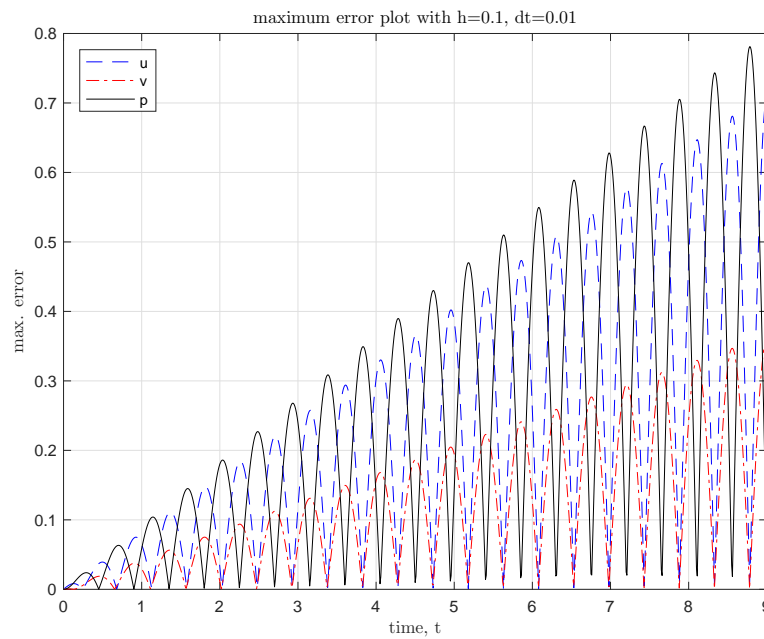


Figure 5.3.10: Maximum error for aligned square domain over $0 < t < 10T$, with $h = 0.1$ and $dt = 0.01$.

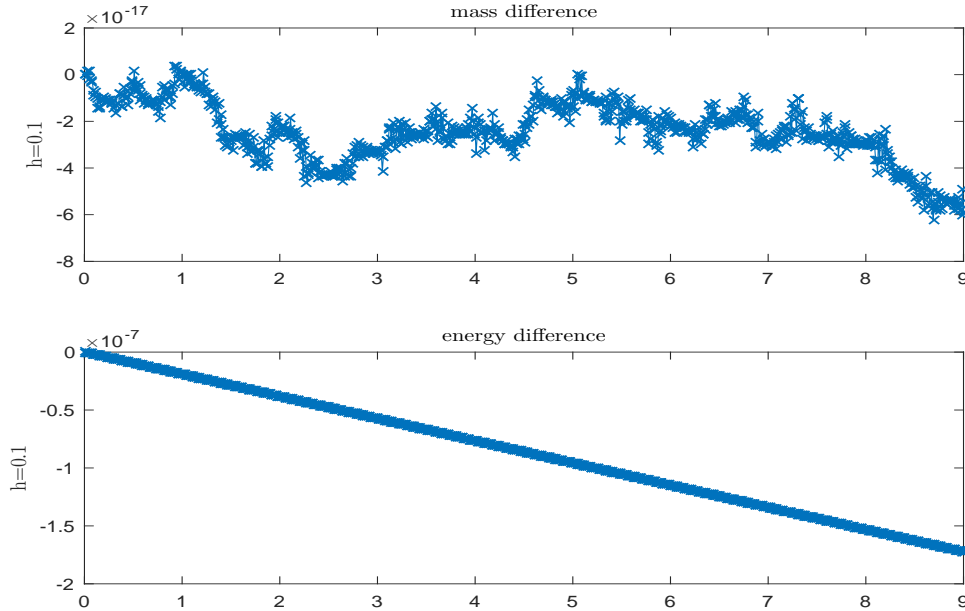


Figure 5.3.11: Mass difference and energy difference for aligned square domain, with $h = 0.1$ and $dt = 0.01$.

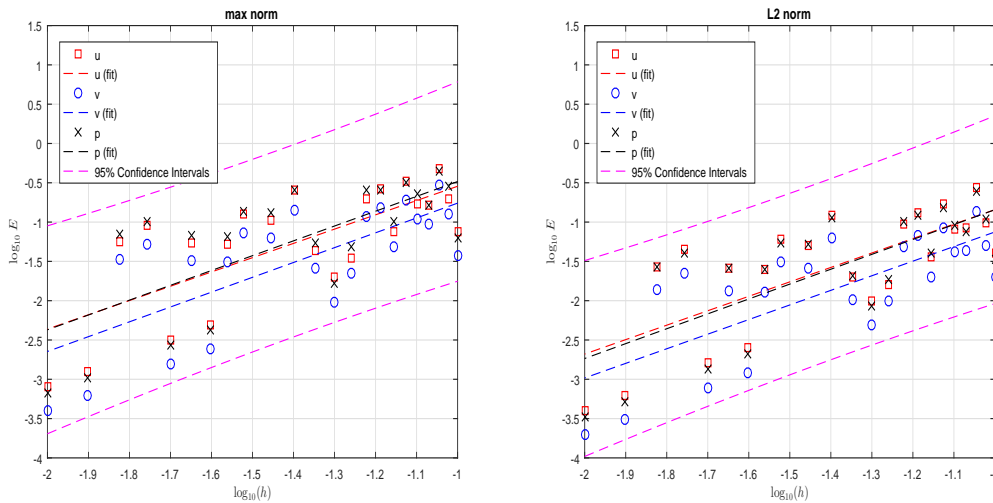


Figure 5.3.12: Convergence plot for aligned square domain at various h in range $0.1 < h < 0.01$ at fixed $dt = 0.01$. The error in (a) is calculated in max norm, and (b) in L_2 norm over domain at various h . Slope of the lines indicate the rate of convergence.

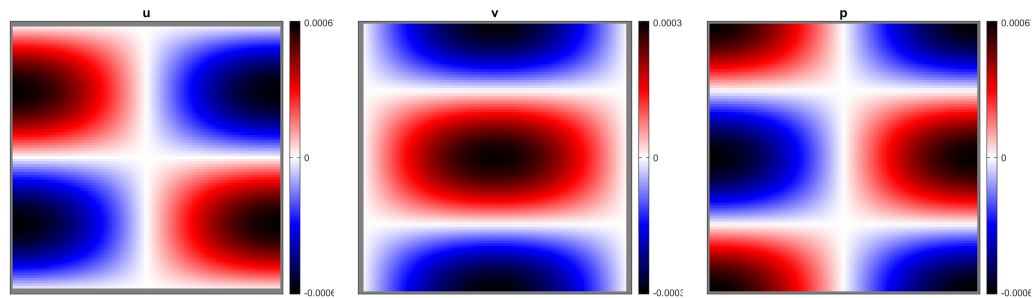


Figure 5.3.13: Error for u , v and p in aligned square domain at $h = 0.01$ and $dt = 0.01$.

5.4 Waves in a square tilted at 45° : perfect staircases

We now perform numerical simulations in square domains where the underlying C-grid is not aligned with the domain boundaries, so that there are staircase boundaries. We start by considering squares tilted by 45° to the x -axis, so that the boundaries appear as perfect staircases. We continue to use the continuum solution of section 5.3.1, appropriately rotated, as both the initial condition and subsequently as our reference for measuring the error in the solution.

We first consider the numerical solutions of a tilted square with low resolution at $h = 0.1$, and compare them with the continuum solution. Figures 5.4.1 and 5.4.2 show the solutions for p over $0 < t < T$ and $9T < t < 10T$, respectively. Obviously, we can see that at the beginning of the experiment, (i.e., $0 < t < T$), the error measured between continuum and numerical solutions is small. However, by the tenth period ($9T < t < 10T$), although the wave is still oscillating in a coherent way, there is a clear phase error relative to the continuum solution. It is the same sort of picture for u and v . We show these solutions for the first period alone in Figures 5.4.3 and 5.4.4, but omit those for the tenth period.

We confirm that there is clear phase error by examining $\max|p|$ versus time, as shown in Figure 5.4.5. Again, we can see that the frequency of the numerical solution is too small; indeed, it is so small that the wave becomes completely out of phase by $t \approx 3.5$ (at this time

there have been 9 maxima in the continuum solution, but only 8 in the discrete solution). It is a similar story for $\max.|u|$ and $\max.|v|$ (not shown). This leads to the error plot shown in Figure 5.4.6, showing that the solution actually comes back into phase when t is only about 7. So, for the plots shown of the tenth period, the wave has already completely gone out of phase, and come back into phase, and is now drifting out of phase again.

Figure 5.4.5 also reveals an amplitude error, although this does not lead to persistent growth or decay. However, the conservation of mass and conservation of energy still hold to a high degree, as shown in Figure 5.4.7.

We now examine numerical solutions at higher spatial resolution, with $h = 0.01$ and $dt = 0.005$. Now the errors over the first period remain tiny (not shown), so we only show the solutions for the tenth period: see Figures 5.4.8, 5.4.9, and 5.4.10, for u , v , and p . The errors here are small, but not negligible (unlike for the aligned case with $h = 0.01$). The ways in which the errors grow in time are shown in Figure 5.4.11. We can now see that there is a weak phase error, which becomes more apparent as time progresses. The amplitude error (evident in $|p|$ at $h = 0.1$) has now disappeared. This manifests to the error plot shown in Figure 5.4.12, showing the error keeps increasing as time progresses. Unlike the case $h = 0.1$, the wave is not completely out of phase by tenth period. However it will gone out of phase at more than tenth period. Note that the maximum error at $h = 0.01$ over tenth period also more tiny compared than the maximum error at $h = 0.1$. Again note the energy and mass are well conserved (Figure 5.4.13).

The experiment also is repeated at various grid spacing h ranging between $0.01 < h < 0.1$ for a fixed $dt = 0.01$. The log-log plot of maximum error over $0 < t < T$ at various grid spacing h is shown in Figure 5.4.14. Here we run the experiments only up to $t = T$, because by $t = 10T \approx 9$, many solutions will have gone completely out of phase at some time $t < 9$, as has happened for those solutions at $h = 0.05$ and $h = 0.1$, which thus have the same error. So to find a clearer convergence, we instead measured the maximum error over $0 < t < T$. The error then varies with h as shown in Figure 5.4.14. There is a clear

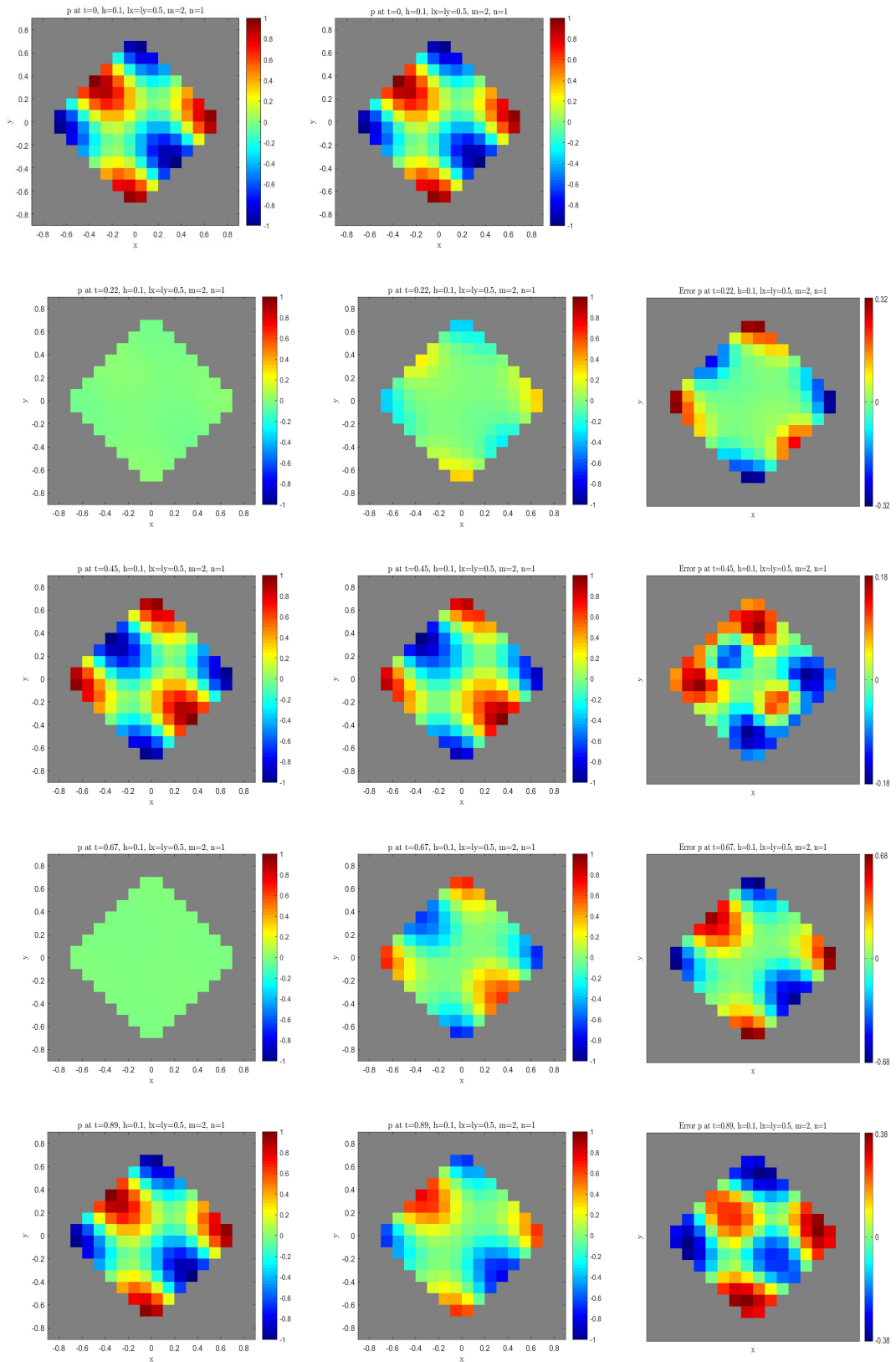


Figure 5.4.1: The solutions of p for square domain tilted at 45° at $t = 0, T/4, T/2, 3T/4, T$, with $h = 0.1$ and $dt = 0.01$. Left column: continuum solutions. Centre column: numerical solutions. Right column: error (i.e., continuum-numerical).

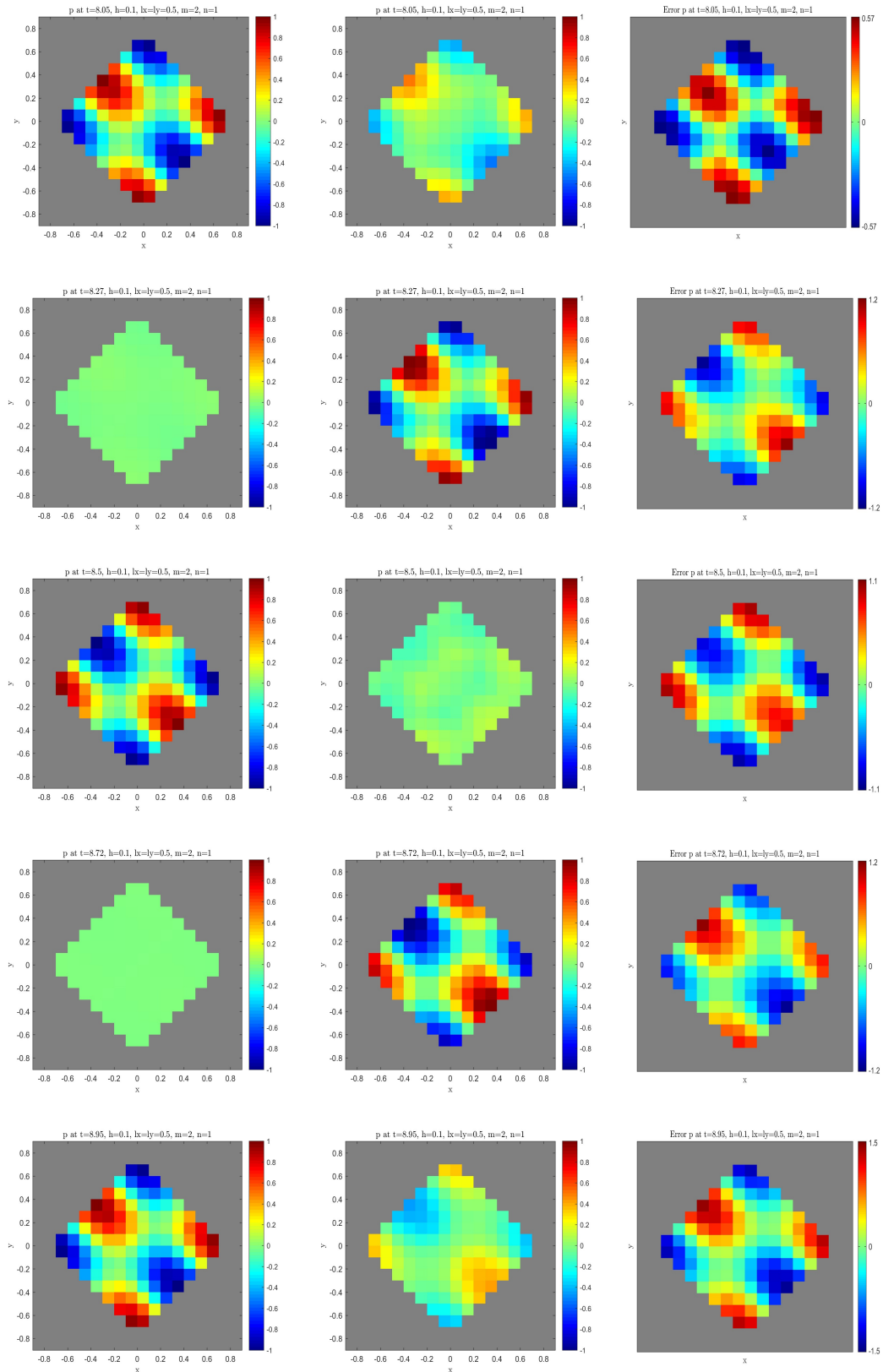


Figure 5.4.2: The solutions of p for square domain tilted at 45° at $t = 9T, 9.25T, 9.5T, 9.75T, 10T$, with $h = 0.1$ and $dt = 0.01$. Left column: continuum solutions. Centre column: numerical solutions. Right column: error (i.e., continuum-numerical).

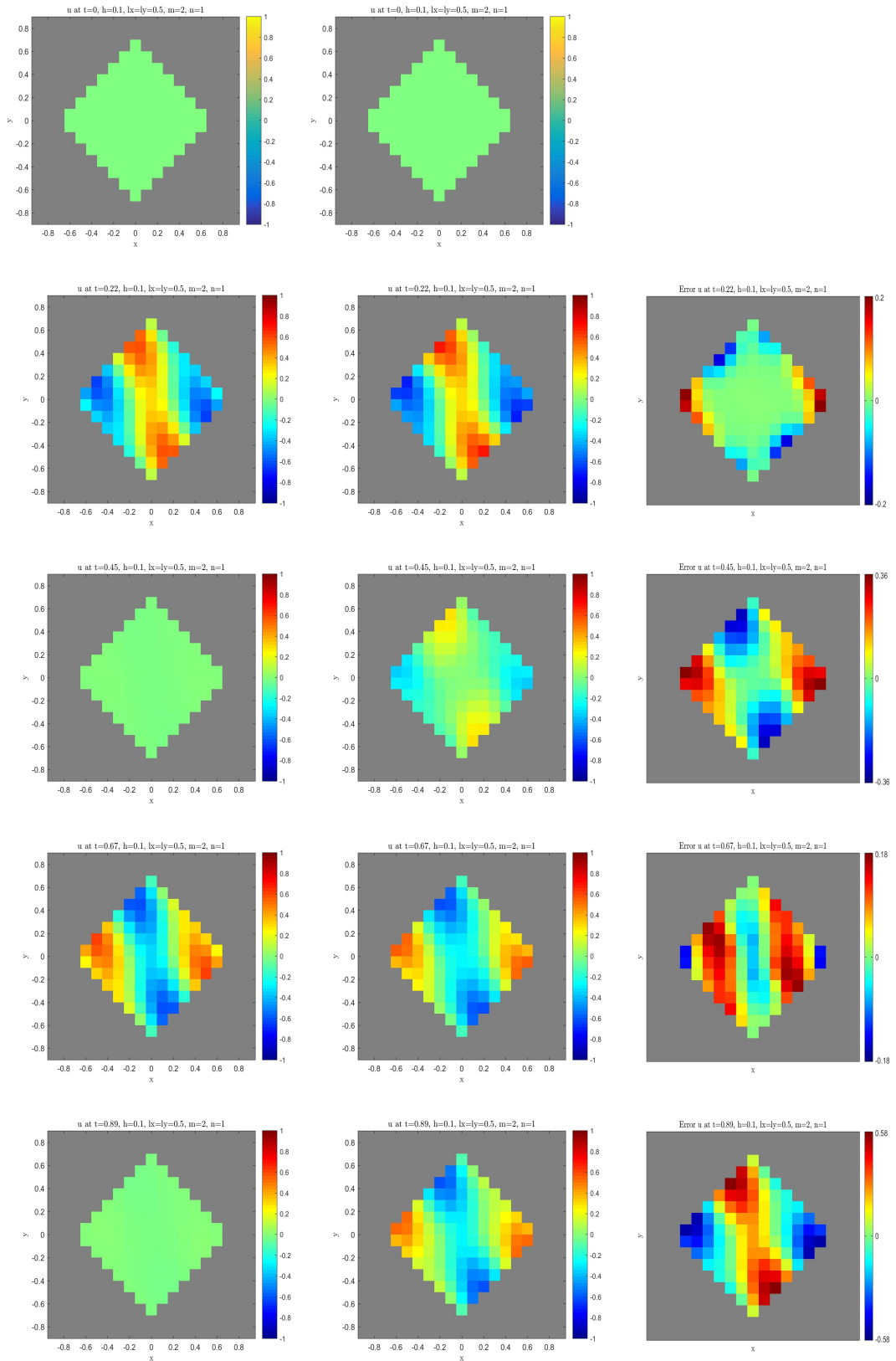


Figure 5.4.3: The solutions of u for square domain tilted at 45° at $t = 0, T/4, T/2, 3T/4, T$, with $h = 0.1$ and $dt = 0.01$. Left column: continuum solutions. Centre column: numerical solutions. Right column: error (i.e., continuum-numerical).

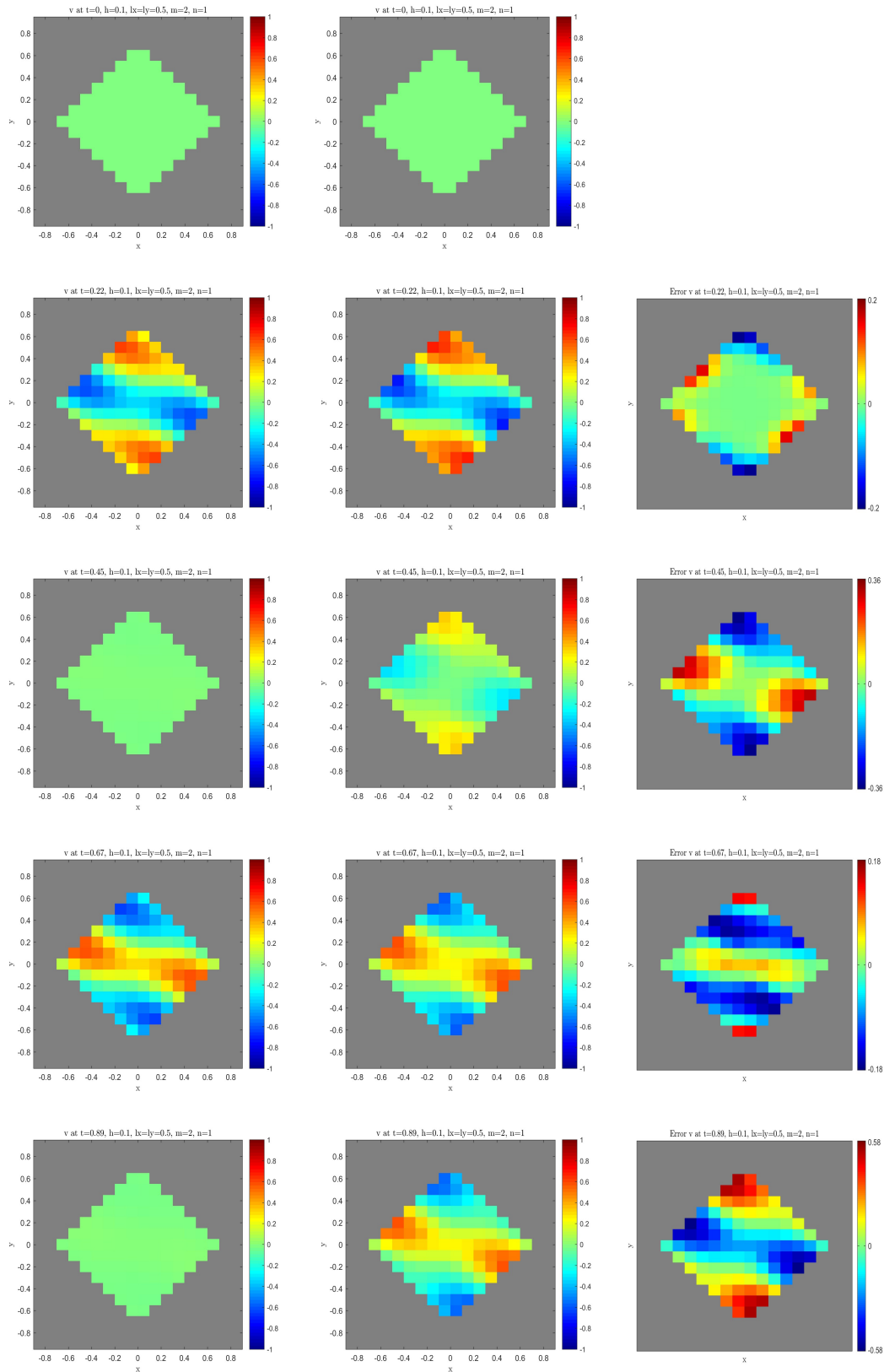


Figure 5.4.4: The solutions of v for square domain tilted at 45° at $t = 0, T/4, T/2, 3T/4, T$, with $h = 0.1$ and $dt = 0.01$. Left column: continuum solutions. Centre column: numerical solutions. Right column: error (i.e., continuum-numerical).

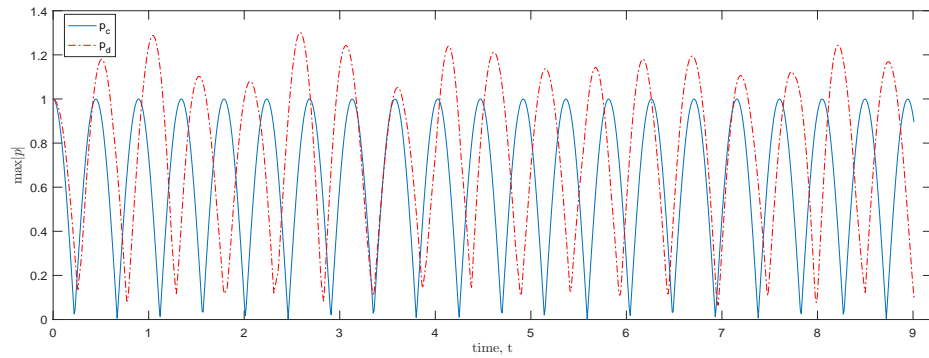


Figure 5.4.5: The maximum of $|p|$ over square domain tilted at 45° at $h = 0.1$, $dt = 0.01$ over $0 < t < 10T$.

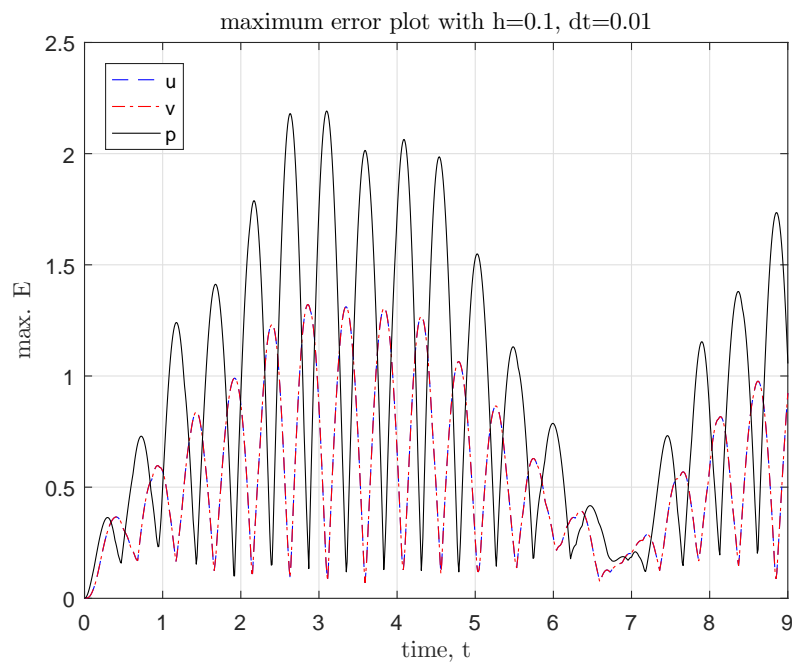


Figure 5.4.6: Maximum error over square domain tilted at 45°, over $0 < t < 10T$ at $h = 0.1$, $dt = 0.01$.

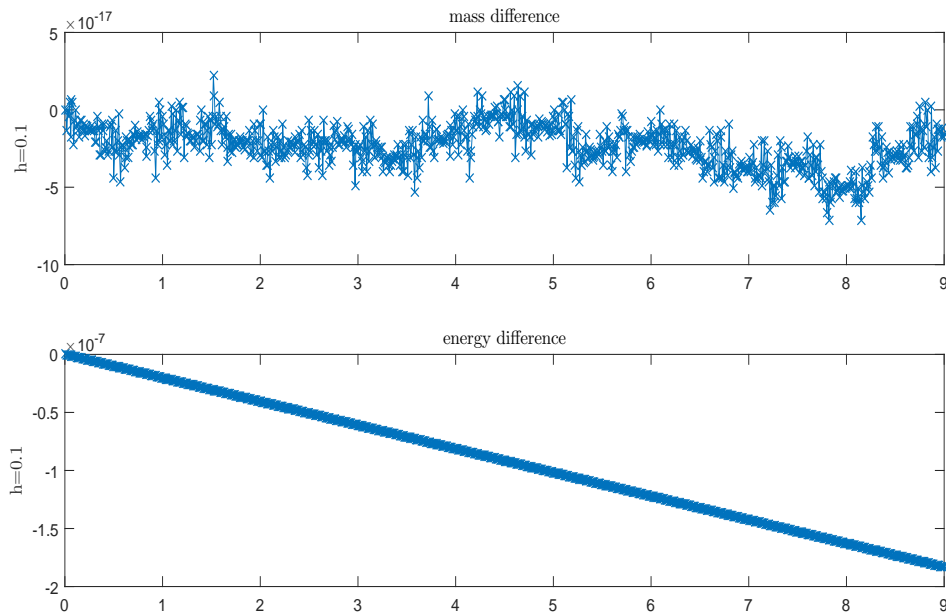


Figure 5.4.7: Mass and energy difference for square domain tilted at 45° , at $h = 0.1$, $dt = 0.01$.

decrease of E with h , with scaling exponents summarised in Table 5.3. Here, we found the slope of each line is 1, in both norms. This indicates first-order convergence in h . This seems to be consistent with a first-order error in h , a result which would be expected given in earlier chapters. Note that, the slope of the lines are fitted based on various h (i.e., at 23 points). From the plots, it can be seen that for each value of h , its error is scattered depends on the value of h . We know that, for each value of h , the convergence is degraded from second order to first order in h . With staircase boundary, as $h \rightarrow 0$ the convergence still first order but close to second order. So, for each value of h , we will have a scattered plot of maximum error, and the fitting of these scattered plot will give first order convergence. It is important to stress here that we need as many as possible values of h to get the best convergence. So, it clear that we can get almost any gradient that we like using just a few points – particularly 3 points were used in [67] to get rate of convergence between 0.5 and 1 for pressure in L_2 norm. We also showing the maximum error for u, v and p with $h = 0.01$

at $dt = 0.01$ in Figure 5.4.15. It is clear that the maximum error is matched with maximum error in Figure 5.4.14(b).

Table 5.3: The convergence rate of u , v and p in max norm and L_2 norm, for square domain tilted at 45° .

	max norm			L_2 norm		
	slope	95% c.i	scaling factor	slope	95% c.i	scaling factor
u	1.16823	(0.9064, 1.43)	6.72825	1.24367	(0.9081, 1.579)	4.55781
v	1.16823	(0.9064, 1.43)	6.72825	1.24367	(0.9081, 1.579)	4.55781
p	1.15256	(0.873, 1.432)	9.72952	1.23954	(0.9047, 1.574)	4.89802

5.5 Effects of tilt angle on simulated waves

Our computational codes also can work for other alignments. We now show how the same square in previous sections looks like when it is aligned at other angle θ . Results for the maximum error in u , v , and p for $\theta = \pi/36, \pi/18, \pi/12$, and $\pi/6$, are shown in Figure 5.5.1, 5.5.2, 5.5.3, and 5.5.4, respectively. Although we can tilt the square from 0 to 2π , we only focus up to $\pi/4$ as the square behaves as a reflection when tilted more than $\pi/4$. This behaviour can be seen from Figure 5.5.5(a), where we plot the maximum error for p , u and v over $0 < t < T$. Here we have performed simulations with $\theta = 0, \pi/4, \pi/2, 2\pi/3, \pi, 5\pi/4, 3\pi/2, 5\pi/3, 2\pi$, at fixed $h = 0.1, dt = 0.005$. We can see that the maximum error at 0 is equal with error at π and 2π . This is because boundaries of the square and the grid are aligned. However, this behaviour does not happen with boundary aligned at $\pi/2$. We can see that the maximum error for u and v is switching with each other at this angle. Although the maximum error for p is same like 0 and π , at this angle the horizontal velocity u has been tilted to be a vertical velocity and vice versa for the vertical velocity v . The same behaviour also can be seen from the maximum error at $2\pi/3$ and $5\pi/3$. Corresponding behaviour but with reduced errors can be observed at small grid spacing $h = 0.01$, as can be seen in Figure 5.5.5(b).

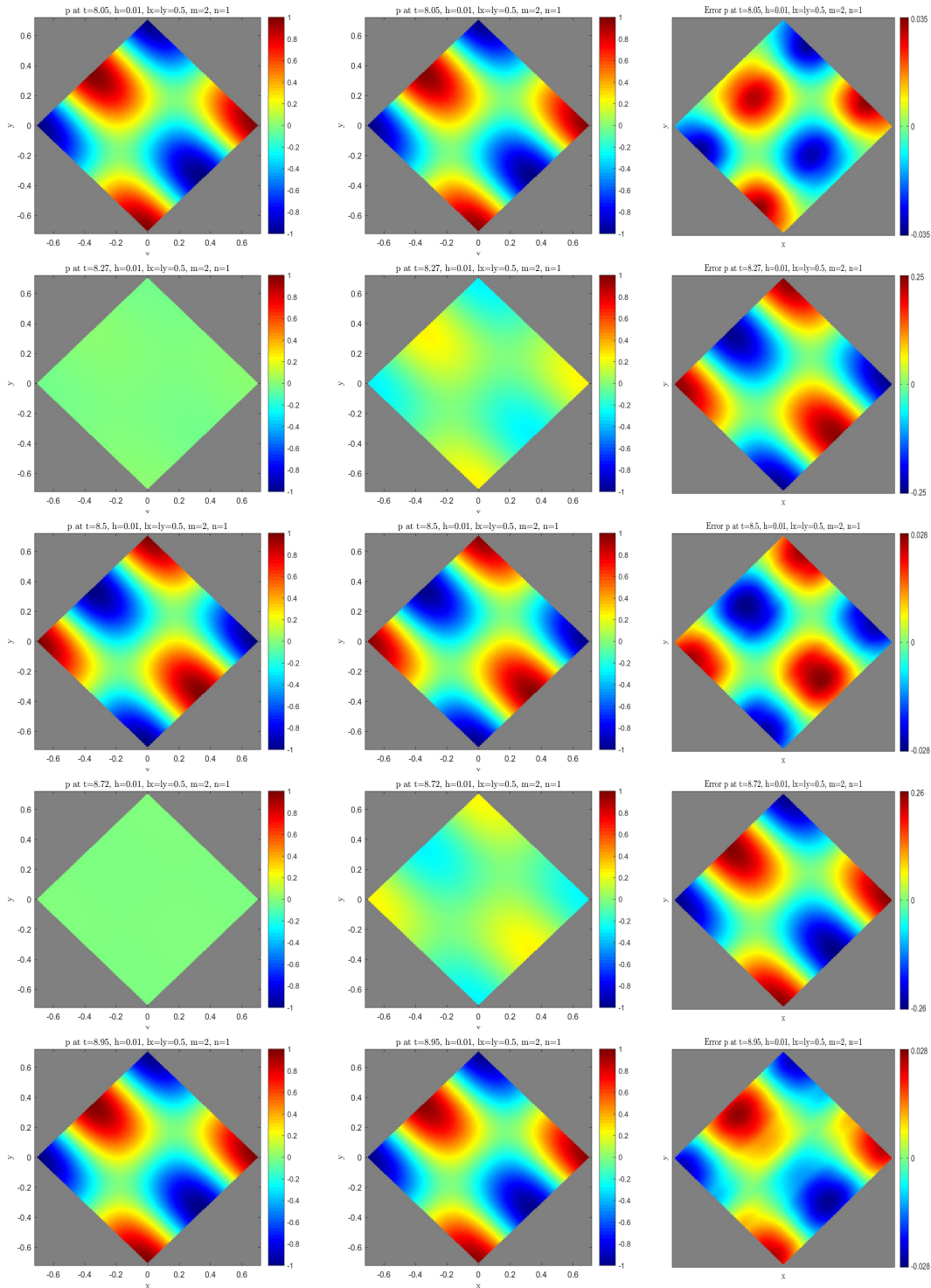


Figure 5.4.8: The solutions of p for square domain tilted at 45° at $t = 9T, 9.25T, 9.5T, 9.75T, 10T$, with $h = 0.01$ and $dt = 0.005$. Left column: continuum solutions. Centre column: numerical solutions. Right column: error (i.e., continuum-numerical).

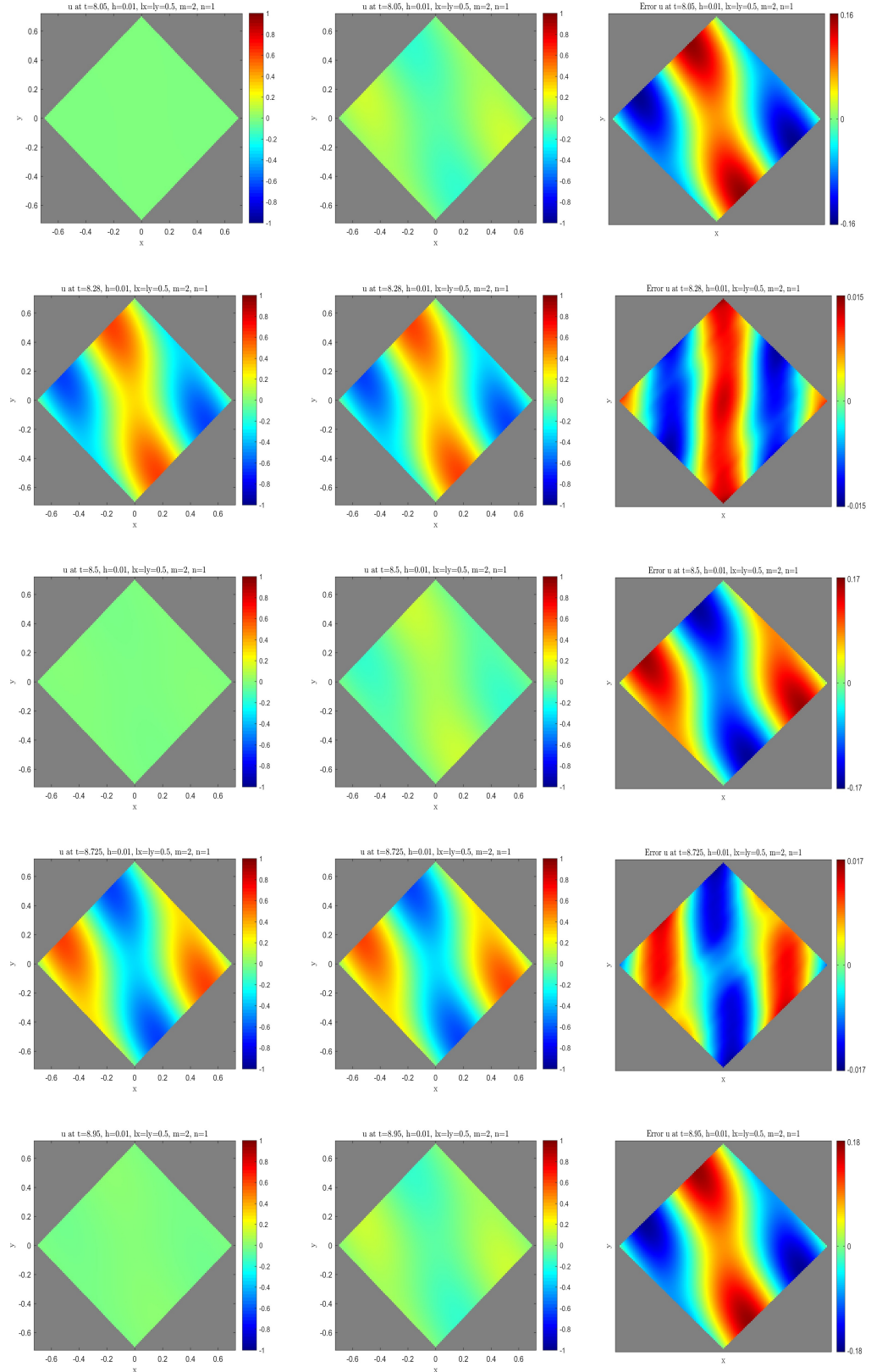


Figure 5.4.9: The solutions of u for square domain tilted at 45° at $t = 9T, 9.25T, 9.5T, 9.75T, 10T$, with $h = 0.01$ and $dt = 0.005$. Left column: continuum solutions. Centre column: numerical solutions. Right column: error (i.e., continuum-numerical).

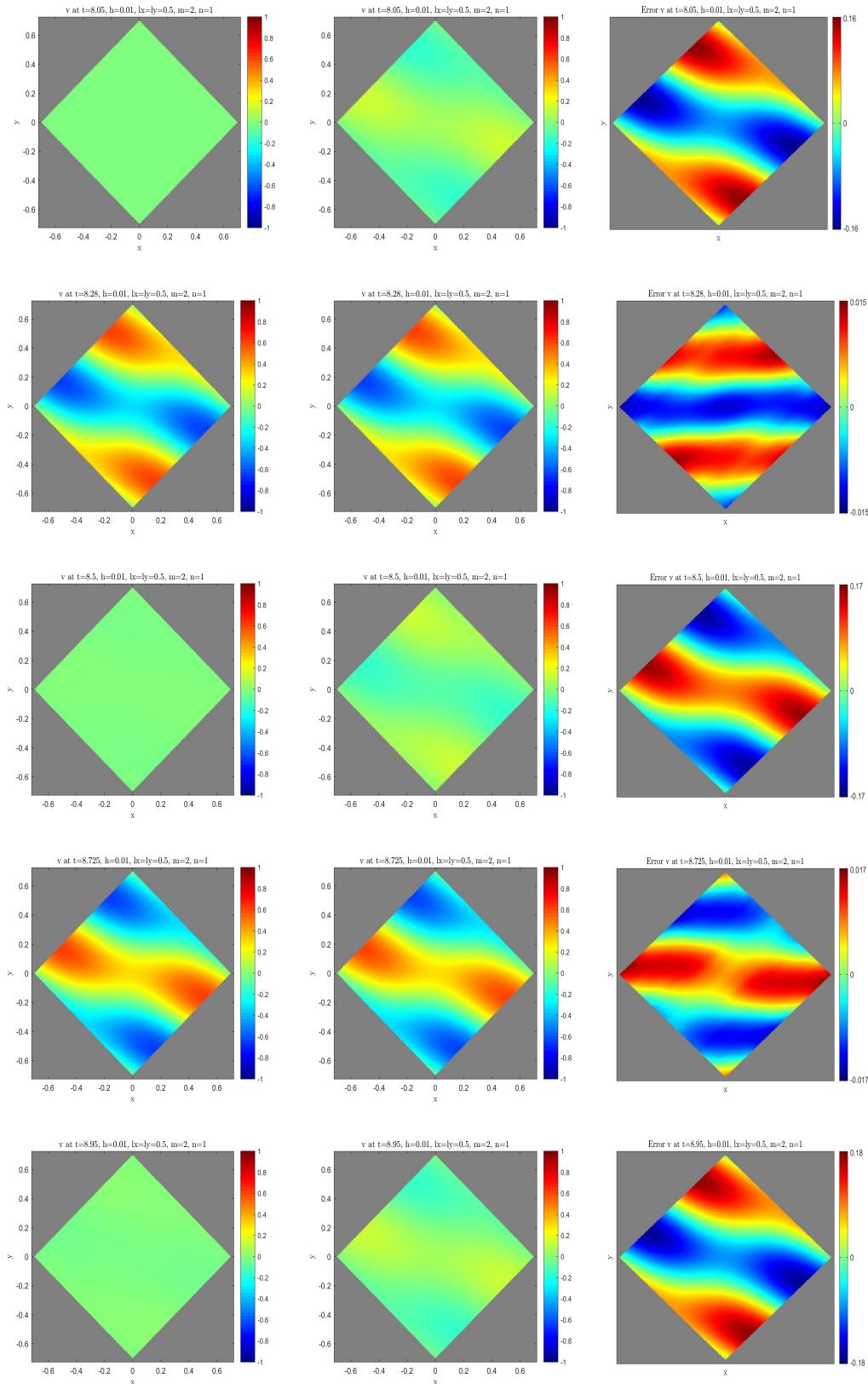


Figure 5.4.10: The solutions of v for square domain tilted at 45° at $t = 9T, 9.25T, 9.5T, 9.75T, 10T$, with $h = 0.01$ and $dt = 0.005$. Left column: continuum solutions. Centre column: numerical solutions. Right column: error (i.e., continuum-numerical).

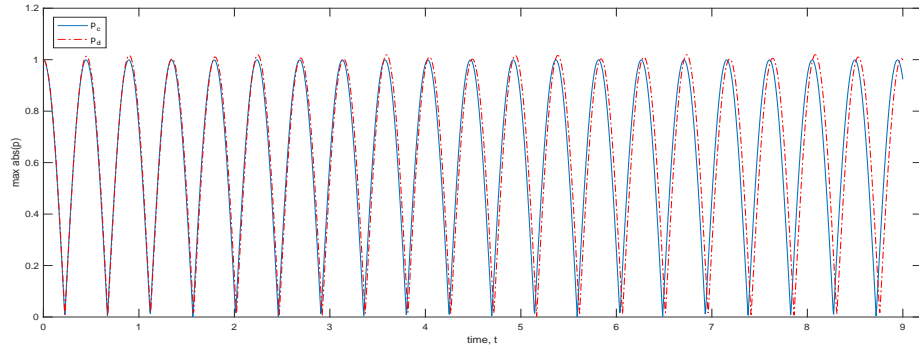


Figure 5.4.11: The maximum $|p|$ for square domain tilted at 45° with $h = 0.01$, $dt = 0.005$ over $0 < t < 10T$.

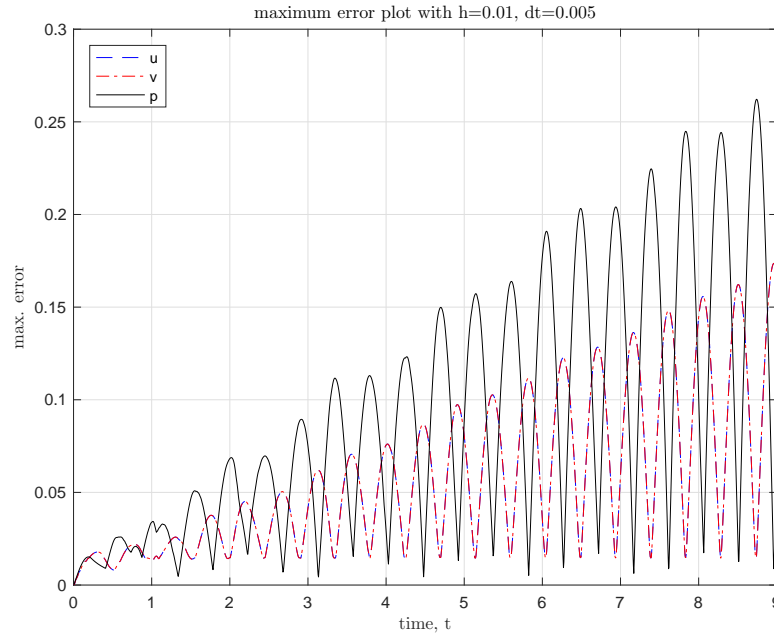


Figure 5.4.12: Maximum error for square domain tilted at 45° , at $h = 0.01$ and $dt = 0.005$ over $0 < t < 10T$.

5.5.1 Quantification of spatial convergence

We may then quantify the rate of convergence of the solution for different θ . As in section 5.4 and the analysis leading to Figure 5.4.14, the errors are calculated over $0 < t < T$.

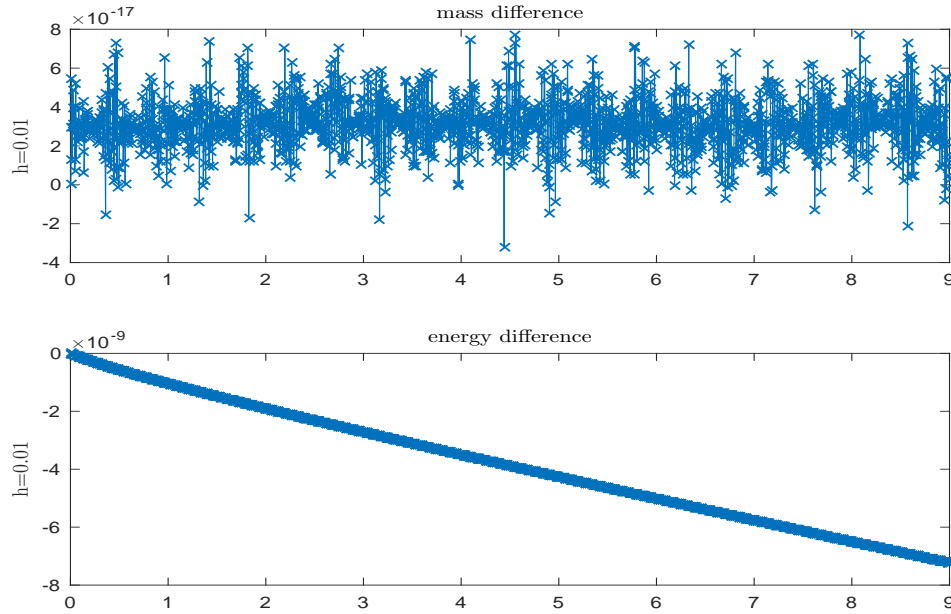


Figure 5.4.13: Mass and energy difference for square domain tilted at 45° , with $h = 0.01$, $dt = 0.005$ over $0 < t < 10T$.

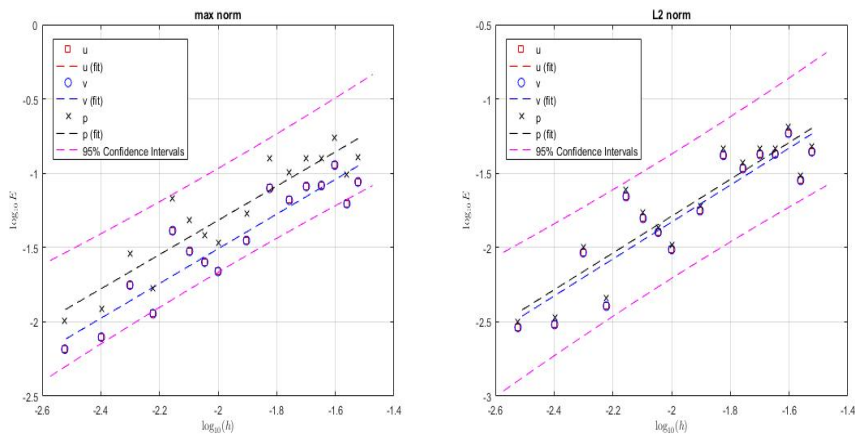


Figure 5.4.14: Convergence plot for square domain tilted at 45° , at various h in range $0.003 < h < 0.03$ at fixed $dt = 0.003$. (a) is convergence in max norm, and (b) in L_2 norm over domain. Slope of the lines indicate the rate of convergence.

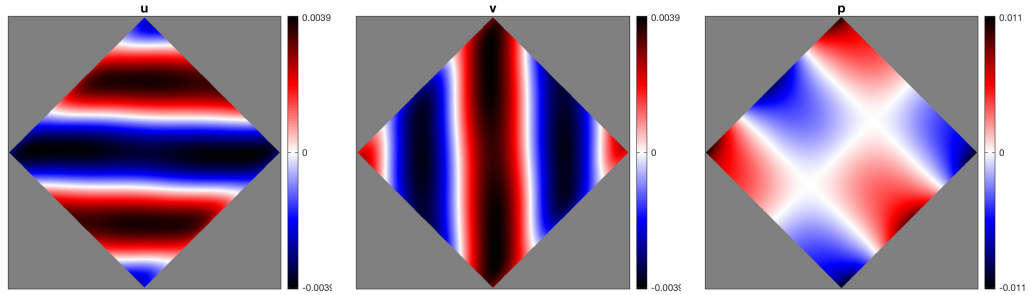


Figure 5.4.15: Maximum error for u , v and p in square domain tilted at 45° , at $h = 0.003$ and $dt = 0.003$.

We know that, the error can be expressed as

$$E = Bh^n \Rightarrow \log_{10} E = \log_{10} B + n \log_{10} h, \quad (5.5.1)$$

where $E = |p_c - p_d|$ and n represents the order of convergence with scaling factor B . The order of convergence is quantified by fitting (5.5.1), in each case θ , as in Figures 5.5.6, 5.5.7, 5.5.8, and 5.5.9. The results are shown in Table 5.4, 5.5, 5.6, and 5.7. We found that for each θ , first-order convergence is attained according to the scaling factor n . We also examined the scaling factor B , for each θ . We can see that B increases with θ , as expected. As we increase the θ the number of steps also increase, so that B increase with θ . This result agree with a channel flow with rotation effects in [32], where it was found that B increased with θ , see Table 1 in [32]. However, it is important to mention here that the results that we presented in this thesis are about wave sloshing in a closed domain, different from the experiments in [32], i.e., waves in a semi-infinite channel.

5.5.2 Frequency reduction

In the past two sections, we have seen that the frequency of the sloshing mode is reduced from the continuum value in our numerical experiments, that is $\omega_d < \omega_c$. Although we have

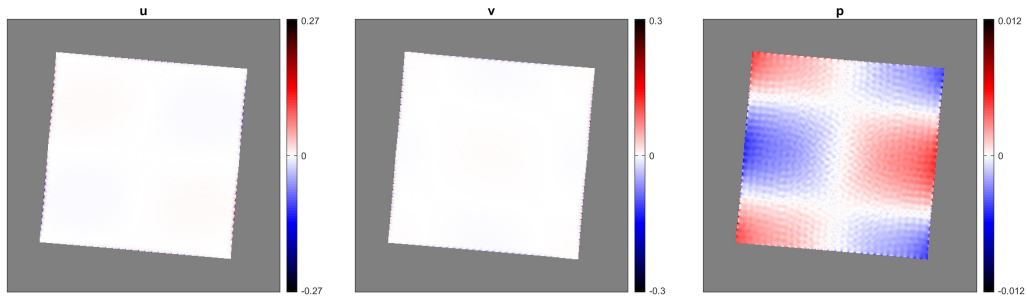


Figure 5.5.1: Maximum error for u , v and p in square domain tilted at 5° , at $h = 0.003$ and $dt = 0.003$.

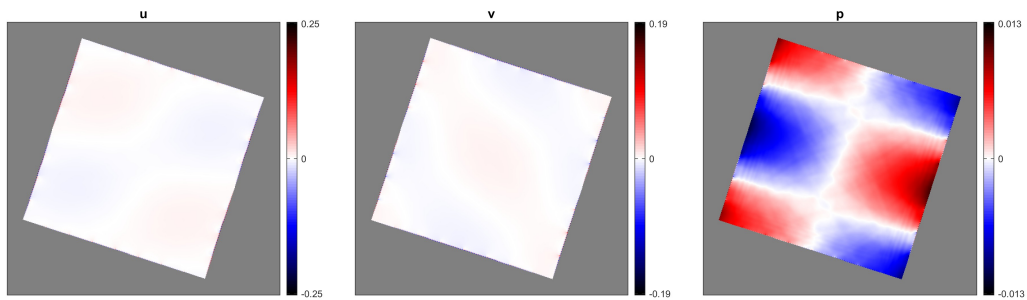


Figure 5.5.2: Maximum error for u , v and p in square domain tilted at 10° , at $h = 0.003$ and $dt = 0.003$.

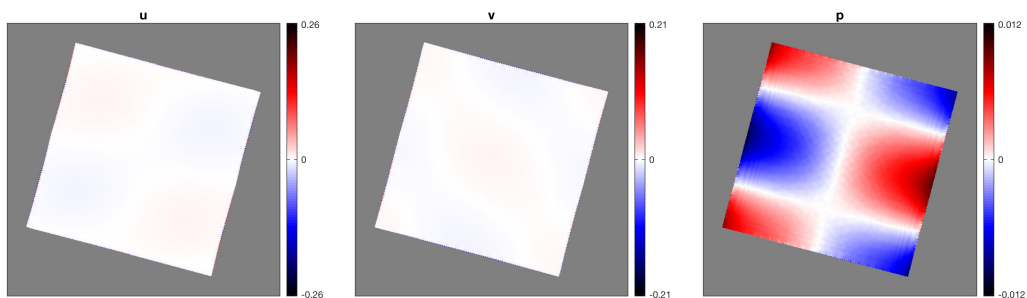


Figure 5.5.3: Maximum error for u , v and p in square domain tilted at 15° , at $h = 0.003$ and $dt = 0.003$.

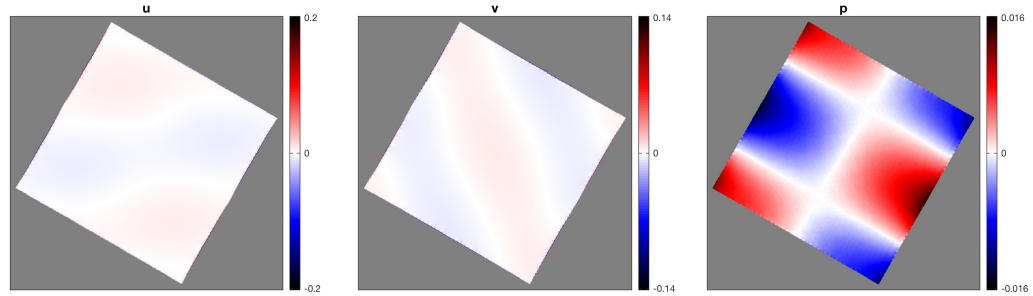


Figure 5.5.4: Maximum error for u , v and p in square domain tilted at 30° , at $h = 0.003$ and $dt = 0.003$.

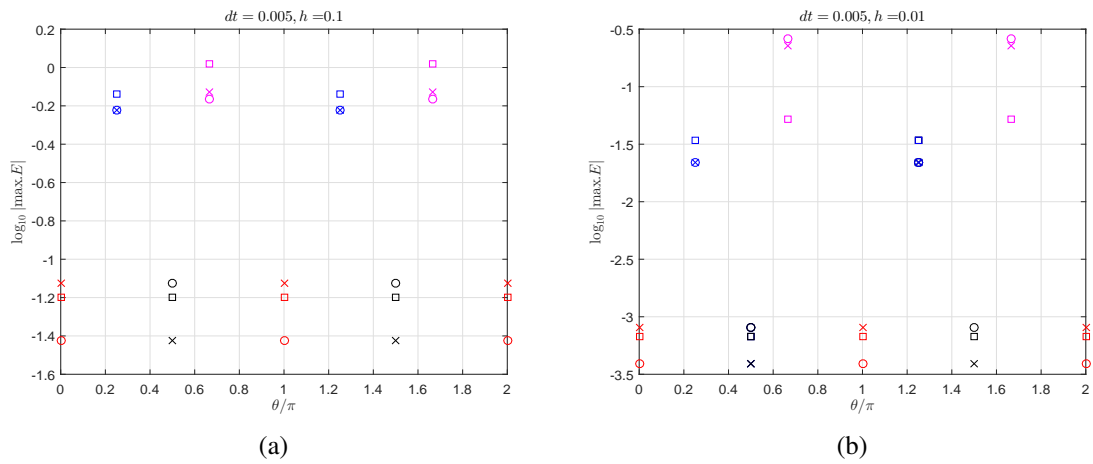


Figure 5.5.5: Maximum error of u , v and p for square domain tilted at various angle of rotation with grid spacing (a) $h = 0.1$, (b) $h = 0.01$. The maximum error is calculated over $0 < t < 10T \approx t = 9$.

Table 5.4: The convergence rate of u , v and p in max norm and L_2 norm, for square domain tilted at 5° .

	max norm			L_2 norm		
	slope	95% c.i	scaling factor	slope	95% c.i	scaling factor
u	-0.0403	(-0.0757, -0.0048)	0.3147	0.6337	(0.5735, 0.6939)	0.3725
v	-0.0069	(-0.0473, 0.0335)	0.4094	0.6441	(0.5851, 0.703)	0.3683
p	0.9477	(0.9025, 0.9929)	5.1315	1.3523	(1.187, 1.517)	3.8090

Table 5.5: The convergence rate of u , v and p in max norm and L_2 norm, for square domain tilted at 10° .

	max norm			L_2 norm		
	slope	95% c.i	scaling factor	slope	95% c.i	scaling factor
u	-0.01602	(-0.0280, -0.004)	0.30996	0.5703	(0.5313, 0.6092)	0.3144
v	0.02455	(-0.0051, 0.0542)	0.4118	0.5876	(0.5535, 0.6216)	0.3107
p	0.9866	(0.9736, 0.9997)	4.9895	1.077	(0.9554, 1.199)	1.4187

Table 5.6: The convergence rate of u , v and p in max norm and L_2 norm, for square domain tilted at 15° .

	max norm			L_2 norm		
	slope	95% c.i	scaling factor	slope	95% c.i	scaling factor
u	-0.0259	(-0.0435, -0.0083)	0.3145	0.5903	(0.5374, 0.6432)	0.3585
v	0.0492	(0.0240, 0.0744)	0.3978	0.6094	(0.5746, 0.6442)	0.3486
p	1.0528	(1.008, 1.097)	5.5161	1.0701	(0.9879, 1.152)	1.7302

Table 5.7: The convergence rate of u , v and p in max norm and L_2 norm, for square domain tilted at 30° .

	max norm			L_2 norm		
	slope	95% c.i	scaling factor	slope	95% c.i	scaling factor
u	-0.0202	(-0.0345, -0.0059)	0.2401	0.7778	(0.6835, 0.8721)	0.8093
v	0.1006	(0.0681, 0.1331)	0.3609	0.7069	(0.6398, 0.774)	0.4741
p	1.0512	(0.9924, 1.11)	6.8320	1.0468	(0.9759, 1.118)	2.2097

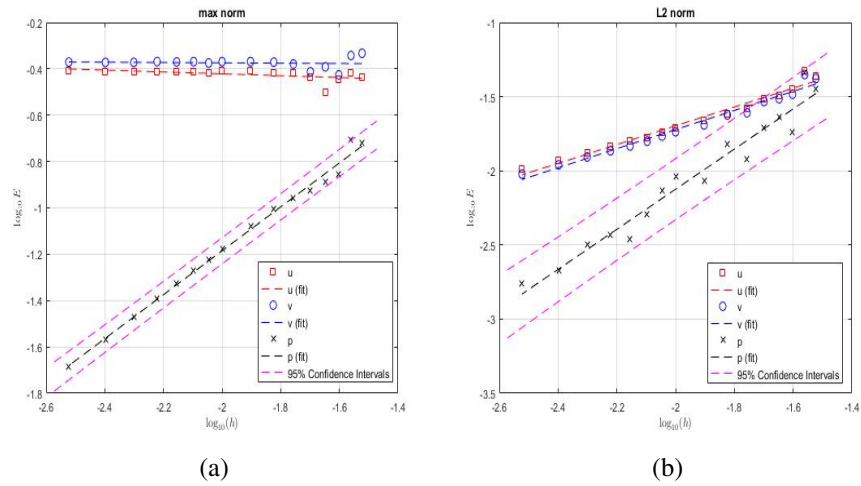


Figure 5.5.6: Convergence plot for square domain tilted at 5° , at various h in range $0.003 < h < 0.03$ at fixed $dt = 0.003$. (a) is convergence in max norm, and (b) in L_2 norm over domain. Slope of the lines indicate the rate of convergence.

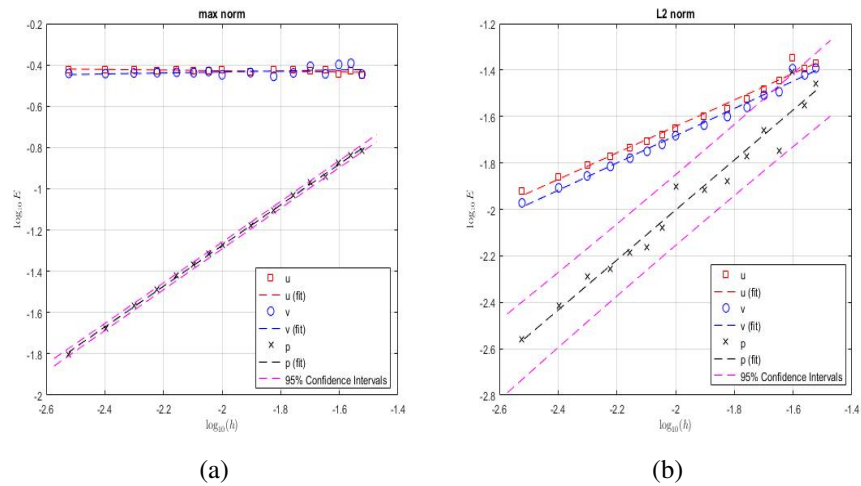


Figure 5.5.7: Convergence plot for square domain tilted at 10° , at various h in range $0.003 < h < 0.03$ at fixed $dt = 0.003$. (a) is convergence in max norm, and (b) in L_2 norm over domain. Slope of the lines indicate the rate of convergence.

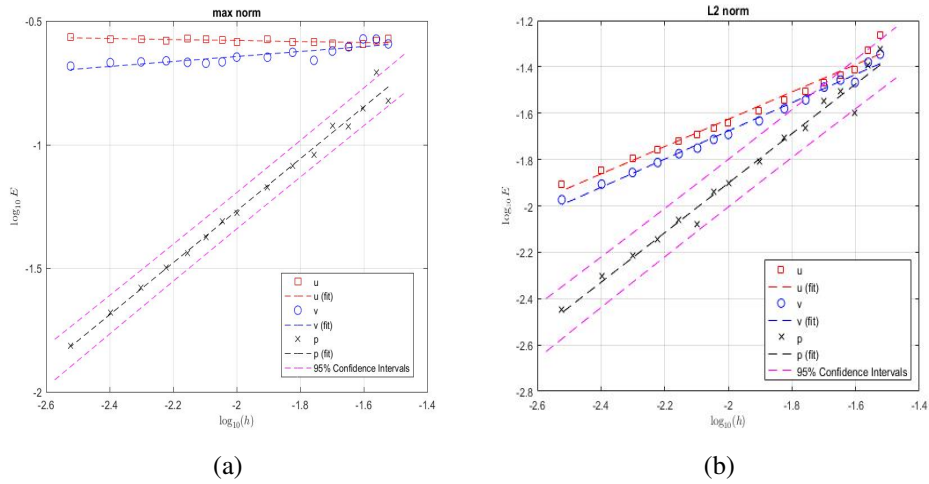


Figure 5.5.8: Convergence plot for square domain tilted at 15° , at various h in range $0.003 < h < 0.03$ at fixed $dt = 0.003$. (a) is convergence in max norm, and (b) in L_2 norm over domain. Slope of the lines indicate the rate of convergence.

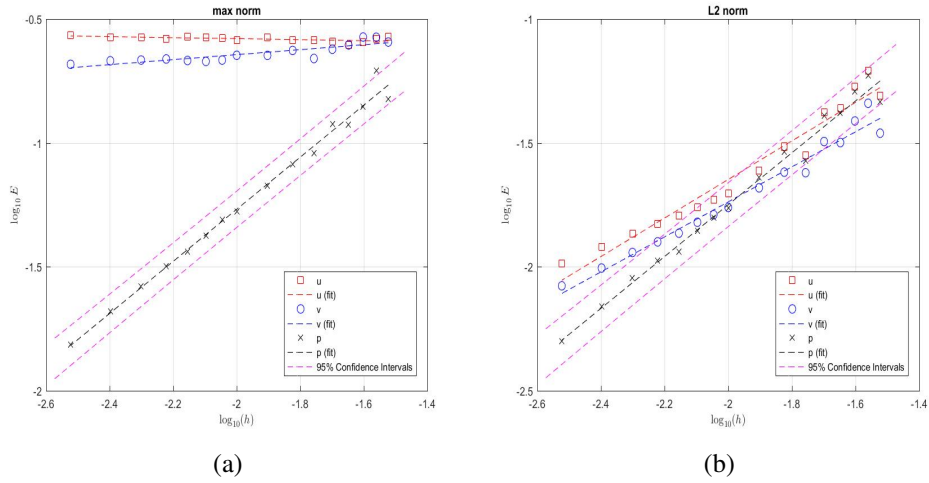


Figure 5.5.9: Convergence plot for square domain tilted at 30° , at various h in range $0.003 < h < 0.03$ at fixed $dt = 0.003$. (a) is convergence in max norm, and (b) in L_2 norm over domain. Slope of the lines indicate the rate of convergence.

measured the error in the time evolution, we have not measured the error in the frequency. We now present some short calculations to measure the frequency reduction directly.

At some θ and h , the codes were run up to a period of wave characteristic (i.e., $t \approx T = 0.8944$), and at each time step, the potential energy was recorded. From the time series of energy, period of wave can be determined by analysing the potential energy and thus discrete frequency ω_d can be calculated. At $t = 0$, kinetic energy is zero, but potential energy is at maximum. The potential energy falls to zero at $t = T/4$, and become maximum again at $t = T/2$. This is also illustrated in Figure 5.5.10. By measuring the maximum time at three points we then interpolate them to find $T/2$. Then this deduce $\omega_d = 2\pi/T$. This experiment was repeated at different values of h ranging between $0.003 < h < 0.03$.

Then, in the usual way, the error of frequency is calculated from $E = |\omega_c - \omega_d|$. We also know that, the error can be expressed as

$$E = Ch^n \Rightarrow \log E = \log C + n \log h, \quad (5.5.2)$$

where n represents the order of convergence with scaling factor C . These values can be found numerically by graph fitting. Thus the frequency reduction from wave sloshing in the domain can be determined. We also repeat this procedure at different values of θ between $0 < \theta < \pi/4$. So that, we can have a set of scaling exponents n , and a set of scaling factors C . Figures 5.5.11, 5.5.12, 5.5.13, 5.5.14, 5.5.15, and 5.5.16 show the frequency behaviour at various h , and with a fixed $dt = 0.003$, for some angles $\theta = 0, \pi/36, \pi/18, \pi/12, \pi/6, \pi/4$. It is clear that $\log_{10} E$ reduces as h reduces. The slope of the line for the case aligned square is 1.80, as showed in Figure 5.5.11, indicates second-order convergence, while for other angles is summarised in Table 5.8, along with 95% confidence interval and scaling factor C . It is found that for all angles, first-order convergence in h is obtained, where we interpret slopes of 1.25 and 1.27 as implying $n = 1$. We also calculated the 95% confidence interval for all slope of convergence. For example, at angle $\theta = \pi/36$, the slope n is determined to be 1.2491 with 95% confidence interval

(1.058, 1.44). This means that, slope $n = 1$ lies within the interval that is consistent with the analysis. Again, scaling factor C increase with θ . This is as expected, as increases in θ lead to larger number of steps, thus C increases. This also based on theoretical approach that we have discussed previously in Chapter 3, i.e., $C \sim h/\sqrt{2}$ as $h \rightarrow 0$. So, when $\theta \ll 1$, our domain may have just a single step, the convergence in the frequency is still reduced to first order in h . This is a pretty robust upwards trend as θ gets larger. But of course that $\pi/6$ is not so much different from $\pi/4$ in terms of how the staircases operate, so it is fine that the numbers are similar. For $\pi/36$, $\pi/18$, and $\pi/12$, all are pretty small angles, and indeed we do see the scaling factor increase. So the staircases are less disruptive as θ becomes small, as anticipated.

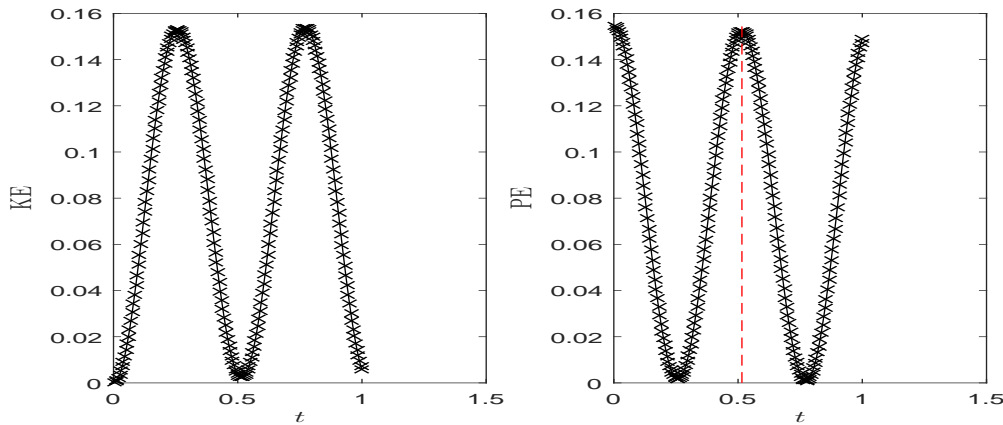


Figure 5.5.10: Time series of kinetic and potential energy for waves in a square domain over $0 < t < 1$.

Table 5.8: The scaling factors C and scaling exponents n , along with 95% confidence interval for error in frequency, at various θ . The values are numerically determined at fixed $dt = 0.003$ and grid spacing $0.003 < h < 0.03$.

θ	n	95% c.i	C
$\pi/36$	1.2491	(1.058,1.44)	1.4128
$\pi/18$	1.0505	(0.9128,1.188)	2.59302
$\pi/12$	1.064	(0.9815,1.147)	3.29813
$\pi/6$	1.0417	(0.972,1.111)	4.92095
$\pi/4$	1.27522	(0.9113,1.639)	4.45275

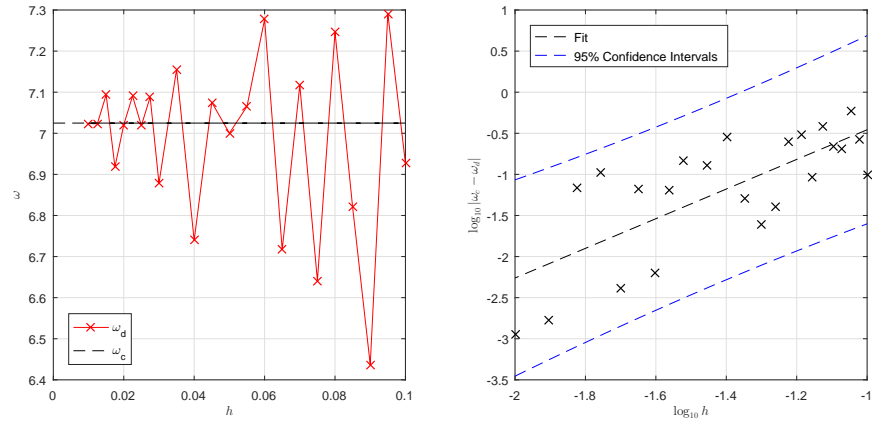


Figure 5.5.11: The frequency of wave in aligned square domain, and log-log plot error in frequency at various h . The slope of the line is 1.80398 with 95% confidence interval (1.045, 2.563).

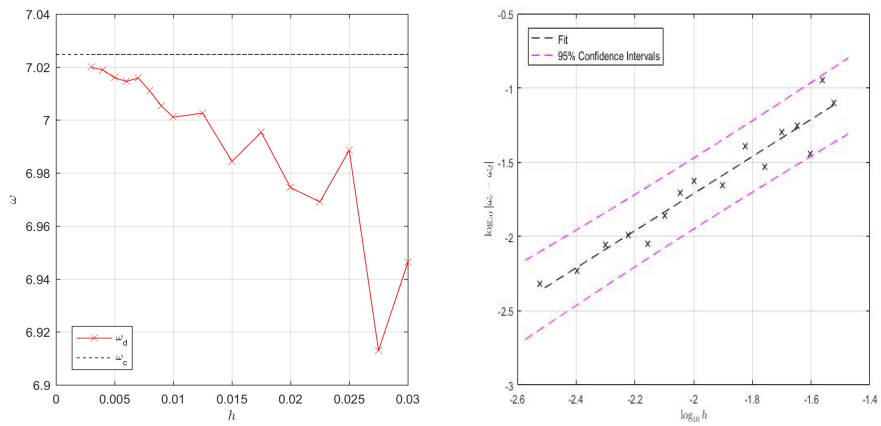


Figure 5.5.12: The frequency of wave in square domain tilted at 5° , and log-log plot error in frequency at various h . The slope of the line is 1.2491.

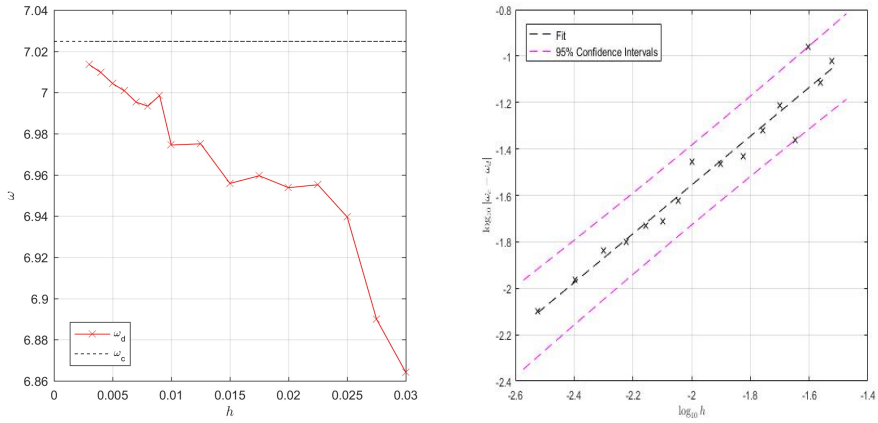


Figure 5.5.13: The frequency of wave in square domain tilted at 10° , and log-log plot error in frequency at various h . The slope of the line is 1.0505.

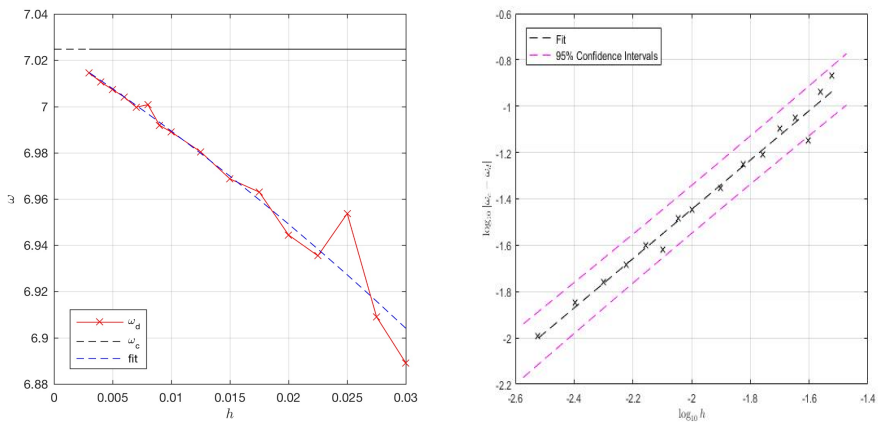


Figure 5.5.14: The frequency of wave in square domain tilted at 15° , and log-log plot error in frequency at various h . The slope of the line is 1.064.

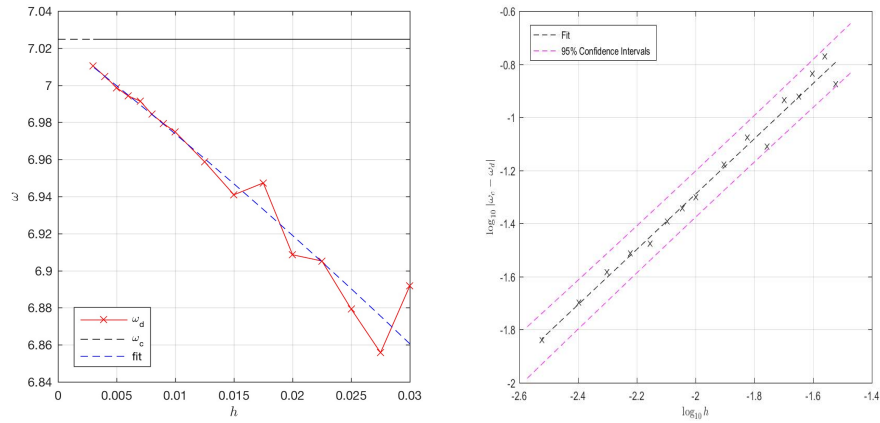


Figure 5.5.15: The frequency of wave in square domain tilted at 30° , and log-log plot error in frequency at various h . The slope of the line is 1.0417.

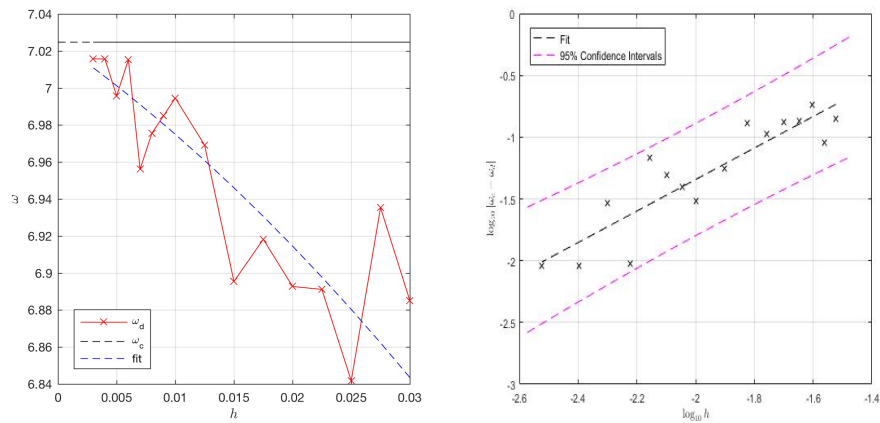


Figure 5.5.16: The frequency of wave in square domain tilted at 45° , and log-log plot error in frequency at various h . The slope of the line is 1.27522, with 95% confidence interval (0.9113, 1.639).

5.6 Waves in a circular domain

In this section, we consider the two-dimensional wave equations in a circular domain. As in the square domain, the equations are to be solved numerically with finite-difference method on the staggered C-grid. The boundary conditions are simply the no-normal flow condition at the circular wall. Unlike the square domain a staircase boundary for this domain is a necessity. However, studying the effects of the staircase boundary in this domain is feasible because we can find a continuum solution for various wave modes, which can be used as an initial condition in the numerical experiments and also can be used to measure the numerical error.

5.6.1 Continuum solutions

An analytical solution of the wave equations in a circular domain can be found by using the method of separation variables. Since we are dealing with a circular domain, we write the equations in polar coordinates as

$$\frac{\partial^2 p}{\partial t^2} - \frac{\partial^2 p}{\partial r^2} - \frac{1}{r} \frac{\partial p}{\partial r} - \frac{1}{r^2} \frac{\partial^2 p}{\partial \theta^2} = 0. \quad (5.6.1)$$

This equation is to be solved with boundary conditions $\mathbf{u} \cdot \mathbf{n} = 0$, which implies that $\partial p / \partial r = 0$. By separating the variables in (5.6.1) as $p(r, \theta, t) = P(r, \theta)T(t)$ and dividing by PT , we then have

$$\frac{1}{T} \frac{\partial^2 T}{\partial t^2} - \frac{1}{P} \left(\frac{\partial^2 P}{\partial r^2} + \frac{1}{r} \frac{\partial P}{\partial r} + \frac{1}{r^2} \frac{\partial^2 P}{\partial \theta^2} \right) = 0. \quad (5.6.2)$$

Since the first term in (5.6.2) is a function of only t , we set it as separation constant $-k^2$ which will give the general solution $T(t) = A \cos kt + B \sin kt$, is to be found later. Then,

(5.6.2) become

$$r^2 \frac{\partial^2 P}{\partial r^2} + r \frac{\partial P}{\partial r} + \frac{\partial^2 P}{\partial \theta^2} + r^2 k^2 P = 0. \quad (5.6.3)$$

Again, we separate the variables in (5.6.3) by assuming $P(r, \theta) = R(r)\Theta(\theta)$ and dividing by $R\Theta$ gives

$$\frac{1}{\Theta} \frac{d^2 \Theta}{d\theta^2} + \frac{r^2}{R} \frac{d^2 R}{dr^2} + \frac{r}{R} \frac{dR}{dr} + r^2 k^2 = 0. \quad (5.6.4)$$

As can be seen, from the first term in (5.6.4), we let $-d^2\Theta/d\theta^2 = n^2$, where the separation constant n^2 must be an integer, because the angular solution $\Theta(\theta) = e^{in\theta}$ must be periodic in the azimuthal angle. Now, we only left with radial, R -equation

$$\frac{d^2 R}{dr^2} + \frac{1}{r} \frac{dR}{dr} + \left(k^2 - \frac{n^2}{r^2} \right) R = 0. \quad (5.6.5)$$

Equation (5.6.5) is known as Bessel's ordinary differential equation. The constant n is called the order of Bessel function R . The detailed solutions and properties of this equation are discussed in [8]. We use the regular solution $R(r) = J_n(kr)$ because the irregular second independent solution is singular at the origin, which is unacceptable here. Thus, the solution of (5.6.1) now is

$$p(r, \theta, t) = J_n(kr) e^{in\theta} (A \cos kt + B \sin kt), \quad (5.6.6)$$

where the constant k is determined from the boundary condition $\partial p / \partial r = 0$ at the boundary of the circular domain. Applying the boundary condition by differentiating (5.6.6) with respect to r allow us to determine the possible values of k with

$$J'_n(k_{mn}) = 0, \quad (5.6.7)$$

with k_{mn} the m -th zero of J'_n . The discrete values of k_{mn} can be found in [1]. Hence, the complete solution now is

$$p(r, \theta, t) = J_n(k_{mn}r)e^{in\theta} (A \cos k_{mn}t + B \sin k_{mn}t), \quad (5.6.8)$$

where A and B are arbitrary constants.

We now need to determine the solution for u and v . We start from the polar velocity, u_r and u_θ , which satisfy

$$\begin{aligned} \frac{\partial u_r}{\partial t} &= -\frac{\partial p}{\partial r} \quad \text{and} \quad \frac{\partial u_\theta}{\partial t} = -\frac{1}{r} \frac{\partial p}{\partial \theta}, \\ \Rightarrow u_\theta &= \frac{n}{\omega_{mn}r} J_n(k_{mn}r)e^{in\theta} (A \cos k_{mn}t + B \sin k_{mn}t), \\ u_r &= -J'_n(k_{mn}r)e^{in\theta} (A \cos k_{mn}t + B \sin k_{mn}t). \end{aligned} \quad (5.6.9)$$

The velocity u transforms into Cartesian coordinate using $u = \cos \theta u_r - \sin \theta u_\theta$ and $v = \sin \theta u_r + \cos \theta u_\theta$:

$$\begin{aligned} u &= -\cos \theta J'_n(k_{mn}r)e^{in\theta} (A \cos k_{mn}t + B \sin k_{mn}t) \\ &\quad - \frac{n \sin \theta}{k_{mn}r} J_n(k_{mn}r)e^{in\theta} (A \cos k_{mn}t + B \sin k_{mn}t), \end{aligned} \quad (5.6.10)$$

and

$$\begin{aligned} v &= -\sin \theta J'_n(k_{mn}r)e^{in\theta} (A \cos k_{mn}t + B \sin k_{mn}t) \\ &\quad + \frac{n \cos \theta}{k_{mn}r} J_n(k_{mn}r)e^{in\theta} (A \cos k_{mn}t + B \sin k_{mn}t). \end{aligned} \quad (5.6.11)$$

The solutions (5.6.8), (5.6.10) and (5.6.11) are the complete solutions of the wave equations for a circular domain which will be used as initial condition to initiate our numerical computations in the next section. In all experiments, we choose $A = 1$ and $B = 0$, and use

the particular solution

$$p = J_n(k_{mn}r)e^{in\theta} \cos k_{mn}t, \quad (5.6.12)$$

$$u = -J'_n(k_{mn}r)e^{in\theta} \cos \theta \cos k_{mn}t - \frac{n \sin \theta}{k_{mn}r} J_n(k_{mn}r)e^{in\theta} \cos k_{mn}t, \quad (5.6.13)$$

$$v = -J'_n(k_{mn}r)e^{in\theta} \sin \theta \cos k_{mn}t + \frac{n \cos \theta}{k_{mn}r} J_n(k_{mn}r)e^{in\theta} \cos k_{mn}t. \quad (5.6.14)$$

5.6.2 Numerical solutions

As previously investigated for a square domain, we now present numerical solutions for a circular domain at both low and high resolution. By considering a circular domain with radius $r = 1$ as the continuum domain, grid cell is activated when the centre coordinate (p -node) lies within the continuum domain. For all centre coordinates that are outside of the continuum domain, they are inactive cells and will not be used in the numerical computations. Unlike square domain, staircase boundaries for a circular domain are automatically generated with rectangular grid cells. Again we consider the two-dimensional acoustic wave equations (5.1.1). The boundary condition at these staircases are similar to the square experiment, where there will be no flow through these boundaries, i.e., $u = 0$ or $v = 0$.

The frequency of wave in the circle is define as $\omega_{mn} = k_{mn}$, where $k_{mn} = z_{mn}$ with z_{mn} the m -th zero of J'_n , as given previously in (5.6.7). Here, we start by presenting numerical solutions for mode $m = 1$ and $n = 0$, so that the frequency now is $\omega_{10} = 3.8317$. Note that the value of 3.8317 is taken from the table of zero J'_0 [1]. As we are trying to see the spatial effect of staircases after a certain period, the numerical solutions are performed up to ten period. The period of wave is define as $T = 2\pi/\omega_{10} \approx 1.6398$. Here, we perfomed the computations up to $t = 17$, the nearest integer after ten periods. Note that, in all computations we use a high order time stepping scheme Runge-Kutta order 4, so that the time-stepping errors can be minimised and we almost exclusively focus on the effect of spatial errors. Analogous to the experiment of the square domain, in all figures we present

continuum solutions in the first column along with their numerical solutions in the second column. In the third column, we present the error between both solutions.

5.6.3 Low resolution: $h = 0.1$

The numerical solutions of pressure p with grid spacing $h = 0.1$ at first and tenth period of oscillation are showed in Figures 5.6.1 and 5.6.2, respectively. Despite a tiny error, it can clearly be seen that the wave propagates outwards at the correct phase speed in the first period; before moving back to the original starting point after hitting the boundary. However, after the tenth period, there are differences between the continuum and numerical solutions. The numerical solutions are slightly out of phase with the continuum solutions, which presumably arises from the staircase boundaries.

This phase error is also clearly seen from $|p|$, as shown in Figure 5.6.3. We can see that there is almost no difference between continuum and numerical solutions over $0 < t < T \approx t = 1.64$. However, after $t = 3$ the numerical solutions (red dashed line) start to diverge from the continuum solutions. This divergence grows showing that the wave frequency is too small.

We also present numerical solutions of the corresponding velocity u in Figures 5.6.4 and 5.6.5, for $0 < t < T$ and $9T < t < 10T$, respectively. Over the first period, the behavior is fine, although we can already see small errors near the boundaries. By tenth period, although the shape is still fine, the wave is again out of phase. Note that we also observed the same behavior in the vertical velocity v , as can be seen in Figures 5.6.6 and 5.6.7.

The ways in which the errors grow in time are shown in Figure 5.6.8. We can see that the maximum errors at each time step generally keep increase over $0 < t < 10T$. This is consistent with an increasing phase error over this period, which would eventually reverse as the waves come back into phase. Despite these errors, the C-grid code is still doing an excellent job conserving energy and mass, as shown in Figure 5.6.9.

5.6.4 High resolution: $h = 0.01$

We then repeat the same numerical experiments by reducing the grid spacing from $h = 0.1$ to $h = 0.01$. In order to ensure the numerical solution is always stable, we also change the time step to be $dt = 0.005$, which obeys (5.2.14). Figure 5.6.10 shows the pressure p for the tenth period: there is almost no error. This is because the waves now stay almost perfectly in phase, as confirmed in Figure 5.6.11. Note that we also observed the same behavior for u and v . These suggest that the waves can propagate at the correct speed and remain coherent at this small grid spacing $h = 0.01$, despite having staircase boundaries. We also note that unlike the square domain discussed in the previous section 5.4, there is no amplitude error in the solutions.

The full time evolution of the maximum errors over $0 < t < 17$ is shown in Figure 5.6.12. It can be seen that the maximum error for p generally increase as time progresses, taking account of the oscillation. It also has similar pattern to the experiment with $h = 0.1$ – see Figure 5.6.8. However, the error patterns for u and v are different from the experiment with $h = 0.1$. Note that, despite having these errors, the C-grid code is conserving energy and mass to a very high degree as shown in Figure 5.6.13.

In order to quantify the rate of convergence, we repeat the same experiment at various grid spacings h , ranging between $0.02 < h < 0.2$, at a fixed $dt = 0.02$. Figure 5.6.14 shows the log-log plot of maximum error in maximum and L_2 -norm for u , v and p . By fitting the straight line $\log_{10} E = \log_{10} Ah^n$, we obtained the value n and A numerically as in Table 5.9. It is perhaps not surprising that we seen to have only first-order convergence in both u and v , since, as we know, staircase boundaries lead to first-order errors. What is surprising is that the convergence in p is so rapid (i.e., ≈ 1.6). This is in contrast to the results of section 5.4, for the square domain tilted at 45° , where p showed a convergence rate of 1 – see Table 5.3. As in section 5.5.2, we next examined the frequency behaviour in the circle at various h . Figure 5.6.15 shows the frequency behaviour along with the log-log plot of $|\omega_c - \omega_d|$. Surprisingly, the slope of the line is obtained to be 1.67, contrast to the

results of section 5.4. However, the 95% confidence interval for the slope is (1.002, 2.321). Here, the slope $n = 1$ lies within the interval. This shows that the slope 1.67 is consistent with first-order convergence.

Table 5.9: The convergence rate of u , v and p in max norm and L_2 norm, for circle domain with mode $m = 1$, $n = 0$. The slope of the lines in Figure 5.6.14.

	max norm			L_2 norm		
	slope	95% c.i	scaling factor	slope	95% c.i	scaling factor
u	1.1113	(0.9063, 1.316)	0.8705	1.5887	(1.373, 1.804)	1.5039
v	1.1113	(0.9063, 1.316)	0.8705	1.5887	(1.373, 1.804)	1.5039
p	1.5861	(1.321, 1.852)	3.0404	1.6809	(1.363, 1.999)	2.6055

5.6.5 The effect of circular mode

In the previous section, we have examined one possible wave solution which has $m = 1$, and $n = 0$, and thus has no nodal diameter and no variations in θ . Now, we repeat the same experiment but with $n = 1$ (i.e., simplest possible θ variation), but still with $m = 1$. Then the frequency of the wave is $\omega_{11} = k_{11}$, where $k_{11} = 1.842$, which is taken from table of zero $J'_1 = 0$ [1]. One period of oscillation now is $T = 2\pi/\omega_{11} \approx 3.4111$. Therefore, our computations are performed up to $T = 35$, which is just after ten period of oscillations.

We start at low resolution: $h = 0.1$. The solutions for p , u and v over periods one and ten are shown in Figures 5.6.16, 5.6.17, 5.6.18, 5.6.19, 5.6.20 and 5.6.21. Over the first period, the behavior is good in p , but there are already some errors near the boundary in both u and v . Over the tenth period, the numerical solutions remain coherent, but they are now out of phase with the continuum solutions. This phase error in p is more clearly apparent in Figure 5.6.22; there is corresponding behavior in u and v . This leads to the error evolution shown in Figure 5.6.23. Note that the mass and energy are well conserved, as shown in Figure 5.6.24.

We next repeated the experiment by using different grid spacing h . The solutions over

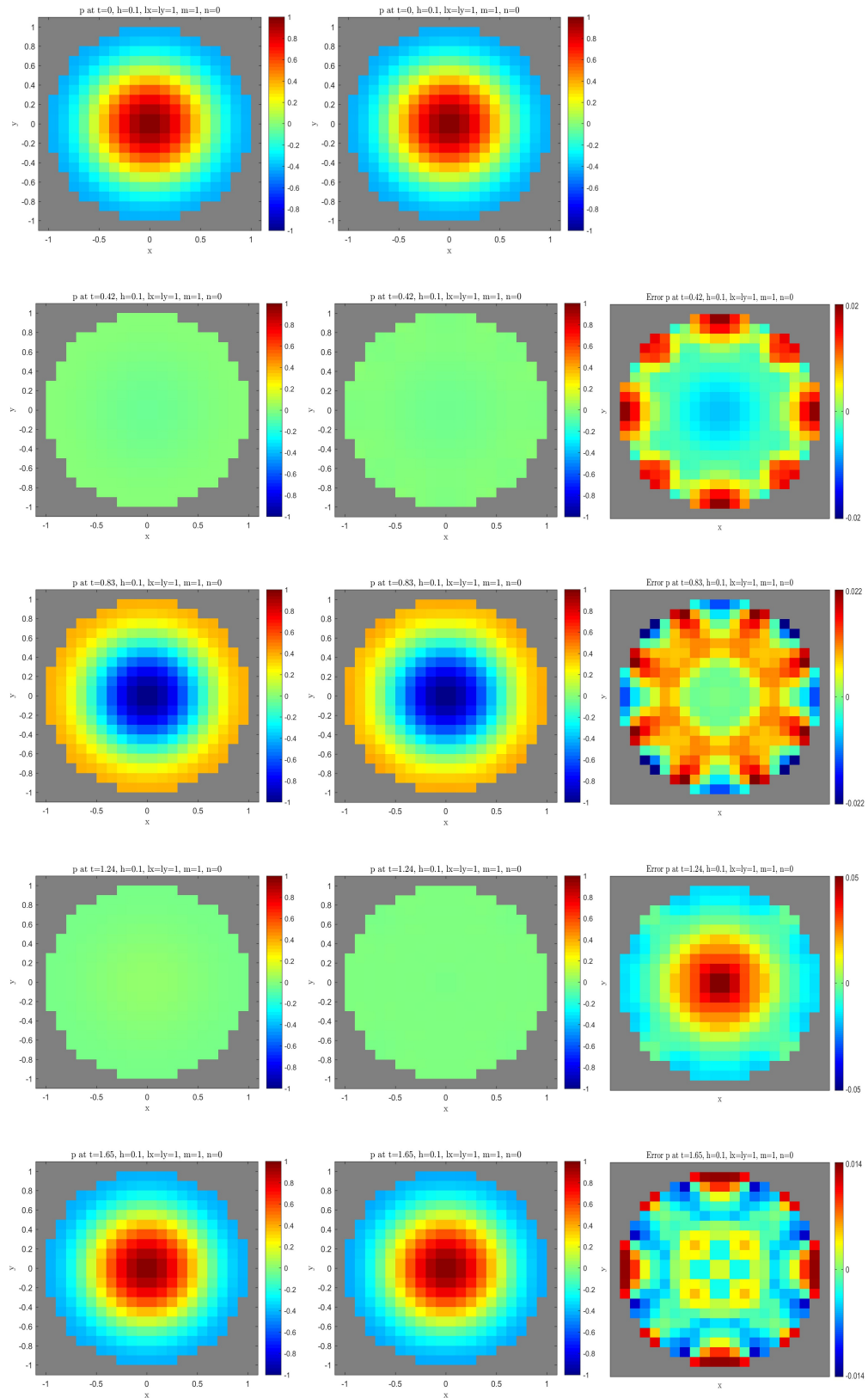


Figure 5.6.1: The solutions of p for circle domain at $t = 0, T/4, T/2, 3T/4, T$, with $h = 0.1$ and $dt = 0.01$ for mode $m = 1, n = 0$. Left column: continuum solutions. Centre column: numerical solutions. Right column: error (i.e., continuum-numerical).

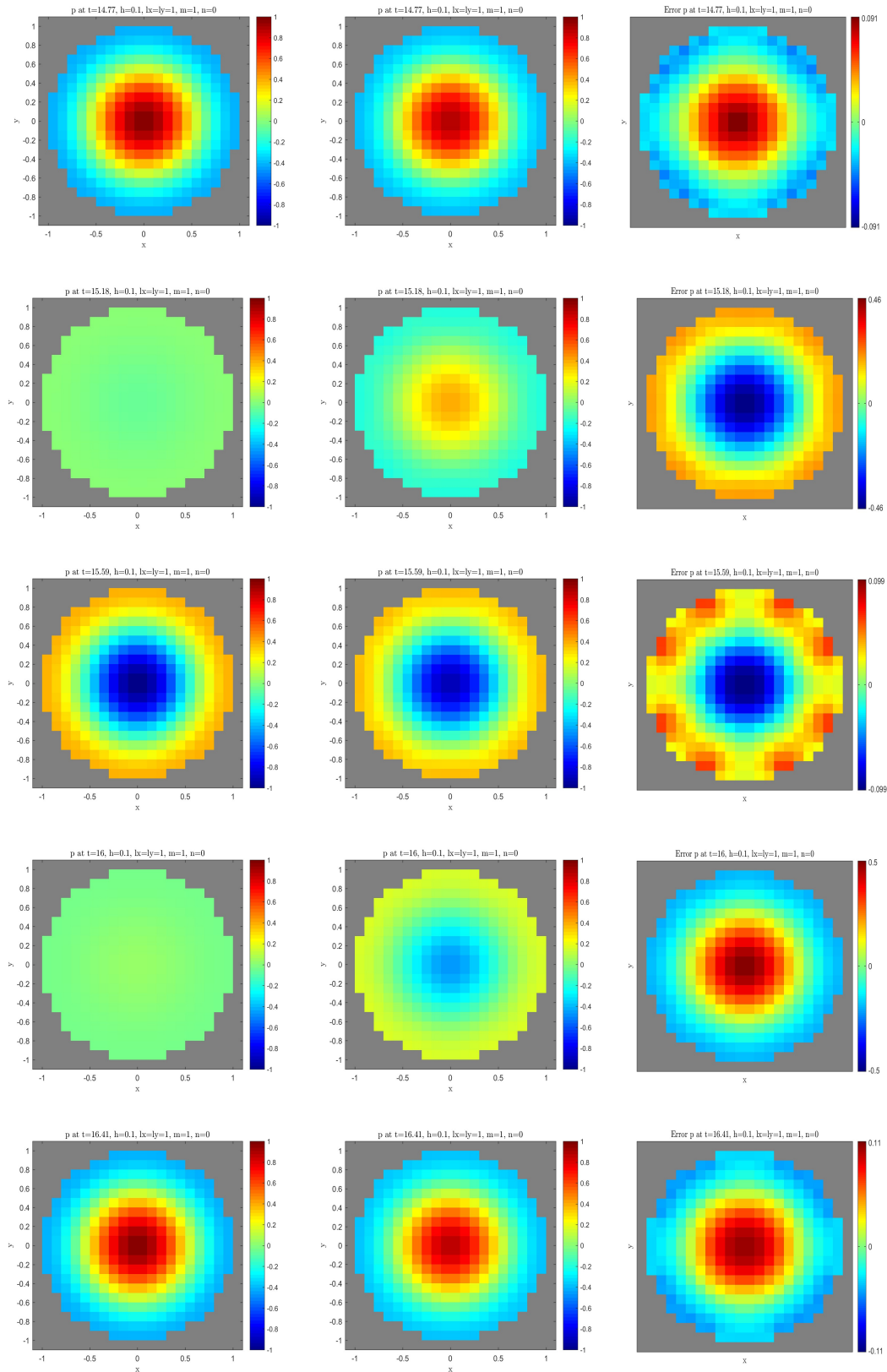


Figure 5.6.2: The solutions of p for circle domain at $t = 9T, 9.25T, 9.5T, 9.75T, 10T$, with $h = 0.1$ and $dt = 0.01$ for mode $m = 1, n = 0$. Left column: continuum solutions. Centre column: numerical solutions. Right column: error (i.e., continuum-numerical).

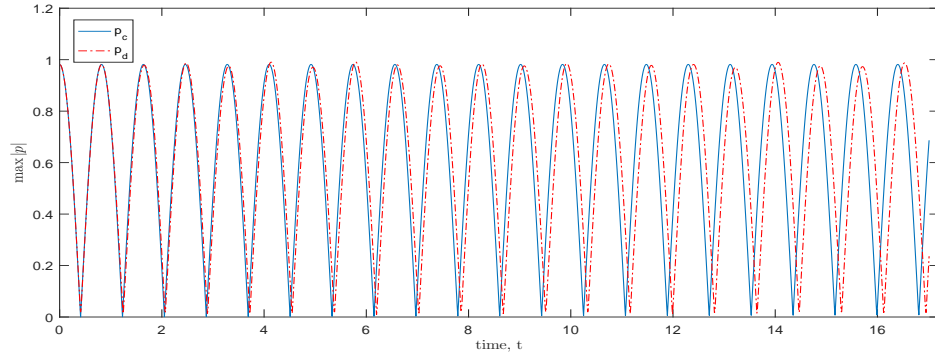


Figure 5.6.3: The maximum $|p|$ over circle domain at $h = 0.1$, $dt = 0.01$ for mode $m = 1$, $n = 0$.

the tenth period are shown in Figures 5.6.25, 5.6.26 and 5.6.27, for p , u and v , respectively. Contrary to the solutions with $h = 0.1$, the numerical solutions remain similar to the continuum solutions, and oscillate at close to the correct frequency. So the phase error is almost eliminated with higher resolution. This is illustrated more clearly in Figures 5.6.28 and 5.6.29. Note that mass and energy are conserved to high accuracy, as shown in Figure 5.6.30.

We have quantified the convergence over the first oscillation period, as in Section 5.4. From the log-log plot of various h against maximum error of p over circle domain, we found a slope of 1.06, indicating first-order convergence in h , as illustrated in Figure 5.6.31. The slope of u and v for both max norm and L_2 norm is summarised in Table 5.10. This time, we can see the unusual behaviour in the slope for u and v . For this case, we get some errors in (u, v) near boundary, as can be seen in Figure 5.6.32. This is why the max. norm does not converge. However, L_2 norm does converge. We also examined frequency behaviour for this experiment as shown in Figure 5.6.33. Over 20 grid spacings h , it is clear that the frequency is underestimated by the continuum frequency. As the error $E \propto h^n$, we then quantified and obtained slope of the line in log-log plot E versus h is 1.09, which interpreted as 1, a first-order convergence. The slope n is determined as 1.09, with 95% confidence interval of (0.7236, 1.453). So a slope $n = 1$ is consistent with this analysis.

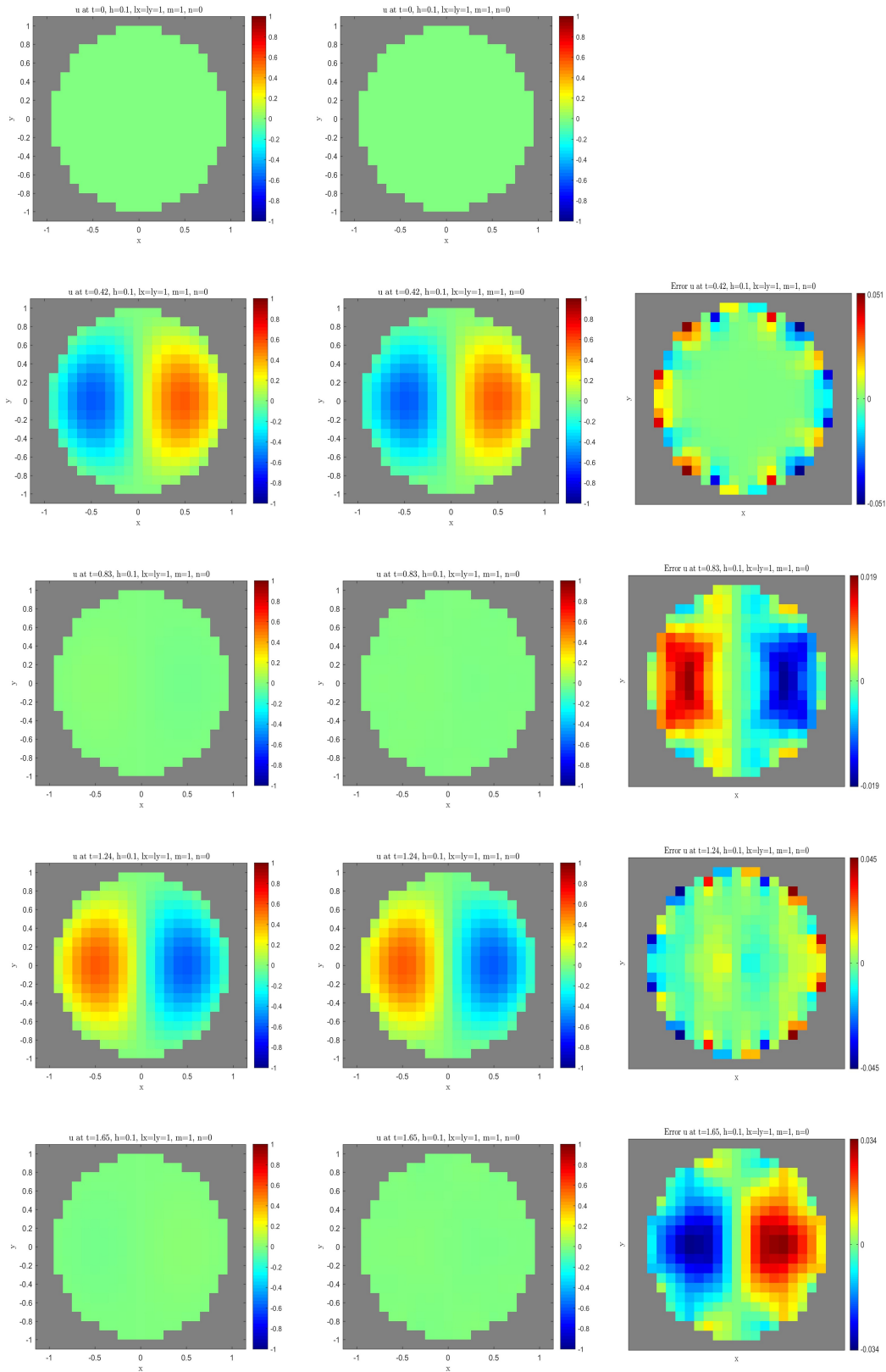


Figure 5.6.4: The solutions of u for circle domain at $t = 0, T/4, T/2, 3T/4, T$, with $h = 0.1$ and $dt = 0.01$ for mode $m = 1, n = 0$. Left column: continuum solutions. Centre column: numerical solutions. Right column: error (i.e., continuum-numerical).

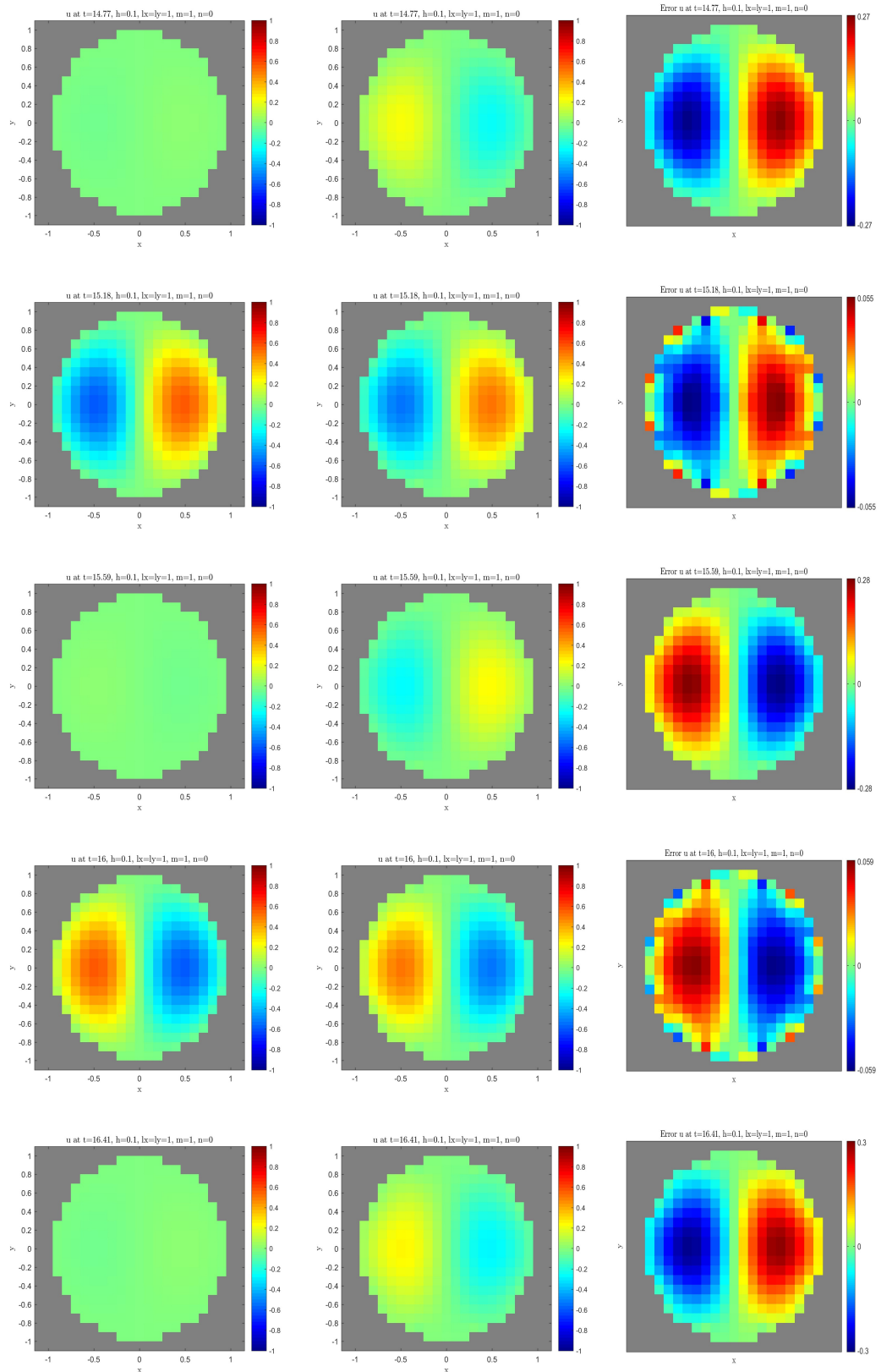


Figure 5.6.5: The solutions of u for circle domain at $t = 9T, 9.25T, 9.5T, 9.75T, 10T$, with $h = 0.1$ and $dt = 0.01$ for mode $m = 1, n = 0$. Left column: continuum solutions. Centre column: numerical solutions. Right column: error (i.e., continuum-numerical).

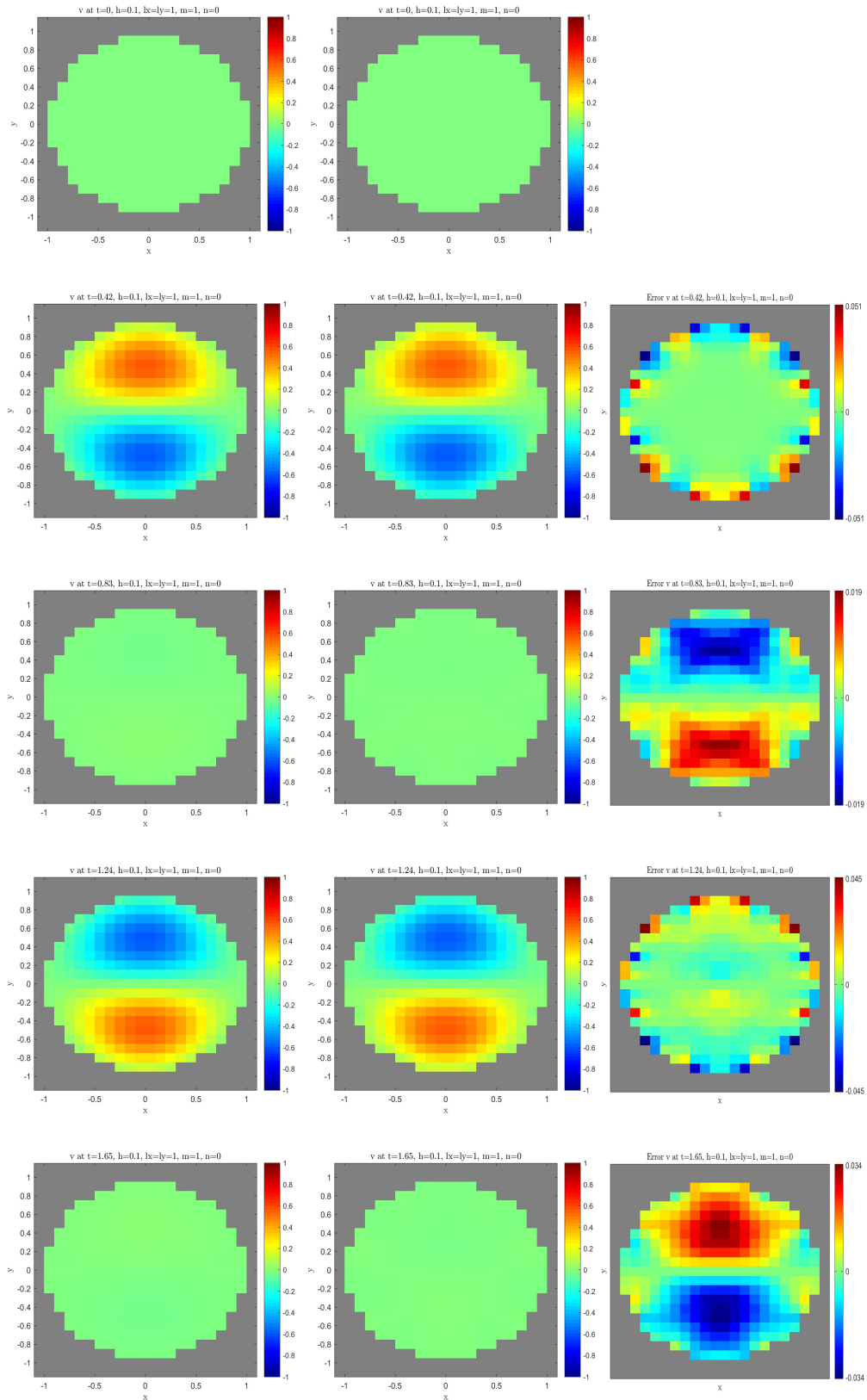


Figure 5.6.6: The solutions of v for circle domain at $t = 0, T/4, T/2, 3T/4, T$, with $h = 0.1$ and $dt = 0.01$ for mode $m = 1, n = 0$. Left column: continuum solutions. Centre column: numerical solutions. Right column: error (i.e., continuum-numerical).

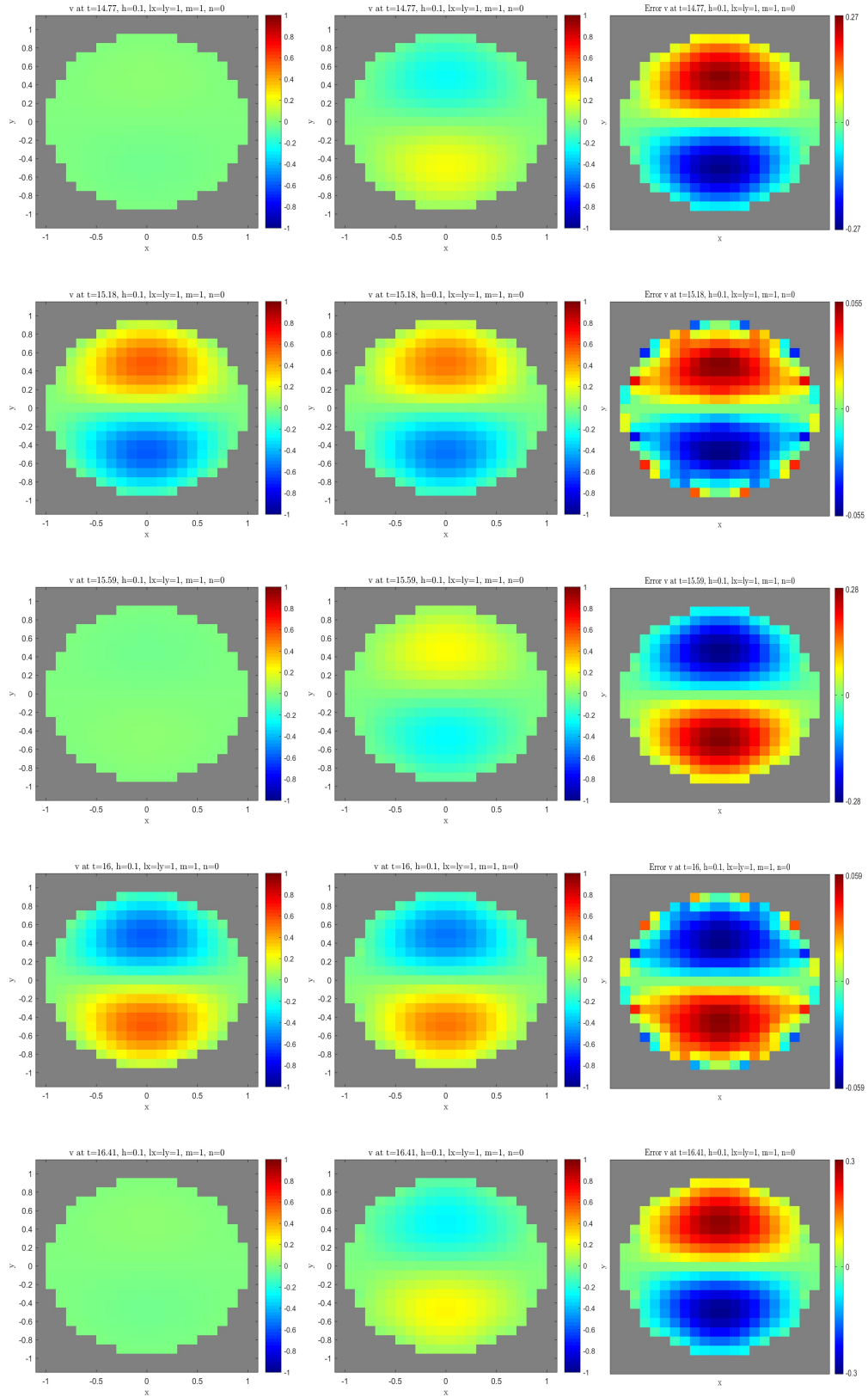


Figure 5.6.7: The solutions of v for circle domain at $t = 9T, 9.25T, 9.5T, 9.75T, 10T$, with $h = 0.1$ and $dt = 0.01$ for mode $m = 1, n = 0$. Left column: continuum solutions. Centre column: numerical solutions. Right column: error (i.e., continuum-numerical).

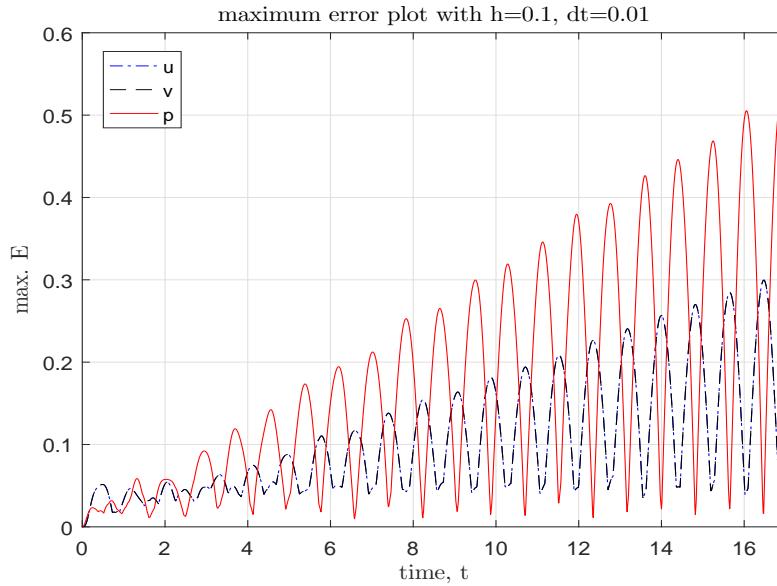


Figure 5.6.8: Maximum error over domain for $0 < t < 17 \approx 10T$, at $h = 0.1$, $dt = 0.01$, for mode $m = 1$, $n = 0$.

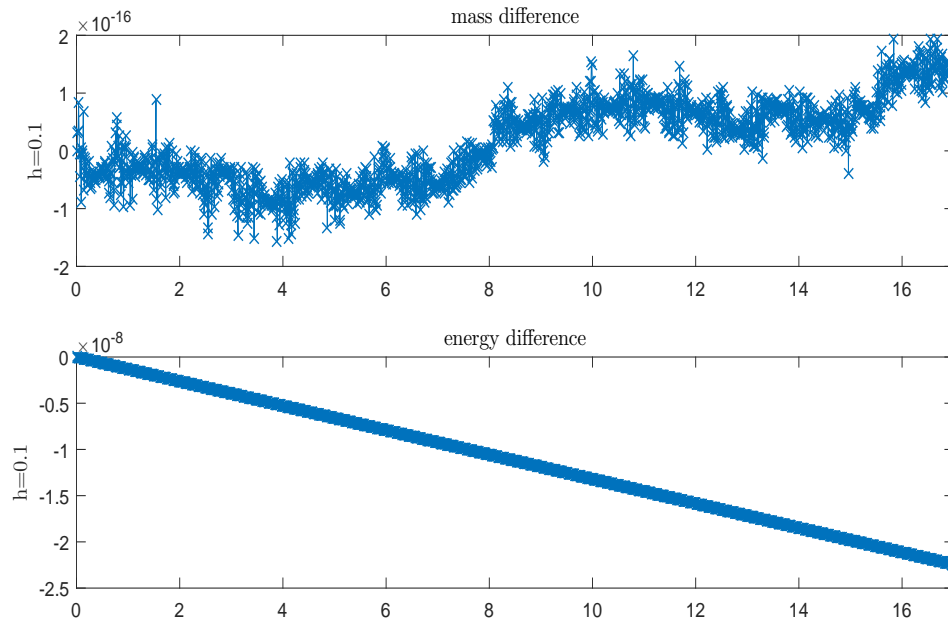


Figure 5.6.9: Mass and energy difference for circle domain, at $h = 0.1$, $dt = 0.01$ over $0 < t < 17 \approx 10T$, for mode $m = 1$, $n = 0$.

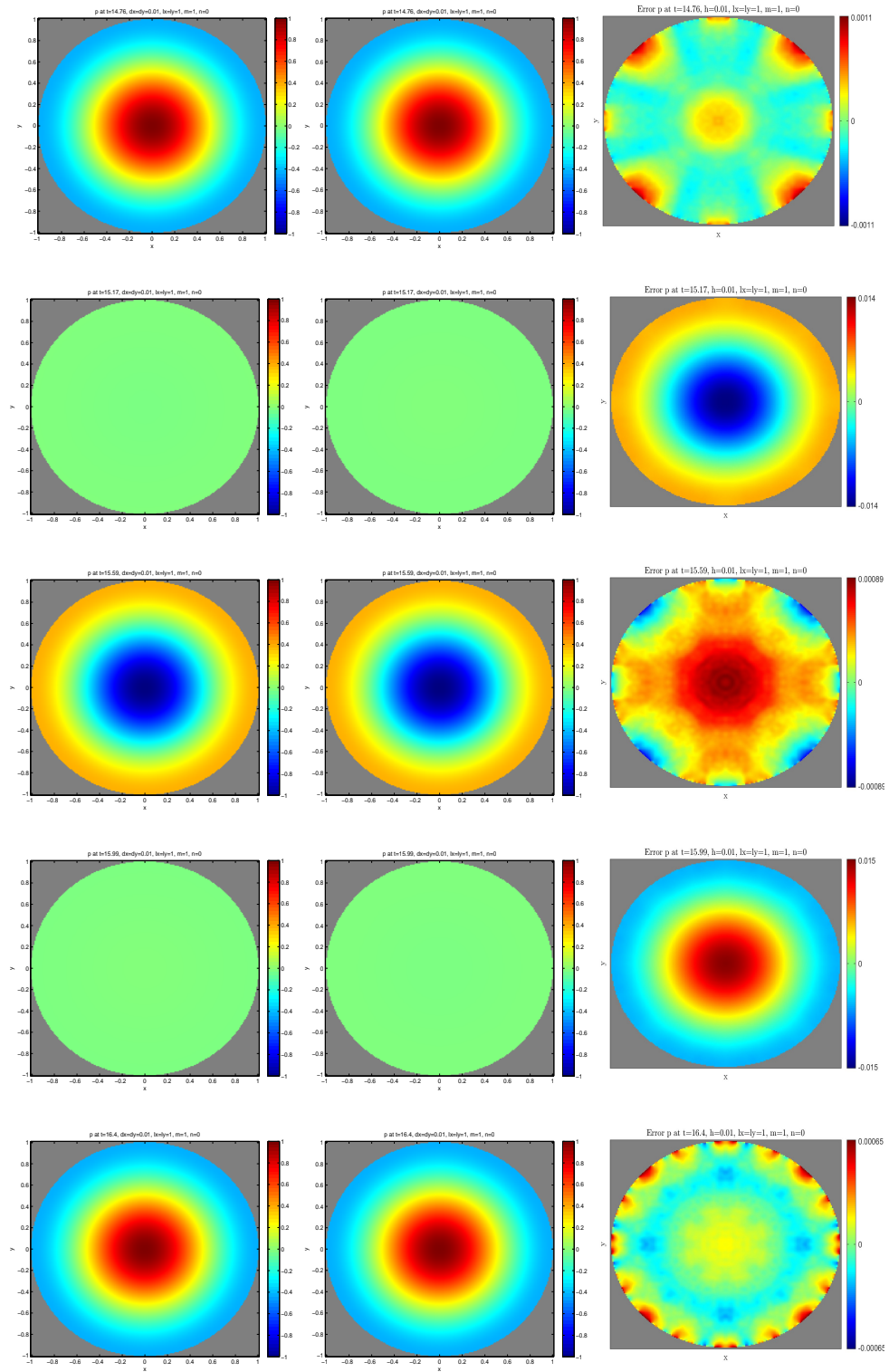


Figure 5.6.10: The solutions p for circle domain at $t = 9T, 9.25T, 9.5T, 9.75T, 10T$, with $h = 0.01$ and $dt = 0.005$ for mode $m = 1, n = 0$. Left column: continuum solutions. Centre column: numerical solutions. Right column: error (i.e., continuum-numerical).

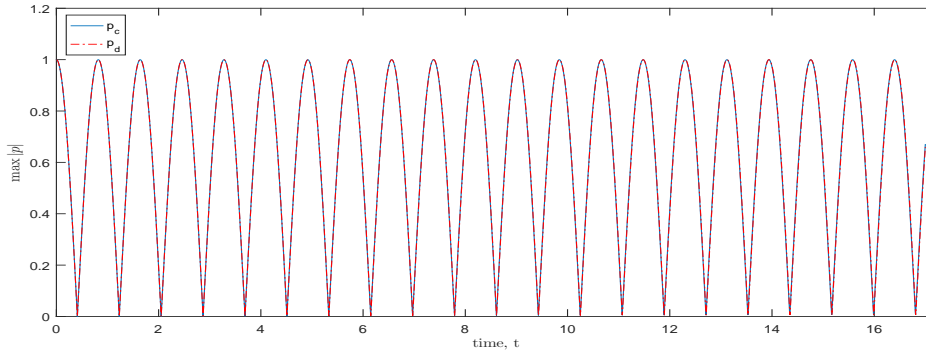


Figure 5.6.11: The maximum of $|p|$ over $0 < t < 17 \approx 10T$ at $h = 0.01$ with $dt = 0.005$ for circle domain mode $m = 1, n = 0$.

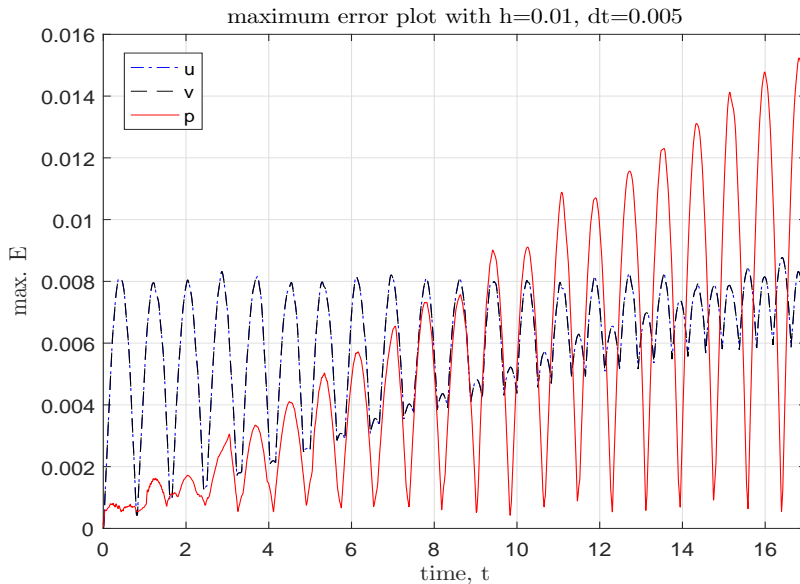


Figure 5.6.12: Maximum error over domain at $0 < t < 17 \approx 10T, h = 0.01, dt = 0.005$ for mode $m = 1, n = 0$.

Table 5.10: The convergence rate of u, v and p in max norm and L_2 norm, for circle domain with mode $m = 1, n = 1$. The slope is for the lines in Figure 5.6.31, indicate the rate of convergence.

	max norm			L_2 norm		
	slope	95% c.i	scaling factor	slope	95% c.i	scaling factor
u	0.0176	(-0.1418, 0.177)	0.13	0.9368	(0.7209, 1.153)	0.5071
v	-0.1816	(-0.3147, -0.0484)	0.07	0.6586	(0.5761, 0.7411)	0.1530
p	1.0571	(0.8242, 1.29)	0.75	1.0789	(0.7508, 1.407)	0.6470

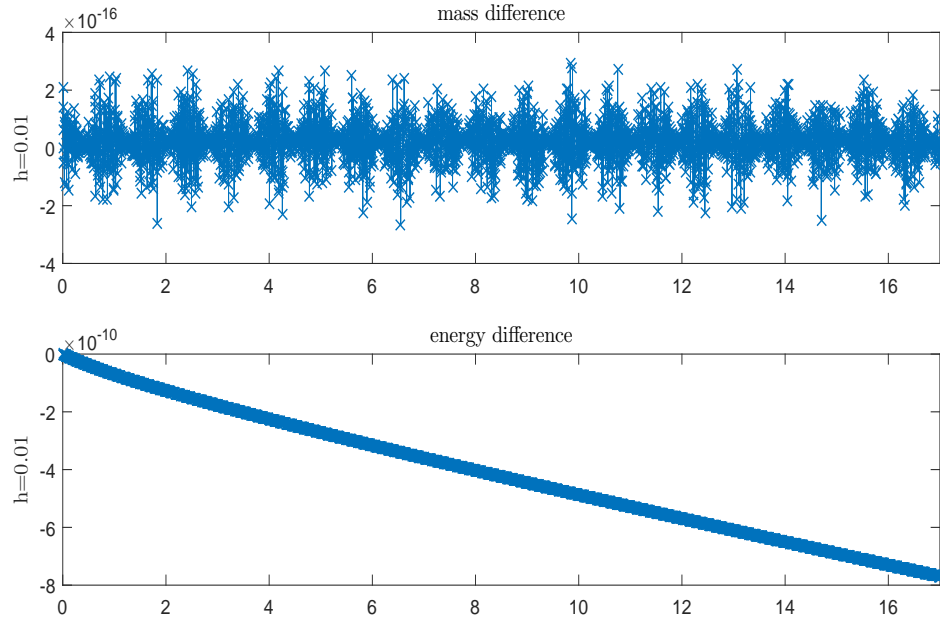


Figure 5.6.13: Mass and energy difference for circle domain, at $h = 0.01$, $dt = 0.005$ over $0 < t < 17 \approx 10T$, for mode $m = 1$, $n = 0$.

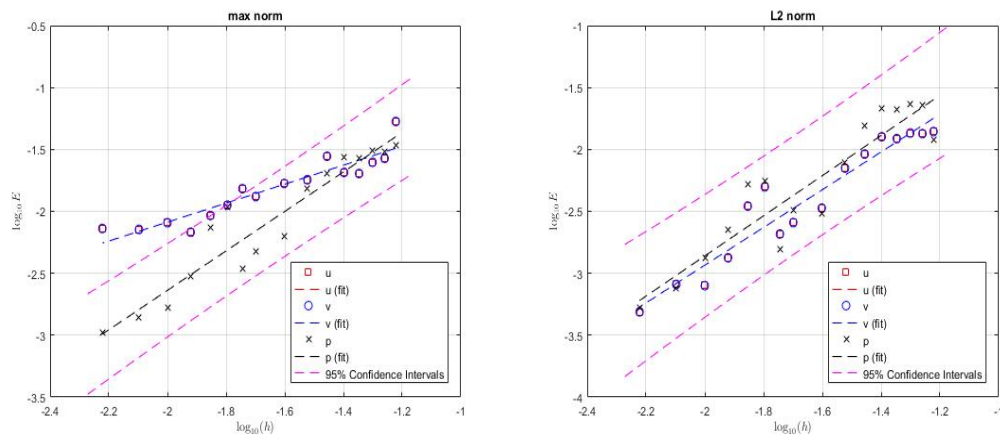


Figure 5.6.14: Convergence plot for circle domain with mode $m = 1$, $n = 0$ at various h in range $0.2 > h > 0.02$ at fixed $dt = 0.02$. The error in (a) is calculated in max norm, and (b) in L_2 norm over domain. Slope of the line is summarised in Table 5.9, indicate the rate of convergence.

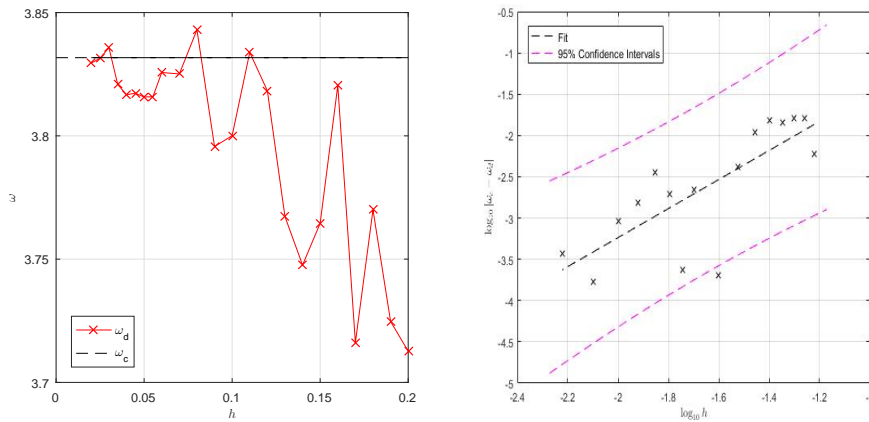


Figure 5.6.15: The frequency of wave in circle domain with mode $m = 1, n = 0$, and log-log plot error in frequency at various h . The slope of the line is 1.66158, with 95% confidence interval (1.002, 2.321). The scaling factor is 1.00801.

5.6.6 The effect of cell selection

In the previous two sections, we have discussed the numerical solutions of wave equations in a circular domain, where the active cells are chosen according to condition (i) in section 5.2. As discussed in that section, there are other possibilities to choose the active cells for our numerical domain. In this section we repeat the experiment of section 5.6.2, but cells are now retained if all the four corners of the cell lie within the continuum domain (condition (ii) of section 5.2). With the mode $m = 1$ and $n = 0$, the frequency $\omega \approx 3.8317$, and the period of the wave is $T = 2\pi/\omega \approx 1.6398$. As in previous sections, we perform simulations up to $t = 10T$ (i.e., $t \approx 17$), and the time stepping stills need to satisfy the condition (5.2.14). All solutions are recorded at every quarter period, but we only present the solutions over one and ten wave periods.

We begin with the experiment with $h = 0.1$ and $dt = 0.01$. Shown in Figures 5.6.34 and 5.6.35 are the solutions for p over $0 < t < T$ and $9T < t < 10T$, respectively. As we can see in the solutions, there is a reasonably large error between continuum and numerical solutions as early one period. The error then grows larger as the experiment continues.

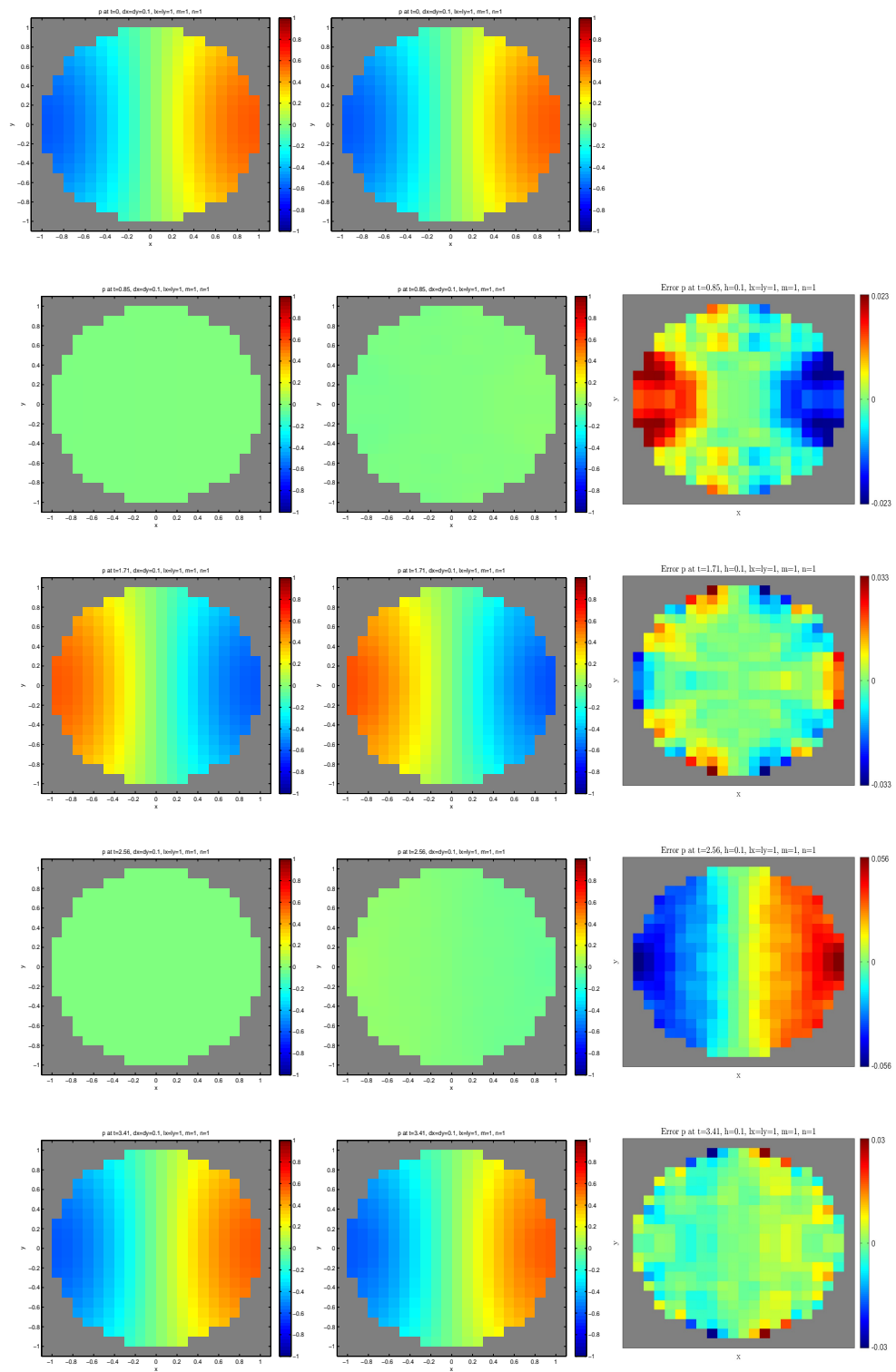


Figure 5.6.16: The solutions for p at $t = 0, 0.25T, 0.5T, 0.75T, T$ with $h = 0.1$, $dt = 0.05$, for $m = 1$, $n = 1$. Left column: continuum solutions. Centre column: numerical solutions. Right column: error (i.e., continuum-numerical).

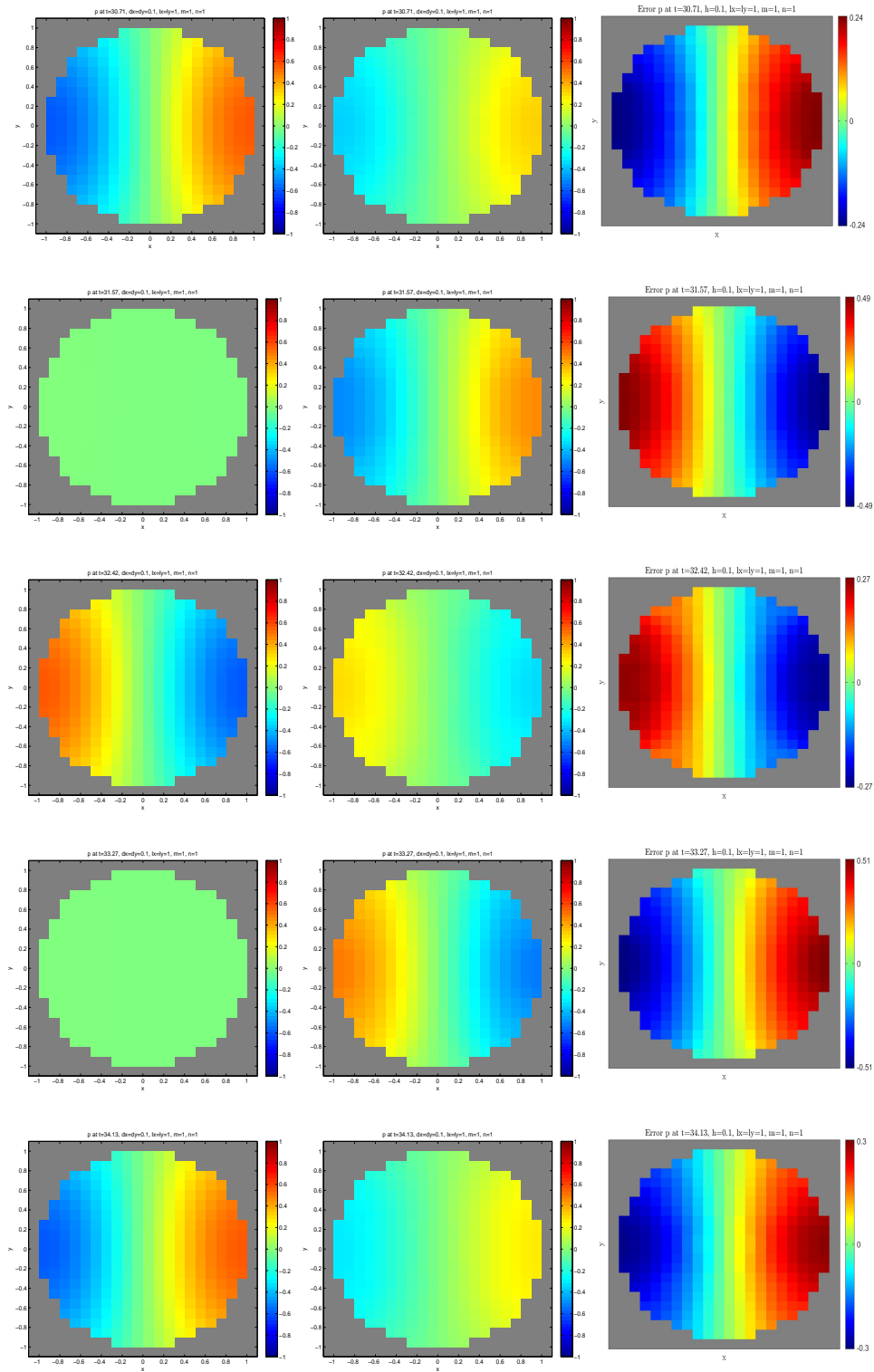


Figure 5.6.17: The solutions for p at $t = 9T, 9.25T, 9.5T, 9.75T, 10T$ with $h = 0.1, dt = 0.05$, for $m = 1, n = 1$. Left column: continuum solutions. Centre column: numerical solutions. Right column: error (i.e., continuum-numerical).

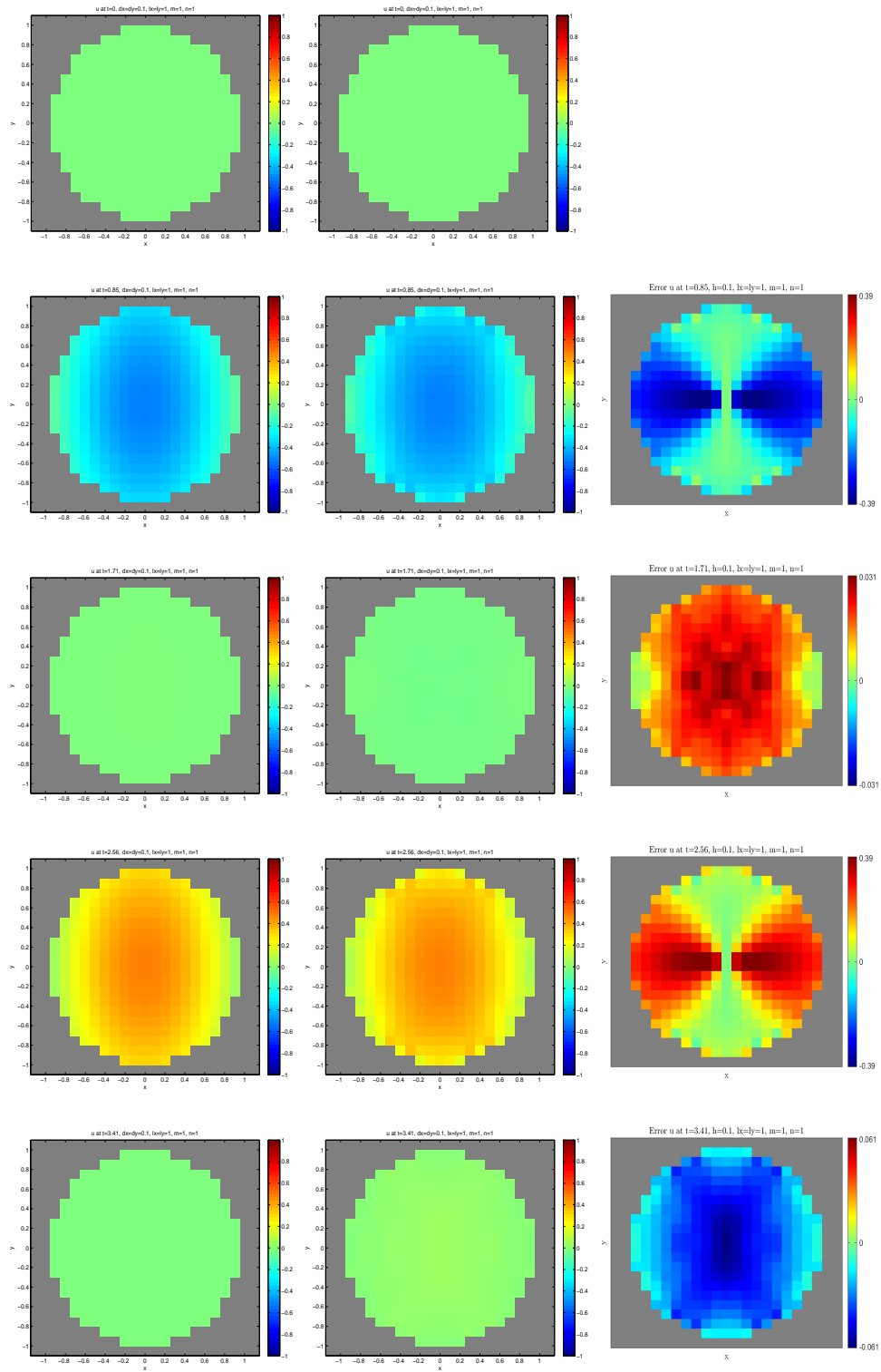


Figure 5.6.18: The solutions for u at $t = 0, 0.25T, 0.5T, 0.75T, T$ with $h = 0.1, dt = 0.05$, for $m = 1, n = 1$. Left column: continuum solutions. Centre column: numerical solutions. Right column: error (i.e., continuum-numerical).

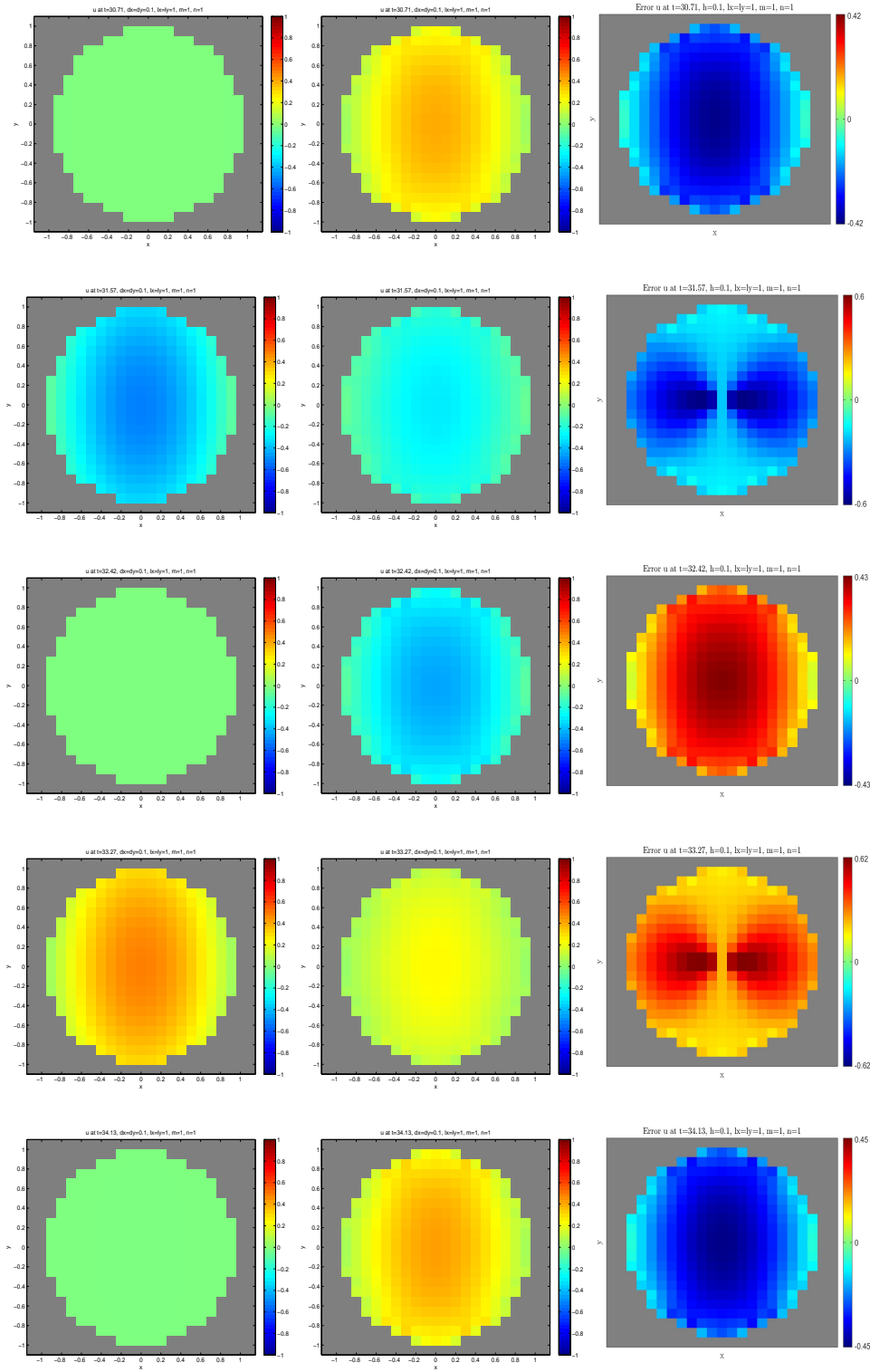


Figure 5.6.19: The solutions for u at $t = 9T, 9.25T, 9.5T, 9.75T, 10T$ with $h = 0.1, dt = 0.05$, for $m = 1, n = 1$. Left column: continuum solutions. Centre column: numerical solutions. Right column: error (i.e., continuum-numerical).

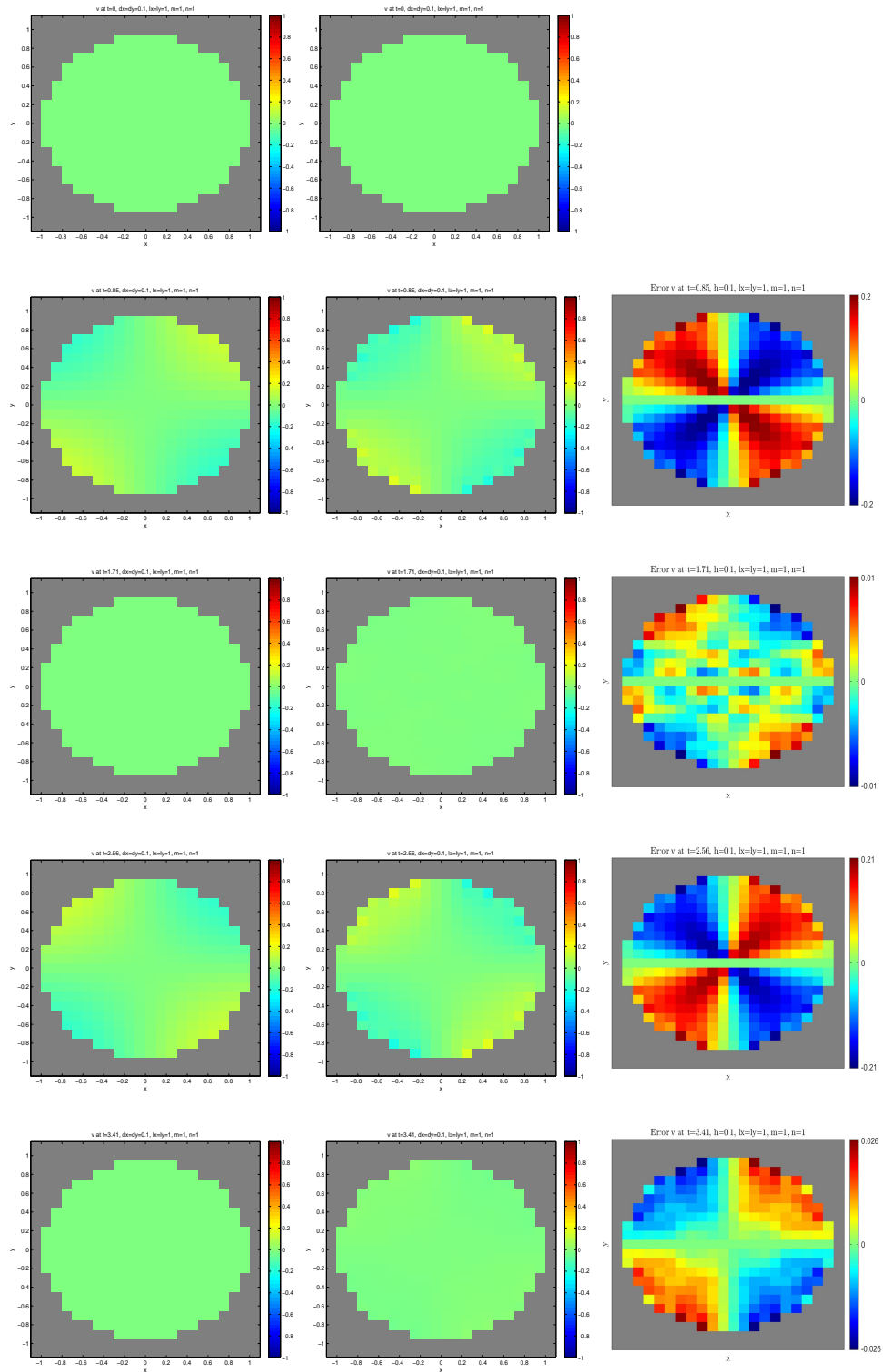


Figure 5.6.20: The solutions for v at $t = 0, 0.25T, 0.5T, 0.75T, T$ with $h = 0.1, dt = 0.05$, for $m = 1, n = 1$. Left column: continuum solutions. Centre column: numerical solutions. Right column: error (i.e., continuum-numerical).

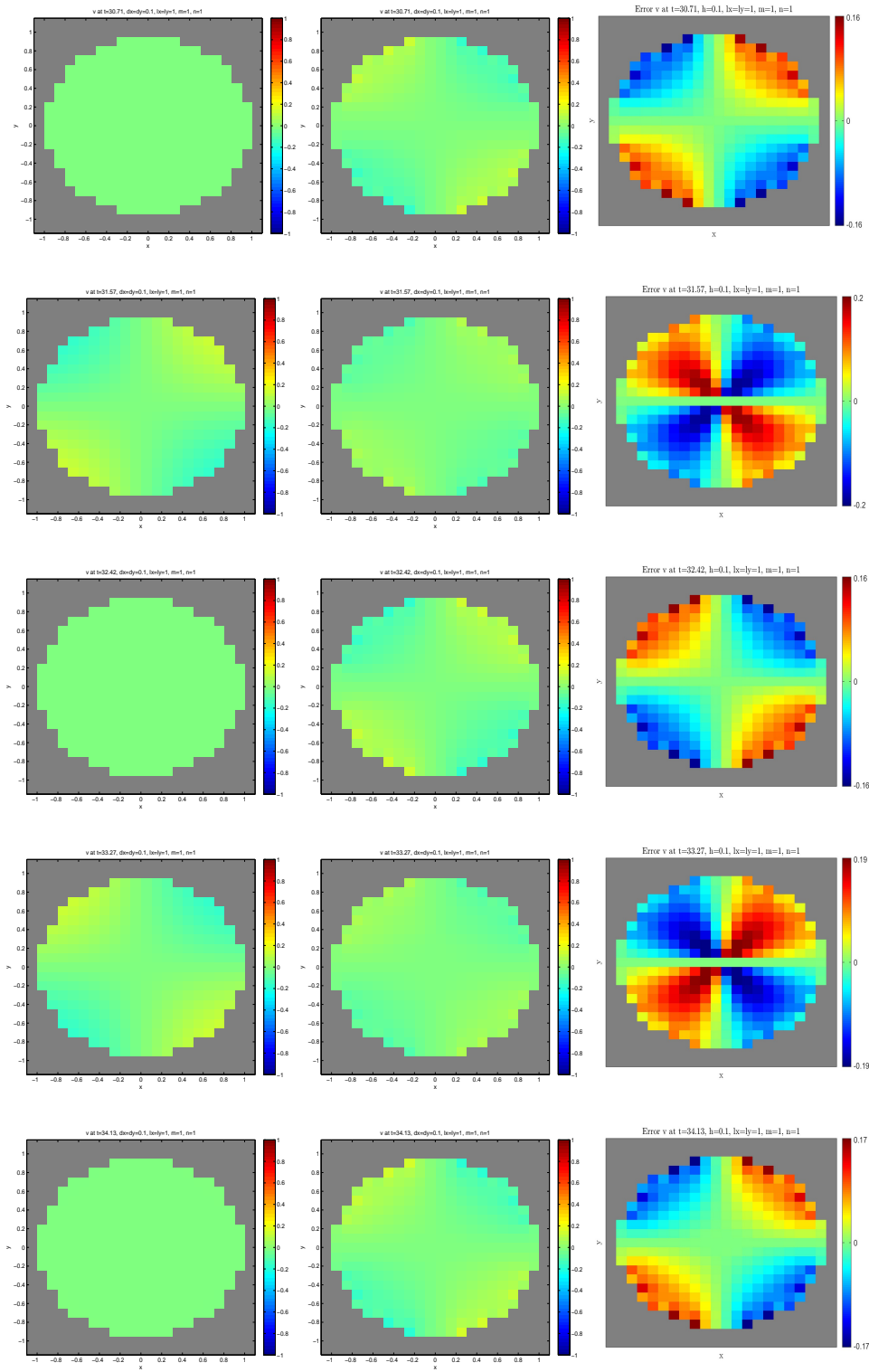


Figure 5.6.21: The solutions for v at $t = 9T, 9.25T, 9.5T, 9.75T, 10T$ with $h = 0.1$, $dt = 0.05$, for $m = 1$, $n = 1$. Left column: continuum solutions. Centre column: numerical solutions. Right column: error (i.e., continuum-numerical).

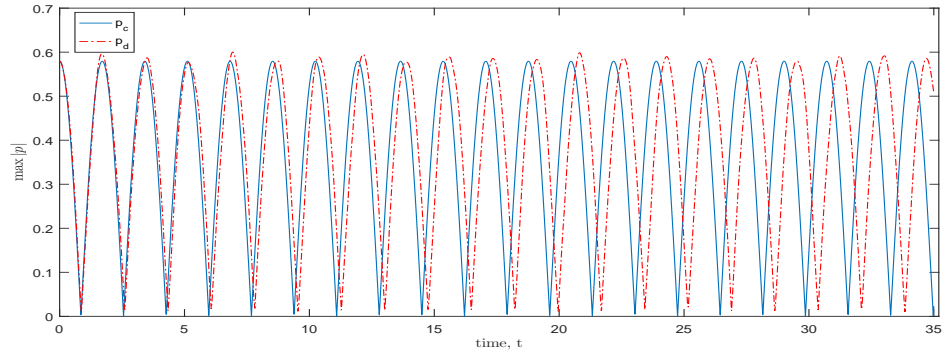


Figure 5.6.22: The maximum $|p|$ for circle domain at $h = 0.1$ with $dt = 0.01$, over $0 < t < 10T$ with mode $m = 1, n = 1$.

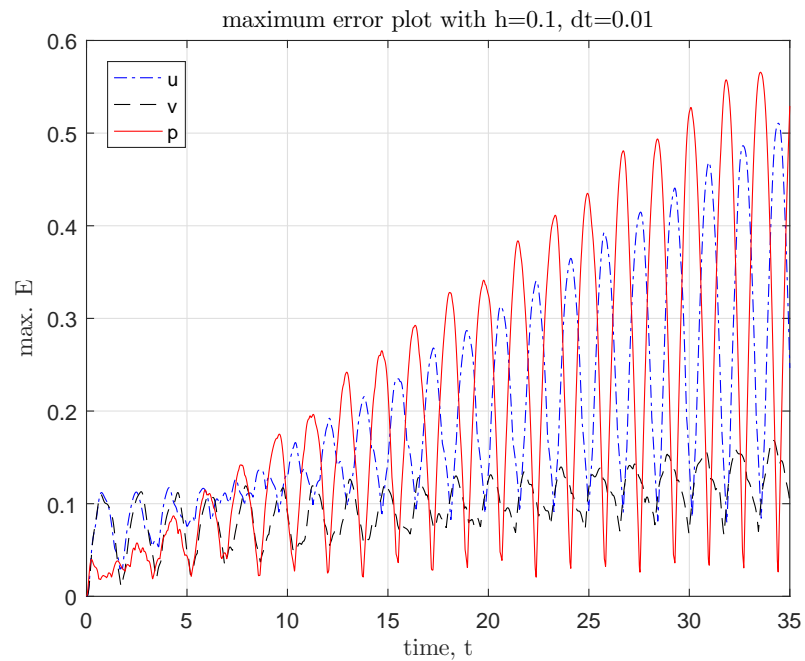


Figure 5.6.23: Maximum error over $0 < t < 10T$ for circle domain at $h = 0.1, dt = 0.01$ with mode $m = 1, n = 1$.

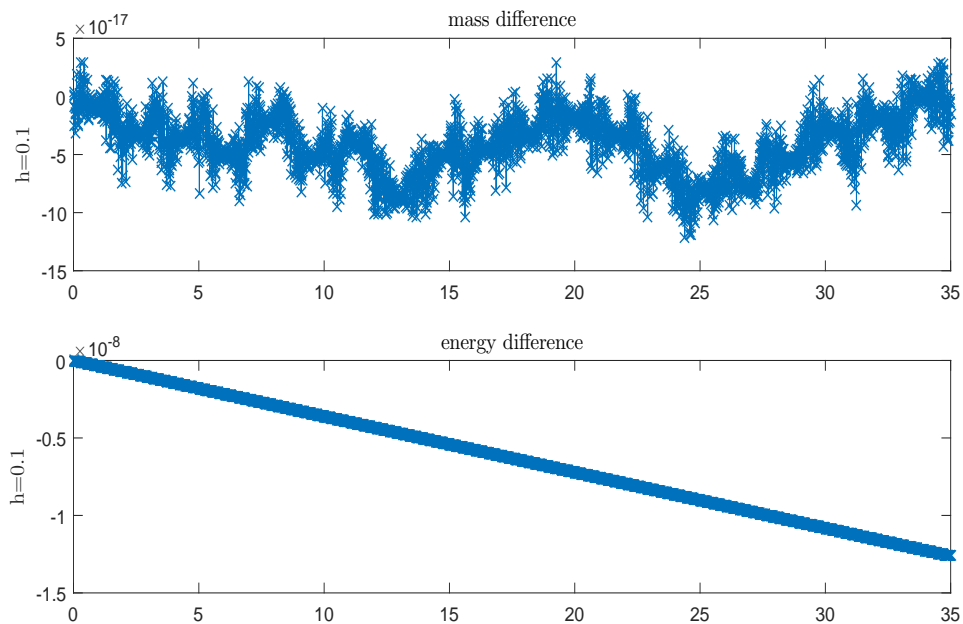


Figure 5.6.24: Mass and energy difference for circle domain, at $h = 0.1$, $dt = 0.01$ over $0 < t < 10T \approx t = 35$, for mode $m = 1$, $n = 1$.

However, it is not clear what kind of error is appearing. To understand this, we look at a series of maximum $|p|$ versus time – see Figure 5.6.36. It is clear that amplitude and phase errors arise in this experiment (unlike for the case with condition (i) in section 5.6.2 where there is no amplitude error recorded). As early $t = T/2 \approx 0.8$, these errors are apparent. We also note that the amplitude errors reduces at $t = 10.3$, which is when the wave is almost exactly out of phase. After $t = 10.3$, the phase error is reducing. So, as shown in Figure 5.6.37, the maximum error for p over $10T$ has an increasing pattern to the out of phase point at $t \approx 10.3$, before reducing after $t \approx 10.4$.

The evolutions of u and v also have a similar pattern. We just show the evolution of u and v over one period as can be seen in Figures 5.6.38 and 5.6.39, along with error plot Figure 5.6.37. Shown in Figures 5.6.40 and 5.6.41 are maximum $|u|$ and $|v|$ over $0 < t < 10T$. We can see that there are large phase errors throughout, but the amplitude error are smaller than those to p . Despite these errors, the C-grid is still doing an excellent job

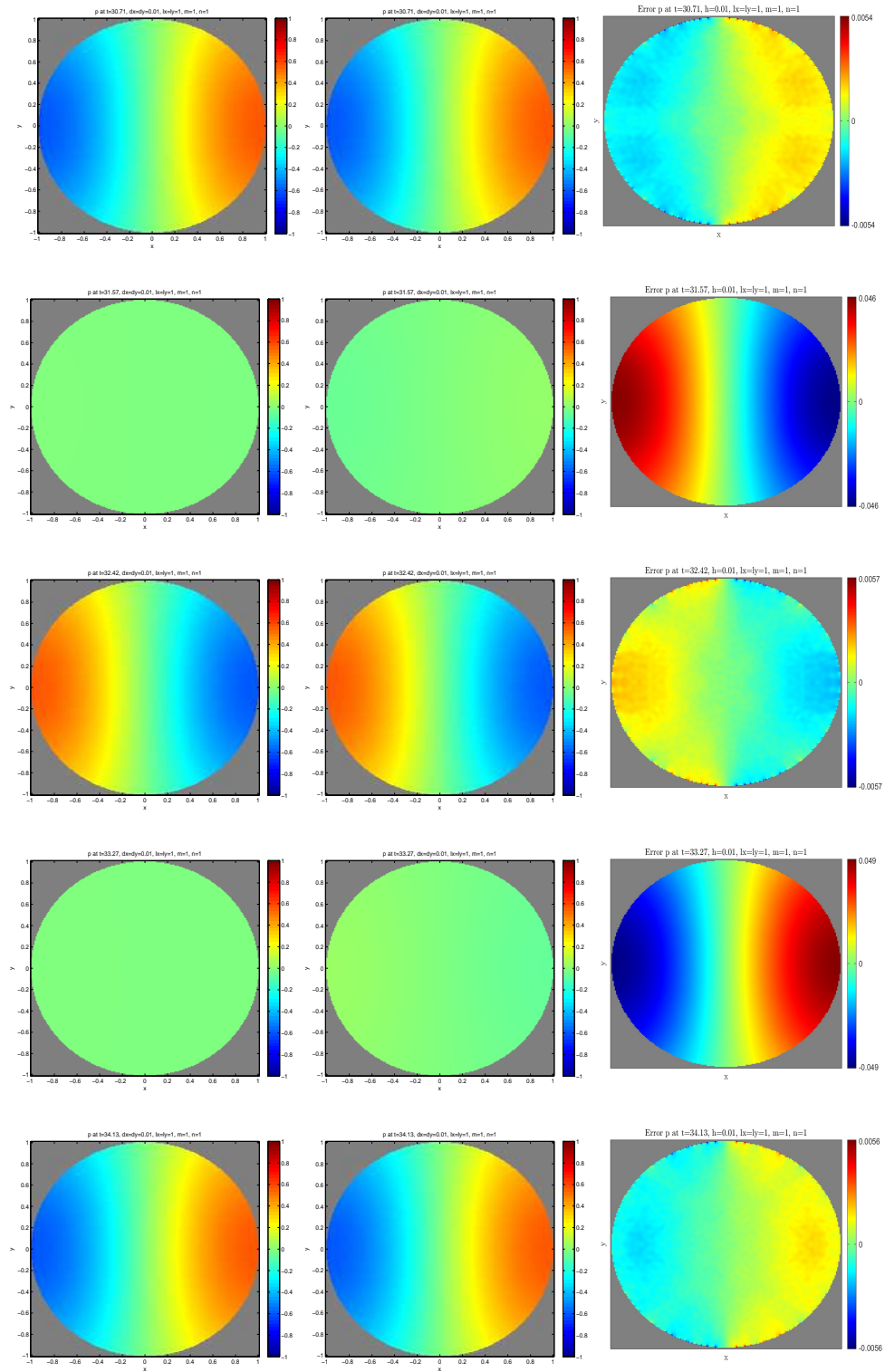


Figure 5.6.25: The solutions for p at $t = 9T, 9.25T, 9.5T, 9.75T, 10T$ with $h = 0.01$, $dt = 0.005$, for $m = 1, n = 1$. Left column: continuum solutions. Centre column: numerical solutions. Right column: error (i.e., continuum-numerical).

conserving energy and mass, as shown in Figure 5.6.42.

We next examine numerical solutions at higher spatial resolution, with $h = 0.01$ and $dt = 0.005$. Figures 5.6.43 and 5.6.44 show the comparison of the solutions for p between continuum and numerical solutions for period one and ten, respectively. Now, all the errors in period one are almost negligible, while those in period ten are small. All the errors also can be seen in a series of maximum $|p|$ versus t as showed in Figure 5.6.45. We can see that there is a weak phase error growing as time increasing to the end of experiment. This is also clear in Figure 5.6.46. We note that the size of the errors now improves with the errors not approaching the maxima because the wave still propagates at wrong phase-speed (unlike the case with $h = 0.1$, the wave already back in phase over $10T$). Corresponding behaviour for u and v over the tenth period, is shown in Figures 5.6.47 and 5.6.48. Again, the mass and energy quantity are conserved in this setting and is shown in Figure 5.6.49.

We also repeated the same experiment at some various values of resolution h with a fixed time step $dt = 0.005$. For each grid spacing, we recorded the maximum error for each variable over ten period of oscillations as can be seen in Figure 5.6.50(a). However, this results in a confused picture. This is because by $t = 10T \approx 17$ many solutions have gone completely out of phase at some time before $t < 17$, as happened for those solutions at $h = 0.2$ and $h = 0.1$, which thus have the same error. So, we instead measure the error over $0 < t < 2$ (i.e., an integer after one period) to quantified the convergence as can be seen in Figure 5.6.50(b). It is clear that the error reduces as h reduces. We find $E \propto h^n$, with scaling exponents n of 0.9 for both u and v , with 95% confidence interval of (0.8362,0.9757). So a slope $n = 1$ is consistent with the analysis that indicates a first-order convergence in h , as expected.

5.7 Summary

In this chapter, we have seen numerical solutions of waves equation sloshing in a square and circle domain. For the square domain, we have seen the solutions at two particular cases: (i) boundaries aligned with the grid, and (ii) boundaries unaligned with the grid. While for the circle domain, we have seen the numerical solutions of two different wave modes (with different azimuthal wavenumber) sloshing in the domain. The exact continuum solutions is first derived to be used as an initial condition in the numerical experiment as well as to compute the error of the solutions.

For the square domain boundaries aligned with the grid, we have shown that second-order convergence in h is achieved, since central second-order finite-difference formulation is used in the experiments. We thus confirmed that the rate of convergence will not be affected as long as the boundaries aligned with the grid (second-order convergence in h is obtained with angle $\theta = 90^\circ$).

On the other hand, there is reduction of the order of accuracy for the case of unaligned boundaries with staircase boundary. We have quantified this degradation in for u , v and p . The quantification is obtained after one period of wave oscillation. We summarised all the results in Table 5.11. It is shown that first-order convergence in h is obtained when the square has staircase boundaries, which is consistent with the analysis in chapters 3 and 4. We also have examined the effect of tilt angle. We have quantified the spatial convergence rate at some angles. We found that the scaling factor for spatial error decrease with θ , which as expected. This is agree with the results found in [32] for channel flow, where it was showed that scaling factor for spatial error decrease with θ .

The solutions for waves sloshing in a circular domain are different. The investigation was split into three experiments: (i) mode $m = 1, n = 0$, (ii) mode $m = 1, n = 1$, and (iii) mode $m = 1, n = 0$. In experiments (i) and (ii), we used cell centre activation, while in (iii) we used 4 corners of each cells as activation. Here, we also quantified the convergence rate

at various h after one period, as summarised in Table 5.11. For all experiments, the best convergence rate that we found is first-order in h .

Up to date, we find no other examples numerical experiments like in this chapter. So we compare our results with other equivalent numerical experiments. As discussed in section 5.1, [67] studied the convergence rate of wave reflection at a straight boundary and cylinder using only three different resolutions (the results is showed in Table 5.12). While in this thesis, we considered wave sloshing in a closed domain focusing on a square and a circular domain. In [67], they only considered the effects of wave reflection after hitting a boundary, not the effects of staircase boundary after a certain time (one and ten period) like we considered in this thesis. It is important to mention here that the main different of our works is we quantified the rate of convergence for u , v and p with a set values of h , not only three as can be found in [67, 33]. We can see that [67] obtained convergence rates between 0.6 and 1 for u , v and p in the L_2 norm, based only at three different resolutions. For the same experiment at three resolutions, but in three-dimensional, [33, 27] report errors of $O(\sqrt{h})$ for all u , v and p in the L_2 norm. It is clear evidence that staircase boundary has degraded the accuracy of numerical solution. However, the quantification must be done at various number of resolutions, as we can get almost any gradient that we like with the few points. Thus we needed many numerical experiments (more than 20 grid points) to see even somewhat reliable slopes. So convergence studies with just a few runs could be very misleading.

Table 5.11: The convergence rate for u , v and p in max norm and L_2 norm, at various h for the specific domain.

Domain	max norm			L_2 norm		
	u	v	p	u	v	p
square (aligned)	1.82	1.89	1.89	1.84	1.86	1.89
square (tilted at $\pi/4$)	1.16	1.16	1.15	1.24	1.24	1.24
square (tilted at $\pi/6$)	$O(1)$	$O(1)$	1.05	0.78	0.71	1.05
square (tilted at $\pi/12$)	$O(1)$	$O(1)$	1.05	0.6	0.6	1.07
square (tilted at $\pi/18$)	$O(1)$	$O(1)$	1.09	0.62	0.64	1.05
square (tilted at $\pi/36$)	$O(1)$	$O(1)$	0.95	0.63	0.64	1.35
circle ($m = 1, n = 0$)	1.11	1.11	1.59	1.59	1.59	1.68
circle ($m = 1, n = 1$)	$O(1)$	$O(1)$	1.06	0.94	0.66	1.08
circle ($m = 1, n = 0$) 4 corners	1.03	1.03	1.04	–	–	–

Table 5.12: The convergence rate obtained by [67] for the case of wave reflection at specific domain in L_2 norm. The convergence rate is measured at three grid spacings.

Domain	u	v	p
straight boundary (aligned at $\pi/4$)	0.96	1.17	1.14
straight boundary (aligned at $\pi/6$)	0.62	0.67	0.75
straight boundary (aligned at $3\pi/8$)	0.86	0.7	0.6
cylinder	0.71	0.6	0.74

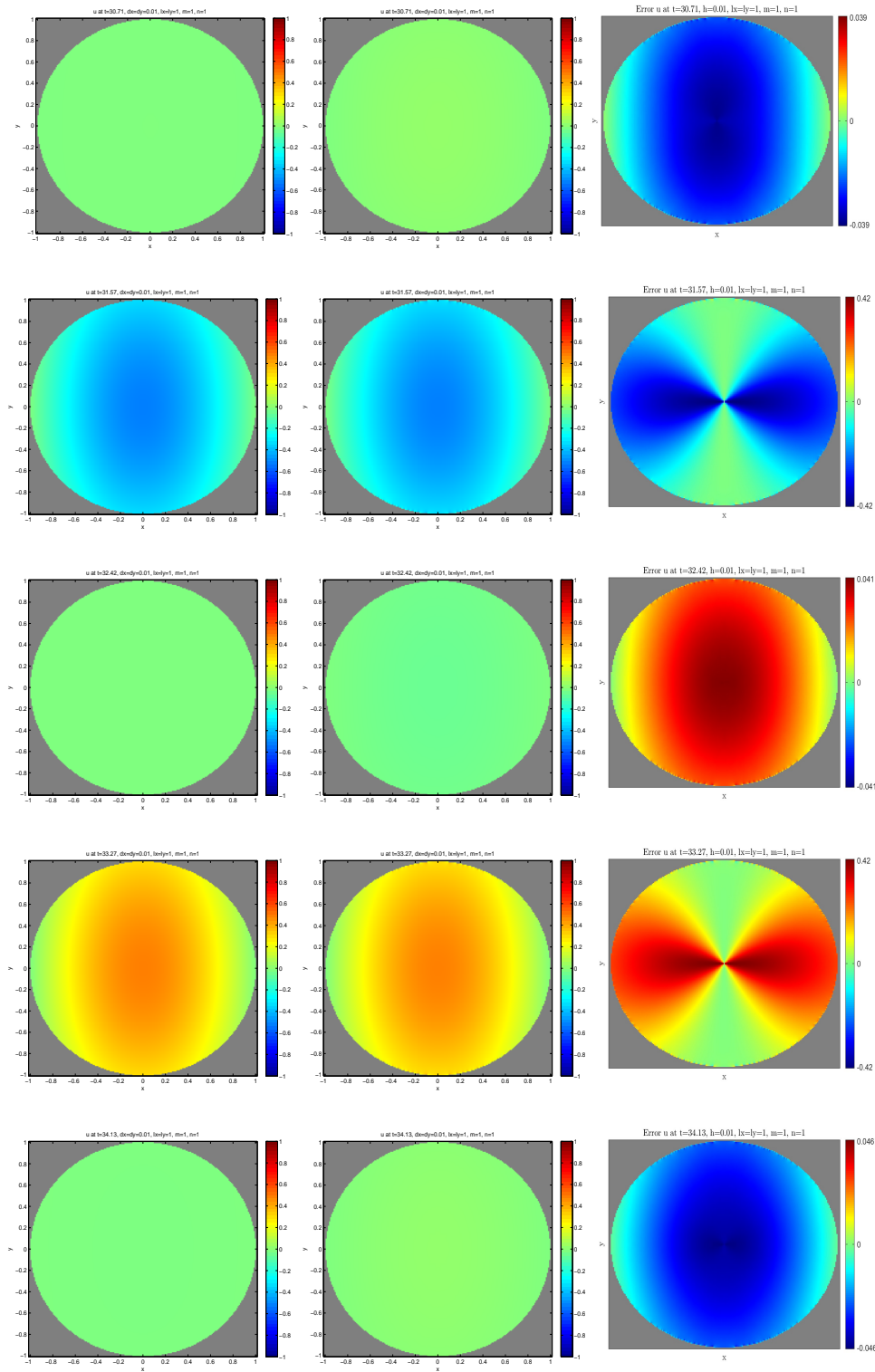


Figure 5.6.26: The solutions for u at $t = 9T, 9.25T, 9.5T, 9.75T, 10T$ with $h = 0.01$, $dt = 0.005$, for $m = 1$, $n = 1$. Left column: continuum solutions. Centre column: numerical solutions. Right column: error (i.e., continuum-numerical).

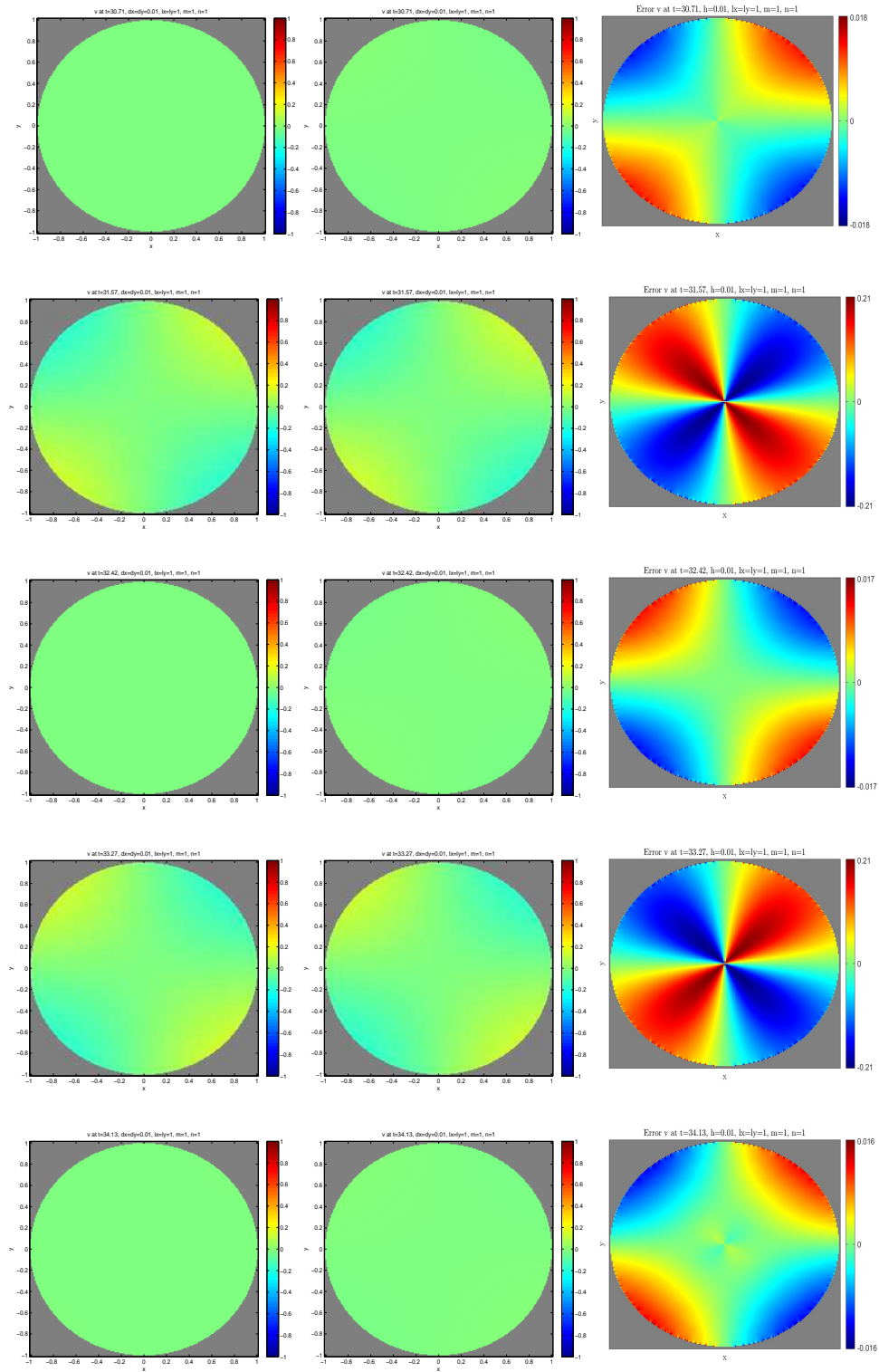


Figure 5.6.27: The solutions for v at $t = 9T, 9.25T, 9.5T, 9.75T, 10T$ with $h = 0.01$, $dt = 0.005$, for $m = 1, n = 1$. Left column: continuum solutions. Centre column: numerical solutions. Right column: error (i.e., continuum-numerical).

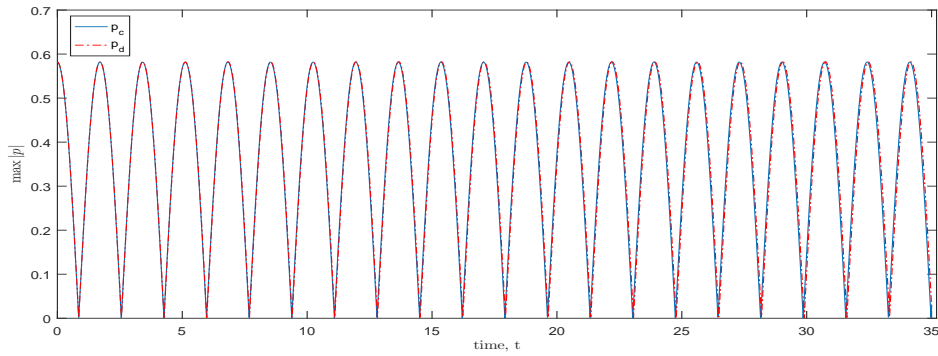


Figure 5.6.28: The maximum $|p|$ for circle domain at $h = 0.01$ with $dt = 0.005$, over $0 < t < 10T$ with mode $m = 1, n = 1$.

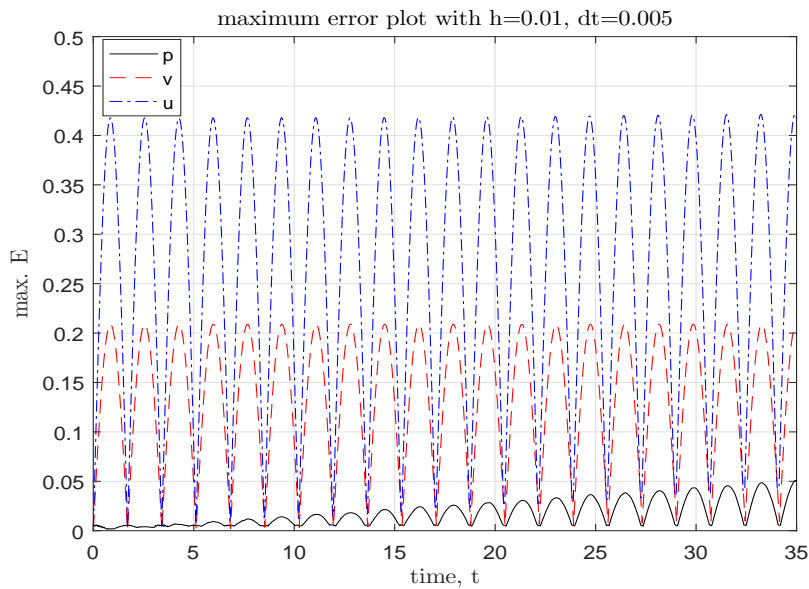


Figure 5.6.29: Maximum error for u, v and p over $0 < t < 10T$, for circle domain, at $h = 0.01, dt = 0.005$ with mode $m = 1, n = 1$.

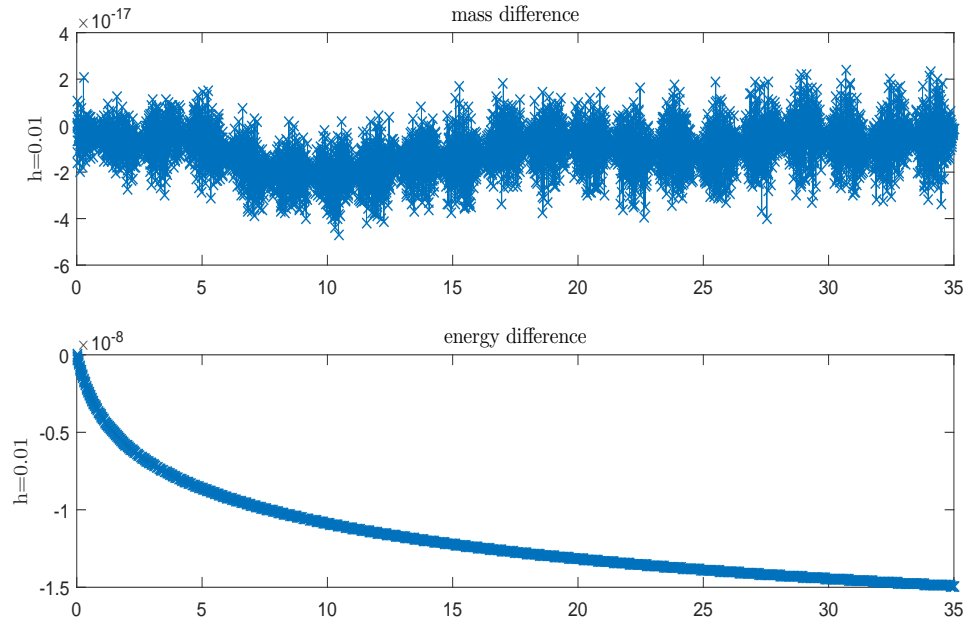


Figure 5.6.30: Mass and energy difference for circle domain, at $h = 0.01$, $dt = 0.005$ over $0 < t < 10T \approx t = 35$, for mode $m = 1$, $n = 1$.

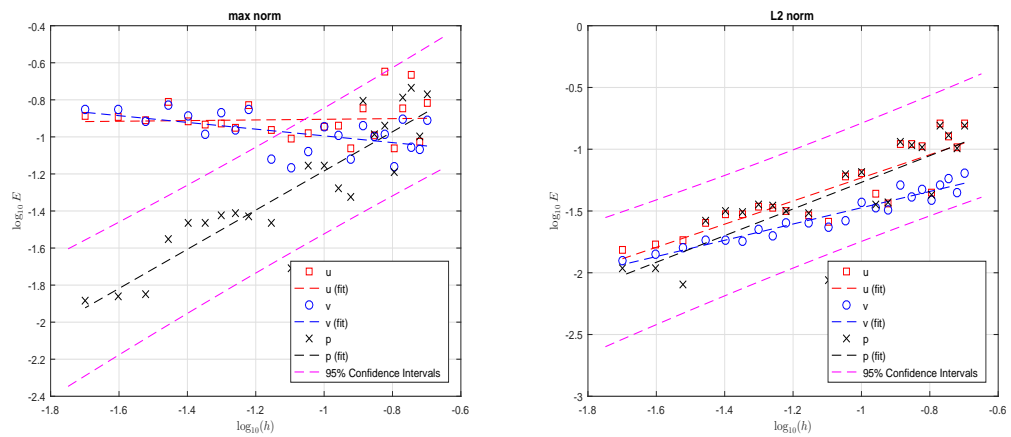


Figure 5.6.31: Convergence plot for circle domain with mode $m = 1$, $n = 1$ at various h in range $0.2 > h > 0.02$ at fixed $dt = 0.02$. The error in (a) is calculated in max norm, and (b) in L_2 norm over domain. Slope of the lines is summarised in Table 5.10.

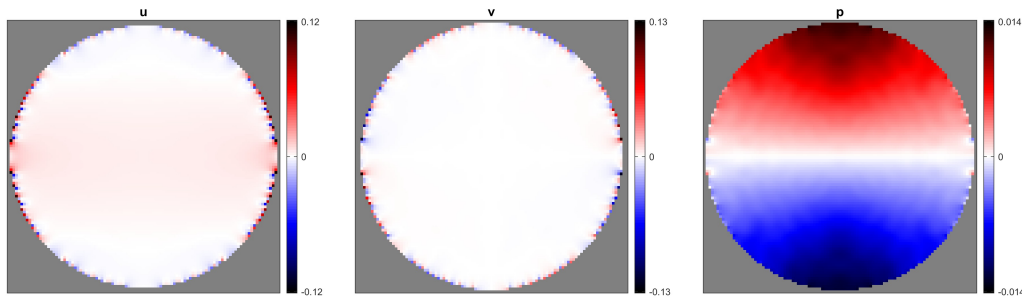


Figure 5.6.32: Maximum error in u , v and p for circle domain with mode $m = 1, n = 1$, at $h = 0.01$ and $dt = 0.01$.

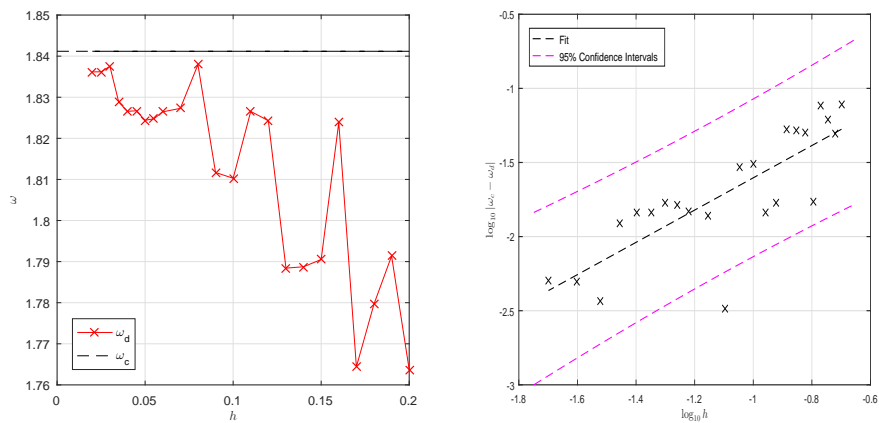


Figure 5.6.33: The frequency of wave in circle domain with mode $m = 1, n = 1$ at various h , and log-log plot error in frequency at various h . The slope of the line is 1.08843, with 95% confidence interval (0.7236, 1.453). The scaling factor is 0.305429.

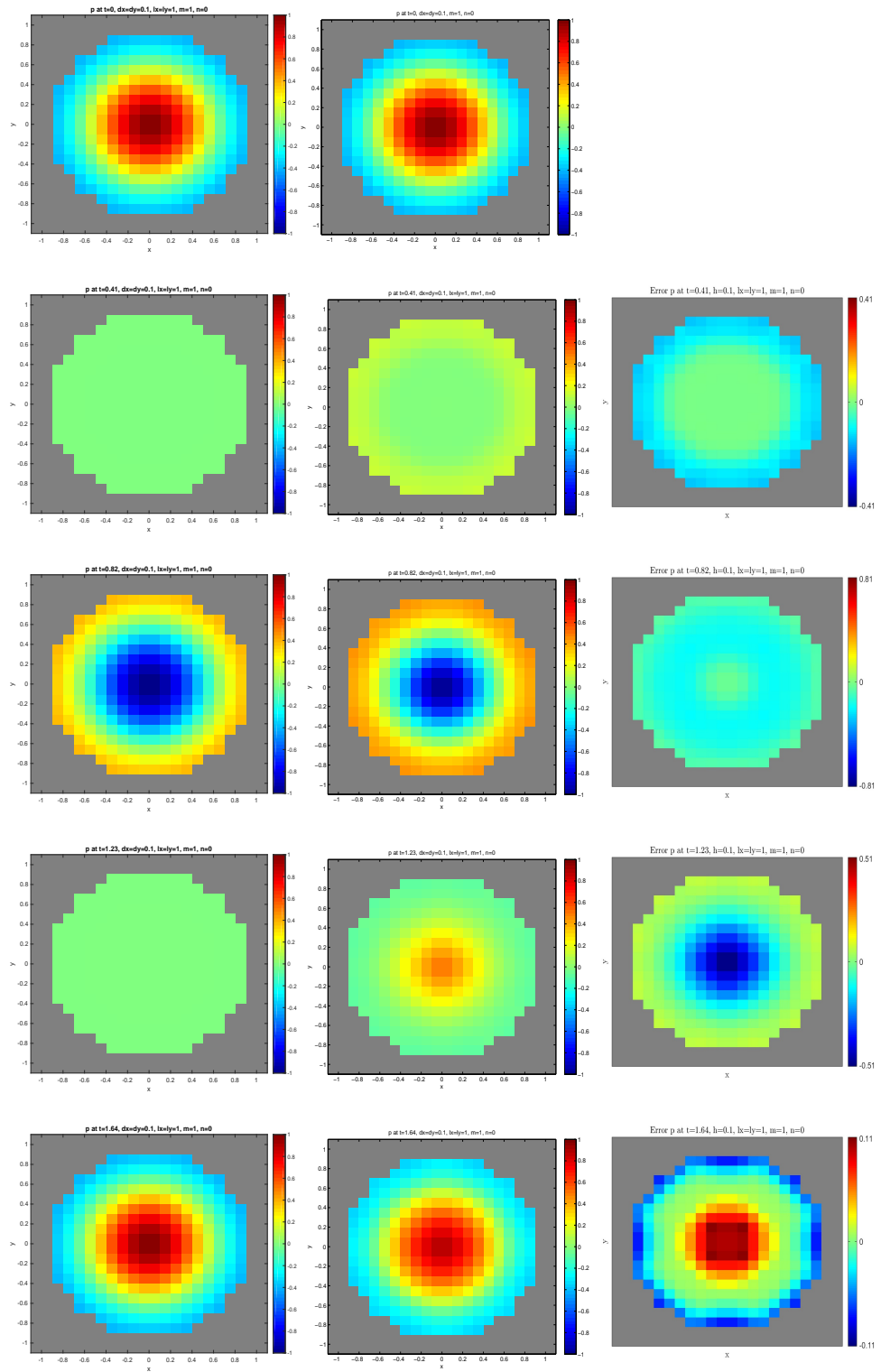


Figure 5.6.34: The solutions of p for circle domain at $t = 0, 0.25T, 0.5T, 0.75T, T$, with $h = 0.1$ and $dt = 0.01$, with mode $m = 1, n = 0$ using 4 corners of cell activation. Left column: continuum solutions. Centre column: numerical solutions. Right column: error (i.e., continuum-numerical).

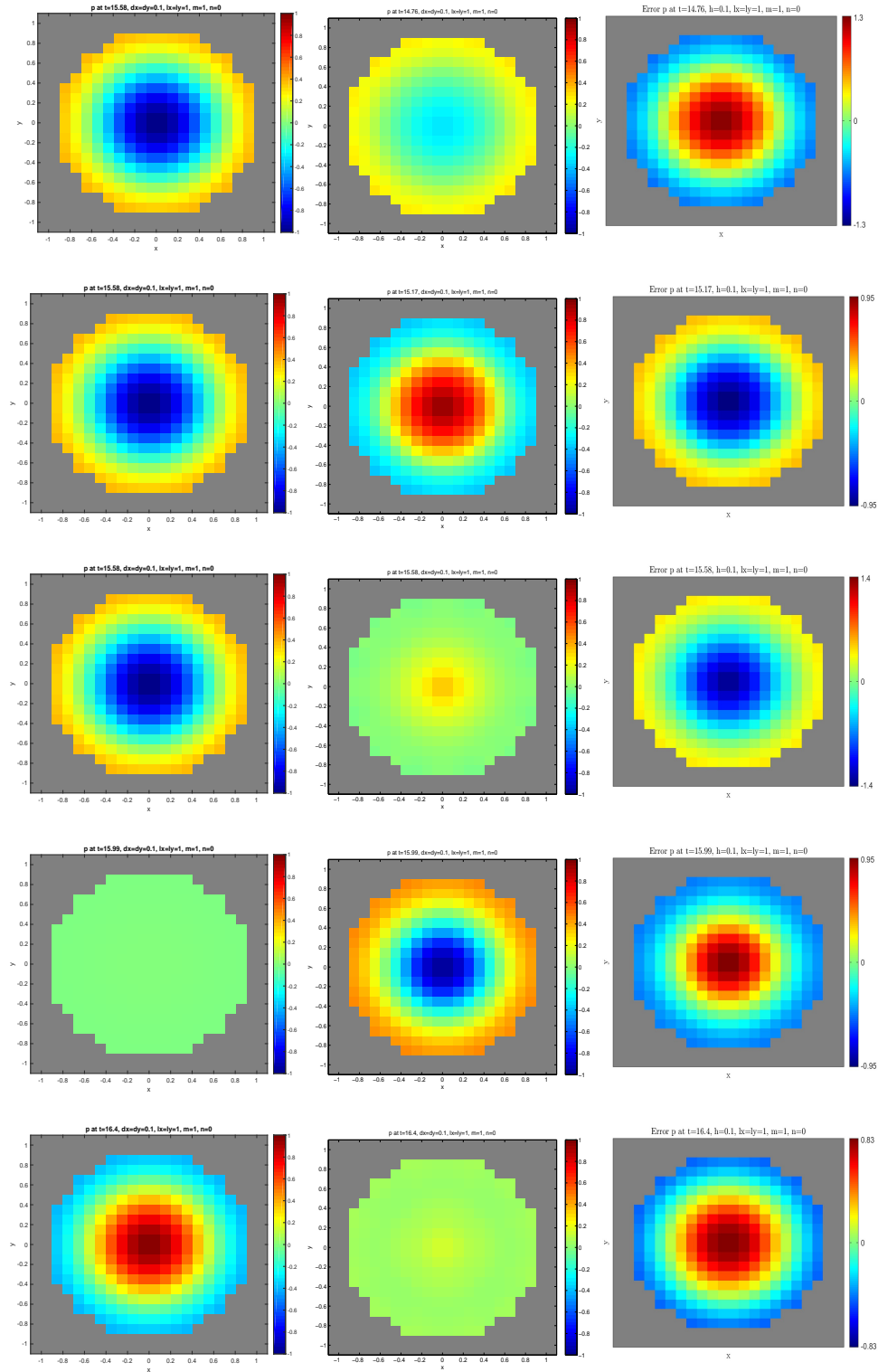


Figure 5.6.35: The solutions of p for circle domain at $t = 9T, 9.25T, 9.5T, 9.75T, 10T$, with $h = 0.1$ and $dt = 0.01$, with mode $m = 1, n = 0$ using 4 corners of cell activation. Left column: continuum solutions. Centre column: numerical solutions. Right column: error (i.e., continuum-numerical).

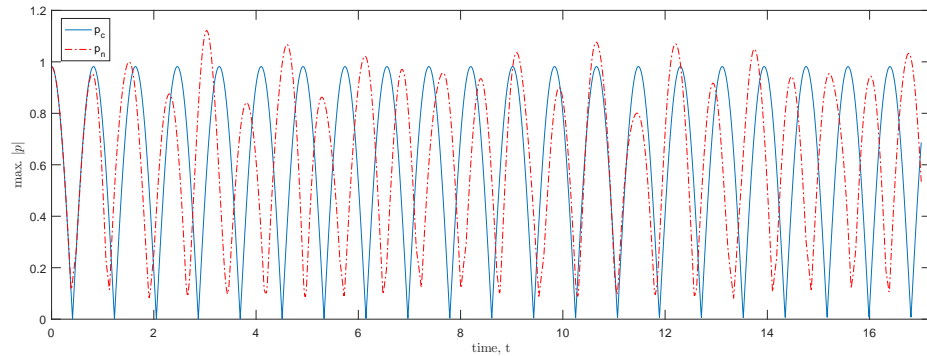


Figure 5.6.36: The maximum $|p|$ for circle domain at $h = 0.1$ with $dt = 0.01$, over $0 < t < 10T$ with mode $m = 1, n = 0$. The active grid is chosen according to 4 corners of each cells.

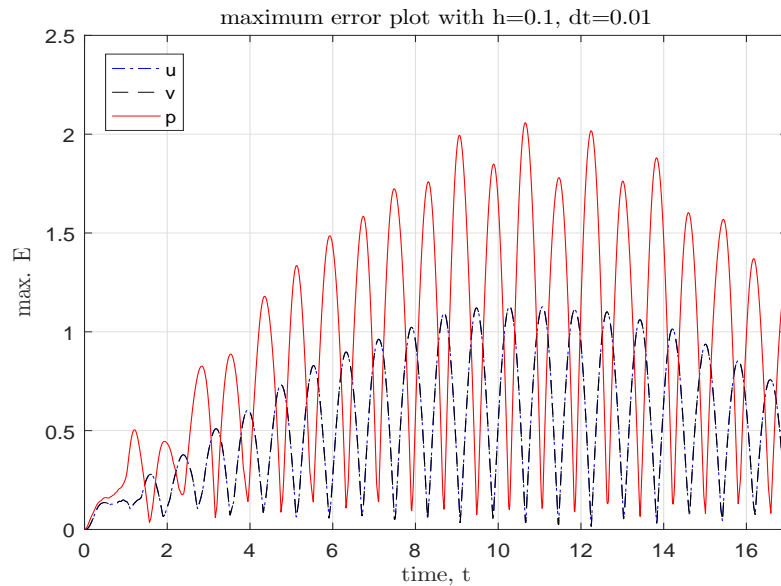


Figure 5.6.37: Maximum error for u, v and p over $0 < t < 10T \approx t = 17$, for circle domain, at $h = 0.1, dt = 0.01$ with mode $m = 1, n = 0$. The active grid is chosen according to 4 corners of each cells.

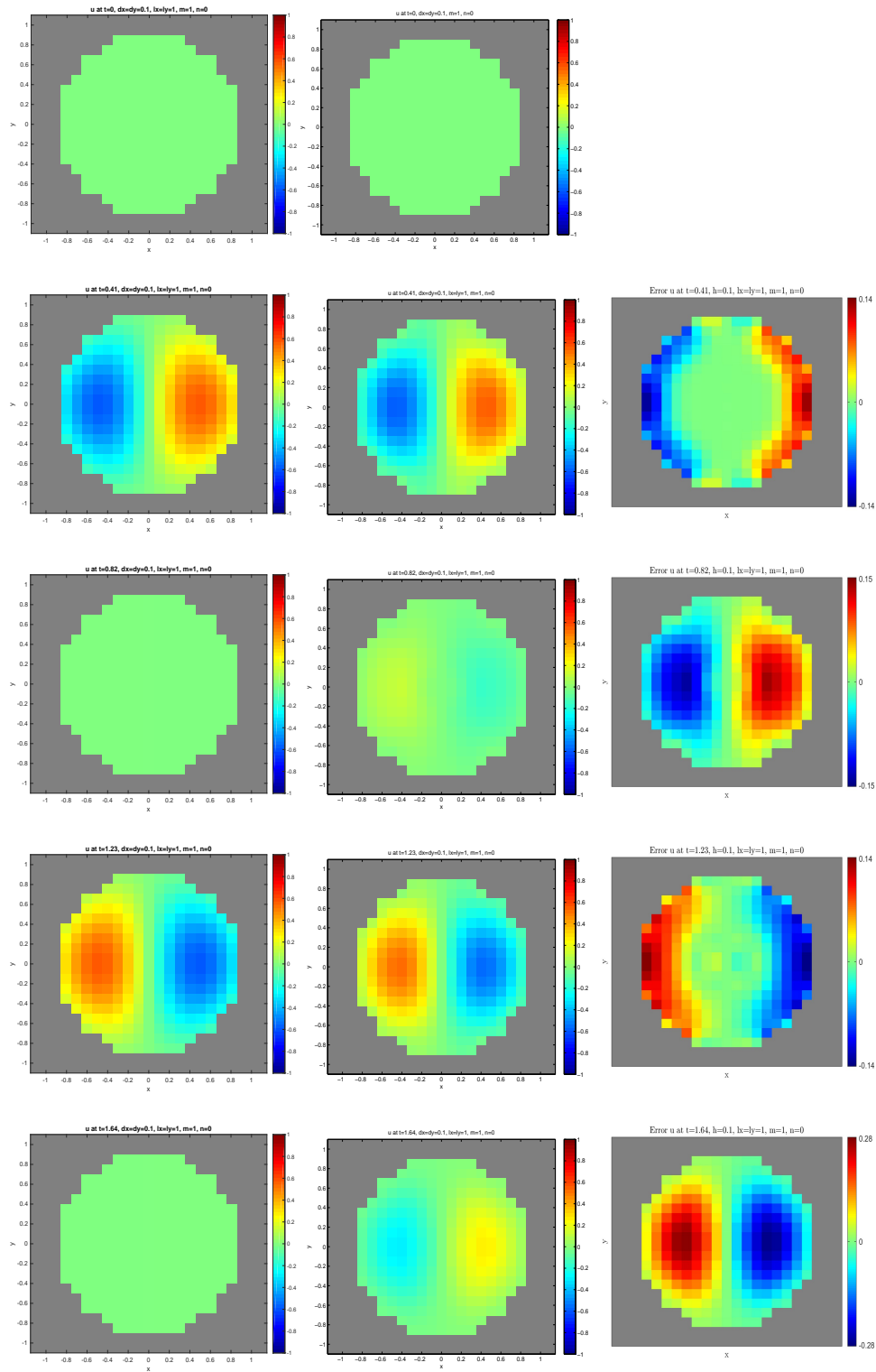


Figure 5.6.38: The solutions of u for circle domain at $t = 0, 0.25T, 0.5T, 0.75T, T$, with $h = 0.1$ and $dt = 0.01$, with mode $m = 1, n = 0$ using 4 corners of cell activation. Left column: continuum solutions. Centre column: numerical solutions. Right column: error (i.e., continuum-numerical).

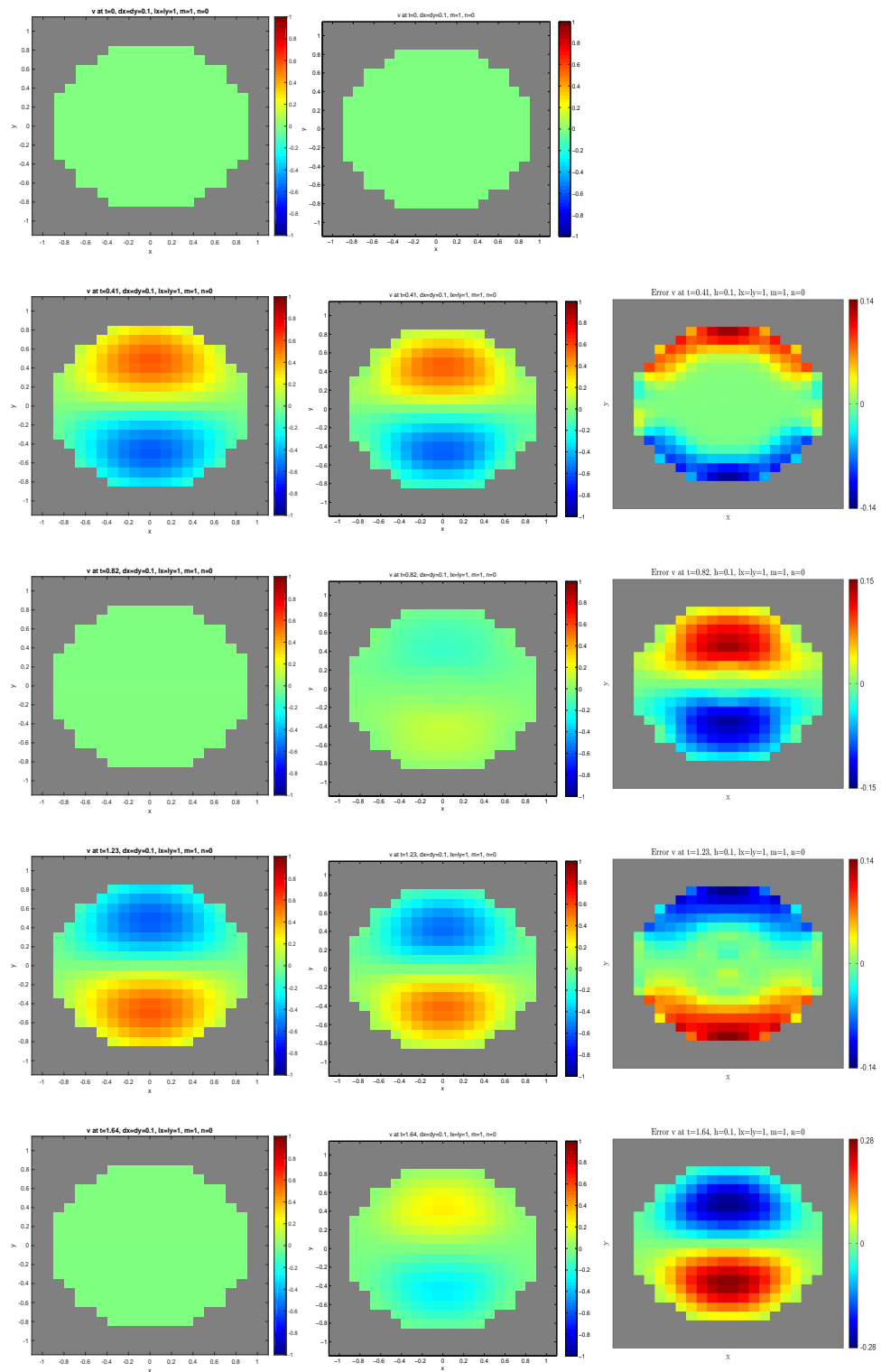


Figure 5.6.39: The solutions of v for circle domain at $t = 0, 0.25T, 0.5T, 0.75T, T$, with $h = 0.1$ and $dt = 0.01$, with mode $m = 1$, $n = 0$ using 4 corners of cell activation. Left column: continuum solutions. Centre column: numerical solutions. Right column: error (i.e., continuum-numerical).

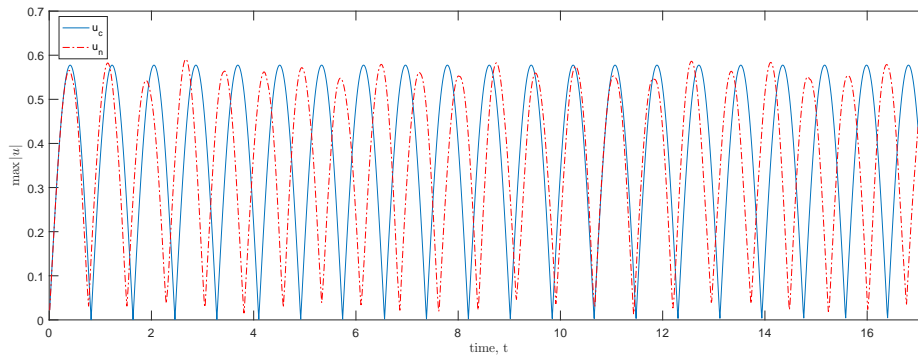


Figure 5.6.40: The maximum $|u|$ for circle domain at $h = 0.1$ with $dt = 0.01$, over $0 < t < 10T$ with mode $m = 1$, $n = 1$. The active grid is chosen according to 4 corners of each cells.

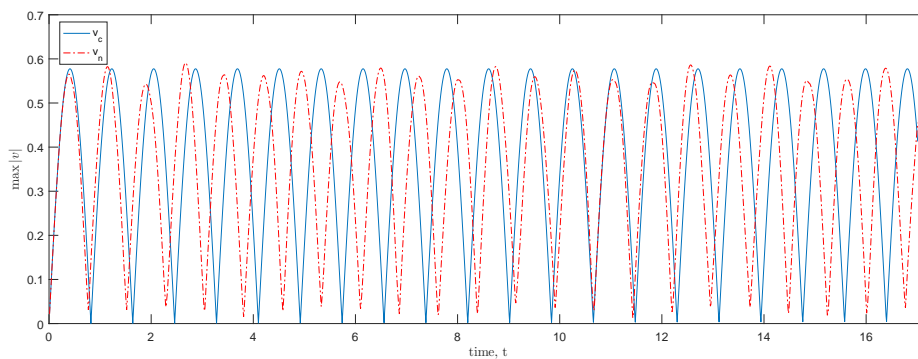


Figure 5.6.41: The maximum $|v|$ for circle domain at $h = 0.1$ with $dt = 0.01$, over $0 < t < 10T$ with mode $m = 1$, $n = 1$. The active grid is chosen according to 4 corners of each cells.

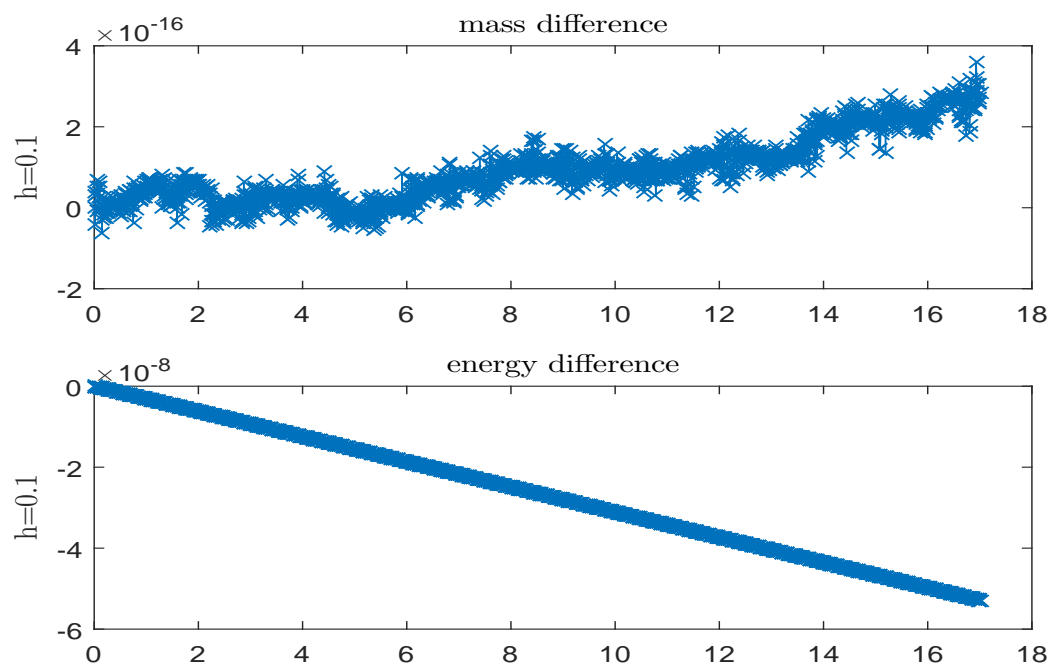


Figure 5.6.42: Mass and energy difference for circle domain, at $h = 0.1$, $dt = 0.01$ over $0 < t < 10T \approx t = 17$, for mode $m = 1$, $n = 0$. The active grid is chosen according to 4 corners of each cells.

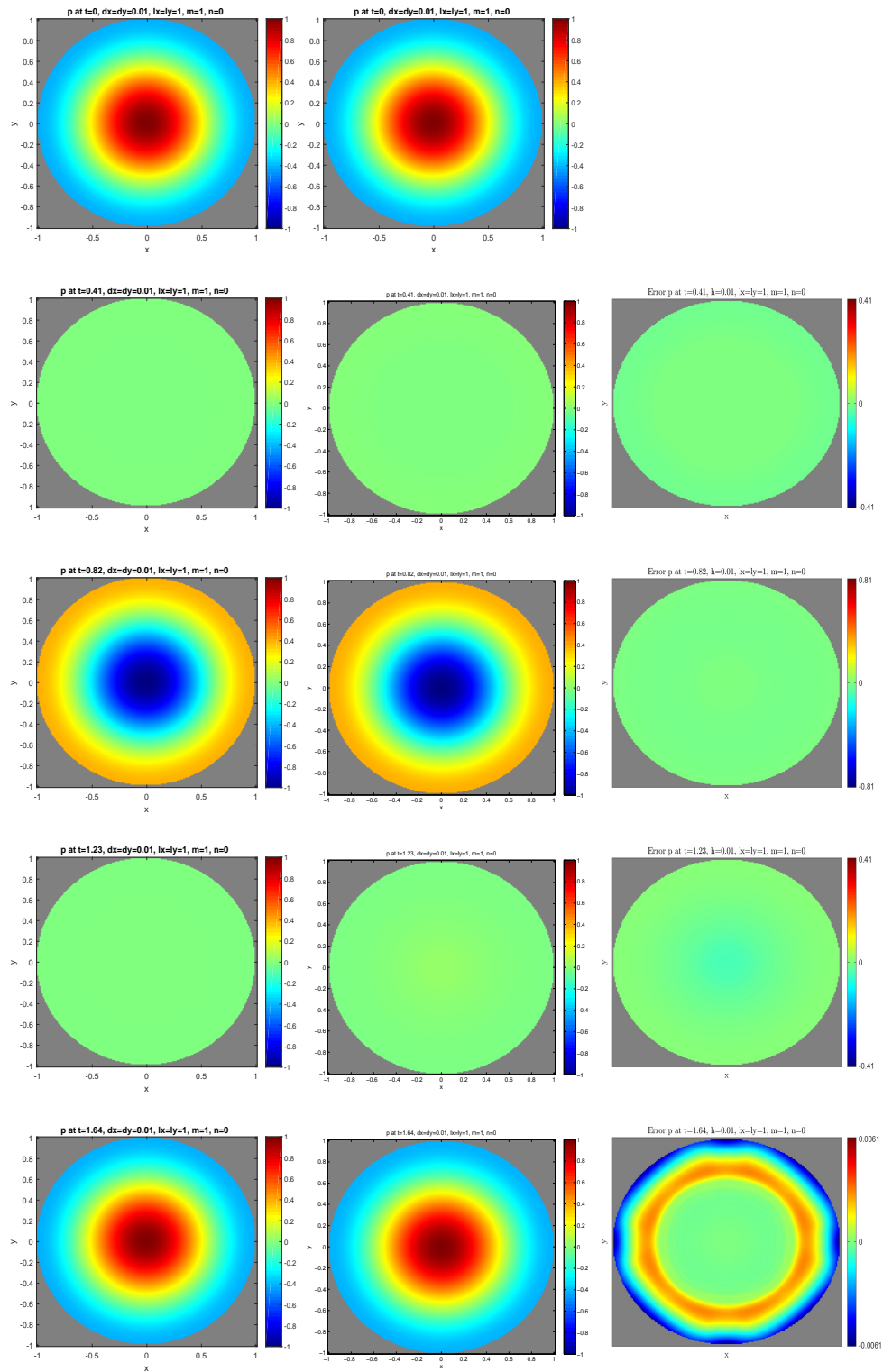


Figure 5.6.43: The solutions of p for circle domain at $t = 0, 0.25T, 0.5T, 0.75T, T$, with $h = 0.01$ and $dt = 0.005$, with mode $m = 1, n = 0$ using 4 corners of cell activation. Left column: continuum solutions. Centre column: numerical solutions. Right column: error (i.e., continuum-numerical).

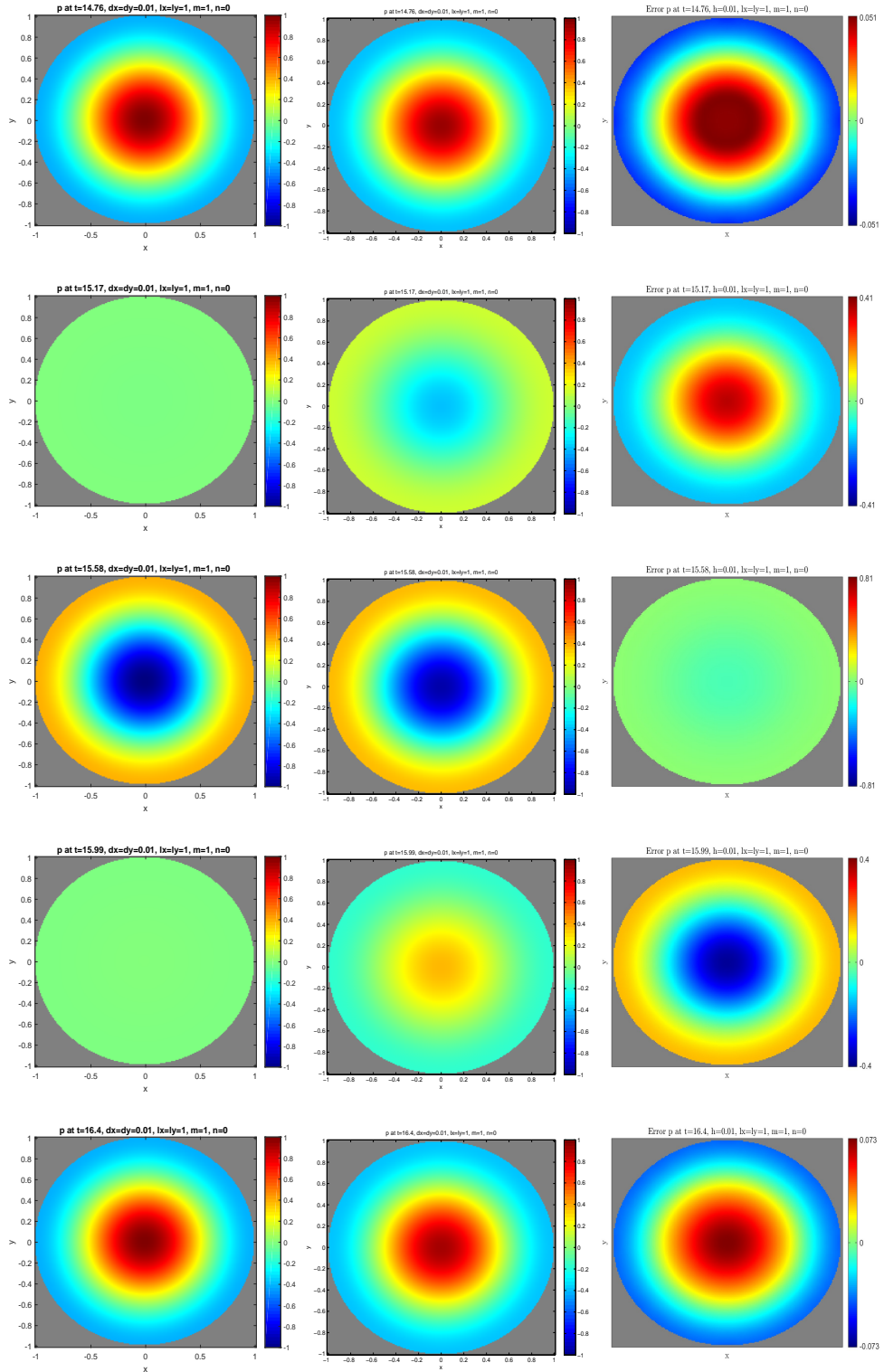


Figure 5.6.44: The solutions of p for circle domain at $t = 9T, 9.25T, 9.5T, 9.75T, 10T$, with $h = 0.01$ and $dt = 0.005$, with mode $m = 1, n = 0$ using 4 corners of cell activation. Left column: continuum solutions. Centre column: numerical solutions. Right column: error (i.e., continuum-numerical).

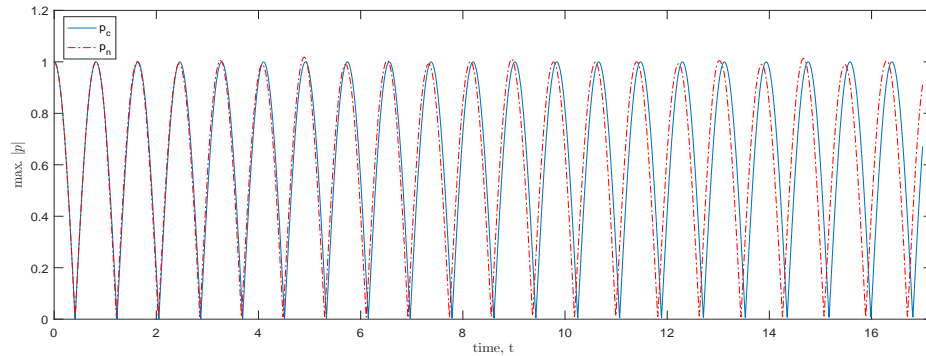


Figure 5.6.45: The maximum $|p|$ for circle domain at $h = 0.01$ with $dt = 0.005$, over $0 < t < 10T$ with mode $m = 1, n = 1$. The active grid is chosen according to 4 corners of each cells.

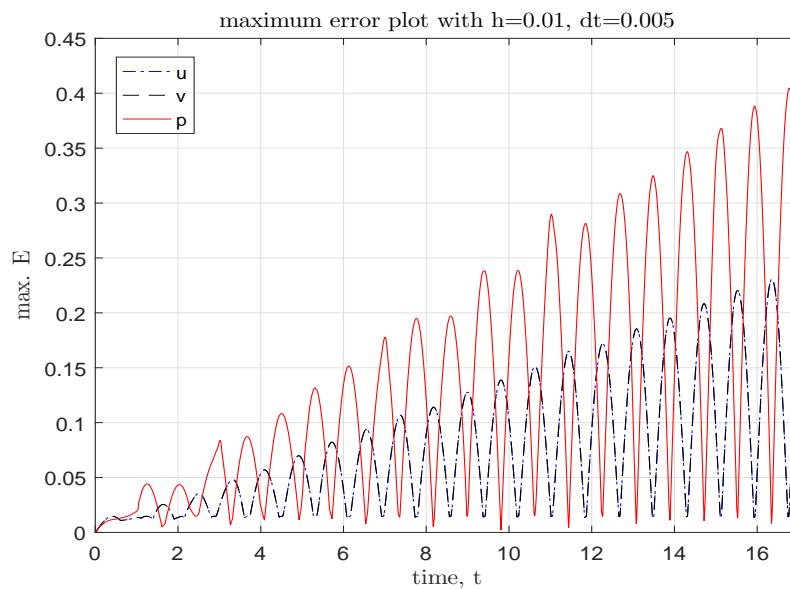


Figure 5.6.46: Maximum error for u, v and p over $0 < t < 10T$, for circle domain, at $h = 0.01, dt = 0.005$ with mode $m = 1, n = 0$. The active grid is chosen according to 4 corners of each cells.

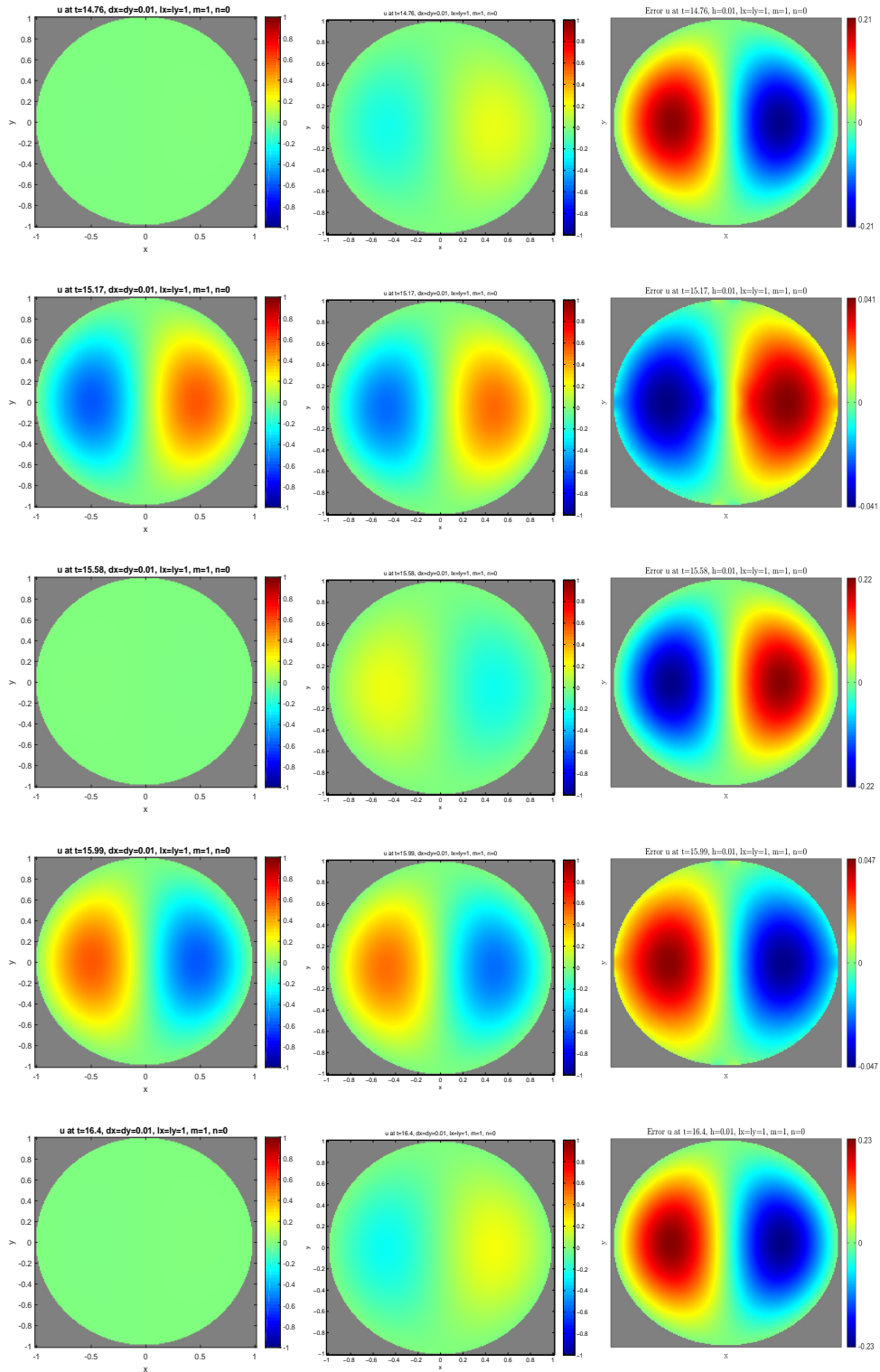


Figure 5.6.47: The solutions of u for circle domain at $t = 9T, 9.25T, 9.5T, 9.75T, 10T$, with $h = 0.01$ and $dt = 0.005$, with mode $m = 1, n = 0$ using 4 corners of cell activation. Left column: continuum solutions. Centre column: numerical solutions. Right column: error (i.e., continuum-numerical).

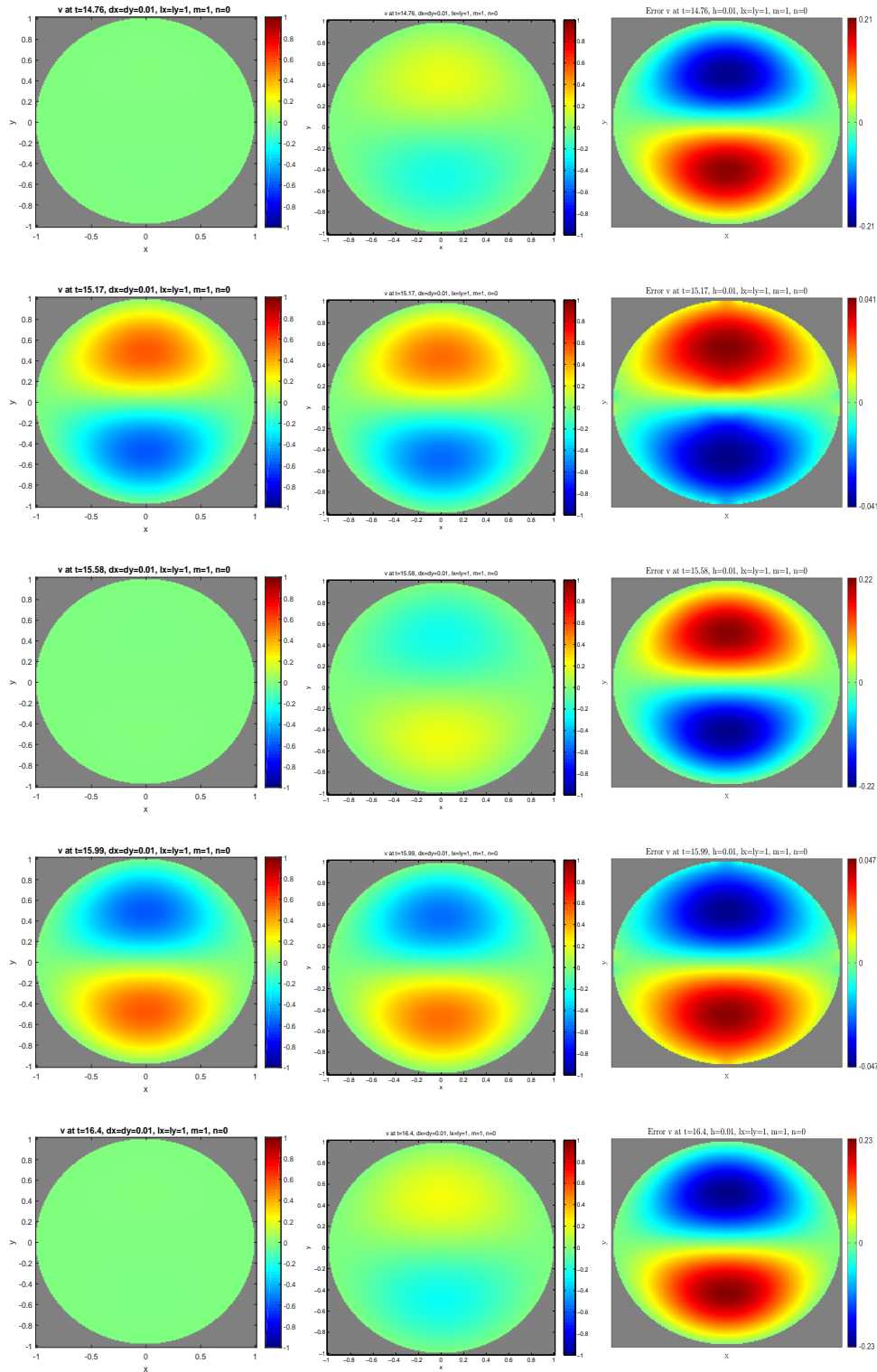


Figure 5.6.48: The solutions of v for circle domain at $t = 9T, 9.25T, 9.5T, 9.75T, 10T$, with $h = 0.01$ and $dt = 0.005$, with mode $m = 1, n = 0$ using 4 corners of cell activation. Left column: continuum solutions. Centre column: numerical solutions. Right column: error (i.e., continuum-numerical).

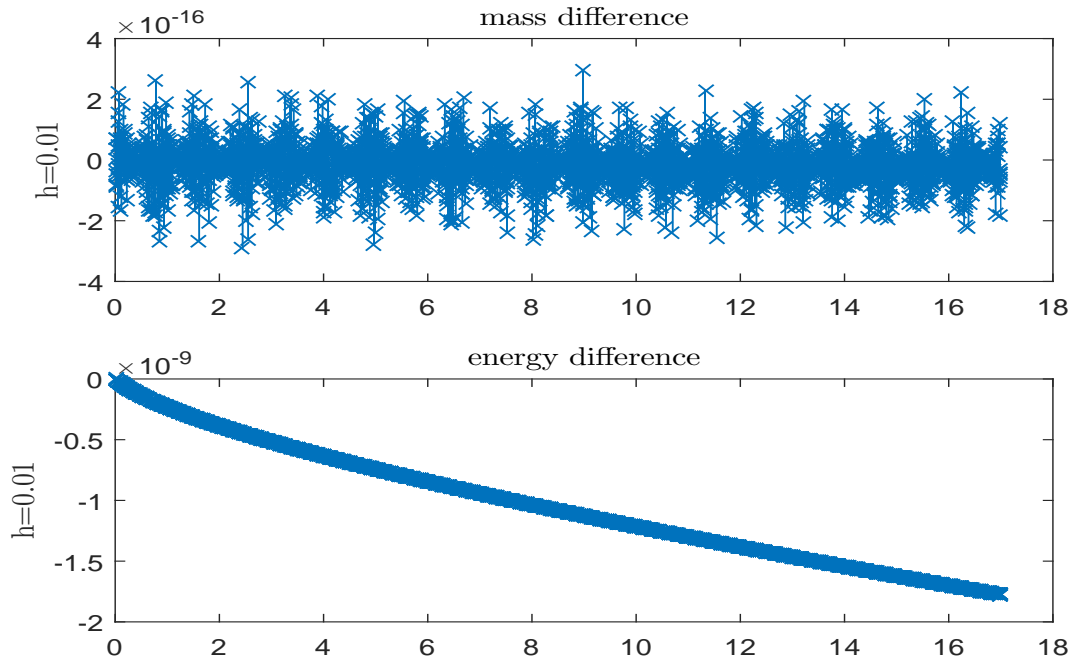


Figure 5.6.49: Mass and energy difference for circle domain, at $h = 0.01$, $dt = 0.005$ over $0 < t < 10T \approx t = 17$, for mode $m = 1$, $n = 0$. The active grid is chosen according to 4 corners of each cells.

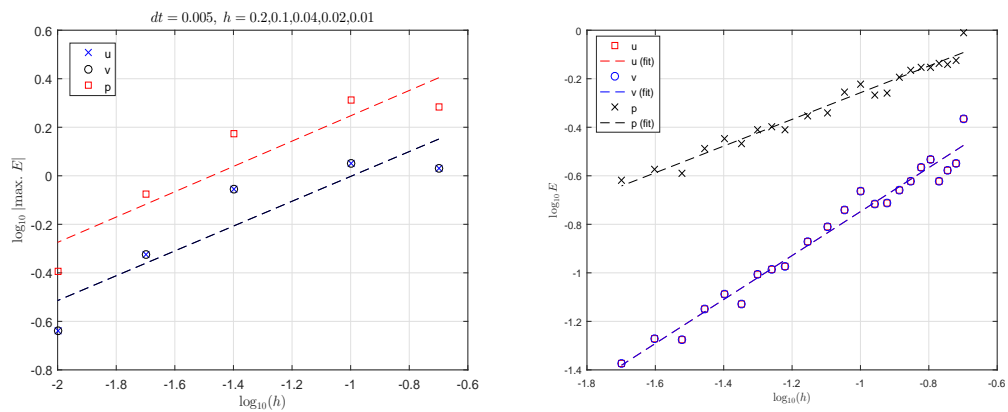


Figure 5.6.50: The log-log plot of maximum error over (a) $0 < t < 10T \approx t = 17$, and (b) $0 < t < t \approx 2 > T$, at various grid spacing h . The slope of the lines indicate the rate of convergence. The slope in (b) are: u and v are 0.905945, with 95% confidence interval (0.8362, 0.9757), p is 0.5498, with 95% confidence interval (0.5049, 0.5948). The active grid is chosen according to 4 corners of each cells.

Chapter 6

REFLECTION AND FOCUSSING OF INTERNAL GRAVITY WAVES

6.1 Introduction

Wave phenomena that we have discussed so far exist on the surface of a boundary. If we look beneath the surface another kind of wave also can be discovered, which is internal waves. They are mostly hidden for eyesight but it is very important. The main ingredient for these waves to be generated is due to the density variations in a fluid. An obvious example of fluid with density differences is the ocean. As we go down into the ocean, the density of the water increase with light fluid overlying dense fluid. Such fluids are said to be stratified. Waves in the fluids exist due to restoring forces; a fluid parcel moved vertically is pushed back to its starting level, giving oscillations. It goes almost without saying that the same mechanism is at work whenever two fluid densities differ. The oscillations in the stratified fluid are normally called internal gravity waves. The main difference with the waves on the surface is that internal waves are generally slower because they rely on a weaker density difference and can propagate both vertically and horizontally.

Early investigation of internal gravity waves was motivated by F. Nansen in 1902 with an observation of a phenomenon on the Arctic Ocean or the so called “Dead Water” [26]. The phenomenon is one of the motivations for the waves in fluids that are stratified. The ocean is an example of stratified fluid in which internal gravity waves can be found. The oceans are stratified in density as a result of many geophysical processes, like evaporation, cooling, and mixing with fresh meltwater [63]. In the ocean, it is speculated that these internal waves may thus play an important role in maintaining the large-scale deep circulation, by providing downward mixing heat [62]. Their mixing may also be relevant for marine ecosystems by providing nutrients to the water column. These phenomena not only happen at the ocean. It also can occur in the atmosphere which can lead to distinctive cloud patterns that results from condensation of water vapour; rising air becomes cooler.

In a stratified medium, buoyancy forces arise subject to gravity. There is a special property that ensure the oscillations mechanism. To illustrate, we suppose fluid to be at rest, with vertical density stratification $\rho = \rho_0(z)$, and the corresponding hydrostatic balance for pressure is

$$\frac{dp_0}{dz} = -g\rho_0(z). \quad (6.1.1)$$

By considering a small fluid parcel at $z = z_*$, and assumed the density on the fluid is conserved such that $d\rho/dt = 0$. On the stationary fluid parcel, there is a balance between gravity and the pressure gradient

$$-\frac{dp_0}{dz} = g\rho_0(z_*).$$

If we displace the fluid parcel vertically to $z = z_* + \delta(t)$, we can use Newton’s 2nd law

$F = ma$ to determine the subsequent motion of the fluid parcel:

$$\begin{aligned}\rho_0(z_*) \frac{d^2\delta}{dt^2} &= -g\rho_0(z_*) - \left. \frac{dp_0}{dz} \right|_{z_*+\delta} \\ &= -g\rho_0(z_*) + g\rho_0(z_* + \delta), \\ &= -g\rho_0(z_*) + g \left(\rho_0(z_*) + \delta \left. \frac{d\rho_0}{dz} \right|_{z_*} + O(\delta^2) \right), \\ \Rightarrow \frac{d^2\delta}{dt^2} &\approx \left(\frac{g}{\rho_0} \frac{d\rho_0}{dz} \right) \Big|_{z_*} \delta.\end{aligned}$$

If $d\rho_0/dz > 0$, then $\delta(t)$ can grow exponentially in time: the configuration is unstable. If $d\rho_0/dz < 0$, there is vertical oscillatory motion: $d^2\delta/dt^2 = -N_*^2\delta$ which implies $\delta = \delta_0 \cos(N_*t)$, where $N_* = N(z_*)$ and

$$N^2(z) = -\frac{g}{\rho_0} \frac{d\rho_0}{dz}. \quad (6.1.2)$$

The quantity $N(z)$ is known as the buoyancy frequency, or Brunt-Väisälä frequency. It gives the theoretical frequency of vertical oscillations of a small parcel of fluid in a stratified medium.

A typical dispersion relation of internal gravity waves is

$$\omega^2 = \frac{N^2 k^2}{k^2 + m^2}, \quad (6.1.3)$$

where k and m are wavenumbers in the horizontal and vertical, respectively, and N^2 now is assumed as a constant. It is clear that the dispersion relation has a relationship between wavenumbers and wave frequency. Obviously, (6.1.3) is depends on N^2 . In general, for $m \neq 0$, we have

$$\omega_c \leq N. \quad (6.1.4)$$

In the absence of vertical wavenumber ($m = 0$), we then have $\omega = N$. The phase speed

then is $c_p = \omega/k = N/k$. This means that the particle motions are purely vertical; in agreement with the definition of buoyancy frequency. On the other side, for the purely vertical wavenumber ($k = 0$), the frequency then vanishes ($\omega = 0$). The particle motions are then horizontal, which implies that there is no wave propagation. Unlike surface wave (acoustic), these waves are anisotropic because the frequency depends on the direction.

A further linear property of internal gravity waves is that if these wave reflect from a solid boundary then in general the wavenumbers of incident and reflected waves are unequal [53]. The consequence of this is that, after reflection the internal gravity waves change their direction, but retain the same frequency. This can be illustrated from the dispersion relation (6.1.3), which shows that the frequency of internal waves independent of the magnitude wavenumber. To bring this out, it is useful to specify wavenumber (k, m) as

$$(k, m) = |\kappa|(\cos \theta, \sin \theta) \quad \Rightarrow \quad \omega = N \cos \theta, \quad (6.1.5)$$

where $|\kappa|$ is the wave magnitude and θ is the angle between the horizontal and the resultant wavenumber vector $|\kappa|$. This means that the frequency depends only on the angle θ .

Upon reflection, this angle must be the same since the frequency depends only on θ , regardless of the angle of the bottom boundary, β . In other words, the angle of incident and reflected to the vertical are equal. However, reflection at an inclined boundary with angle β altered the angle of incident and reflected waves, which makes them unequal, as shown in Figure 6.4.1. If $\beta > \varphi$, the wave is reflected back with horizontal component of group velocity in the opposite direction to the incident wave. On the other hand, if $\beta < \varphi$, the wave will have forward reflection. In the ocean, a shallow wedge acts as a perfect absorber of internal gravity waves, as the waves propagate further. In a shallow wedge, the wavelength will decrease with the change of magnitude of wave, in accord with [53]. Note that, in the case of $\beta = 0$ or $\pi/2$, there is no change in wavenumber and perfect internal wave reflection can occur.

There are numerous investigations on the reflection of internal gravity waves in different approaches and interest, either in analytically [10, 22], numerically [28, 40, 60], or experimentally [16, 64]. Most of them are toward understanding the dynamical aspect of internal wave during reflection. These include the interactions between incident and reflected waves in the development of nonlinearities and topographic influences, and also towards understanding the dynamical aspects in the critical regime which is $\beta = \varphi$ [22, 40, 21]. In the critical regime, reflected internal wave is expected to have zero group velocity, infinite amplitude and infinite wavelength, which results incoming wave trap in the boundary region and wave breaking [61]. In such a case, nonlinearities and turbulence must come into play. As the investigation in this thesis rely on the linear theory, which focus on the reflection of the incoming wave, there is no consideration for the case of the criticality. However, another criterion for the internal wave reflection is the sloping boundary. So that we will focus on this effect for the internal wave reflection with numerical approach.

The representation of an inclined boundary in finite-difference numerical model commonly finished by staircase boundary. A comparison study of the boundary representation in geophysical numerical models was done by [60]. In the study, they compare two techniques to approximate the bottom boundary which are the staircase and piecewise linear fashion, which the performance of both techniques are predict using an analytical solution in Fourier space. The main difference in these two techniques is the boundary condition implementation. In the staircase approximation, the no-flux boundary condition usually enforced on the sidewall of the grid. While the boundary condition in the piecewise linear representation is imposed directly on the linear approximation. Analysis in the study focus on the reflection coefficient for linear internal wave in a rectangular channel containing a linearly stratified fluid and Gaussian bump acts as bottom topography. From the analysis, they found that the reflection coefficient behaviour with staircase Gaussian bump is not uniform towards the analytical solution. There are aliasing effect which is the effect of discrete Fourier transform. On the other hand, reflection coefficient with the piecewise linear approximation behave with the analytical solution. However, the advantage of this technique also minimal

in the case of small grid size.

The linear approximation strategy for the bottom boundary is achieved using the terrain-following coordinates, so that the thickness of the bottom topography is varied along the topography. Moreover, the importance of gravity in the ocean may suffer with this technique since the approach only focus upon the effects of topography. Although the piecewise linear fashion was showed to have a better solution than the staircase approximation [3], the performance of the technique is limited to a few of sensitivity and may not be implemented to all types of flow. While in the staircase approximation, it is generally agree that the smaller the grid size in the approximation, the more smooth the bottom topography, and hence the more accurate the numerical solution. Therefore, it is agreed that the grid size in the staircase approximation play an important role in the accuracy of numerical solution. However, there is no sufficient quantification of the resulting scheme towards the analytical solution as grid spacing tends to zero. It is thus desirable to quantify the effects of grid spacing to the internal wave reflection at a sloping boundary.

Upon reflection at an inclined boundary, internal gravity waves preserve their frequency and consequently their angle with respect to the gravitational direction [44]. These waves also change their wavelength which resulting either focusing or defocusing when reflecting from boundary. The situation where the waves become focused when reflecting from a sloping boundary, and converge towards limit cycle is called wave attractor [46, 48]. Many investigations have been performed to confirm this behavior, either analytically [46, 36, 35], or in numerical experiments [11, 41]. Understanding the dynamical properties of internal gravity waves in a bounded domain is important for explaining the mixing process in ocean basins and lakes. It also has relation to astrophysics and fluid dynamics [50, 41].

For the analytical investigation, the usual governing equations that describe internal gravity waves can be solved with appropriate initial and boundary conditions. However, it becomes more difficult to solve directly because it involves with the initial boundary value problem and the solutions are not easily be written in closed form [35]. Another handful laboratory

experiment is described in [58] where they showed that the waves defocusing when there is no sloping boundaries. Thus, in this chapter we only focused on the numerical experiments on internal gravity wave attractors. For the numerical experiment, we consider the fluid is in the square geometry. This investigation is important since we can make further analysis on the patterns of internal gravity wave attractors when the sloping wall is represented with staircase configurations.

The aim of this chapter is to start extending some of the ideas from chapters 2-5 to internal gravity waves. We start by introducing the equations of motion in section 6.2, and then consider in section 6.3 how these equations may be configured on staggered grids, deriving the relevant dispersion relation for internal gravity waves in an unbounded medium. In section 6.4 we consider plane internal gravity wave reflection at a sloping boundary. The classic continuum reflection is reviewed in section 6.4.1, before we present what is believed to be a completely novel discrete reflection calculation in section 6.4.2. We will find an error of $O(h)$ in the discrete reflection problem, and this suggests that issues may then arise in phenomena driven by internal gravity reflection. Thus, in section 6.5, we consider the phenomena of internal wave focussing in closed domain, which is driven by a particular property of internal gravity wave reflection. Our idea is that staircase boundaries may prevent or alter the focussing phenomena. However, in section 6.5 we are only able to present provisional calculations towards this end in rectangular domains, without staircase boundaries.

6.2 Equations of Motion for Stratified Fluid

To study internal gravity waves, a few assumptions are necessary. Since internal gravity waves generally can be found in the stratified fluid, it is worth to mention here that we will focus on the internal gravity waves in the ocean. So that further simplification and assumption is possible and desirable. In the ocean, the density variations are small when

compared to its average $\bar{\rho}$. Mathematically, this can be represented as $\rho(x, z, t) = \bar{\rho} + (\rho(x, z, t) - \bar{\rho})$, where $|\rho(x, z, t) - \bar{\rho}| \ll \rho$ by assumption. From now on the fluid will be assumed incompressible and there is no dissipative mechanism. This means that

$$\frac{D\rho}{Dt} = 0, \quad (6.2.1)$$

where D/Dt denotes differentiation following the motion. The continuity equation in vector notation is

$$\nabla \cdot \mathbf{u} = 0, \quad (6.2.2)$$

where \mathbf{u} is the velocity vector. The equations of motion of the fluid with the force of gravity are written as

$$\begin{aligned} \rho \frac{D\mathbf{u}}{Dt} &= \nabla p - \rho g \mathbf{e}_z, \\ \Rightarrow \{\bar{\rho} + (\rho - \bar{\rho})\} \frac{D\mathbf{u}}{Dt} &= -\nabla p - \{\bar{\rho} + (\rho - \bar{\rho})\} g \mathbf{e}_z. \end{aligned}$$

Since $|\bar{\rho} - \rho| \ll \bar{\rho}$, so that we can approximate the term in the left-hand side curly bracket by $\bar{\rho}$. The term in the curly bracket on the right-hand side involves gravity. Combinations between gravity and density will lead to buoyancy effect [69], which is the primary importance of the internal waves. Thus, we obtain

$$\bar{\rho} \frac{D\mathbf{u}}{Dt} = -\nabla p - \{\bar{\rho} + (\rho - \bar{\rho})\} g \mathbf{e}_z,$$

and dividing with $\bar{\rho}$ gives

$$\frac{D\mathbf{u}}{Dt} = -\frac{1}{\bar{\rho}} \nabla p - \frac{\rho g}{\bar{\rho}} \mathbf{e}_z. \quad (6.2.4)$$

One can analysed the internal waves with the compressible equations that we used in previous chapter. However, there are other restrictions that must be applied. They are discussed in detail [70]. The obvious difference to the equations of motion in previous chapters are the addition of the effects of buoyancy in the vertical direction and the Boussinesq approximation. Therefore, the governing equations for internal gravity waves are (6.2.1), (6.2.2), (6.2.4). With the preceding assumptions and restrict at two-dimensional flows $\mathbf{u} = u(x, z, t)\mathbf{e}_x + w(x, z, t)\mathbf{e}_z$, $\rho = \rho(x, z, t)$ and $p = p(x, z, t)$, they are written as

$$\frac{\partial u}{\partial t} + u \frac{\partial u}{\partial x} + w \frac{\partial u}{\partial z} = -\frac{1}{\bar{\rho}} \frac{\partial p}{\partial x}, \quad (6.2.5a)$$

$$\frac{\partial w}{\partial t} + u \frac{\partial w}{\partial x} + w \frac{\partial w}{\partial z} = -\frac{1}{\bar{\rho}} \frac{\partial p}{\partial z} - \frac{g\rho}{\bar{\rho}}, \quad (6.2.5b)$$

$$\frac{\partial \rho}{\partial t} + u \frac{\partial \rho}{\partial x} + w \frac{\partial \rho}{\partial z} = 0, \quad (6.2.5c)$$

$$\frac{\partial u}{\partial x} + \frac{\partial w}{\partial z} = 0. \quad (6.2.5d)$$

These equations are commonly known as the Boussinesq approximation [2, 42].

Another simplification for these equations is that of linearisation, the neglect of the non-linear convection terms like $u\partial u/\partial x$ in comparison with $\partial u/\partial t$. The procedure is justified when the motions and velocities are of small amplitude as follow. Suppose that the fluid initially is at rest, with vertical density stratification $\rho = \rho_0(z)$. Then, (6.2.5) are satisfied provided $p = p_0(z)$, so that (6.1.1) is permissible. With a small disturbances to this basic state by writing $u = 0 + u'$, $w = 0 + w'$, $p = p_0 + p'$, $\rho = \rho_0 + \rho'$, (6.2.5) are linearised to

$$\frac{\partial u'}{\partial t} = -\frac{1}{\bar{\rho}} \frac{\partial p'}{\partial x}, \quad (6.2.6a)$$

$$\frac{\partial w'}{\partial t} = -\frac{1}{\bar{\rho}} \frac{\partial p'}{\partial z} - \frac{g\rho'}{\bar{\rho}}, \quad (6.2.6b)$$

$$\frac{\partial \rho'}{\partial t} + w' \frac{d\rho_0}{dz} = 0, \quad (6.2.6c)$$

$$\frac{\partial u'}{\partial x} + \frac{\partial w'}{\partial z} = 0, \quad (6.2.6d)$$

These equations are to be solved subject to any initial and boundary conditions. For simplicity in the further calculations, we first define a variable for buoyancy force to be substituted in the vertical momentum equation. The variable is define as

$$b = -\frac{g\rho}{\bar{\rho}} \Rightarrow \rho = -\frac{\bar{\rho}}{g}b.$$

So that, the governing equations for the internal waves now become

$$\frac{\partial u}{\partial t} = -\frac{1}{\bar{\rho}}\frac{\partial p}{\partial x}, \quad (6.2.7a)$$

$$\frac{\partial w}{\partial t} = -\frac{1}{\bar{\rho}}\frac{\partial p}{\partial z} + b, \quad (6.2.7b)$$

$$\frac{\partial b}{\partial t} + N^2w = 0, \quad (6.2.7c)$$

$$\frac{\partial u}{\partial x} + \frac{\partial w}{\partial z} = 0, \quad (6.2.7d)$$

The emphasis of this study is to investigate the spatial effects of internal gravity waves. We first describe wavelike solutions in the continuum space with a prescribe frequency. A wavelike solution is assumed with all variables are proportional to $\exp(-i\omega t)$; the equations then become

$$-i\omega u = -\frac{1}{\bar{\rho}}\frac{\partial p}{\partial x}, \quad (6.2.8a)$$

$$-i\omega w = -\frac{1}{\bar{\rho}}\frac{\partial p}{\partial z} + b, \quad (6.2.8b)$$

$$-i\omega b + N^2w = 0, \quad (6.2.8c)$$

$$\frac{\partial u}{\partial x} + \frac{\partial w}{\partial z} = 0. \quad (6.2.8d)$$

6.3 Internal gravity waves in an unbounded domain

6.3.1 Continuum internal waves

We first consider internal gravity waves in unbounded domain. We suppose that N is constant in unbounded x and z directions with horizontal wavenumber k , and vertical wavenumber m . By considering wavelike solutions of the form

$$(u, w, p, b) = \text{Re} \left((\hat{u}, \hat{w}, \hat{p}, \hat{b}) \exp\{i(kx + mz)\} \right), \quad (6.3.1)$$

where $\hat{u}, \hat{w}, \hat{p}, \hat{b}$ are complex constant, then (6.2.8) become

$$-i\omega_c \hat{u} = -\frac{ik}{\bar{\rho}} \hat{p}, \quad (6.3.2a)$$

$$-i\omega_c \hat{w} = -\frac{im}{\bar{\rho}} \hat{p} + \hat{b}, \quad (6.3.2b)$$

$$-i\omega_c \hat{b} + N^2 \hat{w} = 0, \quad (6.3.2c)$$

$$ik\hat{u} + im\hat{w} = 0. \quad (6.3.2d)$$

Note that the component of $\text{Re}(\exp\{i(kx + mz)\})$ are omitted since the complex relations must be satisfied. (6.3.2a,b,c,d) may rewritten in matrix form as

$$\begin{pmatrix} -i\omega_c & 0 & 0 & ik \\ 0 & -i\omega_c & -1 & im \\ 0 & N^2 & -i\omega_c & 0 \\ ik & im & 0 & 0 \end{pmatrix} \begin{pmatrix} \hat{u} \\ \hat{w} \\ \hat{b} \\ \hat{p} \end{pmatrix} = \begin{pmatrix} 0 \\ 0 \\ 0 \\ 0 \end{pmatrix}. \quad (6.3.3)$$

For non-trivial solution, determinant of the matrix must be zero, which implies that

$$\begin{aligned} \det A &= -i\omega_c \begin{vmatrix} -i\omega_c & -1 & im \\ N^2 & -i\omega_c & 0 \\ im & 0 & 0 \end{vmatrix} - 0 + 0 - ik \begin{vmatrix} 0 & -i\omega_c & -1 \\ 0 & N^2 & -i\omega_c \\ ik & im & 0 \end{vmatrix}, \\ &= -i\omega_c (-i\omega_c m^2) - ik (-i\omega_c^2 k + iN^2 k) = -\omega_c^2 m^2 - \omega_c^2 k^2 + N^2 k^2. \end{aligned}$$

As the determinant must be zero, then we obtain

$$\omega_c^2 = \frac{N^2 k^2}{k^2 + m^2}. \quad (6.3.4)$$

This is the dispersion relation for internal gravity waves, where we now describe it as ω_c as continuum dispersion relation. It is a relationship of wavenumbers and buoyancy frequency. Internal gravity waves can be visualised by assuming the lines of constant phase (wave-crests and wave-troughs) to be constant. These lines have normal vector, i.e., $\nabla(kx + mz - \omega t) = (k, 0, m)$ where its direction is called wavevector $\mathbf{k} = (k, 0, m)$. The wave crests appear to move in the direction \mathbf{k} , i.e., the wave frequency ω_c is independent of the wave magnitude. In the absence of vertical wavenumber ($m = 0$), we then have $\omega_c = N$. The phase speed then is $c_p = \omega_c/k = N/k$. This means that the particle motions are purely vertical; in agreement with the definition of buoyancy frequency. On the other side, for the purely vertical wavenumber ($k = 0$), the frequency is then vanishes ($\omega_c = 0$). The particle motions are then horizontally, which imply that there is no wave propagation.

We have seen that at fixed z , the phase lines move in the x -direction and vice versa. However, for the full two-dimensional case of (6.1.3), the wave speed is not simply $\mathbf{c}_p = (\omega_c/k, \omega_c/m)$. Instead, it is

$$|\mathbf{c}_p| = \frac{|\omega_c|}{|\mathbf{k}|}. \quad (6.3.5)$$

Furthermore, the group velocity \mathbf{c}_g which is the gradient of ω_c with respect to the wavenum-

ber is

$$\mathbf{c}_g = \left(\frac{\partial \omega}{\partial k}, \frac{\partial \omega}{\partial m} \right) = \left(\frac{\pm Nm^2}{(k^2 + m^2)^{3/2}}, -\frac{\pm Nkm}{(k^2 + m^2)^{3/2}} \right) = \frac{\pm Nm}{(k^2 + m^2)^{3/2}} (m, -k). \quad (6.3.6)$$

There is a special property of internal gravity waves that can be illustrated from \mathbf{c}_p and \mathbf{c}_g . The vector product of these two velocities is $\mathbf{c}_p \cdot \mathbf{c}_g = 0$. This shows that the group velocity direction is perpendicular to the phase velocity. When the group velocity has an upward component, the phase velocity has a downward propagating component, and vice-versa. This is the main difference between the surface waves that we have discussed in previous chapters. Having all of these properties, we now can look further into the discrete version of internal gravity waves in unbounded domain.

6.3.2 Discrete internal waves

The main purpose here is to examine the discrete solutions of waves in stratified fluid without boundary. So, consider the staggered finite-difference C-grid, which means that all variables are staggered. We know that, there are four dependent variables (u, w, p, b) to be staggered on the C-grid. Following the same manner as in [6], the velocity nodes and pressure are arranged at the same nodes. As the main ingredient in the internal gravity waves is the buoyancy variable b , that generate the flow in the stratified fluid, this variable must be located precisely on the C-grid to give an accurate numerical solutions. There are of course various ways for this variable to be located on the grid [45, 38].

Since buoyancy is dependent on z , the variable can be located together on the pressure nodes or vertical velocity nodes. In this study, the variable is to be located on the vertical velocity nodes, as illustrated in Figure 6.3.1. Then, by using second-order centered differences the

equations are discretized as

$$-i\omega_d u_{m,n+\frac{1}{2}} = -\frac{1}{\bar{\rho}h} \left(p_{m+\frac{1}{2},n+\frac{1}{2}} - p_{m-\frac{1}{2},n+\frac{1}{2}} \right), \quad (6.3.7a)$$

$$-i\omega_d w_{m+\frac{1}{2},n} = -\frac{1}{\bar{\rho}h} \left(p_{m+\frac{1}{2},n+\frac{1}{2}} - p_{m+\frac{1}{2},n-\frac{1}{2}} \right) + b_{m+\frac{1}{2},n}, \quad (6.3.7b)$$

$$-i\omega_d b_{m+\frac{1}{2},n} + N^2 w_{m+\frac{1}{2},n} = 0, \quad (6.3.7c)$$

$$\frac{1}{h} \left(u_{m+1,n+\frac{1}{2}} - u_{m,n+\frac{1}{2}} + w_{m+\frac{1}{2},n+1} - w_{m+\frac{1}{2},n} \right) = 0. \quad (6.3.7d)$$

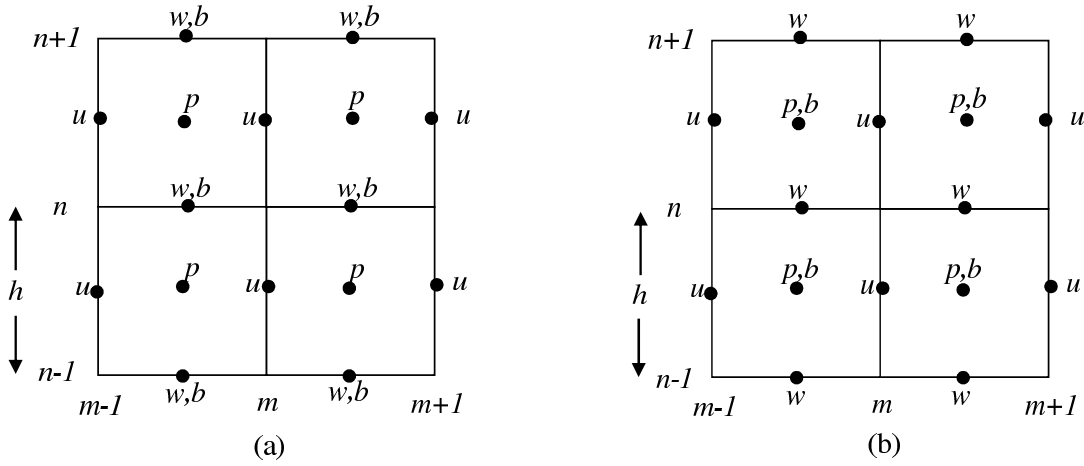


Figure 6.3.1: Different choice of variables staggering on a C-grid.

We seek solutions of the form

$$\begin{aligned} u_{m,n+\frac{1}{2}} &= \text{Re} \left(\hat{u} e^{i(kx_m + ly_{n+\frac{1}{2}})} \right), \\ w_{m+\frac{1}{2},n} &= \text{Re} \left(\hat{w} e^{i(kx_{m+\frac{1}{2}} + ly_n)} \right), \\ b_{m+\frac{1}{2},n} &= \text{Re} \left(\hat{b} e^{i(kx_{m+\frac{1}{2}} + ly_n)} \right). \end{aligned} \quad (6.3.8)$$

Substituting into (6.3.7a), (6.3.7b), (6.3.7c), (6.3.7d) yields

$$-i\omega_d \hat{u} + \frac{2i}{h} \sin\left(\frac{kh}{2}\right) \hat{p} = 0, \quad (6.3.9a)$$

$$-i\omega_d \hat{w} + \frac{2i}{h} \sin\left(\frac{lh}{2}\right) \hat{p} - \hat{b} = 0, \quad (6.3.9b)$$

$$-i\omega_d \hat{b} + N^2 \hat{w} = 0, \quad (6.3.9c)$$

$$\frac{2i}{h} \left(\sin\left(\frac{kh}{2}\right) \hat{u} + \cos\left(\frac{lh}{2}\right) \hat{w} \right) = 0. \quad (6.3.9d)$$

Rewritten in matrix form

$$\begin{pmatrix} -i\omega_d & 0 & 0 & \frac{2i}{h} \sin\left(\frac{kh}{2}\right) \\ 0 & -i\omega_d & -1 & \frac{2i}{h} \sin\left(\frac{lh}{2}\right) \\ 0 & N^2 & -i\omega_d & 0 \\ \frac{2i}{h} \sin\left(\frac{kh}{2}\right) & \frac{2i}{h} \sin\left(\frac{lh}{2}\right) & 0 & 0 \end{pmatrix} \begin{pmatrix} \hat{u} \\ \hat{w} \\ \hat{b} \\ \hat{p} \end{pmatrix} = \begin{pmatrix} 0 \\ 0 \\ 0 \\ 0 \end{pmatrix}. \quad (6.3.10)$$

The determinant of the matrix must be zero for non-trivial solution. So that, we recovered the dispersion relation

$$\omega_d^2 = \frac{N^2 \sin^2\left(\frac{kh}{2}\right)}{\sin^2\left(\frac{kh}{2}\right) + \sin^2\left(\frac{lh}{2}\right)}. \quad (6.3.11)$$

6.4 Internal Gravity Waves at A Sloping Boundary

We now turn to the next setting which is boundary tilted at 45° to the x axis. The straight boundary lies along the line $z = x$, at which there is no normal flow $\mathbf{u} \cdot \mathbf{n} = 0$. So there is perfect reflection when a wave with wavenumber (k_I, m_I) propagates towards the boundary. Our task is to find the reflected wave, with wavenumber (k_R, m_R) , both in the continuum solution and discrete solution.

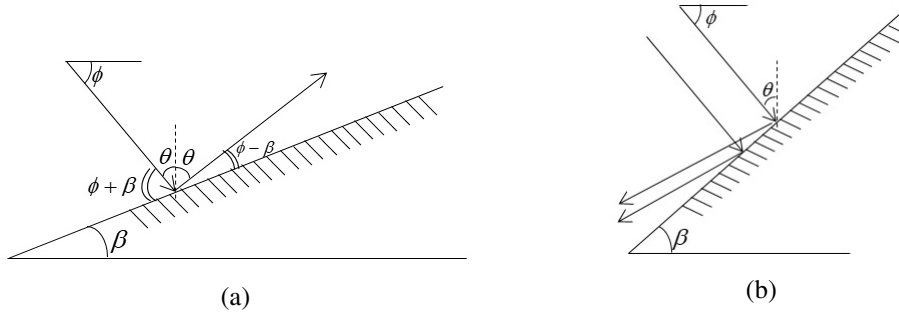


Figure 6.4.1: The mechanism of internal wave reflection at a sloping boundary. (a) reflection at a shallow slope, (b) reflection at $\beta > \phi$. This figure is re-illustrated from [53].

6.4.1 Continuum Solution

We first derive the continuum solution. We consider a two-dimensional semi-infinite domain bounded below by a sloping bottom at an angle 45° to the horizontal. The linearised governing equations for internal gravity waves in incompressible continuously stratified fluid satisfied (6.2.6). By considering wavelike solutions of the form (6.2.8), the equations then become

$$-i\omega u = -ikp \quad \Rightarrow u = \frac{k}{\omega}p, \quad (6.4.1a)$$

$$-i\omega w = -i\omega p + b, \quad (6.4.1b)$$

$$-i\omega b + N^2 w = 0 \quad \Rightarrow ib = \frac{N^2 w}{\omega}, \quad (6.4.1c)$$

$$iku + imw = 0 \quad \Rightarrow w = -\frac{ku}{m} \Rightarrow w = -\frac{k^2}{m\omega}p. \quad (6.4.1d)$$

Suppose a plane wave propagates towards the boundary, it then reflects away from the wall obeying the linear theory of internal waves. The free wave solutions can be decomposed in the form of an incident and reflected wave. If we take the pressure as a wave solution, we then have

$$p(x, z, t) = \text{Re} \left(A_I e^{i(k_I x + m_I z - \omega_I t)} + A_R e^{i(k_R x + m_R z - \omega_R t)} \right), \quad (6.4.2)$$

where the subscript I and R refer to the incident and reflected waves, respectively, k is the horizontal wavenumber in the x direction, m is the vertical wavenumber in z direction, ω is the wave frequency. At the boundary $z = x$, the wave has to satisfy the boundary condition no normal flow, which is

$$\mathbf{u} \cdot \mathbf{n} = 0 \quad \Rightarrow \quad -u + w = 0. \quad (6.4.3)$$

By substituting (6.4.1a) and (6.4.1d) into (6.4.3), and using (6.4.2) we have

$$\begin{aligned} & -\frac{k}{\omega} \left(A_I e^{i(k_I x + m_I x - \omega_I t)} + A_R e^{i(k_R x + m_R z - \omega_R t)} \right) \\ & - \frac{k^2}{m\omega} \left(A_I e^{i(k_I x + m_I z - \omega_I t)} + A_R e^{i(k_R x + m_R x - \omega_R t)} \right) = 0, \\ & - A_I e^{i((k_I + m_I)x - \omega_I t)} \left(\frac{k_I}{\omega_I} + \frac{k_I^2}{m_I \omega_I} \right) - A_R e^{i((k_R + m_R)x - \omega_R t)} \left(\frac{k_R}{\omega_R} + \frac{k_R^2}{m_R \omega_R} \right) = 0, \\ & - A_I e^{i((k_I - k_R + m_I - m_R)x - (\omega_I - \omega_R)t)} \left(\frac{k_I}{\omega_I} + \frac{k_I^2}{m_I \omega_I} \right) - A_R \left(\frac{k_R}{\omega_R} + \frac{k_R^2}{m_R \omega_R} \right) = 0. \end{aligned} \quad (6.4.4)$$

If (6.4.4) to be true for all x and t , then the following 3 conditions must be satisfied:

$$k_I - k_R + m_I - m_R = 0, \quad (6.4.5a)$$

$$\omega_I - \omega_R = 0, \quad (6.4.5b)$$

$$-A_I \left(\frac{k_I}{\omega_I} + \frac{k_I^2}{m_I \omega_I} \right) - A_R \left(\frac{k_R}{\omega_R} + \frac{k_R^2}{m_R \omega_R} \right) = 0. \quad (6.4.5c)$$

The dispersion relation for the internal gravity waves in (6.1.3) must satisfied for both incident and reflected waves. Thus, (6.4.5b) implies

$$\omega_I^2 = \frac{N^2 k_I^2}{(k_I^2 + m_I^2)} = \frac{N^2 k_R^2}{(k_R^2 + m_R^2)} = \omega_R^2. \quad (6.4.6)$$

Some algebraic manipulations of (6.4.6) give

$$\begin{aligned} \frac{N^2 k_I^2}{(k_I^2 + m_I^2)} &= \frac{N^2 k_R^2}{(k_R^2 + m_R^2)} \quad \Rightarrow \quad N^2 k_I^2 (k_R^2 + m_R^2) = N^2 k_R^2 (k_I^2 + m_I^2), \\ k_I^2 k_R^2 + k_I^2 m_R^2 &= k_R^2 k_I^2 + k_R^2 m_I^2, \quad \Rightarrow \quad k_I^2 m_R^2 = k_R^2 m_I^2. \end{aligned} \quad (6.4.7)$$

As the incident wave reflects at the boundary, the reflected wavenumber k_R and m_R must be in terms of incident and A_I . They can be obtained from (6.4.7). By eliminating m_R in (6.4.7) from (6.4.5a), we obtain

$$m_R = k_I + m_I - k_R \quad \Rightarrow \quad m_R^2 = k_I^2 + 2k_I m_I - 2k_I k_R - 2k_R m_I + m_I^2 + k_R^2,$$

and substituting into (6.4.7) gives

$$\begin{aligned} k_I^2 (k_I^2 + 2k_I m_I - 2k_I k_R - 2k_R m_I + m_I^2 + k_R^2) &= k_R^2 m_I^2, \\ k_I^4 + 2k_I^3 m_I - 2k_I^3 k_R - 2k_I^2 k_R m_I + k_I^2 m_I^2 + k_R^2 k_I^2 - k_R^2 m_I^2 &= 0, \\ k_R^2 (k_I^2 - m_I^2) - 2k_I^2 k_R (k_I + m_I) + k_I^2 (k_I^2 + 2k_I m_I + m_I^2) &= 0, \\ (k_I + m_I) [k_R^2 (k_I - m_I) - 2k_I^2 k_R + k_I^2 (k_I + m_I)] &= 0. \end{aligned}$$

An obvious possibility of reflected wavenumber is

$$k_I + m_I = 0 \quad \Rightarrow \quad k_I = -m_I, \quad \text{then (6.4.5a) gives } k_R = -m_R.$$

This shows that the wave is not reflected. Otherwise, the wave is only propagates along the boundary. So we must have the other possibility, i.e., $k_R^2 (k_I - m_I) - 2k_I^2 k_R + k_I^2 (k_I + m_I) =$

0. It implies

$$\begin{aligned} k_R &= \frac{2k_I^2 \pm \sqrt{4k_I^4 - 4k_I^2(k_I + m_I)(k_I - m_I)}}{2(k_I - m_I)}, \\ &= \frac{2k_I^2 \pm \sqrt{4k_I^4 - 4k_I^4 + 4k_I^2 m_I^2}}{2(k_I - m_I)}, \\ &= \frac{k_I^2 \pm k_I m_I}{(k_I - m_I)}. \end{aligned}$$

Here, if the negative sign is chosen, we then have

$$k_R = \frac{k_I(k_I - m_I)}{(k_I - m_I)} \Rightarrow k_R = k_I, \quad \text{and (6.4.5a) gives } m_R = m_I.$$

Again, this is not the interesting solution as there is no reflection occur at the boundary. So, the only possibility left is

$$k_R = \frac{k_I(k_I + m_I)}{k_I - m_I} \Rightarrow m_R = -\frac{m_I(k_I + m_I)}{k_I - m_I}. \quad (6.4.9)$$

Note that, this is only true for the case of $k_I \neq m_I$, for which reflection to be occurred. Otherwise, we only have wave propagation along the boundary. The reflected wavenumber (6.4.9) expresses the change in reflected wavenumber upon reflection. Both are consistent with the well known result in [53] who written reflected wavenumber in terms of trigometrical function. (6.4.9) also equivalent to equation (5) in [28], who consider three-dimensional linearised inviscid Boussinesq incompressible motion in a uniformly stratified rotating fluid.

Having these reflected wavenumber and same frequency during reflection, (6.4.5c) can be

solved to give reflected amplitude A_R . We found the reflected amplitude as

$$\begin{aligned} -A_I \frac{k_I}{m_I \omega_I} (k_I + m_I) - A_R \frac{k_R}{m_R \omega_R} (k_R + m_R) &= 0, \\ -A_I \frac{k_I}{m_I \omega_I} (k_I + m_I) + A_R \frac{k_I}{m_I \omega_R} (k_I + m_I) &= 0, \end{aligned} \quad (6.4.10)$$

$$A_I = A_R.$$

With these expressions, the velocity field and buoyancy are found to be

$$u(x, y, t) = \text{Re} \left(\frac{k_I}{\omega} A_I e^{i(k_I x + m_I z - \omega t)} + \frac{k_I (k_I + m_I)}{\omega (k_I - m_I)} A_I e^{i \left(\frac{(k_I - m_I)}{(k_I - m_I)} (k_I x - m_I z - \omega t) \right)} \right), \quad (6.4.11)$$

$$w(x, y, t) = \text{Re} \left(-\frac{k_I^2}{\omega m_I} A_I e^{i(k_I x + m_I z - \omega t)} + \frac{k_I^2 (k_I + m_I)}{\omega m_I (k_I - m_I)} A_I e^{i \left(\frac{(k_I - m_I)}{(k_I - m_I)} (k_I x - m_I z - \omega t) \right)} \right), \quad (6.4.12)$$

$$b(x, y, t) = \text{Re} \left(\frac{i(k^2 + m^2)}{m} \left(A_I e^{i(k_I x + m_I z - \omega t)} - \frac{(k_I + m_I)}{(k_I - m_I)} A_I e^{i \left(\frac{(k_I + m_I)}{(k_I - m_I)} (k_I x - m_I z - \omega t) \right)} \right) \right) \quad (6.4.13)$$

Although we obtain different expression for the reflected amplitude as in equation (7) in [28], we note that the second term in our velocity (6.4.11, 6.4.12) and buoyancy (6.4.13) components (i.e., $\frac{(k_I + m_I)}{(k_I - m_I)} A_I$) is similar to the reflected amplitude, A_R , Eq. (7) in [28]. This is because we assume the pressure as our plane wave solution, instead of vertical velocity as was done by [28]. So that, our continuum solutions are consistent with the well known linear theory of internal waves. Having completed these continuum solutions, the performance of the discrete solutions that will derive in the next section can be tested in the limit of grid spacing tends to zero.

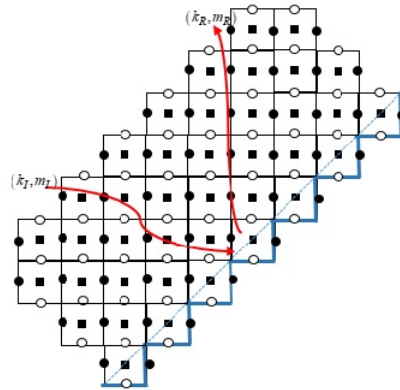


Figure 6.4.2: Internal wave reflection at staircase boundary on the C-grid.

6.4.2 Discrete solution

Now, we consider the staggered C-grid with velocity components located on the edges on each cell while pressure nodes at the centre of the cell. The buoyancy variable is located together with the vertical velocity as illustrated in Figure 6.3.1. As the pressure nodes are located at the centre of each cell, the distance between the pressure and velocities node is half grid size ($h/2$), and we write coordinate $x_m = mh$, $z_n = nh$, where m, n are the indices in the x and z direction, respectively. The bottom boundary has an angle 45° to the vertical, we then have perfect staircase boundaries parallel with $z = x$, as shown in Figure 6.4.2. The representation of the planar boundary with staircase allows us to investigate the behaviour of internal gravity waves reflection at the boundary. The problem setup is analogous to the previous continuum setup, so that internal gravity waves equations satisfied (6.2.8). By using second order centred finite difference formulation, the equations are discretized on

the C-grid as

$$-i\omega_d u_{m,n+\frac{1}{2}} = -\frac{1}{h} \left(p_{m+\frac{1}{2},n+\frac{1}{2}} - p_{m-\frac{1}{2},n+\frac{1}{2}} \right), \quad (6.4.14a)$$

$$-i\omega_d w_{m+\frac{1}{2},n} = -\frac{1}{h} \left(p_{m+\frac{1}{2},n+\frac{1}{2}} - p_{m+\frac{1}{2},n-\frac{1}{2}} \right) + b_{m+\frac{1}{2},n}, \quad (6.4.14b)$$

$$-i\omega_d b_{m+\frac{1}{2},n} + N^2 w_{m+\frac{1}{2},n} = 0, \quad (6.4.14c)$$

$$\frac{1}{h} \left(u_{m+1,n+\frac{1}{2}} - u_{m,n+\frac{1}{2}} + w_{m+\frac{1}{2},n+1} - w_{m+\frac{1}{2},n} \right) = 0, \quad (6.4.14d)$$

where ω_d represents the discrete frequency. From (6.4.14c), we can have buoyancy as

$$b_{m+\frac{1}{2},n} = -\frac{iN^2}{\omega_d} w_{m+\frac{1}{2},n},$$

and substituting into (6.4.14b) gives

$$\begin{aligned} -i\omega_d w_{m+\frac{1}{2},n} &= -\frac{p_{m+\frac{1}{2},n+\frac{1}{2}} - p_{m+\frac{1}{2},n-\frac{1}{2}}}{h} - \frac{iN^2}{\omega_d} w_{m+\frac{1}{2},n}, \\ \left(-i\omega_d + \frac{iN^2}{\omega_d} \right) w_{m+\frac{1}{2},n} &= -\frac{1}{h} \left(p_{m+\frac{1}{2},n+\frac{1}{2}} - p_{m+\frac{1}{2},n-\frac{1}{2}} \right), \\ w_{m+\frac{1}{2},n} &= \frac{i\omega_d}{h(N^2 - \omega_d)} \left(p_{m+\frac{1}{2},n+\frac{1}{2}} - p_{m+\frac{1}{2},n-\frac{1}{2}} \right). \end{aligned} \quad (6.4.15)$$

Simplifying (6.4.14a) gives discrete horizontal velocity as

$$u_{m,n+\frac{1}{2}} = -\frac{i}{\omega_d h} \left(p_{m+\frac{1}{2},n+\frac{1}{2}} - p_{m-\frac{1}{2},n-\frac{1}{2}} \right). \quad (6.4.16)$$

We suppose that a free internal gravity wave propagates towards the sloping boundary and reflects away. The wave solution is the combination of both incoming and reflected wave. By assuming the pressure as our discrete solution, we have

$$\begin{aligned} p_{m+\frac{1}{2},n+\frac{1}{2}} &= A_I \exp(i\{k_I x_{m+\frac{1}{2}} + m_I z_{n+\frac{1}{2}} - \omega_d t\}) \\ &\quad + A_R \exp(i\{k_R x_{m+\frac{1}{2}} + m_R z_{n+\frac{1}{2}} - \omega_d t\}). \end{aligned} \quad (6.4.17)$$

At the boundary, the wave must satisfy the no normal flow boundary conditions

$$u_{j,j-\frac{1}{2}} = 0, \quad w_{j+\frac{1}{2},j} = 0, \quad j \in \mathbb{Z}. \quad (6.4.18)$$

Substituting (6.4.15) and (6.4.16) into (6.4.14d) and imposing the boundary conditions gives

$$\begin{aligned} & \frac{1}{h} \left(\frac{i}{\omega_d h} \left(p_{j+\frac{1}{2},j+\frac{1}{2}} - p_{j-\frac{1}{2},j+\frac{1}{2}} \right) + \frac{i\omega_d}{h(N^2 - \omega_d^2)} \left(p_{j+\frac{1}{2},j+\frac{3}{2}} - p_{j+\frac{1}{2},j+\frac{1}{2}} \right) \right) = 0, \\ & \frac{i}{h^2} \left(\left(\frac{1}{\omega_d} - \frac{\omega_d}{(N^2 - \omega_d^2)} \right) p_{j+\frac{1}{2},j+\frac{1}{2}} + \frac{\omega_d}{(N^2 - \omega_d^2)} p_{j+\frac{1}{2},j+\frac{3}{2}} - \frac{1}{\omega_d} p_{j-\frac{1}{2},j+\frac{1}{2}} \right) = 0, \end{aligned}$$

substituting (6.4.17) gives

$$\begin{aligned} & \left(\frac{1}{\omega_d} - \frac{\omega_d}{(N^2 - \omega_d^2)} \right) \left(A_I e^{i(k_I(j+\frac{1}{2})h+m_I(j+\frac{1}{2})h-\omega_d t)} + A_R e^{i(k_R(j+\frac{1}{2})h+m_R(j+\frac{1}{2})h-\omega_d t)} \right) \\ & + \frac{\omega_d}{(N^2 - \omega_d^2)} \left(A_I e^{i(k_I(j+\frac{1}{2})h+m_I(j+\frac{3}{2})h-\omega_d t)} + A_R e^{i(k_R(j+\frac{1}{2})h+m_R(j+\frac{3}{2})h-\omega_d t)} \right) \\ & - \frac{1}{\omega_d} \left(A_I e^{i(k_I(j-\frac{1}{2})h+m_I(j+\frac{1}{2})h-\omega_d t)} + A_R e^{i(k_R(j+\frac{1}{2})h+m_R(j+\frac{1}{2})h-\omega_d t)} \right) = 0. \end{aligned}$$

$$\begin{aligned} & A_I e^{i((k_I+m_I-k_R-m_R)jh-(\omega_I-\omega_R)t)} \left[\left(-\frac{1}{\omega_I} + \frac{\omega_I}{(N^2 - \omega_I^2)} \right) e^{i\left(\frac{k_I h}{2} + \frac{m_I h}{2}\right)} \right. \\ & \quad \left. - \frac{\omega_I}{(N^2 - \omega_I^2)} e^{i\left(\frac{k_I h}{2} + \frac{3m_I h}{2}\right)} + \frac{1}{\omega_d} e^{i\left(\frac{m_I h}{2} - \frac{k_I h}{2}\right)} \right] \\ & = A_R \left[\left(\frac{1}{\omega_R} - \frac{\omega_R}{(N^2 - \omega_R^2)} \right) e^{i\left(\frac{k_R h}{2} + \frac{m_R h}{2}\right)} \right. \\ & \quad \left. + \frac{\omega_R}{(N^2 - \omega_R^2)} e^{i\left(\frac{k_R h}{2} - \frac{3m_R h}{2}\right)} - \frac{1}{\omega_R} e^{i\left(\frac{m_R h}{2} - \frac{k_R h}{2}\right)} \right]. \end{aligned}$$

If this must hold for all j and t , the following conditions must be satisfied:

$$k_I + m_I - k_R - m_R = 0, \quad (6.4.19a)$$

$$\omega_I - \omega_R = 0, \quad (6.4.19b)$$

$$\begin{aligned} & A_I \left[\left(-\frac{1}{\omega_I} + \frac{\omega_I}{(N^2 - \omega_I^2)} \right) e^{i\left(\frac{k_I h}{2} + \frac{m_I h}{2}\right)} - \frac{\omega_I}{(N^2 - \omega_I^2)} e^{i\left(\frac{k_I h}{2} + \frac{3m_I h}{2}\right)} + \frac{1}{\omega_d} e^{i\left(\frac{m_I h}{2} - \frac{k_I h}{2}\right)} \right] \\ = & A_R \left[\left(\frac{1}{\omega_R} - \frac{\omega_R}{(N^2 - \omega_R^2)} \right) e^{i\left(\frac{k_R h}{2} + \frac{m_R h}{2}\right)} + \frac{\omega_R}{(N^2 - \omega_R^2)} e^{i\left(\frac{k_R h}{2} - \frac{3m_R h}{2}\right)} - \frac{1}{\omega_R} e^{i\left(\frac{m_R h}{2} - \frac{k_R h}{2}\right)} \right]. \end{aligned} \quad (6.4.19c)$$

Through the dispersion relation (6.3.11) and (6.4.19b), we have

$$\begin{aligned} & \frac{N^2 \sin^2\left(\frac{k_I h}{2}\right)}{\sin^2\left(\frac{k_I h}{2}\right) + \sin^2\left(\frac{m_I h}{2}\right)} = \frac{N^2 \sin^2\left(\frac{k_R h}{2}\right)}{\sin^2\left(\frac{k_R h}{2}\right) + \sin^2\left(\frac{m_R h}{2}\right)}, \\ \sin^2\left(\frac{k_I h}{2}\right) \left[\sin^2\left(\frac{k_R h}{2}\right) + \sin^2\left(\frac{m_R h}{2}\right) \right] &= \sin^2\left(\frac{k_R h}{2}\right) \left[\sin^2\left(\frac{k_I h}{2}\right) + \sin^2\left(\frac{m_I h}{2}\right) \right], \\ \sin^2\left(\frac{k_I h}{2}\right) \sin^2\left(\frac{m_R h}{2}\right) &= \sin^2\left(\frac{k_R h}{2}\right) \sin^2\left(\frac{m_I h}{2}\right), \\ \frac{\left(1 - \cos 2\left(\frac{k_I h}{2}\right)\right)}{2} \cdot \frac{\left(1 - \cos 2\left(\frac{m_R h}{2}\right)\right)}{2} &= \frac{\left(1 - \cos 2\left(\frac{k_R h}{2}\right)\right)}{2} \cdot \frac{\left(1 - \cos 2\left(\frac{m_I h}{2}\right)\right)}{2}, \\ (1 - \cos(k_I h))(1 - \cos(m_R h)) &= (1 - \cos(k_R h))(1 - \cos(m_I h)), \\ -\cos(m_R h) - \cos(k_I h) + \cos(k_I h) \cos(m_R h) &= -\cos(m_I h) - \cos(k_R h) + \cos(k_R h) \cos(m_I h). \end{aligned}$$

In the limit of $h \rightarrow 0$, Taylor series expansion gives

$$k_I^2 m_R^2 = k_R^2 m_I^2 + O(h^2), \quad (6.4.20)$$

which is equivalent to equation (6.4.7) in the continuum case, with second order correction, as expected due to the second order finite-differences. But, from (6.4.19a) we have

$$m_R = k_I + m_I - k_R \Rightarrow m_R^2 = k_I^2 + 2k_I m_I - 2k_I k_R - 2k_R m_I + m_I^2 + k_R^2.$$

This means that the reflected wavenumber k_R can be found by eliminating m_R from (6.4.20). So that (6.4.20) gives

$$\begin{aligned} k_I^2 (k_I^2 + 2k_I m_I - 2k_I k_R - 2k_R m_I + m_I^2 + k_R^2) &= k_R^2 m_I^2 + O(h^2), \\ k_I^4 + 2k_I^3 m_I - 2k_I^3 k_R - 2k_R k_I^2 m_I + k_I^2 m_I^2 + k_I^2 k_R^2 - k_R^2 m_I^2 + O(h^2) &= 0, \\ k_R^2 (k_I^2 - m_I^2) - 2k_R (k_I^3 - k_I^2 m_I) + k_I^2 (m_I^2 + k_I^2 + 2k_I m_I) + O(h^2) &= 0, \\ k_R^2 (k_I + m_I)(k_I - m_I) - 2k_R k_I^2 (k_I + m_I) + k_I^2 (k_I + m_I)^2 + O(h^2) &= 0, \\ (k_I + m_I) \left[k_R^2 (k_I - m_I) - 2k_R k_I^2 + k_I^2 (k_I + m_I) \right] + O(h^2) &= 0. \end{aligned}$$

An obvious possibility is

$$k_I + m_I + O(h^2) = 0 \quad \Rightarrow \quad k_I = -m_I + O(h^2), \quad \text{which implies} \quad k_R = -m_R + O(h^2).$$

However, this is impossible because this shows wave propagates along the boundary. If the terms in the square bracket is possible, then we can have

$$\begin{aligned}
k_R^2 - \frac{2k_R k_I^2}{k_I - m_I} + \frac{k_I^2(k_I + m_I)}{k_I - m_I} + O(h^2) &= 0, \\
k_R &= \frac{1}{2} \left[\frac{2k_I^2}{(k_I - m_I)} \pm \sqrt{\frac{4k_I^4}{(k_I - m_I)^2} - 4(1) \left(\frac{k_I^2(k_I + m_I)}{(k_I - m_I)} + O(h^2) \right)} \right], \\
k_R &= \frac{k_I^2}{(k_I - m_I)} \pm \frac{1}{2} \sqrt{\frac{4k_I^4}{(k_I - m_I)^2} - 4 \left(\frac{k_I^2(k_I + m_I)}{(k_I - m_I)} + O(h^2) \right)}, \\
k_R &= \frac{k_I^2}{(k_I - m_I)} \pm \frac{1}{2} \sqrt{\frac{4k_I^4}{(k_I - m_I)^2} - 4 \frac{k_I^2(k_I + m_I)(k_I - m_I)}{(k_I - m_I)^2} + O(h^2)}, \\
k_R &= \frac{k_I^2}{(k_I - m_I)} \pm \frac{1}{2} \sqrt{\frac{4k_I^4 - 4k_I^4 + 4k_I^2 m_I^2 + O(h^2)}{(k_I - m_I)^2}}, \\
k_R &= \frac{k_I^2}{(k_I - m_I)} \pm \frac{k_I m_I}{(k_I - m_I)} (1 + O(h^2)),
\end{aligned}$$

which again gives another two possibilities of reflected wavenumber. On the first possibility is rejected since there is no wave reflection occur at the boundary

$$k_R = \frac{k_I(k_I + m_I)}{(k_I - m_I)} + O(h^2) \quad \text{or} \quad k_R = \frac{k_I(k_I - m_I)}{(k_I - m_I)} + O(h^2) = k_I + O(h^2). \quad (6.4.21)$$

It is noted from (6.4.19a) that, the latter implies $m_R = m_I + O(h^2)$, which is impossible because of the same wave. Hence, the former is the only possibility of k_R . So that, we also have

$$m_R = -\frac{m_I(k_I + m_I)}{k_I - m_I} + O(h^2). \quad (6.4.22)$$

Now, we only need to find A_R . From (6.4.19c), we have

$$\begin{aligned} A_I \left[\frac{2\omega_I^2 - N^2}{\omega_I (N^2 - \omega_I^2)} - \frac{\omega_I e^{im_I h}}{(N^2 - \omega_I^2)} + \frac{e^{-ik_I h}}{\omega_I} \right] e^{i\frac{h}{2}(k_I + m_I)} \\ = A_R \left[\frac{N^2 - 2\omega_R^2}{\omega_R (N^2 - \omega_R^2)} + \frac{\omega_R e^{im_R h}}{(N^2 - \omega_R^2)} - \frac{e^{-ik_R h}}{\omega_R} \right] e^{i\frac{h}{2}(k_R + m_R)}, \end{aligned}$$

but, by using (6.4.19a) and (6.4.19b) we obtained

$$A_I \left[\frac{2\omega^2 - N^2}{\omega (N^2 - \omega^2)} - \frac{\omega e^{im_I h}}{(N^2 - \omega^2)} + \frac{e^{-ik_I h}}{\omega} \right] = A_R \left[\frac{N^2 - 2\omega^2}{\omega (N^2 - \omega^2)} + \frac{\omega e^{im_R h}}{(N^2 - \omega^2)} - \frac{e^{-ik_R h}}{\omega} \right]. \quad (6.4.23)$$

Factorising and canceling the denominator followed by the Taylor series expansion of the exponential terms give

$$\begin{aligned} A_I \left[2\omega^2 - N^2 - \omega^2 (1 + im_I h + O(h^2)) + (N^2 - \omega^2) (1 - ik_I h + O(h^2)) \right] \\ = A_R \left[N^2 - 2\omega^2 + \omega^2 (1 + im_R h + O(h^2)) - (N^2 - \omega^2) (1 - ik_R h + O(h^2)) \right], \\ A_I \left[\omega^2 (k_I - m_I) - N^2 k_I - \frac{ih}{2} (\omega^2 (k_I^2 + m_I^2) - N^2 k_I^2) + O(h^2) \right] \\ = A_R \left[\omega^2 (m_R - k_R) + N^2 k_R + \frac{ih}{2} (\omega^2 (k_R^2 + m_R^2) - N^2 k_R^2) + O(h^2) \right], \end{aligned}$$

and substituting the reflected wavenumber (6.4.21) yield

$$\begin{aligned}
& A_I \left[-\frac{N^2 k_I m_I (k_I + m_I)}{(k_I^2 + m_I^2)} - \frac{ih}{2} \left(\frac{N^2}{(k_I^2 + m_I^2)} \right) + O(h^2) \right] \\
&= A_R \left[-\frac{N^2 k_I m_I (k_I + m_I)}{(k_I^2 + m_I^2)} + \frac{ih}{2} \left(\frac{N^2 (k_I + m_I)^2}{(k_I - m_I)^2 (k_I^2 + m_I^2)} \right) + O(h^2) \right], \\
\Rightarrow A_R &= \frac{A_I \left[-\frac{N^2 k_I m_I (k_I + m_I)}{(k_I^2 + m_I^2)} - \frac{ih}{2} \left(\frac{N^2}{(k_I^2 + m_I^2)} \right) + O(h^2) \right]}{\left[-\frac{N^2 k_I m_I (k_I + m_I)}{(k_I^2 + m_I^2)} + \frac{ih}{2} \left(\frac{N^2 (k_I + m_I)^2}{(k_I - m_I)^2 (k_I^2 + m_I^2)} \right) + O(h^2) \right]}.
\end{aligned}$$

Factorising the first term in bracket and simplifying, we obtained

$$A_R = A_I \left(1 + ih \frac{(k_I^2 + m_I^2)}{k_I m_I (k_I - m_I)^2 (k_I + m_I)} \right) + O(h^2). \quad (6.4.24)$$

It is found that the reflected amplitude of internal gravity wave has first-order (complex) error. This is also known as the phase error. It is showed that the staircase boundaries give influence to the internal wave speed.

6.5 Internal Waves Attractor

Now, we turn to more realistic or natural situation of the existing of internal gravity waves, i.e., in a closed basin. It is important to consider such realistic situation of internal gravity waves as it will give a key to understand the patterns of internal gravity wave in fluids. In a closed basin, internal gravity waves propagate and reflect from the side of the basin. In a closed domain with at least one sloping boundary, it has been proved that multiple reflections of internal gravity wave will lead to a closed orbit that is called internal wave attractor [47, 48]. Various theoretical and laboratory settings were assumed in order to study the existence and the structure of the of the attractors as they varied the parameters

of the geometry. In a numerical experiment context, one needs to consider a suitable numerical scheme to investigate the existence of internal wave attractor since it will involve large computational. As internal wave attractor could be existed upon multiples reflections, boundary approximation also is a crucial issue in any numerical scheme. In this section we will discuss a numerical experiment of internal gravity wave in a square domain.

As we know, internal wave attractor appearance depends on the angle of reflection. For a square domain, internal gravity waves focusing only occurs when a boundary of the domain is inclined with respect to gravity [47]. For this reason here we assumed our square domain to be rotated through an angle $0 \leq \theta \leq \pi/4$. Then, the governing equations now satisfy

$$\frac{\partial u}{\partial t} = -\frac{\partial p}{\partial x} + b \sin \theta, \quad (6.5.1a)$$

$$\frac{\partial w}{\partial t} = -\frac{\partial p}{\partial z} + b \cos \theta, \quad (6.5.1b)$$

$$\frac{\partial b}{\partial t} + N^2(u \sin \theta + w \cos \theta) = 0, \quad (6.5.1c)$$

$$\frac{\partial u}{\partial x} + \frac{\partial w}{\partial z} = 0, \quad (6.5.1d)$$

where θ is the angle of (x, z) -coordinate system. This angle θ plays an important role in the appearance of the internal gravity waves attractor. These equations cannot be solved analytically if the square domain is tilted [11]. Thus, we only can compare the results of numerical solutions qualitatively with other existing numerical solutions. These equations have to be solved with the no normal flow boundary condition $\mathbf{u} \cdot \mathbf{n} = 0$ on the square domain.

6.5.1 Numerical setting

In setting up a numerical experiment of (6.5.1), the equations are discretised such that finite-differencing is applicable to the C-grid. As discussed in section 6.3.2, on this grid the velocity vector (u, w) is located at the boundary of a finite-difference cell, while pressure p

and buoyancy b are co-located at the centre of cell. We choose the grid spacings $dx = dy = h$ for all experiments. We consider a square domain placed on top of this grid, and we then construct a grid on a quadrilateral of extend $2l_x \times 2l_y$ that just extends beyond the specified domain, where $2l_x = n_x h$ and $2l_y = n_y h$ for some integers n_x and n_y .

All variables are stored as matrices. In our experiments, we are using the same second-order centred differences as first discussed in Chapter 2, to evaluate the derivative in our model. Since all variables are staggered, (6.5.1) are written in matrix form as

$$\frac{\partial U}{\partial t} = -D_{pu}P + \sin \theta B, \quad (6.5.2a)$$

$$\frac{\partial W}{\partial t} = -PD_{pw} + \cos \theta B, \quad (6.5.2b)$$

$$\frac{\partial B}{\partial t} + N^2 (\sin \theta U + \cos \theta W) = 0, \quad (6.5.2c)$$

$$D_{up}U + WD_{wp} = 0, \quad (6.5.2d)$$

where U , V , P and B are the matrices of the variables. Thus, we have four different differentiation matrices for the derivatives in our model. By adapting Crank-Nicolson scheme, (6.5.2) become

$$\frac{U^{n+1} - U^n}{\Delta t} = -D_{pu} \frac{P^{n+1} + P^n}{2} + \sin \theta \frac{B^{n+1} + B^n}{2}, \quad (6.5.3a)$$

$$\frac{W^{n+1} - W^n}{\Delta t} = -\frac{P^{n+1} + P^n}{2} D_{pw} + \cos \theta \frac{B^{n+1} + B^n}{2}, \quad (6.5.3b)$$

$$\frac{B^{n+1} - B^n}{\Delta t} + N^2 \left(\sin \theta \frac{U^{n+1} + U^n}{2} + \cos \theta \frac{W^{n+1} + W^n}{2} \right) = 0, \quad (6.5.3c)$$

$$D_{up}U^n + W^n D_{wp} = 0. \quad (6.5.3d)$$

where superscript n represents time step. Unlike in the previous chapter, here we are using Crank-Nicolson method, rather than RK4, so it is a second order scheme. The main reason we are using this scheme is because it is a natural scheme for enforcing incompressibility (6.5.2d) or (6.5.3d). As we know, RK4 is an explicit scheme, then the flow that

is generated at t_{n+1} does not necessarily satisfy (6.5.3d), and a further projection step is necessary to make it incompressible. The Crank Nicolson scheme has this projection step embedded. The other reason is because of the accuracy requirement. In the earlier chapters we were trying to measure spatial convergence, and thus absolutely needed to have the time-discretization errors to be tiny, so that all that remained were the spatial-discretization errors. However, in this chapter this same accuracy is not needed.

We can eliminate U and W in (6.5.3c) using (6.5.3a) and (6.5.3b), respectively. Then we have

$$B^{n+1} \left(1 + \frac{N^2 \Delta^2}{4} \right) = B^n \left(1 - \frac{N^2 \Delta^2}{4} \right) - N^2 \Delta (\sin \theta U^n + \cos \theta W^n) + \frac{N^2 \Delta^2}{4} (\sin \theta D_{pu} + \cos \theta D_{pw}) (P^{n+1} + P^n). \quad (6.5.4)$$

In (6.5.4), we first solve for P and B by performing inversion on the right-hand side. In our experiment, we used initial condition

$$u = \text{Re} [-A \exp\{-i\omega t\} \sin(kx) \cos(my)], \quad (6.5.5a)$$

$$w = \text{Re} [A \exp\{-i\omega t\} \cos(kx) \sin(my)], \quad (6.5.5b)$$

$$b = \text{Re} \left[A \exp\{-i\omega t\} \frac{i\omega m}{k} \cos(kx) \sin(my) \right], \quad (6.5.5c)$$

$$p = \text{Re} \left[-A \exp\{-i\omega t\} \frac{iN^2}{\omega} \cos(kx) \sin(my) \right], \quad (6.5.5d)$$

where $k = \pi l / 2l_x$ and $m = \pi n / 2l_y$, (l, n) is initial condition wavemode are chosen at two different values: (i) $(l, n) = (1, 1)$ and (ii) $(1, 3)$. The initial condition $(l, n) = (1, 1)$ is expected to produce $(1, 1)$ wave attractor while initial condition $(l, n) = (1, 3)$ is expected to produce $(1, 3)$ wave attractor [11].

6.5.2 Freely evolving flow

In this section, we investigate the initial boundary value problem (6.5.1) in a freely evolving flow. We first consider the experiment of aligned square domain. In order to study the appearance of wave attractor, the angle of gravity θ is tilted at $\pi/20$ to the axis. By using initial mode $(l, n) = (1, 1)$, stratification frequency $N^2 = 1$, so that the frequency is $\omega = \sqrt{2}$. By using $h = 0.002$ and $dt = 0.05$, we run the experiment up to $t_{\max} = 50T$. The result for buoyancy b at $t = 0, 100, 200, 300, 400, 500$ is showed in Figure 6.5.1. We can see that there is a similar structure approaching to the family $(1, 1)$ attractor. We also run the experiment up to $350T$ in order to seen the appearance of attractor. Figure 6.5.2 shows the solution for b at $t = 1000, 1500, 2000, 2500, 3000, 3500$. We can see that the wave keep reflecting at the boundary and a similar structure approaching attractor is obtained. We also observed that there is an reflection point at each sides of the square, where we called it as $(1, 1)$ attractor. It can be seen that as we continue our experiments, the internal gravity waves propagate and the family of $(1, 1)$ attractor is appearing with one reflection at each boundary. Note that this results is important because it shows that our numerical setting is agreed with the results in [11], (see Figure 2(b,c) in [11]), which was produced by using structure-preserving discretization scheme (Störmer-Verlet method).

We also repeat the same experiment by only changing the initial wavemode to be $(l, n) = (1, 3)$, and the frequency now is $\omega = \sqrt{10}$. Figure 6.5.3 shows the results for b at $t = 0, 100, 200, 300, 400, 500$. In this figure, it is not clear about the appearance of wave attractor. So that we run our experiment up to $175T$, and the result is showed in Figure 6.5.4. Similar to the case $(l, n) = (1, 1)$, now the family of $(1, 3)$ attractor is appearing. We can see that there is one reflection point at the upper and lower boundary, while three reflection points on the left and right sides of the square, which is called $(1, 3)$ attractor.

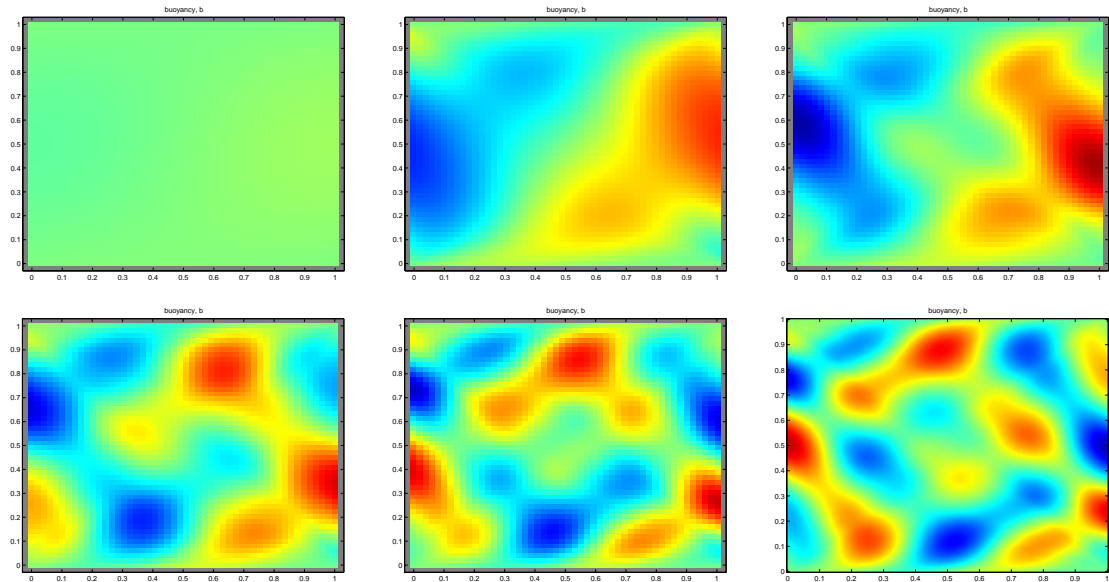


Figure 6.5.1: Evolution of buoyancy, b at $t = 0, 100, 200, 300, 400, 500$ (i.e., $0 < t < 50T$) with mode $(l, n) = (1, 1)$ at $h = 0.002$, $dt = 0.05$. The period of wave is $T = 2\pi/\omega = 2\sqrt{2}\pi \approx 8.8858$.

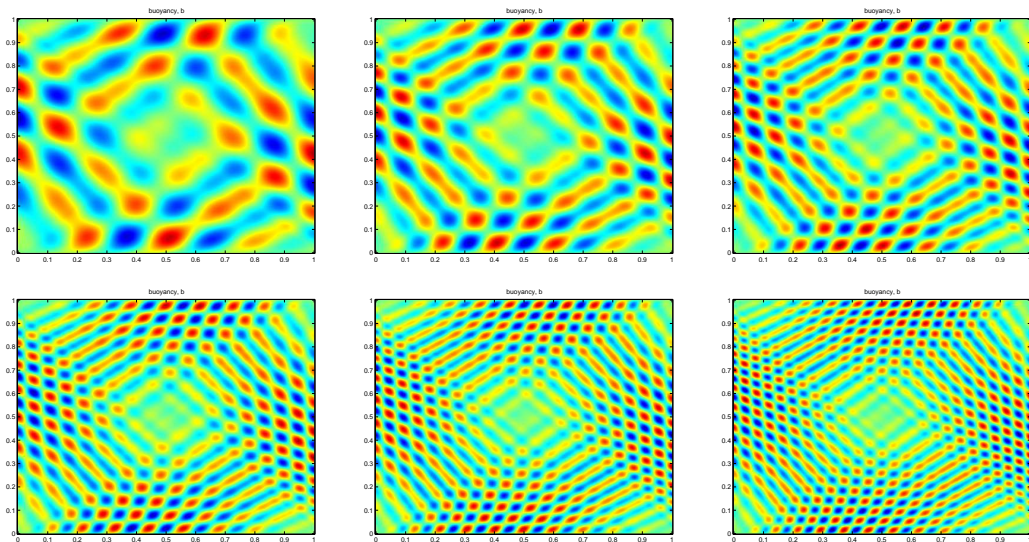


Figure 6.5.2: Evolution of buoyancy, b at $t = 1000, 1500, 2000, 2500, 3000, 3500$ (i.e., $100T < t < 350T$) with mode $(l, n) = (1, 1)$ at $h = 0.002$, $dt = 0.05$.

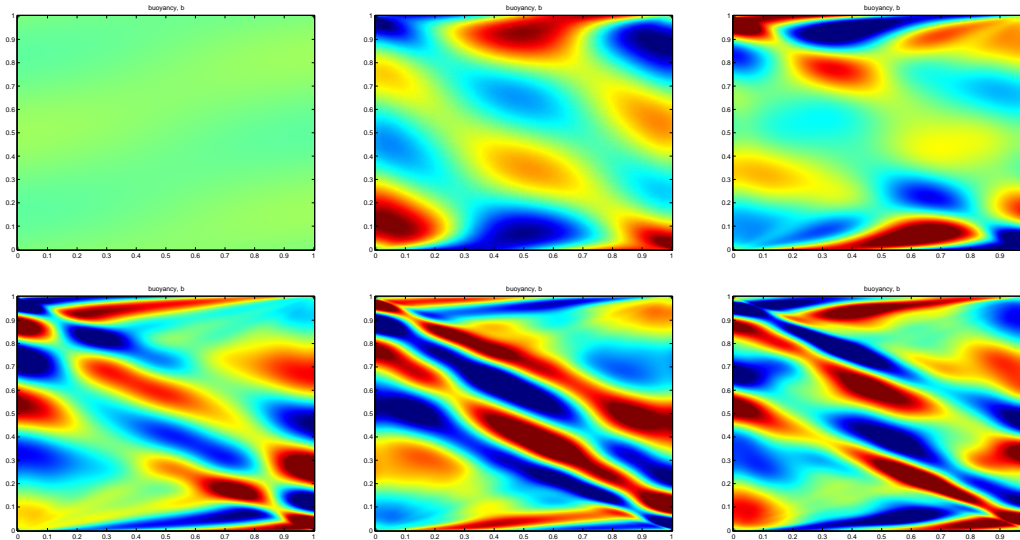


Figure 6.5.3: Evolution of buoyancy, b at $t = 0, 100, 200, 300, 400, 500$ (i.e., $0 < t < 25T$) with mode $(l, n) = (1, 3)$ at $h = 0.002$, $dt = 0.05$. The period is $T = 2\pi/\omega = 2\sqrt{10}\pi \approx 19.8692$.

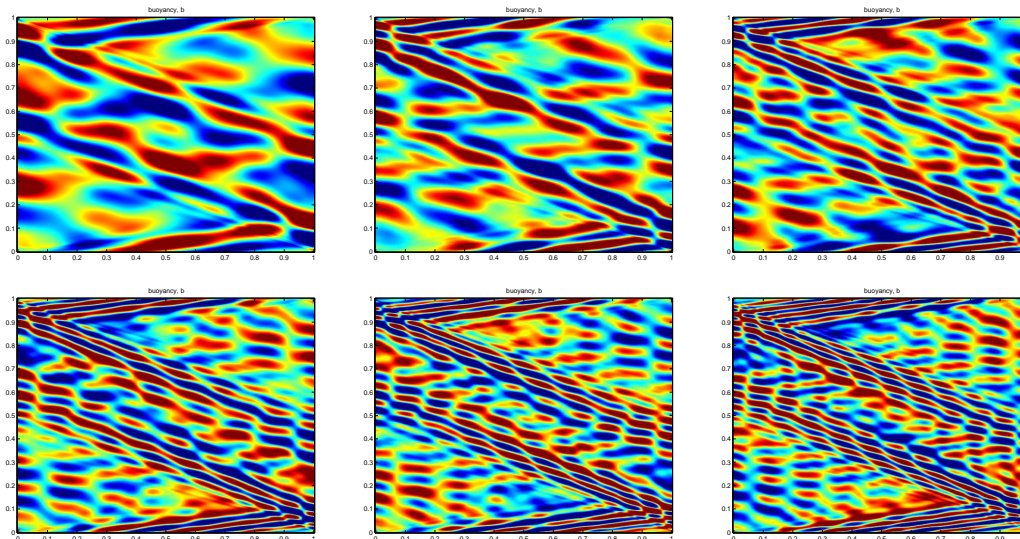


Figure 6.5.4: Evolution of buoyancy, b at $t = 1000, 1500, 2000, 2500, 3000, 3500$ (i.e., $50T < t < 175T$) with mode $(l, n) = (1, 3)$ at $h = 0.002$, $dt = 0.05$.

6.5.3 Parametric excitation

It has been proved that wave attractors can be generated by periodically forcing a stratified fluid in a domain with inclined boundaries. The appearance of wave attractor can be found experimentally by vertically oscillating a container with a sloping wall [48, 37]. This vertical oscillation also can be viewed as time-dependent modulation of the gravitational parameter g , which originally enters the momentum equation [11]. So, by multiplying momentum equation with a time-dependent function $\alpha(t)$, the vertical oscillation, which is also called *parametric excitation* can be incorporated. A handful numerical study on the appearance of internal wave attractor was done in [11]. By considering a tilted square domain, [11] studied the appearance of internal wave attractor on the staggered C-grid with the parametric excitation effects. At a specific parameter values, they showed internal wave attractor is appeared by using two initial wavemodes ($(l, n) = (1, 1)$ and $(l, n) = (1, 3)$).

However, they focused on the energy preserving in the internal wave attractors. Unlike them, our focus is on the effects of staircase boundaries. So, by following the same excitation mode, the internal wave equations (6.5.1) now becomes

$$\frac{\partial u}{\partial t} = -\alpha(t) \left(\frac{\partial p}{\partial x} + b \sin \theta \right), \quad (6.5.6a)$$

$$\frac{\partial w}{\partial t} = -\alpha(t) \left(\frac{\partial p}{\partial z} + b \cos \theta \right), \quad (6.5.6b)$$

$$\frac{\partial b}{\partial t} + N^2(u \sin \theta + w \cos \theta) = 0, \quad (6.5.6c)$$

$$\frac{\partial u}{\partial x} + \frac{\partial w}{\partial z} = 0, \quad (6.5.6d)$$

where $\alpha(t) = 1 - \epsilon \cos(2\omega t)$, with a small positive constant ϵ and 2ω is the forcing frequency.

We now examine internal wave attractor as an initial value problem with the parametric excitation effects by solving (6.5.6) using our numerical setting. We consider forcing frequency $2\omega = \pi$, so that the wave period is $T = 4$, $\epsilon = 0.1$, gravity tilted at angle $\theta = 7\pi/72$,

and $\omega/N_f = 0.74$ to simulate the $(1, 1)$ attractor. Figure 6.5.5 shows the evolution of buoyancy b at $t = 5, 50, 100, 150, 200$, with $h = 0.002$ and $dt = 0.02$. In the figure, we compare the results of [11] (left column) and our result with initial condition (6.5.5). In both figures, we can see that the $(1, 1)$ attractor is obtained up to $t = 100$. However, the attractor disappeared after $t = 100$. This is probably because the energy is not preserve and keep increasing after $t = 100$, as can be seen in Figure 6.5.6.

We next change the angle of gravity tilted to be $\theta = \pi/18$, $\omega/N_f = 0.34$, initial wavemode $(l, n) = (1, 3)$, and run up to $50T$ (i.e., $t = 200$). Figure 6.5.7 shows the result of simulation at $t = 5, 50, 100, 150, 200$. Again, it can be seen that $(1, 3)$ attractor is appeared up to $t = 100$, and start to dissappear when $t > 100$. Again, this is probably because the energy is not preserve anymore after $t = 100$, as can be seen in Figure 6.5.8.

6.6 Summary

Since we have found an error of $O(h)$ in the discrete reflection problem, this suggests that issues may arise in phenomena driven by internal gravity reflection. Since internal wave focussing in a closed domain is driven by a particular property of internal gravity wave reflection, our idea is that staircase boundaries may prevent or alter the focussing phenomena. We intend to make such calculations in the future – for rectangular domains with staircase boundaries – along the lines of the solutions presented in section 6.5 for rectangular domains with aligned grids and thus no staircases.

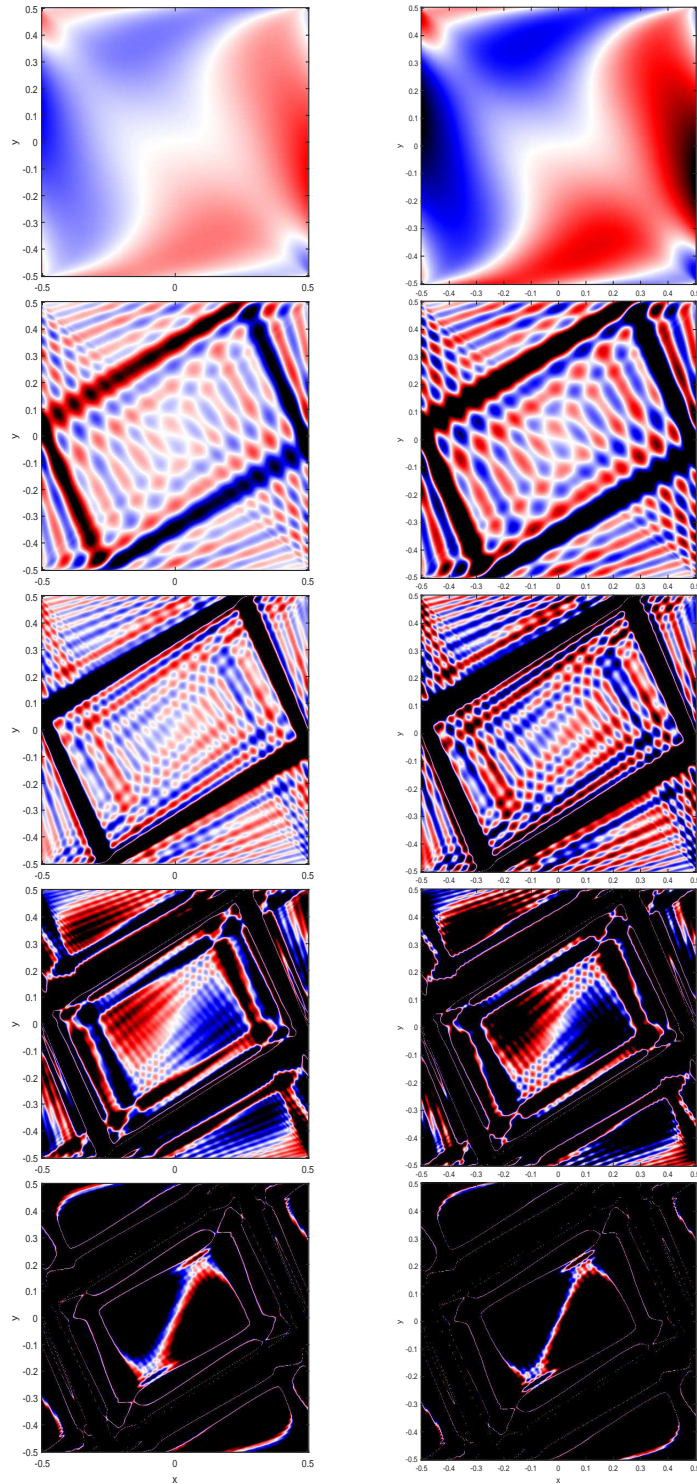


Figure 6.5.5: The evolution of buoyancy b at $t = 5, 50, 100, 150, 200$ for $(l, n) = (1, 1)$, $\bar{\omega}/N_f = 0.74$. Gravity tilted at angle $7\pi/72$. The left column is the results using [11] attractor initial condition. On the right column, the results with (6.5.5) normal mode initial condition with parametric excitation.

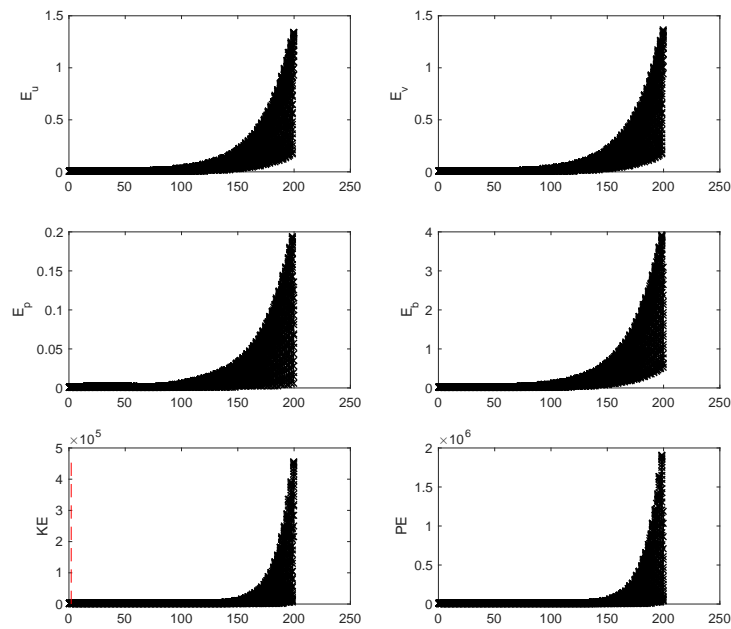


Figure 6.5.6: Energy analysis for the simulations on normal mode (right column Figure 6.5.5), $(l, n) = (1, 1)$, $\omega_c = 1.55786$, $\omega_d = 1.50097$, $|\omega_c - \omega_d| = 0.056882$.

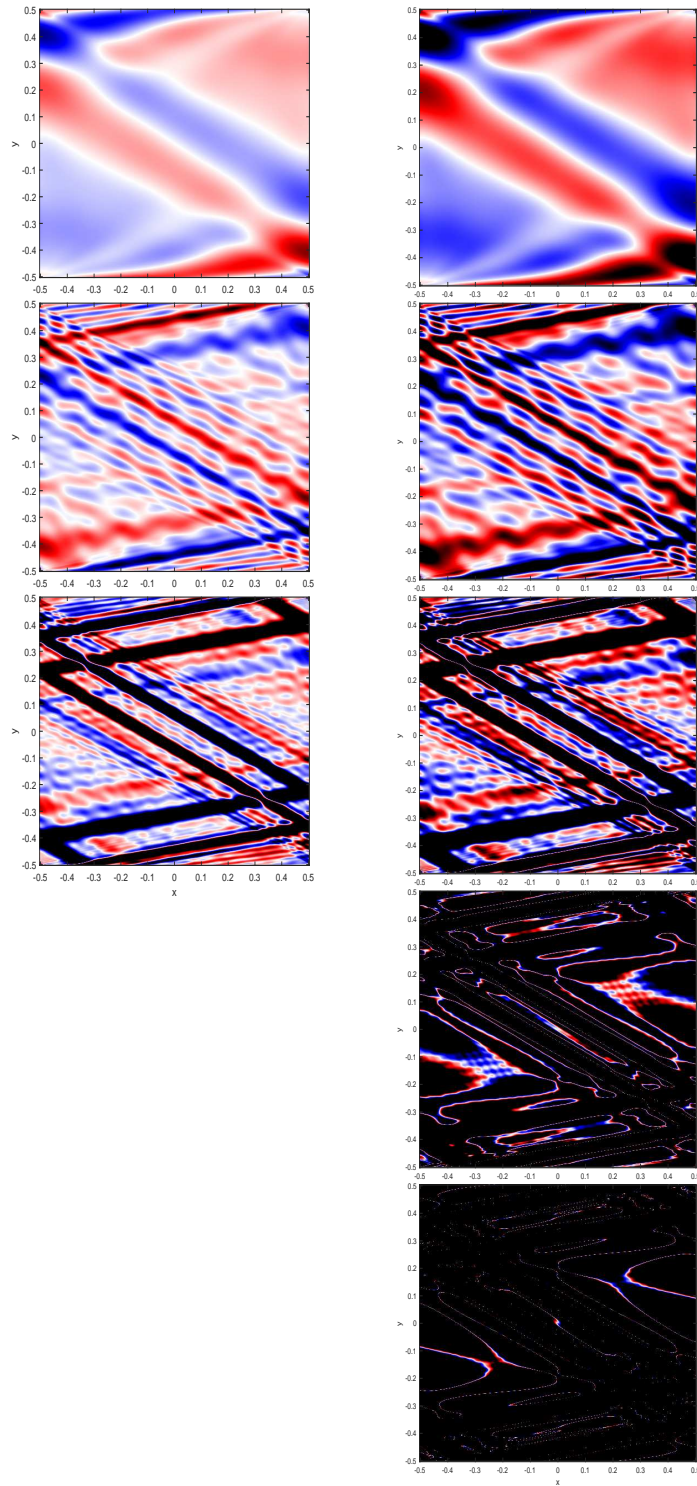


Figure 6.5.7: The evolution of buoyancy b at $t = 5, 50, 100, 150, 200$ for $(l, n) = (1, 3)$, $\bar{\omega}/N_f = 0.34$. Gravity tilted at angle $\pi/18$. The left column is the results with [11] attractor initial condition. On the right column, the results with (6.5.5) normal mode initial condition with parametric excitation.

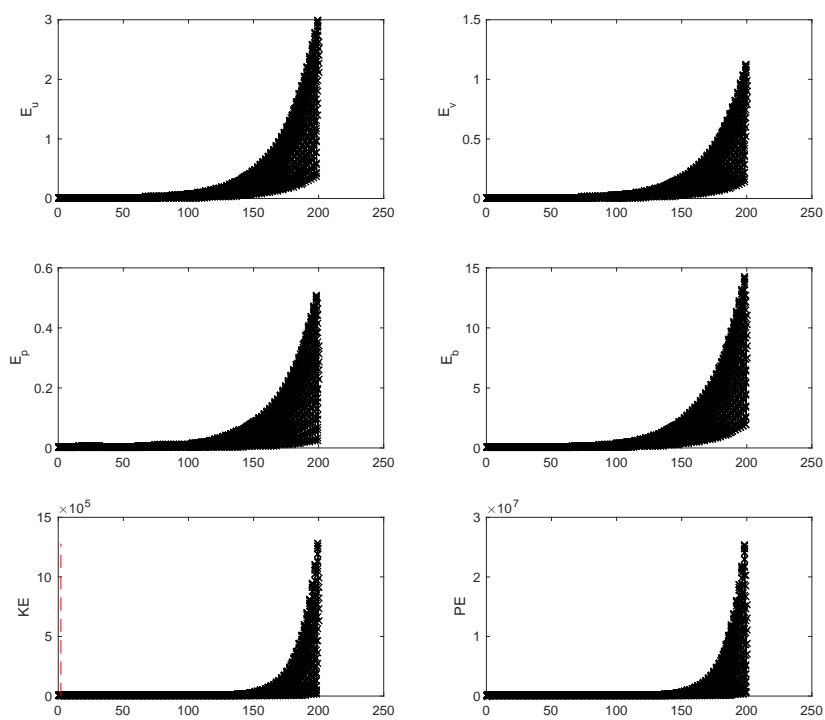


Figure 6.5.8: Energy analysis for the simulations on normal mode (right column Figure 6.5.7), $(l, n) = (1, 3)$, $\omega_c = 1.54485$, $\omega_d = 1.46097$, $|\omega_c - \omega_d| = 0.0838847$.

Chapter 7

CONCLUSION

7.1 Summary

The main aim of this thesis is to investigate the effects of staircase boundaries in finite-difference models of wave propagation in several physical settings. For most of the thesis we focused on the standard set two-dimensional wave equations that is widely used in some applications such as acoustic, electromagnetism and shallow-water flow. In this thesis, we also considered internal gravity wave equations for stratified flow that is slightly different from the standard set wave equations. For most of our models, we have considered harmonic waves in time, so that we can exclusively focused on the spatial effects of finite-differencing. For all problems of interest, we first derived the continuum solutions followed by discrete solutions on the C-grid. We then compared both solutions and assessed the convergence rate of discrete solutions towards the continuum solutions.

In Chapter 2, we reviewed the two-dimensional wave equations and showed that three physical systems of wave propagation (i.e., acoustic, electromagnetism, shallow-water flow) also has equivalent system of equations. We also reviewed some important conservation laws for this equations. As our main aim is to investigate wave propagation on finite-difference models, we then reviewed finite-difference scheme of system of wave equations on doubly

periodic domain on three different finite-difference grids which are A-, B- and C-grid. By using second-order central finite-difference formulation, we showed that the discrete frequency for each grids has second-order convergence in grid spacing h . However, the relative error for each grids behave differently. For each discrete frequencies, we discussed its representation and we showed that C-grid is the most satisfactory grid.

In Chapter 3, we considered wave propagation along a channel. We first considered channel's boundaries and grid are aligned, and we proved that the discrete frequency is obtained at second-order in h . Then, we considered wave propagation along a channel with perfect staircase boundaries. The perfect staircase boundaries is obtained by tilting the channel by 45° relative to the grid. This is our main problem of interest. By performing asymptotics in the limit of small grid spacing h , the discrete solution is derived and compared with the continuum solution. Unlike the aligned channel, we proved that there is degradation of order of convergence due to the staircasing. The discrete frequency of this unaligned channel converge towards the continuum values at first-order in grid spacing h , despite the second-order finite-differences used within the domain. Further, we showed that for this unaligned case there are two options of perfect staircase boundary condition can be selected. First is called split centre retention where we showed that the relative error is purely depend on h , the staircasing error. While the second is called cell-centre retention and we showed that the relative error dependent on both across and along channel wavenumber j and k , respectively, despite having staircasing error. We also visualised the discrete analytical solution agreed with the numerical solution. In chapter 3, most of the results are new. Presumably the grid-aligned analysis leading to (3.3.17) exists somewhere in the vast research literature covering acoustics, electromagnetic waves and shallow-water waves, but we have not found it. However, the perfectly-aligned staircase analysis is completely original, as far as we can tell. The closest study is that of [51], but he used rather different methods and gave no results for $h \rightarrow 0$ at fixed channel width, and thus gave nothing analogous to our main results (3.4.32) and (3.4.33). The study of [32] used similar methods to here, but was completely focussed on the case of Kelvin waves for an unbounded channel and shallow-water

dynamics. Those results rely upon rotation, and cannot be converted to our results here for non-rotating dynamics.

In Chapter 4, we have studied reflection of waves at a straight boundary. In the continuum solution, we found that the wave reflected amplitude is the same as that of the incoming wave, the along-boundary wavenumber remains unchanged, and the across-boundary wavenumber changes sign. For the discrete solutions, we studied two versions of the discrete problem. For the first discrete problem we consider the grid and boundary were aligned at $y = 0$. We showed that the reflected amplitude and reflected wavenumber remain unchanged as continuum amplitude. However, it is to be noted that there is a second-order error in the wave frequency of both incident and reflected waves. For the second discrete problem, we studied wave reflection upon a straight boundary tilted at 45° (i.e., $y = x$). In this problem, the boundary now is perfect staircase. Remarkably, we showed that the reflected wavenumbers were recovered exactly. However, the reflected amplitude was not recovered exactly. We showed that there was a phase-error which a first-order error in h . This is our new result. As the study in this chapter looks similar in [17], there are some differences. The first main difference arises because they analysed the problem in a specific time-stepping framework, so that their expression also involved a time step. Here we simply assume time-periodic waves, the frequency of which will be consistent with the discrete dispersion relation. The second main difference arises because they made an assumption about the values of k_R and l_R , without deriving them from k_I and l_I . Here we make no such assumption, and rather determine k_R and l_R from k_I and l_I , leading to (4.4.15).

In Chapter 5, we studied numerical solutions of waves equation in two closed domains which are square and circle. Here the numerical solutions that we obtained bring together results of Chapter 3 and 4. For both domains, we first derived the continuum solutions, and we initialised numerical computations by using the continuum solution up to a tenth period. We studied numerical solutions after multiple reflections and analysed its maximum

error. Further, we quantified our numerical solutions at various grid spacings h , towards the continuum solution to find convergence rate of physical quantity. For a square domain, we have considered two separate experiments. In the first of these, the square boundary and grid were aligned. We quantified the numerical solutions and found that there is a second-order convergence in h , as expected. In the second experiment, the same square is tilted at 45° so that the boundary has perfect staircases at various h (over 20). For this case, we found that the rate of convergence for u , v , p , and discrete frequency, degraded to a first-order in h over one period. We also quantified this domain when tilted at some angles (i.e., $\pi/6$, $\pi/12$, $\pi/18$, and $\pi/20$). We found that the convergence rate for u , v , p , and ω degraded to a first-order in h in max. norm, and between 0.6 and 1 in L_2 norm, over one period.

For a circular domain, we considered three separate experiments depending on the wave-mode (m, n) . First we considered numerical solution with mode $(1, 0)$. Here, we found that the rate of convergence for u and v is at first order in h , while for p is 1.6, after one period in L_2 norm, and convergence rate of 1.6 in max. norm. For the second experiment, we considered wavemode $(1, 1)$. We found that the rate of convergence in max. norm for p is 1.06, but there is no convergence was found (i.e., $O(1)$) for u and v . While in the L_2 -norm, the rate of convergence of all u , v and p is between 0.6 and 1. For these two experiments of circular wavemode we used cell centre node as activation cell to generate staircase boundary. So, in the third experiment we considered same wavemode $(1, 0)$ as in first, but with four corner cell activation. Here, we showed that there is a first-order convergence in h for u , v and p in max. norm. As far as we concern, we cannot find other examples of numerical experiments of wave sloshing in a closed domain with staircase boundaries like in this chapter. So that all works in chapter 5 are new.

In Chapter 6, in order to get some ideas to extend the results from chapters 2-5, we first reviewed internal gravity wave equations by introducing the equations of motion and configuring these equations on staggered grids. We then derived the relevant dispersion relation for internal gravity waves in an unbounded medium. We next considered internal

wave reflection at a sloping boundary, and reviewed the classic continuum reflection. We then presented what is believed to be a completely novel discrete reflection calculation on the staggered grid. We found an error of $O(h)$ in the discrete reflection problem and this suggests that issues may arise in phenomena driven by internal gravity reflection. Since internal wave focussing in a closed domain is driven by a particular property of internal gravity wave reflection, our idea is that staircase boundaries may prevent or alter the focussing phenomena. We intend to make such calculations in the future – for rectangular domains with staircase boundaries.

7.2 Overview

Throughout this thesis, we have studied the relative error of the discrete wave's frequency in each of our physical settings. Here, we summarised all results for Chapter 3 in Table 7.1-7.4. As can be seen, the relative error for the case of channel with aligned boundary has second-order convergence in h . While the relative error for the case of tilted channel at 45° , has first-order convergence in h . For the case of split cell retention we found that the relative error is purely from staircase boundaries. However, for the case cell-centre retention the relative error consists of staircasing error and geometrical error which is manifested by across channel wavenumber j and along-channel wavenumber k . For example, for the case of mode $j = 0$, to obtain the frequency accurate to within 1% (i.e., $\Delta < 0.01$), we need $kh = \sqrt{0.12}$ or 18 grid points per along-channel wavelength for the case of aligned boundaries. On the other hand, for the case of unaligned boundaries we need 71 grid-boxes across the channel, for both split cell and cell centre retention boundary condition. To obtain the frequency accurate to within 10% (i.e., $\Delta < 0.1$), we need 6 grid points per along-channel for the aligned boundaries, and 7 grid-boxes across the channel for the unaligned case.

For the case of mode $j = 1$ and $k = 1$ in order to obtain the frequency accurate to within

1%, we need 9 grid boxes across the channel for the aligned boundary. For the case of unaligned boundary, again we need 71 grid boxes across the channel for split cell retention boundary condition. However, for cell-centre retention boundary condition we only need 7 grid boxes across the channel. For the case of mode $j = 5$ and $k = 1$, in order to obtain the frequency accurate to within 1%, we need 46 grid boxes across the channel for the aligned boundary. For the case of unaligned boundary, again we need 71 grid boxes across the channel for split cell retention boundary condition, but only 1 for cell-centre retention boundary condition. Thus, we have been able to make a clear conclusion about the influence of staircase boundaries on wave propagation along a channel.

In Chapter 4, we considered wave reflection at a straight wall aligned with grid and the wall (at $y = x$) was aligned at 45° to the grid, thus forming a perfect staircase boundary. In the discrete wave reflection at staircase boundary, we showed that the wavenumbers of the reflected wave were recovered exactly, which is perhaps surprising. However, the (complex) amplitude A_R of the reflected wave was not recovered exactly. Even though its magnitude was recovered correctly, i.e., $|A_R| = |A_I|$, there was a phase error, i.e., A_R/A_I had non-zero imaginary part. We derived an expression for A_R/A_I (which was previously given by [17]), and analysed it in some detail. In particular, we showed that there is first-order error φ in the phase, in terms of the grid spacing h with $\varphi = (k^2 + l^2)h/(k - l)$, where (k, l) is the wavevector of the incident wave. For example, for the case when the incident wave is normal to the boundary, i.e., $l = -k$. Then the phase error $\varphi = kh$ (a result which we showed to be exact, even at finite h). For a minimally resolved wave with 4 grid points per wavelength (i.e., $4h = 2\pi/k \Rightarrow kh = \pi/2$), the phase error upon reflection is then $\pi/2$. So if the wave were to reflect off two such boundaries, then the phase error would be π (assuming that the phase errors were additive), and the wave would become completely out of phase with its continuum counterpart. However, note that the error in the wave frequency here would only be 19% (i.e., this might be considered to be an adequately resolved wave on the C-grid). So, the effects of staircasing are clear, and how they could lead to serious errors in the phase of the wave after 1 (or, more likely, multiple) reflections.

In chapter 5, we have seen numerical solutions of waves equation sloshing in a square and circle domain. For the square domain, we have seen the solutions at two particular cases: (i) boundaries aligned with the grid, and (ii) boundaries unaligned with the grid. While for the circle domain, we have seen the numerical solutions of two different wave modes (with different azimuthal wavenumber) sloshing in the domain. The exact continuum solutions is first derived to be used as an initial condition in the numerical experiment as well as to compute the error of the solutions.

For the square domain boundaries aligned with the grid, we have shown that second-order convergence in h is achieved, since central second-order finite-difference formulation is used in the experiments. We thus confirmed that the rate of convergence will not be affected as long as the boundaries aligned with the grid (second-order convergence in h is obtained with angle $\theta = 90^\circ$).

On the other hand, there is reduction of the order of accuracy for the case of unaligned boundaries with staircase boundary. We have quantified this degradation in for u , v and p . The quantification is obtained after one period of wave oscillation. We summarised all the results in Table 7.5. It is shown that first-order convergence in h is obtained when the square has staircase boundaries, which is consistent with the analysis in chapters 3 and 4. We also have examined the effect of tilt angle. We have quantified the spatial convergence rate at some angles. We found that the scaling factor for spatial error decrease with θ , which as expected. This is agree with the results found in [32] for channel flow, where it was showed that scaling factor for spatial error decrease with θ .

The solutions for waves sloshing in a circular domain are different. The investigation was split into three experiments: (i) mode $m = 1, n = 0$, (ii) mode $m = 1, n = 1$, and (iii) mode $m = 1, n = 0$. In experiments (i) and (ii), we used cell centre activation, while in (iii) we used 4 corners of each cells as activation. Here, we also quantified the convergence rate at various h after one period, as summarised in Table 7.5. For all experiments, the best convergence rate that we found is first-order in h . It is clear evidence that staircase boundary

has degraded the accuracy of numerical solution. However, the quantification must be done at many points to see a reliable slope of convergence (i.e., many numerical experiments at many grid points). This has not been discussed to our knowledge, and, indeed, the standard behaviour seems to be to take far fewer points – even as few as 3.

Table 7.1: The relative error Δ for wave propagation along a channel with aligned boundaries and unaligned boundaries for $j = 0, k = 1$.

aligned boundaries			staircase boundaries					
$\Delta = \frac{h^2}{12} \left(\frac{k^4 + j^4 \pi^4}{k^2 + j^2 \pi^2} \right)$	GPPW	GPAC	$\Delta = \frac{h}{\sqrt{2}}$	GPPW	GPAC	$\Delta = \frac{h}{\sqrt{2}} \left(\frac{k^2}{k^2 + j^2 \pi^2} \right)$	GPPW	GPAC
0.1%	57	9	0.1%	4443	708	0.1%	4443	708
1%	18	3	1%	444	71	1%	444	71
10%	6	1	10%	45	7	10%	45	7

Table 7.2: The relative error Δ for wave propagation along a channel with aligned boundaries and unaligned boundaries for $j = 0, k = 2$.

aligned boundaries			staircase boundaries					
$\Delta = \frac{h^2}{12} \left(\frac{k^4 + j^4 \pi^4}{k^2 + j^2 \pi^2} \right)$	GPPW	GPAC	$\Delta = \frac{h}{\sqrt{2}}$	GPPW	GPAC	$\Delta = \frac{h}{\sqrt{2}} \left(\frac{k^2}{k^2 + j^2 \pi^2} \right)$	GPPW	GPAC
0.1%	58	19	0.1%	2222	708	0.1%	556	177
1%	19	6	1%	222	71	1%	56	18
10%	6	2	10%	22	7	10%	6	2

Table 7.3: The relative error Δ for wave propagation along a channel with aligned boundaries and unaligned boundaries for $j = 1, k = 1$.

aligned boundaries			staircase boundaries					
$\Delta = \frac{h^2}{12} \left(\frac{k^4 + j^4 \pi^4}{k^2 + j^2 \pi^2} \right)$	GPPW	GPAC	$\Delta = \frac{h}{\sqrt{2}}$	GPPW	GPAC	$\Delta = \frac{h}{\sqrt{2}} \left(\frac{k^2}{k^2 + j^2 \pi^2} \right)$	GPPW	GPAC
0.1%	173	28	0.1%	4443	708	0.1%	409	65
1%	55	9	1%	444	71	1%	41	7
10%	18	3	10%	45	7	10%	1	1

Table 7.4: The relative error Δ for wave propagation along a channel with aligned boundaries and unaligned boundaries for $j = 5, k = 1$.

aligned boundaries			staircase boundaries					
$\Delta = \frac{h^2}{12} \left(\frac{k^4 + j^4 \pi^4}{k^2 + j^2 \pi^2} \right)$	GPPW	GPAC	$\Delta = \frac{h}{\sqrt{2}}$	GPPW	GPAC	$\Delta = \frac{h}{\sqrt{2}} \left(\frac{k^2}{k^2 + j^2 \pi^2} \right)$	GPPW	GPAC
0.1%	900	144	0.1%	4443	708	0.1%	18	3
1%	284	46	1%	444	71	1%	2	1
10%	90	15	10%	44	7	10%	1	1

Table 7.5: The convergence rate for u , v and p in max norm and L_2 norm, at various h for the specific domain.

Domain	max norm			L_2 norm		
	u	v	p	u	v	p
square (aligned)	1.82	1.89	1.89	1.84	1.86	1.89
square (tilted at $\pi/4$)	1.16	1.16	1.15	1.24	1.24	1.24
square (tilted at $\pi/6$)	$O(1)$	$O(1)$	1.05	0.78	0.71	1.05
square (tilted at $\pi/12$)	$O(1)$	$O(1)$	1.05	0.6	0.6	1.07
square (tilted at $\pi/18$)	$O(1)$	$O(1)$	1.09	0.62	0.64	1.05
square (tilted at $\pi/36$)	$O(1)$	$O(1)$	0.95	0.63	0.64	1.35
circle ($m = 1, n = 0$)	1.11	1.11	1.59	1.59	1.59	1.68
circle ($m = 1, n = 1$)	$O(1)$	$O(1)$	1.06	0.94	0.66	1.08
circle ($m = 1, n = 0$) 4 corners	1.03	1.03	1.04	–	–	–

Appendices

Appendix A

Stability Testing

We consider a system of first-order of linear with constant coefficient ordinary differential equations (ODEs) of the form

$$\mathbf{a}' = L\mathbf{a}, \quad \mathbf{a}(0) = \mathbf{a}_0, \quad (\text{A.0.1})$$

where L is a constant matrix and $\mathbf{a} = \mathbf{a}(t)$ is m -dimensional vector. We calculate a numerical solution $\mathbf{a}_n = \mathbf{a}(n\Delta t)$ by using some scheme.

To understand the stability of the scheme, we first consider the eigenvalues of matrix L in the form

$$|L - \lambda_i I| = 0, \quad (\text{A.0.2})$$

where $\lambda_i (i = 1, 2, \dots, m)$ is the eigenvalue of matrix $L_{m \times m}$ and I is the identity matrix, and every eigenvalues has corresponding eigenvectors \mathbf{x}_i which satisfy

$$L\mathbf{x}_i = \lambda_i \mathbf{x}_i. \quad (\text{A.0.3})$$

Then, the solution of the system of ODEs can be written as

$$\mathbf{a}(t) = \sum_{i=1}^m c_i(t) \mathbf{x}_i. \quad (\text{A.0.4})$$

where $c_i(t)$ are fixed by the initial condition. Hence, (A.0.1) is satisfied if

$$\sum_{i=1}^m c_i'(t) \mathbf{x}_i = \sum_{i=1}^m c_i(t) L \mathbf{x}_i = \sum_{i=1}^m c_i(t) \lambda_i \mathbf{x}_i. \quad (\text{A.0.5})$$

It is easily seen from (A.0.5) that

$$c_i' = \lambda_i c_i, \quad \text{or} \quad \frac{dc_i}{dt} = \lambda_i c_i, \quad c_i(0) = c_{i_0}. \quad (\text{A.0.6})$$

Equation (A.0.6) is a scalar equation with eigenvalues of matrix L . O, understanding solution of (A.0.1) reduces to understanding solution of (A.0.5), and eigenvalues of L are the key to understanding.

We are interested in wave equation for which the eigenvalue of L will be pure imaginary. It is because wave oscillates with sin and cos function. To illustrate it, we give an example by considering the system

$$\frac{du}{dt} = p, \quad \frac{dp}{dt} = -u. \quad (\text{A.0.7})$$

Then the system can be written as

$$\frac{d}{dt} \begin{pmatrix} u \\ p \end{pmatrix} = \begin{pmatrix} 0 & 1 \\ -1 & 0 \end{pmatrix} \begin{pmatrix} u \\ p \end{pmatrix}. \quad (\text{A.0.8})$$

So, $L = \begin{pmatrix} 0 & 1 \\ -1 & 0 \end{pmatrix}$, and the eigenvalues are $\lambda = \pm i$. The solution is $\psi(t) = \psi_0 e^{it}$. The

remainder of the discussion will discuss about the stability of scheme to the test equation

$$\frac{d\psi}{dt} = i\psi, \quad \psi(0) = \psi_0. \quad (\text{A.0.9})$$

The stability of a numerical scheme can be determined by analyzing the amplification factor. So, we now explicitly derive amplification factor for some standard numerical scheme. They are all well known results that can be found in various books [25, 43]. The amplification factor, A , is defined as the ratio of the numerical solution φ , between two adjacent times or mathematically in the form

$$A = \frac{\varphi^{n+1}}{\varphi^n}. \quad (\text{A.0.10})$$

where φ^n is the numerical approximation to the true solution at discrete time level $t^n = n\Delta t$. The numerical scheme is said stable if $|A| \leq 1$ and unstable if $|A| > 1$. All schemes that will be discussed will be examined based on this amplification factor. Note that, from (A.0.10), we want $|A| = 1$ where $A = e^{i\Delta t}$. If we expanding the solution becomes

$$A = 1 + i\Delta t - \frac{\Delta t^2}{2} - i\frac{\Delta t^3}{6} + \frac{1}{24}\Delta t^4 + (O(\Delta t^5)). \quad (\text{A.0.11})$$

For every numerical scheme, we also calculate numerical solution and consider the maximum error at $t = 10$.

A.0.1 Euler

The most famous and simple numerical scheme to approximate the derivative in equation (A.0.9) is Euler's scheme by using forward difference. When applied to the test equation (A.0.9) the scheme reads

$$\frac{\varphi^{n+1} - \varphi^n}{\Delta t} = i\varphi^n. \quad (\text{A.0.12})$$

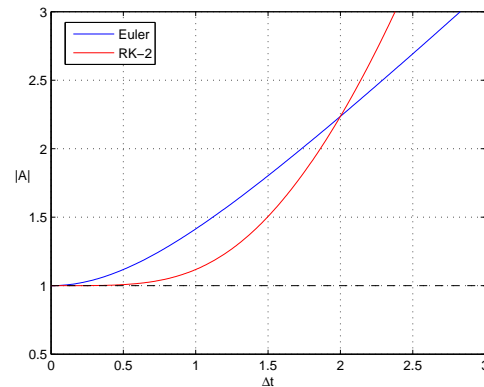


Figure A.0.1: Modulus of amplification factor for the Euler's scheme as a function of Δt .

Dividing by φ^n gives

$$A = 1 + i\Delta t. \quad (\text{A.0.13})$$

So we get the first 2 terms in the right hand side of (A.0.11). This means that the scheme is first-order accurate in Δt . The modulus of the amplification factor can be written as

$$|A| = (1 + \Delta t^2)^{1/2}. \quad (\text{A.0.14})$$

It can be easily seen that, $|A| > 1$. Thus, this scheme is said unstable. The instability of the scheme is graphically showed in Figure A.0.1. This scheme is not suitable because the numerical solution will diverge from the true solution.

A.0.2 Runge-Kutta order 2

For the general problem $d\varphi/dt = F(\varphi)$, the Runge-Kutta order 2 scheme can be written as

$$\varphi^{n+1} = \varphi^n + \Delta t F(\tilde{\varphi}^{n+1/2}), \quad (\text{A.0.15a})$$

$$\tilde{\varphi}^{n+1/2} = \varphi^n + \frac{1}{2} \Delta t F(\varphi^n). \quad (\text{A.0.15b})$$

When applying to the test equation (A.0.9), where $F(\varphi) = i\varphi$ it becomes

$$\varphi^{n+1} = \varphi^n + i\Delta t \varphi^n - \frac{1}{2} \Delta t^2 \varphi^n = \left(1 + i\Delta t - \frac{1}{2} \Delta t^2\right) \varphi^n.$$

Dividing by φ^n , yields

$$A = 1 + i\Delta t - \frac{1}{2} \Delta t^2. \quad (\text{A.0.16})$$

Here, we get first three terms of (A.0.11). So this scheme is second-order accurate in Δt .

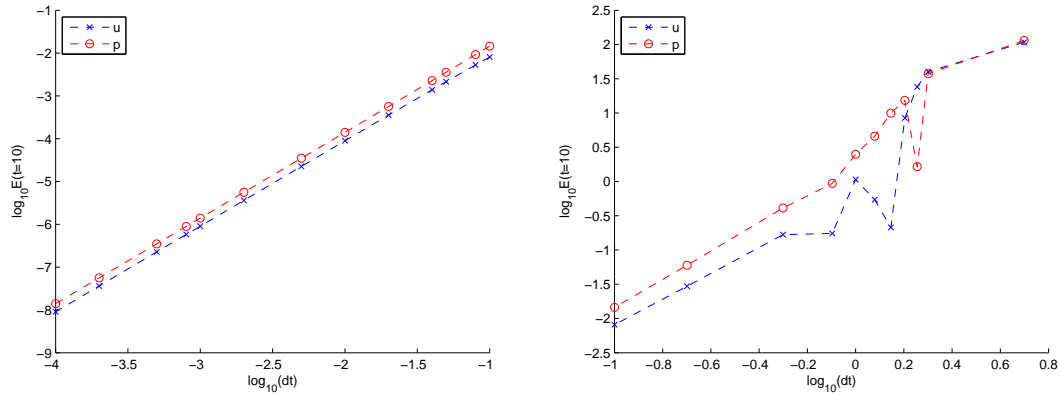
The modulus square of amplification factor (A.0.16) is

$$|A|^2 = \left(1 - \frac{1}{2} \Delta t^2\right)^2 + \Delta t^2 = 1 + \frac{1}{4} \Delta t^4, \quad (\text{A.0.17})$$

which also gives

$$|A| = 1 + \frac{1}{8} \Delta t^4, \quad \text{as } \Delta t \rightarrow 0. \quad (\text{A.0.18})$$

It can be seen from (A.0.17) that the scheme is unstable for all Δt since $|A| > 1$. This instability is graphically shown in the Figure (A.0.1). Although this scheme is unstable, the growth factor is of $O(\Delta t^4)$ which makes the amplification weak. This scheme can be used in the limited length of time integration and the time stepping Δt is sufficiently small.



(a) Stability domain. The slope is 1.98834 for u and 2.00441 for p . $dt = 0.1, 0.08, 0.05, 0.04, 0.02, 0.01, 0.005, 0.002, 0.001, 0.0008, 0.0005, 0.0002, 0.0001, 0.00005$.

(b) instability domain

Figure A.0.2: Convergence plot for RK-2 method.

A.0.3 Runge-Kutta order 4

The Runge-Kutta order 4 scheme can be written as

$$\begin{aligned}\varphi^{n+1} &= \varphi^n + \frac{\Delta t}{6} (K_1 + 2K_2 + 2K_3 + K_4), \\ K_1 &= F(\varphi^n), \\ K_2 &= F(\varphi^n + \frac{1}{2}\Delta t K_1), \\ K_3 &= F(\varphi^n + \frac{1}{2}\Delta t K_2), \\ K_4 &= F(\varphi^n + \Delta t K_3).\end{aligned}\tag{A.0.19}$$

Applying to the test equation (A.0.9) where $F(\varphi) = i\varphi$, the scheme reads

$$\begin{aligned}
 K_1 &= i\varphi^n, \\
 K_2 &= i \left(\varphi^n + \frac{1}{2}i\Delta t\varphi^n \right) = i\varphi^n \left(1 + \frac{1}{2}i\Delta t \right), \\
 K_3 &= i \left(\varphi^n + \frac{1}{2}i\Delta t\varphi^n \left\{ 1 + \frac{1}{2}\Delta t \right\} \right), \\
 &= i\varphi^n \left(1 + \frac{1}{2}i\Delta t - \frac{1}{4}\Delta t^2 \right), \\
 K_4 &= i \left(\varphi^n + i\Delta t\varphi^n \left\{ 1 + \frac{1}{2}i\Delta t - \frac{1}{4}\Delta t^2 \right\} \right), \\
 &= i\varphi^n \left(1 + i\Delta t - \frac{1}{2}\Delta t^2 - \frac{1}{4}i\Delta t^3 \right).
 \end{aligned} \tag{A.0.20}$$

Hence,

$$\varphi^{n+1} = \varphi^n + \frac{i\Delta t}{6}\varphi^n \left(6 + 3i\Delta t - \Delta t^2 - \frac{1}{4}i\Delta t^3 \right). \tag{A.0.21}$$

Dividing by φ^n gives

$$A = \frac{\varphi^{n+1}}{\varphi^n} = 1 + i\Delta t - \frac{1}{2}\Delta t^2 - \frac{1}{6}i\Delta t^3 + \frac{1}{24}\Delta t^4. \tag{A.0.22}$$

For this scheme, we get first four terms of (A.0.11). So, this scheme is four order accurate in Δt . The modulus square of amplification factor (A.0.22) is

$$\begin{aligned}
 |A|^2 &= \left(1 - \frac{1}{2}\Delta t^2 + \frac{1}{24}\Delta t^4 \right)^2 + \left(\Delta t - \frac{1}{6}\Delta t^3 \right)^2, \\
 &= 1 - \frac{1}{72}\Delta t^6 + O(\Delta t^8).
 \end{aligned} \tag{A.0.23}$$

which gives

$$|A| = 1 - \frac{1}{144}\Delta t^6 + O(\Delta t^8), \quad \text{as } \Delta t \rightarrow 0. \tag{A.0.24}$$

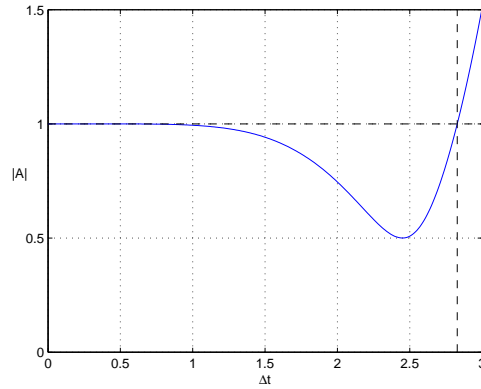


Figure A.0.3: Modulus of amplification factor for the RK-4 scheme as a function of Δt .

From (A.0.23) it can be seen that as $\Delta t \rightarrow 0$, $|A| < 1$. Thus, this scheme is said to be stable as $\Delta t \rightarrow 0$. Figure (A.0.3) shows the amplification factor (A.0.22) plotted as function of Δt . As shown in the figure, the RK-4 scheme is stable approximately for $\Delta t < 2.82$. However, we can be more precise. As $\Delta t \rightarrow 0$, equation (A.0.23) is expanded as

$$|A|^2 = \left(1 - \Delta t^2 + \frac{1}{12}\Delta t^4 + \frac{1}{4}\Delta t^4 + \frac{1}{24^2}\Delta t^8 - \frac{1}{24}\Delta t^6\right) + \left(\Delta t^2 - \frac{1}{3}\Delta t^4 + \frac{1}{36}\Delta t^6\right). \quad (\text{A.0.25})$$

So, if $|A|^2 = 1$, equation (A.0.25) gives

$$\frac{1}{24^2}\Delta t^8 = \left(\frac{1}{24} - \frac{1}{36}\right)\Delta t^6, \quad \Rightarrow \quad \Delta t^2 = 8, \quad \Rightarrow \quad \Delta t = 2\sqrt{2} \approx 2.82. \quad (\text{A.0.26})$$

So, this scheme is stable for $\Delta t \leq 2\sqrt{2}$. We also calculate the numerical solution for this scheme. The error for this scheme is plot at $t = 10$ as in Figure A.0.4. As shown in Figure A.0.4(a), the slope of the error are 3.97696 for u and 4.0036 for p . The slope of the error illustrates the order of this scheme. As shown in Figure A.0.4(c), there are massive error when $\Delta t > 2\sqrt{2}$ which illustrates the instability of the scheme as discussed previously.

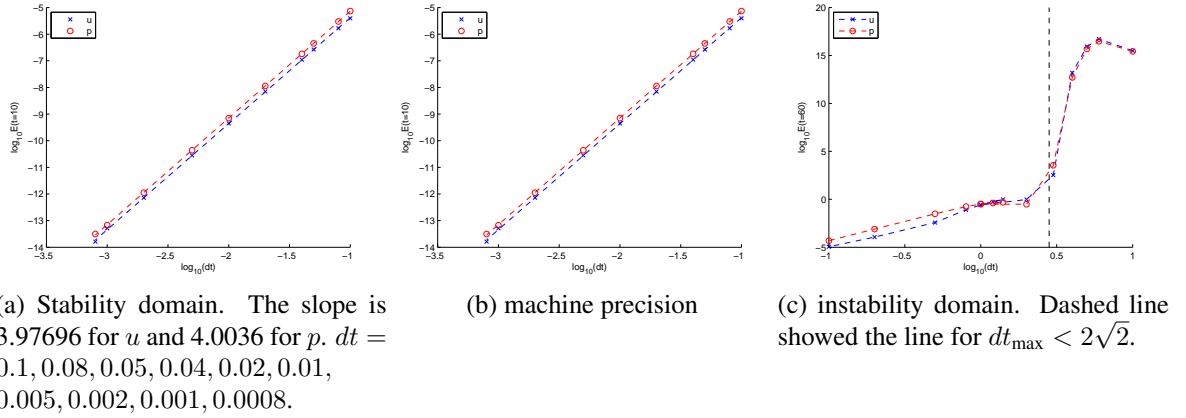


Figure A.0.4: Convergence plot for RK-4 method.

A.0.4 Adam-Bashforth order 2

Explicit scheme of Adam-Bashforth of order two can be written as

$$\varphi^{n+1} = \varphi^n + \frac{3}{2}\Delta t F(\varphi^n) - \frac{1}{2}\Delta t F(\varphi^{n-1}). \quad (\text{A.0.27})$$

Applying the scheme to the test equation (A.0.9) where $F(\varphi) = i\varphi$, gives

$$\varphi^{n+1} = \varphi^n + \frac{3}{2}i\Delta t\varphi^n - \frac{1}{2}i\Delta t\varphi^{n-1}, \quad (\text{A.0.28})$$

and dividing by φ^n yields

$$\begin{aligned} A = \frac{\varphi^{n+1}}{\varphi^n} &= 1 + \frac{3}{2}i\Delta t - \frac{1}{2}i\Delta t \frac{\varphi^{n-1}}{\varphi^n}, \\ &= 1 + \frac{3}{2}i\Delta t - \frac{1}{2}i\Delta t \frac{1}{A}, \end{aligned} \quad (\text{A.0.29})$$

where $1/A$ in the right hand side of preceding equation is obtained by decreasing 1 step from equation (A.0.10). Simplify equation (A.0.29) will give quadratic stability polynomial

$$A^2 - \left(1 + \frac{3}{2}i\Delta t\right) A + \frac{1}{2}i\Delta t = 0. \quad (\text{A.0.30})$$

Note that, this scheme is two level schemes which involve φ^{n-1} , φ^n and φ^{n-1} , and that is why we have a quadratic of A , with two roots. The first root is represent physical mode and the second root represent computational mode. So the two roots of the stability polynomial (A.0.30) are

$$A_{\pm} = \frac{1}{2} \left(1 + \frac{3}{2}i\Delta t \pm \left(1 + i\Delta t - \frac{9}{4}\Delta t^2 \right)^{1/2} \right). \quad (\text{A.0.31})$$

As $\Delta t \rightarrow 0$, we obtain

$$\begin{aligned} A_+ &= \frac{1}{2} \left(2 + 2i\Delta t - \Delta t^2 + \frac{1}{2}i\Delta t^3 - \frac{1}{4}\Delta t^4 \right) + O(\Delta t^5), \\ &= 1 + i\Delta t - \frac{1}{2}\Delta t^2 + \frac{1}{4}i\Delta t^3 - \frac{1}{8}\Delta t^4 + O(\Delta t^5), \end{aligned} \quad (\text{A.0.32})$$

$$\begin{aligned} A_- &= \frac{1}{2} \left(i\Delta t + \Delta t^2 - \frac{1}{2}i\Delta t^3 \right) + O(\Delta t^4), \\ &= \frac{1}{2}i\Delta t + \frac{1}{2}\Delta t^2 - \frac{1}{4}i\Delta t^3 + O(\Delta t^4), \end{aligned} \quad (\text{A.0.33})$$

From (A.0.11), A_+ is the physical mode and A_- is the computational mode. The modulus of amplification factor for both roots are

$$|A_+| = 1 + \frac{1}{4}\Delta t^4 + \dots; \quad |A_-| = \frac{1}{2}\Delta t + \dots, \quad \text{as } \Delta t \rightarrow 0. \quad (\text{A.0.34})$$

From equation (A.0.34), the physical root is stable while the computational root is converge as $\Delta t \rightarrow 0$. Also can be seen that, the $O(\Delta t^4)$ in the physical mode makes the growth of the amplification weak. Thus, the AB-2 scheme is weakly stable with an $O(\Delta t^4)$ growth. This scheme has the same case as in the Runge-Kutta of order two scheme. The stability

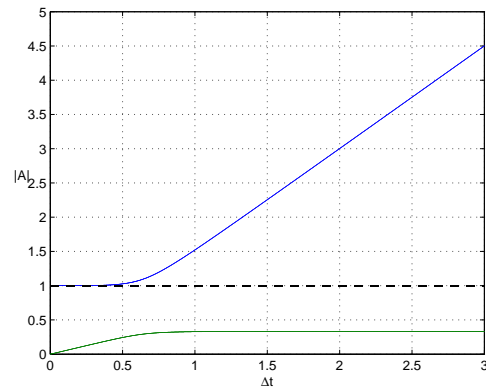
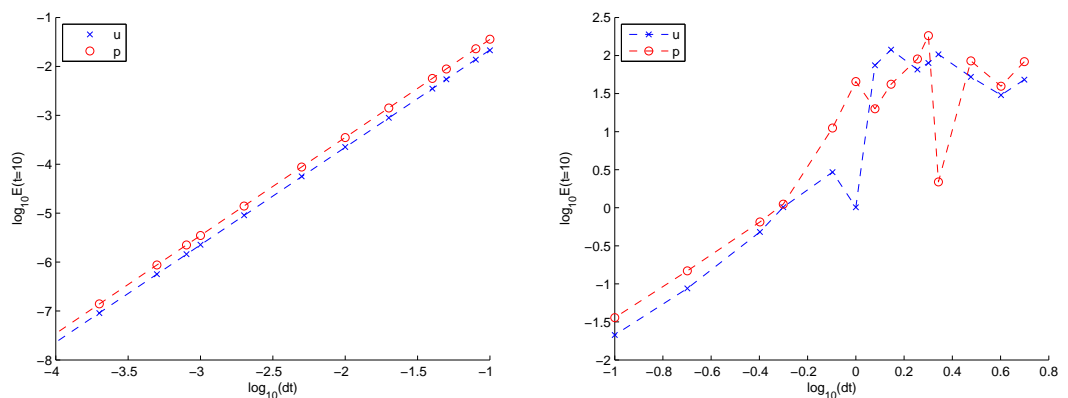


Figure A.0.5: Modulus of amplification factor for the AB-2 scheme as a function of Δt .

behaviour of this scheme is graphically shown in Figure A.0.5.



(a) Stability domain. The slope is 1.9926 for u and 2.00302 for p . $dt = 0.1, 0.08, 0.05, 0.04, 0.02, 0.01, 0.005, 0.002, 0.001, 0.0008, 0.0005, 0.0002, 0.0001, 0.00005$.

(b) instability domain

Figure A.0.6: Convergence plot for AB-2 method.

A.0.5 Leapfrog

The Leapfrog scheme can be written as

$$\varphi^{n+1} = \varphi^{n-1} + 2\Delta t F(\varphi^n). \quad (\text{A.0.35})$$

Then, when applied to the test equation (A.0.9) will give

$$\varphi^{n+1} = \varphi^{n-1} + 2i\Delta t \varphi^n, \quad (\text{A.0.36})$$

and dividing by φ^n gives the quadratic equation

$$A^2 - 2i\Delta t A - 1 = 0. \quad (\text{A.0.37})$$

The two roots of equation (A.0.37) are

$$A_{\pm} = i\Delta t \pm (1 - \Delta t^2)^{1/2}. \quad (\text{A.0.38})$$

As can be seen, the roots of this scheme have two different behaviour. When $\Delta t \rightarrow 0$, the first root is $A_+ \rightarrow 1$ which represent physical mode and the second root is $A_- \rightarrow -1$ which represent computational mode. If $|\Delta t| < 1$, then the second term in equation (A.0.38) is real which will give

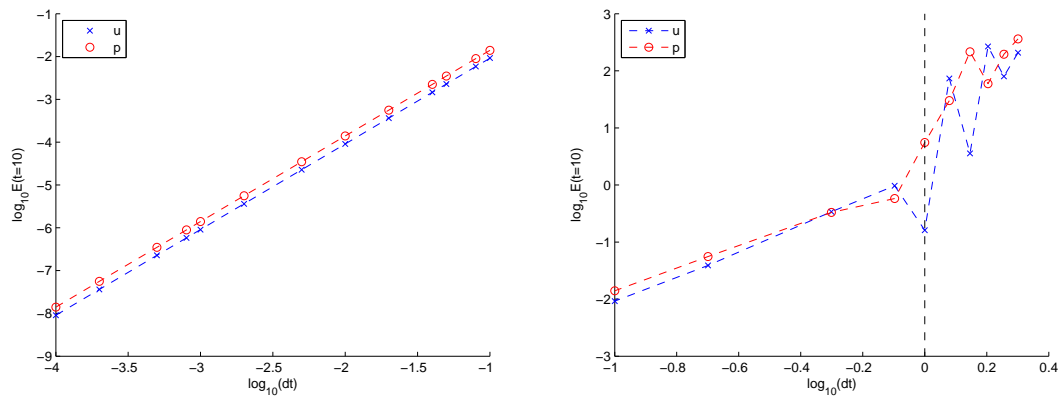
$$|A_{\pm}| = \left((1 - \Delta t^2)^{1/2} \right)^2 + (\Delta t)^2 = 1, \quad (\text{A.0.39})$$

which means that both physical and computational modes are stable. If $\Delta t = 1$, then both physical and computational modes are same, i.e., $A_+ = A_- = i$. This scheme is stable for $\Delta t = 1$ because both roots represent the exact solution. If $\Delta t > 1$, then the second term is

complex and we have

$$|A_+| = \left| i\Delta t + i(\Delta t^2 - 1)^{1/2} \right| > |\Delta t| > 1, \quad (\text{A.0.40})$$

and the scheme is unstable.



(a) Stability domain. The slope is 2.00133 for u and (b) instability domain. Dashed line showed the line 1.99995 for p . $dt = 0.1, 0.08, 0.05, 0.04, 0.02, 0.01$, for $dt_{\max} < 1$.
0.005, 0.002, 0.001, 0.0008, 0.0005,
0.0002, 0.0001, 0.00005.

Figure A.0.7: Convergence plot for Leapfrog method.

A.0.6 Adam-Bashforth order 3

Explicit scheme of Adam-Bashforth of order three can be written as

$$\varphi^{n+1} = \varphi^n + \frac{\Delta t}{12} (23F(\varphi^n) - 16F(\varphi^{n-1}) + 5F(\varphi^{n-2})). \quad (\text{A.0.41})$$

Applying to the test equation gives

$$\varphi^{n+1} = \varphi^n + \frac{\Delta t}{12} (23i\varphi^n - 16i\varphi^{n-1} + 5i\varphi^{n-2}). \quad (\text{A.0.42})$$

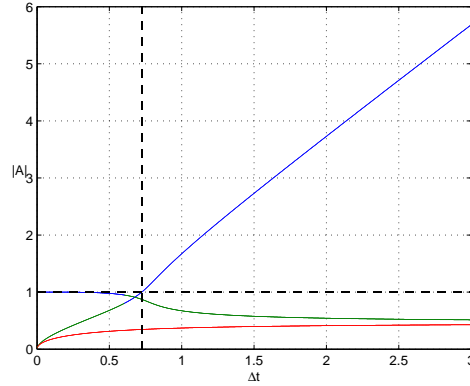


Figure A.0.8: Modulus of amplification factor for the AB-3 scheme as a function of Δt .

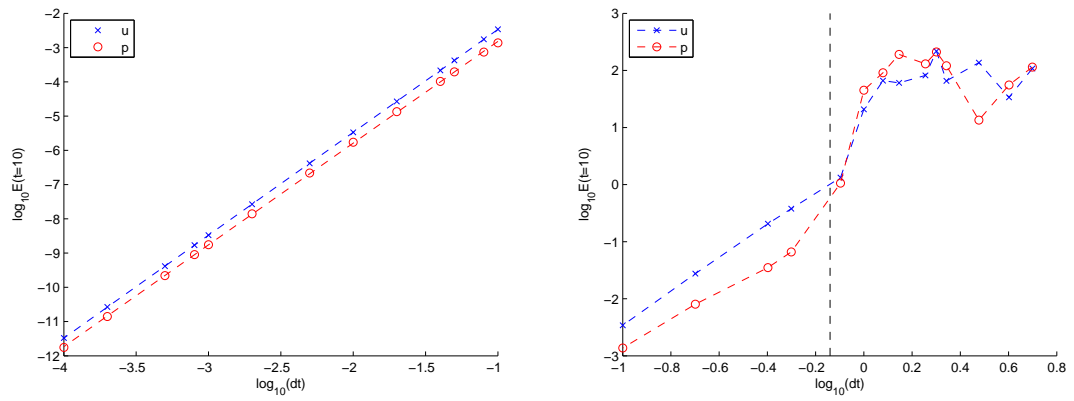
Dividing by φ^n , gives

$$\begin{aligned}
 A &= 1 + \frac{\Delta t}{12} \left(23i - 16i \frac{\varphi^{n-1}}{\varphi^n} + 5i \frac{\varphi^{n-2}}{\varphi^n} \right), \\
 &= 1 + \frac{\Delta t}{12} \left(23i - 16i \frac{1}{A} + 5i \frac{\varphi^{n-2}}{\varphi^{n-1}} \frac{\varphi^{n-1}}{\varphi^n} \right), \\
 &= 1 + \frac{\Delta t}{12} \left(23i - 16i \frac{1}{A} + 5i \frac{1}{A^2} \right),
 \end{aligned} \tag{A.0.43}$$

and equation (A.0.43) is simplify as

$$A^3 - A^2 + \frac{i\Delta t}{12} (-23A^2 + 16A - 5) = 0. \tag{A.0.44}$$

Equation (A.0.44) will give three roots, which represent the one physical mode, and two computational modes. For this scheme, the roots are plotted as a function of Δt as showed in Figure A.0.8. From the figure, we can see that the physical mode is the root where $|A| = 1$ as $\Delta t \rightarrow 0$. The computational modes are represented by the other two roots where they are always stable as $\Delta t \rightarrow 0$. However, one of them will become unstable at approximately when $\Delta t > 0.724$. This instability analysis is graphically shown in Figure A.0.8(b).



(a) Stability domain. The slope is 3.00178 for u and (b) instability domain. Dashed line is the line for 2.97045 for p . $dt = 0.1, 0.08, 0.05, 0.04, 0.02, 0.01, dt_{\max} < 0.724$.
 0.005, 0.002, 0.001, 0.0008, 0.0005,
 0.0002, 0.0001, 0.00005.

Figure A.0.9: Convergence plot for AB-3 method.

Bibliography

- [1] M. Abramowitz and I. A. Stegun. *Handbook of mathematical functions: with formulas, graphs, and mathematical tables*, volume 55. Courier Corporation, 1964.
- [2] D. J. Acheson. *Elementary fluid dynamics*. Oxford University Press, 1990.
- [3] A. Adcroft, C. Hill, and J. Marshall. *Representation of topography by shaved cells in a height coordinate ocean model*. *Monthly Weather Review*, **125**(9):2293–2315, 1997.
- [4] H. Aochi, T. Ulrich, A. Ducellier, F. Dupros, and D. Michea. *Finite difference simulations of seismic wave propagation for understanding earthquake physics and predicting ground motions: Advances and challenges*. In *Journal of Physics: Conference Series*, volume 454, page 012010. IOP Publishing, 2013.
- [5] J. R. Apel, H. M. Byrne, J. R. Proni, and R. L. Charnell. *Observations of oceanic internal and surface waves from the earth resources technology satellite*. *Journal of Geophysical Research*, **80**(6):865–881, 1975.
- [6] A. Arakawa and V. R. Lamb. *Computational design of the basic dynamical processes of the UCLA general circulation model*. *Methods in Computational Physics*, **17**:173–265, 1977.
- [7] A. Arakawa and V. R. Lamb. *A potential enstrophy and energy conserving scheme for the shallow water equations*. *Monthly Weather Review*, **109**(1):18–36, 1981.
- [8] G. B. Arfken and H. J. Weber. *Mathematical methods for physicists*. AAPT, 1999.
- [9] P. Baines. *The generation of internal tides by flat-bump topography*. In *Deep Sea Research and Oceanographic Abstracts*, volume 20, pages 179–205. Elsevier, 1973.
- [10] P. G. Baines. *The reflexion of internal inertial waves from bumpy surfaces*. *Journal of Fluid Mechanics*, **46**(2):273–291, 1971.
- [11] J. Bajars, J. Frank, and L. R. Maas. *On the appearance of internal wave attractors due to an initial or parametrically excited disturbance*. *Journal of Fluid Mechanics*, **714**:283–311, 2013.

- [12] W. Barham, S. Bachman, and I. Grooms. *Some effects of horizontal discretization on linear baroclinic and symmetric instabilities*. *Ocean Modelling*, **125**:106–116, 2018.
- [13] S. Bilbao. *Modeling of complex geometries and boundary conditions in finite difference/finite volume time domain room acoustics simulation*. *IEEE Transactions on Audio, Speech, and Language Processing*, **21**(7):1524–1533, 2013.
- [14] J. Blazek. *Computational fluid dynamics: principles and applications*. Butterworth-Heinemann, 2015.
- [15] J. C. Butcher. *The Numerical Analysis of Ordinary Differential Equations: Runge-Kutta and General Linear Methods*. Wiley-Interscience, New York, NY, USA, 1987.
- [16] D. Cacchione and C. Wunsch. *Experimental study of internal waves over a slope*. *Journal of Fluid Mechanics*, **66**(2):223–239, 1974.
- [17] A. C. Cangellaris and D. B. Wright. *Analysis of the numerical error caused by the stair-stepped approximation of a conducting boundary in FDTD simulations of electromagnetic phenomena*. *IEEE Transactions on Antennas and Propagation*, **39**(10):1518–1525, 1991.
- [18] R. Clarke. *The morning glory: An atmospheric hydraulic jump*. *Journal of Applied Meteorology*, **11**(2):304–311, 1972.
- [19] S. N. Collins, R. S. James, P. Ray, K. Chen, A. Lassman, and J. Brownlee. *Grids in numerical weather and climate models*. In *Climate Change and Regional/Local Responses*. IntechOpen, 2013.
- [20] B. Cushman-Roisin and J.-M. Beckers. *Introduction to geophysical fluid dynamics: physical and numerical aspects*. Academic Press, 2011.
- [21] T. Dauxois, A. Didier, and E. Falcon. *Observation of near-critical reflection of internal waves in a stably stratified fluid*. *Physics of Fluids*, **16**(6):1936–1941, 2004.
- [22] T. Dauxois and W. R. Young. *Near-critical reflection of internal waves*. *Journal of Fluid Mechanics*, **390**:271–295, 1999.
- [23] S. Dobricic. *An improved calculation of Coriolis terms on the C-grid*. *Monthly Weather Review*, **134**(12):3764–3773, 2006.
- [24] K. Dridi, J. S. Hesthaven, and A. Ditkowski. *Staircase-free finite-difference time-domain formulation for general materials in complex geometries*. *IEEE Transactions on Antennas and Propagation*, **49**(5):749–756, 2001.
- [25] D. R. Durran. *Numerical methods for wave equations in geophysical fluid dynamics*, volume 32. Springer Science & Business Media, 2013.

- [26] V. Ekman. *On dead water: the norwegian north polar expedition 1893-1896. scientific results. edited by f*, 1904.
- [27] B. Engquist, J. Häggblad, and O. Runborg. *On energy preserving consistent boundary conditions for the Yee scheme in 2D. BIT Numerical Mathematics*, **52**(3):615–637, 2012.
- [28] C. C. Eriksen. *Observations of internal wave reflection off sloping bottoms. Journal of Geophysical Research: Oceans*, **87**(C1):525–538, 1982.
- [29] D. A. Greenberg, F. Dupont, F. H. Lyard, D. R. Lynch, and F. E. Werner. *Resolution issues in numerical models of oceanic and coastal circulation. Continental Shelf Research*, **27**(9):1317–1343, 2007.
- [30] S. M. Griffies, C. Böning, F. O. Bryan, E. P. Chassignet, R. Gerdes, H. Hasumi, A. Hirst, A.-M. Treguier, and D. Webb. *Developments in ocean climate modelling. Ocean Modelling*, **2**(3-4):123–192, 2000.
- [31] D. J. Griffiths. *Introduction to electrodynamics*. Prentice Hall, 1962.
- [32] S. D. Griffiths. *Kelvin wave propagation along straight boundaries in C-grid finite-difference models. Journal of Computational Physics*, **255**, 2013.
- [33] J. Häggblad and B. Engquist. *Consistent modeling of boundaries in acoustic finite-difference time-domain simulations. The Journal of the Acoustical Society of America*, **132**(3):1303–1310, 2012.
- [34] J. Häggblad and O. Runborg. *Accuracy of staircase approximations in finite-difference methods for wave propagation. Numerische Mathematik*, **128**(4):741–771, 2014.
- [35] U. Harlander. *Towards an analytical understanding of internal wave attractors. Advances in Geosciences*, **15**:3–9, 2008.
- [36] U. Harlander and L. R. Maas. *Two alternatives for solving hyperbolic boundary value problems of geophysical fluid dynamics. Journal of Fluid Mechanics*, **588**:331–351, 2007.
- [37] J. Hazewinkel, N. Grisouard, and S. B. Dalziel. *Comparison of laboratory and numerically observed scalar fields of an internal wave attractor. European Journal of Mechanics-B/Fluids*, **30**(1):51–56, 2011.
- [38] P. Hérelil and R. Laprise. *Sensitivity of internal gravity waves solutions to the time step of a semi-implicit semi-lagrangian nonhydrostatic model. Monthly weather review*, **124**(5):972–999, 1996.
- [39] J. D. Jackson. *Classical electrodynamics*. Wiley, 1999.

- [40] A. Javam, J. Imberger, and S. Armfield. *Numerical study of internal wave reflection from sloping boundaries*. *Journal of Fluid Mechanics*, **396**:183–201, 1999.
- [41] L. Jouve and G. I. Ogilvie. *Direct numerical simulations of an inertial wave attractor in linear and nonlinear regimes*. *Journal of Fluid Mechanics*, **745**:223–250, 2014.
- [42] P. K. Kundu. *Fluid Mechanics*. Elsevier Academic Press, 1990.
- [43] J. Lambert. *Numerical Methods for Ordinary Differential Systems: The Initial Value Problem*. Wiley, 1991.
- [44] J. Lighthill. *Waves in fluids*. Cambridge university press, 1978.
- [45] D. Lilly. *A proposed staggered-grid system for numerical integration of dynamic equations*. *Mon. Wea. Rev.*, **89**:59–65, 1961.
- [46] L. Maas and F. Lam. *Geometric focusing of internal waves*. *J. Fluid Mech.*, **300**:1–41, 1995.
- [47] L. R. Maas. *Wave attractors: linear yet nonlinear*. *International Journal of Bifurcation and Chaos*, **15**(09):2757–2782, 2005.
- [48] L. R. Maas, D. Benielli, J. Sommeria, and F.-P. A. Lam. *Observation of an internal wave attractor in a confined, stably stratified fluid*. *Nature*, **388**(6642):557, 1997.
- [49] M. Mercier, R. Vasseur, and T. Dauxois. *Resurrecting dead-water phenomenon*. *Non-linear Processes in Geophysics*, **18**:193–208, 2011.
- [50] G. I. Ogilvie and D. Lin. *Tidal dissipation in rotating giant planets*. *The Astrophysical Journal*, **610**(1):477, 2004.
- [51] G. Pedersen. *On the effects of irregular boundaries in finite difference models*. *International Journal for Numerical Methods in Fluids*, **6**(8):497–505, 1986.
- [52] J. Pedlosky. *Geophysical fluid dynamics*. Springer Science & Business Media, 2013.
- [53] O. M. Phillips. *The Dynamics of the Upper Ocean*. Cambridge University Press, New York, 1966.
- [54] D. A. Randall. *Geostrophic adjustment and the finite-difference shallow-water equations*. *Monthly Weather Review*, **122**(6):1371–1377, 1994.
- [55] M. Rattray Jr. *On the coastal generation of internal tides*. *Tellus*, **12**(1):54–62, 1960.
- [56] J. W. S. B. Rayleigh. *The theory of sound*. Macmillan, 1896.

- [57] L. F. Richardson. *The approximate arithmetical solution by finite differences of physical problems involving differential equations, with an application to the stresses in a masonry dam. Philosophical Transactions of the Royal Society of London. Series A*, **307–357**, 1911.
- [58] F. S. Robert and S. B. Dalziel. *Internal wave attractors without sloping boundaries. 7th. Int. Symp. on Stratified Flows, Rome, Italy, August 22 - 26, 2011*, 2011.
- [59] J. Russell. *Report of the committee on waves. report of the seventh meeting of the british association for the advancement of science, liverpool (murray j, 1838*.
- [60] M. Simanjuntak, J. Imberger, and K. Nakayama. *Effect of stair-step and piecewise linear topography on internal wave propagation in a geophysical flow model. Journal of Geophysical Research: Oceans*, **114**(C12), 2009.
- [61] D. N. Slinn and J. Riley. *Internal wave reflection from sloping boundaries. Submitted to J. Fluid Mech*, 2001.
- [62] L. St. Laurent and C. Garrett. *The role of internal tides in mixing the deep ocean. Journal of Physical Oceanography*, **32**(10):2882–2899, 2002.
- [63] B. R. Sutherland. *Internal gravity waves*. Cambridge university press, 2010.
- [64] B. R. Sutherland, S. B. Dalziel, G. O. Hughes, and P. F. Linden. *Visualization and measurement of internal waves by synthetic schlieren. part 1: Vertically oscillating cylinder. Journal of Fluid Mechanics*, **390**:93 126, 1999.
- [65] A. Taflove and S. C. Hagness. *Computational electrodynamics*. Artech house publishers, 2000.
- [66] F. D. Tombe. *The centrifugal force and the coriolis force*. 2014.
- [67] A.-K. Tornberg and B. Engquist. *Consistent boundary conditions for the Yee scheme. Journal of Computational Physics*, **227**(14):6922–6943, 2008.
- [68] A.-K. Tornberg, B. Engquist, B. Gustafsson, and P. Wahlund. *A new type of boundary treatment for wave propagation. BIT Numerical Mathematics*, **46**(1):145–170, 2006.
- [69] J. S. Turner. *Buoyancy effects in fluids*. Cambridge University Press, 1979.
- [70] G. K. Vallis. *Atmospheric and oceanic fluid dynamics: fundamentals and large-scale circulation*. Cambridge University Press, 2006.
- [71] K. S. Yee. *Numerical solution of initial boundary value problems involving Maxwell's equations in isotropic media. IEEE Trans. Antennas Propag*, **14**(3):302–307, 1966.